Corrosion Protection by Paint
- Cathodic Disbonding

A THESIS SUBMITTED FOR THE DEGREE OF DOCTOR OF PHILOSOPHY AT THE UNIVERSITY OF OXFORD,

MICHAELMAS TERM, 2010



Huichao Bi

Mansfield College

Department of Materials

University of Oxford

ABSTRACT

Huichao Bi D. Phil. Thesis

Mansfield College Michaelmas Term 2010

Corrosion Protection by Paint

- Cathodic Disbonding

This work investigated cathodic disbonding of an unpigmented phenalkamine-cured epoxy coating on mild steel, EC, exposed to 3.5 wt.% NaCl solution. Scanning Acoustic Microscopy (SAM), Scanning Kelvin Probe (SKP), Electrochemical Impedance Spectroscopy (EIS) and optical microscopy have been combined to conduct this study. Several factors affecting the cathodic disbonding process: Film thickness, Cation mobility, Electrolyte concentration, Temperature, Paint composition, Polarisation and Open circuit potential, have been investigated.

SAM results show that the disbonding of EC with a linear scribe spreads outwards from the defect with blisters forming at the anodes (as shown in SKP potential maps) within the disbond. The disbonded region does not correspond to complete adhesion loss as verified by peel-testing.

Semi-immersion tests show that disbonding under full- and semi-immersion conditions have similar behaviours and both follow parabolic kinetics indicating the disbonding is likely to be controlled by a transport process along the coating/metal interface.

An intact epoxy coated mild steel panel coupled with bare mild steel shows that the cathodic reaction beneath the coating obeys Tafel law.

A mathematical model simulating cathodic disbonding which produces realistic potential files and shows the oxygen reduction is mostly located near the disbond mouth has been developed.

PREFACE

The work presented in this thesis was carried out at the Department of Materials, University of Oxford between October 2007 and October 2010, under the supervision of Prof. John Sykes. No part of this work has been submitted for a degree at this or any other university. Work of others included has been acknowledged and references are given at the end of this thesis.

Extracts of this work have been presented at the following conferences:

- Oral presentation at 51st Corrosion Science Symposium, 2010, Southampton, UK – Winner of the L. L. Shreir Prize for the best presentation.
- Poster presented at "The 60th Annual Meeting of International Society of Electrochemistry", 2009, Beijing, China.

ACKNOWLEDGEMENTS

Special thanks go to my supervisor, Prof. John Sykes, whose guidance, support (patient), encouragement (endless), knowledge (profound), enthusiasm and sense of humour have made this work possible and enjoyable.

I would like to thank Akzo Nobel Pty Ltd. (International Paint) for provision of paint and Chinese Ministry of Education/University of Oxford for provision of a scholarship for my PhD study at Oxford.

I also thank Dr. Paul Jackson and Dr. Reza Tohid, who acted as industrial advisors during various stages of this project. Thanks also go to some members of the department who helped me along the way: particularly Ms Lyn Richmond from the department reception for her kindness which made me feel at home; Mr. Laurie Walton from the main workshop for his ingenious experimental equipment designs and Mr. Richard Cripps for his patient instructions in electronics.

A big thanks goes to my fellow members of the Corrosion Group, Yan, Zalilah, David, Na and Chris, also the visiting student from Spain, Jesus; friends at the Department of Materials and Mansfield College and all the other friends at Oxford.

Finally, to my family, I would like to offer my deepest thanks for providing encouragement needed throughout my education and for their financial support over the years.

Huichao Bi

October 2010

University of Oxford

"Know what you want, otherwise, you have to accept what you get."

CONTENTS

Chapter 1 Introduction 1

1.1 Corrosion 1

1.2 Corrosion Mechanism 1

1.3 Corrosion Protection by Paint 2

1.3.1 Organic Coatings 2

1.3.2 Coating Protection 5

1.3.2.1 Physical barrier properties 6

1.3.2.2 Electrical resistance 8

1.3.2.3 Chemical inhibition 11

1.3.2.4 Adhesion 14

1.4 Coating Failure 16

1.4.1 Cathodic disbonding 17

1.4.1.1 Cathodic Disbonding Characterisation 17

1.4.1.2 Factors affecting cathodic disbonding 22

1.4.1.3 Mechanism of Cathodic Disbonding 34

1.4.2 Blistering 38

1.4.3 Filiform Corrosion 42

Chapter 2 Experimental Method 44

2.1 Introduction 44

2.2 Materials 44

2.2.1 Substrate 44

2.2.2 Organic Coatings 44

2.3 Sample preparation 46

2.4 Techniques 48

2.4.1 Scanning Acoustic Microscopy (SAM) 48

2.4.1.1 Introduction 48

2.4.1.2 SAM Theory 48
2.4.1.3 Functioning Principles 52
2.4.1.4 SAM Examination Setup and Operation 58
2.4.1.5 SAM Image Analysis 60
2.4.2 Scanning Kelvin Probe (SKP) 61
2.4.2.1 Introduction 61
2.4.2.2 SKP Operation Principles 62
2.4.2.3 SKP Experimental Setup 70
2.4.2.3.1 Examination Details 70
2.4.2.3.2 SKP Tip Resolution Test 71
2.4.2.3.3 SKP Calibration 73
2.4.3 Electrochemical Impedance Spectroscopy (EIS) 77
2.4.3.1 Introduction 77
2.4.3.2 EIS Equipment 78
2.4.3.3 AC Circuit Theory 79

Chapter 3 Cathodic Disbonding Characterisation 89
3.1 Introduction 89
3.2 Cathodic Disbonding Characterisation 90
3.2.1 Experimental 90
3.2.2 Results and Discussion 91
3.2.2.1 Full-immersion Tests 91
3.2.2.1.1 SAM and SKP Characterisation 91
3.2.2.1.2 Circular Feature and Blister Discussion 99
3.2.2.1.3 Adhesion tests 103
3.2.2.2 Semi-immersion Tests 108
3.2.2.2.1 SAM and SKP Characterisation 108
3.2.2.2.2 Disbonding Kinetics 118
3.3 Conclusion 120

Chapter 4 An Investigation of Factors Affecting Cathodic Disbonding 122

4.1 Introduction 122

4.2 Factors Affecting Cathodic Disbonding 122

4.2.1 Effect of Film Thickness 122

4.2.1.1 Introduction 122

4.2.1.2 Results and Discussion 123

4.2.2 Effect of Cations 126

4.2.2.1 Introduction 126

4.2.2.2 Results and Discussion 127

4.2.3 Effect of Solution Concentration 131

4.2.3.1 Introduction 131

4.2.3.2 Results and Discussion 131

4.2.4 Effect of Temperature 136

4.2.4.1 Introduction 136

4.2.4.2 Results and Discussion 136

4.2.5 Effect of Polarisation 140

4.2.5.1 Introduction 140

4.2.5.2 Results and Discussion 141

4.2.6 Free Corrosion Potential in the Defect 151

4.2.6.1 Introduction 151

4.2.6.2 Results and Discussion 152

4.2.7 Effect of Paint Composition 153

4.2.7.1 Introduction 153

4.2.7.2 Results and Discussion 154

4.3 Summary of Conclusions 166

Chapter 5 Corrosion Properties of Intact Coatings 169

5.1 Introduction 169

5.2 Experimental 169

5.3 Results and Discussion 171

5.4 Conclusions 175

Chapter 6 Mathematical Model for Cathodic Disbonding 176

6.1 Introduction 176

6.2 Mathematical model for potential and current within the disbond 176

6.2.1 Model development 176

6.2.2 Numerical simulation 180

6.3 Conclusions 185

Chapter 7 Summary of Conclusions and Future Work 186

7.1 Summary of Conclusions 186

7.2 Future Work 189

APPENDIX 191

SKP Data Processing 191

References 194

Chapter 1 Introduction

1.1 Corrosion

Corrosion comes from the Latin *corrodere*, which means “to chew away”, “to attack” [1]. According to the international standard ISO 8044, corrosion is defined as the physicochemical interaction between a metal and its environment which results in changes in the properties of the metal and which may often lead to impairment of the metal, the environment, or the technical system of which these form a part. Corrosion is an interdisciplinary subject, combining elements of physics, chemistry, metallurgy and engineering. The rusting of iron and steel is the most well-known form of corrosion and similar processes occur in other metals. Corrosion also refers to non-metallic materials, such as plastics, concrete and ceramics. It is estimated [1] that every year corrosion destroys one quarter of the world’s annual steel production, which corresponds to about 150 million tons per year, or 5 tons per second.

1.2 Corrosion Mechanism

Corrosion is an electrochemical reaction and under neutral (or alkaline) conditions, for example, when exposed to air and humidity, iron forms rust, FeOOH. The overall reaction can be written as:

$$4\,Fe + 3\,O_2 + 2\,H_2O \rightarrow 4\,FeOOH$$

This is a redox process and can be represented as two half reactions, with one producing electrons and the other consuming them, thus:

$$2\ Fe \rightarrow 2\ Fe^{2+} + 4\ e^{-} \text{ (anodic reaction)}$$

$$O_2 + 2\ H_2O + 4\ e^{-} \rightarrow 4\ OH^{-} \text{ (cathodic reaction)}$$

The iron ions then react with the hydroxyl ions and form iron hydroxide which is soluble but becomes oxidised into rust. This is usually expressed as,

$$4\ Fe(OH)_2 + O_2 \rightarrow 2\ Fe_2O_3 \cdot H_2O + 2\ H_2O$$

It may be (a lot) more complicated in the real corrosion process. However, it is apparent that oxygen and water are necessities for corrosion reactions to occur. If the steel were covered by a film completely impervious to water or oxygen, corrosion would not occur. Application of paint on metals is a convenient and effective way to provide protection from corrosion, but it does not completely exclude either air or water.

1.3 Corrosion Protection by Paint

Today, many types of coatings, organic or inorganic, metallic or non-metallic, are applied to protect metal surfaces from corrosion. The wide range of applications of organic coatings is remarkable, ranging from aeroplanes, ships, automotive cars, construction materials and oil pipelines to food cans.

1.3.1 Organic Coatings

There are usually four types of components found in paints used for corrosion protection: binder, solvent, pigment and additives.

Binder, which guarantees the cohesiveness of the film and its adhesion on the

substrate, is the most important component of any paint. Paints are usually named after the binder they contain, such as alkyd paints, vinyl paints or epoxy paints.

Solvent facilitates the application of a paint in the liquid state by lowering the viscosity. Modern paint formulations increasingly use water as a "solvent" to avoid pollution of the environment and health risks caused by solvent evaporation with the polymer disused as an emulsion.

Pigments in paints can play many different roles, not only supplying colour or enhancing their chemical or physical strength or improving barrier properties, but also acting as a source of inhibitor which can increase the resistance of metal surfaces to corrosion [2]. The mechanism of corrosion control by pigments is complex because of the various roles they play. Some pigments, like micaceous iron oxide and aluminium flakes, which have the ability to separate the metallic substrate from the corrosive medium, act by improving the barrier properties of the coating. Micaceous iron oxide and aluminium flakes which protect by this mechanism generally have a lamellar, flaky or plate-like shape that reduce the permeability to oxygen and water and other corrosive media through the coating [3]. On the other hand, zinc dust pigment provides cathodic protection (sacrificial protection) to the substrate metal. By acting as a sacrificial anode, which uses the principle of bimetallic corrosion, zinc dust cathodically protects a metal structure by forming an electrochemical cell (corrosion cell) in which the metal to be protected acts as the cathode. Other pigments which have a chemical activity, can be classified into four groups according to their mechanism of action [4]. 1. Pigments decrease the rate of anodic reaction by binding

the metal ions produced by corrosion reactions, resulting in the formation of coordination compounds at anodic zones. 2. Pigments decrease the activity of both anodic and cathodic processes by liberating passivating ions. 3. Pigments react with the resin, giving rise to compounds that decrease metal corrosion. 4. Pigment acts by increasing the concentration of OH^- ions in water diffusing through the porous paint.

When pigments are added to a particular coating, the amount added is usually described by the pigment volume concentration (PVC). It has a great effect on corrosion protection [5]. The pigment has to be completely surrounded by the polymer which can fill the voids between the pigment particles and create a protective coating. The PVC is calculated by the following equation:

$$\% \text{ PVC} = 100 * V_{pigment} / (V_{pigment} + V_{non\text{-}volatile\ binder}) \quad \textit{[Equation 1.1]}$$

Where $V_{pigment}$ is the pigment volume and $V_{non\text{-}volatile\ binder}$ is the non-volatile binder volume.

The pigment volume concentration at which value the polymer is just sufficient to fill the voids between the pigment particles is known as the critical pigment volume concentration (CPVC). Below the CPVC, there is enough polymer to fill the voids, whereas, above the CPVC, there is not enough polymer, therefore, if the concentration of the pigment is above the CPVC, some voids between the pigment particles create defects, resulting in high permeability and decreased coating protection ability.

Additives, for instance, dryers, can often accelerate the drying process or better enable the dry coating to withstand the working environment. Also, some, such as hardening agents, stabilising agents, surface active compounds and dispersion agents, can

improve coating flow, emulsification, uniformity, and reduce pigment settling.

Epoxy coatings were developed just after world war II, but were not used until the late 1950s and early 1960s. Epoxy is a thermosetting polymer formed from two chemicals which are "resin" and "curing agent" (also known as "hardener"). These are often described as "two-pack" coatings. The resin consists of monomers or short chain polymers with an epoxide group at either end. The curing agent is generally based upon amines or amides. The selection of curing agent plays an important role in determining the properties of the final cured epoxy, like pot life, dry time, wetting ability and penetration. When the resin and the curing agent compounds are mixed together, the hydrogen from the amine groups react with the epoxide groups causing interlocking structures (a process known as "cross-linking"). Epoxies offer a variety of properties depending upon the molecular structure of the final cross-linked network and its various fillers and pigments. Nowadays, they are widely used to protect steel and concrete structures and due to the adhesion and corrosion resistance, the combination of the epoxy with urethanes for topcoats is one of the major offshore and marine coating systems [6].

1.3.2 Coating Protection

Several mechanisms by which organic coatings protect the underlying metal substrate have been proposed [7-9], but they are often based on two alternative mechanisms put forward by Mayne and Funke. Briefly speaking, Mayne [7, 8] proposed the protective mechanism for unpigmented coatings was "resistance inhibition" which prevent

corrosion occurring (or current flow) as a consequence of the high ionic resistance of coatings; Haagen and Funke [9] asserted that low permeability to water and oxygen and the maintenance of strong adhesion when exposed to water are the essential properties for protective coatings.

1.3.2.1 Physical barrier properties

Organic coating films act as a barrier between the metal substrate and the environment. They can provide protection from corrosion if they are impermeable to corrosive agents, *e.g.* water and oxygen, which are essential for the electrochemical corrosion process, between the metal substrate and the environment. However, it is normally not this case which can be explained from two aspects: 1) there may some defects (*e.g.* pores or scratches) in the coating; 2) the intact organic coatings are permeable to water and oxygen though there is no defect in them. A number of factors may have influence on the physical barrier effect of coatings (permeability of a coating to water or oxygen) [10]. The permeability depends primarily on the structure (*e.g.* cross-linking) and the chemical composition and properties of the binder. The presence of pigments or fillers and the interaction between polymer and filler also have some effect on the permeability of the coating. The smaller the permeability is, the better is the protection ability of the coating.

Mayne [11] studied the rates of water and oxygen transport through paint films and found that the rate of water supply is at least an order of magnitude greater than that required to support corrosion on unpainted steel and for oxygen, actual corrosion rates

are substantially lower than permitted by oxygen transport, thus it was suggested that for most paints, water and oxygen diffusion cannot be rate controlling for corrosion. It was proposed that the ability of a coating to provide corrosion protection is due to its introduction of a path of high ionic resistance in between the metal and the environment which impedes the movement of ions from the anode to the cathode and thus limits the corrosion current to a low value. In other words, ion transport through the coating is rate controlling. In a later paper, Mayne and Mills [12] made the following statement: "In order for a polymer film to protect a metallic substrate against corrosion, the film should possesses low permeability to ions, that is to say it should have a high electrolytic resistance."

In earlier work, Bacon, Smith and Rugg [13] had already demonstrated that coated panels with high DC resistance showed good performance. This will be further discussed in section 1.3.2.2.

Armstrong *et al.* [14] investigated the behaviour of unpigmented epoxy-polyamine protective coatings upon a coated steel substrate exposed to NaCl solution. They showed that the water permeation rate through unpigmented epoxy-polyamine membranes was much higher than that needed to sustain the cathodic currents observed. And it was again suggested that ion transport through the protective layer is the most likely current limiting factor, which corresponds well with Mayne's assertion. However, the pathway suggested for ions through the films was through interconnected water-filled cracks and crevices, rather than through the homogeneous interior of the film.

Leidheiser and Kendig [15] studied the mechanism of corrosion of polybutadiene-coated steel in aerated sodium chloride and noted that the transmission rate of water and the permeation rate of oxygen through the coating was very high. This suggests that water and oxygen permeation cannot be rate controlling.

However, Guruviah [16] measured oxygen permeability through alkyd, epoxy and chlorinated rubber coatings and found that for pigmented paints, the oxygen permeability was much lower than that required to corrode base steel. Thus, it was concluded that the diffusion of oxygen through the film may control the corrosion rate of panels coated with pigmented paint, but for the corrosion rate of panels with unpigmented epoxy, it was not controlled by oxygen diffusion.

1.3.2.2 Electrical resistance

Bacon *et al*. [13] examined the electrolytic resistance of over 300 organic coatings on mild steel under immersion conditions and observed that good corrosion protection was obtained when the resistance of the paint film was greater than $10^8\ \Omega{\cdot}cm^2$, poor protection (visible corrosion) was obtained when the resistance of the coating was less than $10^6\ \Omega{\cdot}cm^2$. It was also reported that the higher the resistance of the coating on a substrate after a period of immersion into salt solution, the better the protection it afford to the underlying metal, see Fig.1.1. It should be recognised that in practice, these results include both the DC resistance of the coating and polarisation of reactions on the substrate.

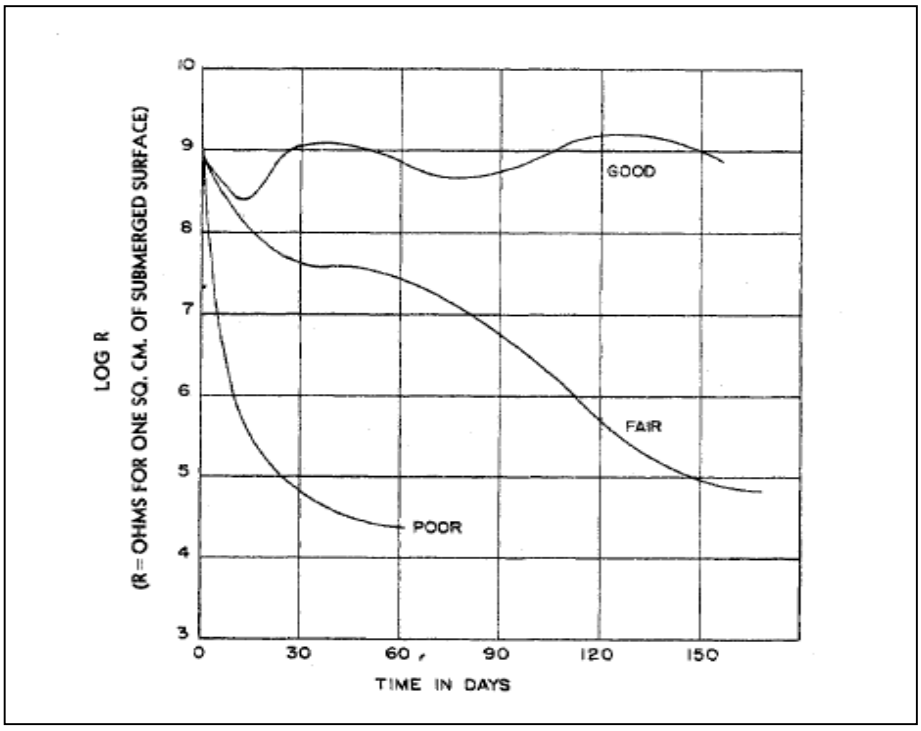


Fig.1.1 Schematic resistance behaviour of coatings on immersed metals [13]

It was proposed by Kinsella and Mayne [17] that there are two distinct modes of ionic conduction through polymer films. The first was *I*-, or *inverse*-type conduction, where the resistance of a film increased with the increased concentration of the solution. This type of conduction was in line with that identified by Bacon, Smith and Rugg [13]. The second mode is identified as *D*-, or *direct*-type conduction where the film resistance decreases with the increasing solution concentration. The existence of the *D*- and *I*-type conductions of free films was also reported by Maitland and Mayne [18].

Mayne and Scantlebury [19] examined the distribution of *D*- and *I*-type areas across films of a pentaerythritol alkyd, a phenol-formaldehyde tung oil and a polyamide-cured expoxide varnish. It was found that the films investigated were remarkably heterogeneous and had a distribution of both *D*- and *I*-type areas over the

film, which they believed to be caused by differences in cross-linking density within the film.

In 1975, Mayne and Mills [20] examined the resistance of alkyd tung oil and epoxy films attached to mild steel during corrosion process and found that corrosion occurred at *D*-type areas, where the resistance of the coating was in the range of 10^6 - 10^8 $\Omega \cdot cm^2$. There was no corrosion detected under *I*-type areas with the coating resistance of the order of 10^{12} $\Omega \cdot cm^2$.

Wapner *et al.* [21] state that most polymeric coatings or adhesives act as effective barriers for any kind of hydrated ionic species due to the low dielectric constant and the restricted transport within the polymer's free volume. Thus the transport of hydrated ions is mainly occurring along coating/metal interfaces, starting from locations where the ion-containing electrolyte builds a three phase boundary line with the polymer and the metal phase. Scanning attenuated total reflection infrared spectroscopy (ATR-IR), scanning kelvin probe (SKP), along with the complimentary Fourier transform infrared spectroscopy (FTIR) techniques have been used to study water and ion transport at polymer/metal interfaces. It was shown that interfacial diffusion of water, in the case of epoxy adhesive on iron, is about two orders of magnitude faster than the transport through the adhesive itself and similar transport kinetics at the interface has also shown by hydrated ions.

Electrochemical Impedance Spectroscopy (EIS) is a non-destructive electrochemical technique that has been extensively employed to evaluate the electrical resistance of polymer coated metals and to characterise the breakdown of organic coatings for

decades [22-26]. Early applications of EIS for the study of the corrosion protection by organic coatings have been reported by Beaunier *et al.* [22], Scantlebury *et al.* [23], Kendig *et al.* [24] and Mansfeld [25]. The increasing literature makes it easy to see that EIS has become an important technique to study the protective organic coatings.

More recently, Whyte and Sykes [26] have successfully applied EIS to investigate the corrosion behaviour of a zinc-iron bimetallic couple coated with unpigmented polyvinyl butyral (PVB) during intermittent exposure to salt solution. EIS was able to measure the response of the specimen with electrodes coupled and also for the individual electrodes with the impedance of the coating showing different behaviour on the two substrates. Based on a combination of results from EIS, zero-resistance ammetry (ZRA) and SKP, it was concluded that for the PVB coated zinc-steel couples immersed in NaCl solution, the corrosion current flowed between the anode and cathode both through the coating and via a very thin solution layer at the coating/substrate interface.

1.3.2.3 Chemical inhibition

The chemical inhibition of the corrosion process is generally as a consequence of the presence of corrosion inhibitors. A corrosion inhibitor is a chemical compound which is added to the environment to reduce the rate of corrosion. The presence of a corrosion inhibitor reduces the rate of corrosion by affecting the rate of the partial electrochemical reactions involved.

Zinc chromate and zinc phosphate are commonly used as anti-corrosive pigments

which act as corrosion inhibitors. In the past, zinc chromate was one of the most frequently used anticorrosive pigments in the formulation of primers. However, due to the environmental concern and toxicity of CrO_4^{2-}, it is now severely restricted by environmental protection requirements. Zinc phosphate, which is known as a "green" pigment (non-toxic) compared to toxic pigments like chromate, has been proposed as a possible alternative to replace zinc chromate. Pigments, like zinc phosphate, are sparingly soluble and release low concentration of inhibitive ions.

Barraclough and Harrison [27] first proposed the use of zinc phosphate as an inhibitive pigment and claimed that it acts as an anodic inhibitor which slowly phosphates the metal surface causing it to become passive.

Turgoose [28, 29] studied the inhibitive action of zinc-chromate, zinc-phosphate and zinc-molybdate pigments, which are traditionally defined as mixed inhibitors. It was found that the zinc-anion mixtures provided a more effective performance than the individual components. The zinc-anion mixture is better at resisting oxygen diffusion than that formed from just zinc cations, therefore gives better corrosion protection. In later work [30], it was proposed that zinc phosphate acts as a cathodic inhibitor because its solubility is far too low for passivation, which is contrary to the position of Barraclough and Harrison.

Amirudin *et al.* [31] suggested that under the chosen conditions, zinc phosphate acts as a mixed inhibitor on steel, inhibiting both anodic and cathodic reactions, but it is better in inhibiting the cathodic reaction. It was also supposed that the major limitation of zinc phosphate as an inhibiting pigment seems to be its poor solubility.

From a scientific point of view and the environmental consideration, the use of ion-exchange pigments is another alternative to replace chromates as inhibitive pigments.

Goldie [32] evaluated the performance of calcium exchanged silica anti-corrosive pigment (Ca/silica) in solvent-based alkyd, chlorinated rubber and two-pack epoxy primer for mild steel. He found that Ca/silica performed better than a range of alternative non-toxic pigments (a typical one is zinc phosphate), and *equivalent* to both zinc and strontium chromates. It was thus proposed that the mechanism for corrosion control with Ca/silica is that calcium, released from the silica surface, migrates to the paint/metal interface where a thin, inorganic layer is deposited which is essentially impermeable to moisture/ions and hence prevents the corrosion reaction from proceeding. Fig.1.2 demonstrates the calcium release and the corrosion protection afforded by calcium exchanged silica.

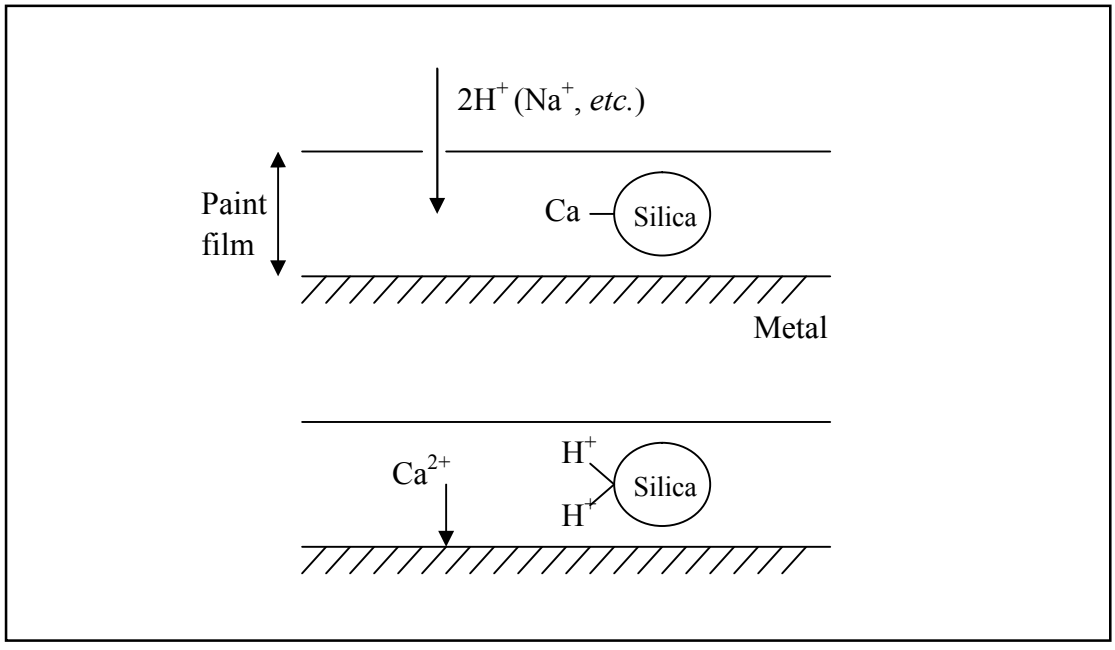


Fig.1.2 Schematic diagram showing calcium release process (After [32]).

A similar behaviour to that observed with calcium silicate was reported by Armstrong and Zhou [33]. They investigated the behaviour of a modified silicate as an inhibitor for the corrosion of iron and proposed that the modified silicate pigment is an effective inhibitor to prevent corrosion of iron by generating Ca^{2+} and polysilicate anions in solution which are adsorbed at the iron surface. This adsorption inhibits a) oxygen reduction, b) hydrogen evolution and c) iron dissolution.

Chico *et al.* [34] studied the anticorrosive behaviour of alkyd paints formulated with vanadate-hydrotalcite (HT/V) (anionic) and calcium silica (Ca/silica) (cationic) ion-exchange pigments by means of natural and accelerated corrosion tests (humidity, salt spray and Kesternich, 0.21 SO_2) and EIS. A comparison has been made between these ion-exchange pigments and a traditional zinc chromate pigment. It was found that none of the ion-exchange pigments equalled the anticorrosive behaviour of the zinc chromate in the different tests. The anionic pigment seems to present good behaviour in chloride environments (salt spray, NaCl solutions, *etc.*) while the cationic pigment performs well in the humidity condensation and SO_2 tests.

1.3.2.4 Adhesion

Adhesion is viewed as an important property of organic coatings for corrosion protection. Much work [35-39] has been carried out in the past few years to study the mechanism involved in the coating/metal adhesion and the measurement of adhesion. Bullett and Prosser state that “the ability to adhere to the substrate throughout the desired life of the coating is one of the basic requirements of a surface coating, second

only to the initial need to wet the substrate" [40].

Funke [41-44] proposed that the adhesion of a coating may be one of the possible means of corrosion protection based on the fact that corrosion cannot occur in the absence of an electrolyte connecting the anodic and cathodic areas under the coating. Funke also described adhesion as the most important and decisive property of a coating and stated that it would not be possible to form a sufficiently thick layer of liquid to support corrosion reaction without significant reduction in adhesion.

Dickie [37] states that "maintenance of adhesion under environmental exposure is a key performance parameter used to evaluate the protective capability of corrosion-protective paint systems."

Stratmann *et al.* [45] studied the corrosion properties of a defect-free unpigmented alkyd resin coating on iron and concluded that the corrosion rate will stay at very low values, as long as the polymer adheres to the substrate and no separate aqueous phase is formed.

However, Schwenk [46] conducted a study of the relationship between adhesion and corrosion on a number of coated samples immersed in sodium chloride solutions, and found that loss of adhesion had no adverse effect on the corrosion protection.

Walker [47-49] too examined the adhesion behaviour of a large number of commonly used surface coatings after water exposure and found that adhesion loss was rapid and in certain cases fell to very low levels. Despite this, certain coatings which exhibited low wet adhesion were shown to perform well in service conditions. It was thus concluded that there was no real correlation between adhesion behaviour and

corrosion resistance and that adhesion is unlikely to play a major role in terms of the overall corrosion protection.

Jin, Gowers and Scantlebury [38] evaluated the adhesion behaviour and salt-spray resistance of a chlorinated rubber coating, and found that no appreciable adhesion loss was observed despite the observation of substantial corrosion. This contradictory evidence caused them to question the relationship between adhesion and corrosion protection.

Though there are conflicting evidences and debates over the importance of adhesion in corrosion prevention, it is still an important parameter showing the reduction of mechanical force between coatings and substrates in the presence of water and also the spread of corrosion. It can be concluded that in practice it is important to have adequate adhesion of the coating to the metal substrate and there is still much to be learned about the adhesion properties of coatings and the relationship between adhesion and corrosion protection.

1.4 Coating Failure

Many possible mechanisms can contribute to the degradation of organic coatings, such as poor or inadequate preparation, aging of the polymer, cathodic disbonding, formation of blisters and filiform corrosion. The last three are talked about in more detail below.

1.4.1 Cathodic disbonding

Many coated steel products are subjected to coating damage, *e.g.* by stone impact or scratches, leading to exposure of bare metal to the environment. If a coated metal with a defect on it is continuously immersed in salt solution, the coating adjoining the defect may separate from the substrate metal. This loss of adhesion is as a result of the cathodic reaction (oxygen reduction) which in the presence of alkali metal cations causes the generation of a strong alkalinity (*e.g.* NaOH. The final reduction product is OH^-, which combines with Na^+ yielding NaOH.) at the coating/metal interface and is known as "cathodic disbonding", also known as "cathodic delamination". It is the main degradation mechanism for cathodically protected coated steel structures exposed to seawater and also occurs in the case of organic coated steel under free corrosion conditions.

It has been a challenge in the last few decades to study and to understand the processes occurring at the coating/metal interface during cathodic disbonding. A large amount of tests have been conducted. Nevertheless, the complex mechanism of cathodic disbonding of an organic coating has not yet been fully understood.

1.4.1.1 Cathodic Disbonding Characterisation

- **Scanning Acoustic Microscopy (SAM) Examination**

SAM is an in-situ technique that senses changes in mechanical properties of the interface allowing the examination of the polymer/metal interface during cathodic disbonding. Chapter 2 will give a detailed description.

Kendig *et al.* [50] conducted a study on cathodic disbonding of hydroxyl-terminated polybutadiene on steel using SAM to make in-situ images of the extension of the cathodic disbonding from the scribe mark. It was found that circular features appeared within the disbond and propagated away from the scribe with increasing exposure time. Initially, they believed that these circular features were the results of the local swelling of the polymer and electroosmotic influx of electrolyte which caused the surface of the polymer to be raised [51] and in a further testing [52], they suggested that there is an irreversible localised change in the elastic properties of the coating due to the alkaline hydrolysis of the polymer.

Crossen *et al*. [53] used SAM for the examination of changes at the interface during the cathodic disbonding of an epoxy-polyamide coating from mild steel exposed to NaCl solution. It was observed that a region of disbonding developed adjacent to the scribe within the first hour following by the growth of blisters ahead of the disbonded front.

- **Scanning Kelvin Probe (SKP) Measurement**

SKP is another powerful tool to characterise the process occurring underneath the coating during cathodic disbonding. It is a non-contact, non-destructive vibrating capacitor device for measuring the Work Function (WF) differences between a sample and the probe tip, which also allows localised measurements of the electrochemical properties from beneath the film (See Chapter 2 for a detailed description for SKP). Stratmann [54] first introduced it to measure the localised corrosion potential.

Stratmann *et al*. [45, 55] analyzed the spatial distribution of the corrosion potential

measured by SKP as a function of time for samples with defects covered by the solution but the remainder of the coating exposed to humid air (to permit SKP measurements). Samples used to carry out these studies have been prepared as shown in Fig.1.3.

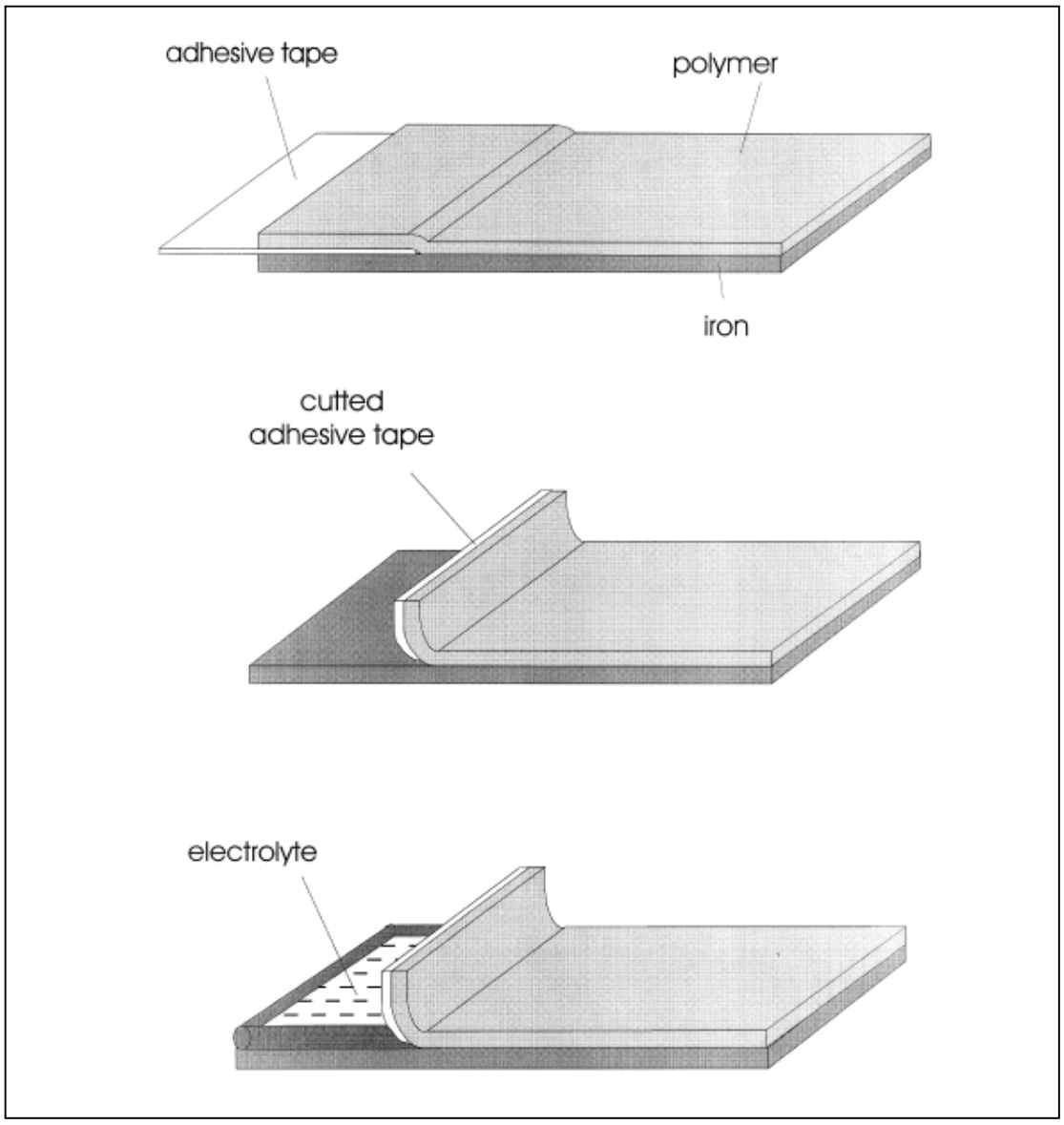


Fig.1.3 Sample preparation for the delamination experiments. [56]

Fig.1.3 shows typical procedures of the sample preparation for disbonding tests. Part of the specimen was covered by an adherent tape. Then the whole sample was covered

with coating by spraying. After one week's curing and drying, the tape was removed from the surface with a well defined and sharp artificial defect created. A two component epoxy modelling paste was then used to build the reservoir for the solution. By this sample set up, only the defect is wetted, with the rest of the coating exposed to high humidity, so the transport of ions is only possible from the reservoir along the coating/metal interface.

The disbonding kinetics was studied by tracking the delamination front from the SKP potential profile. Fig.1.4 gives a typical potential distribution profile as a function of distance and disbonding time, given against Saturated Hydrogen Electrode (SHE) by suitable calibration. It was observed that there is a large potential difference between the active metal surface at the defect and the intact coating/metal interface and the distinct potential increase marks the delamination front. Besides, the potential in the delaminated area does not show as an equipotential surface but increases towards the disbonding front.

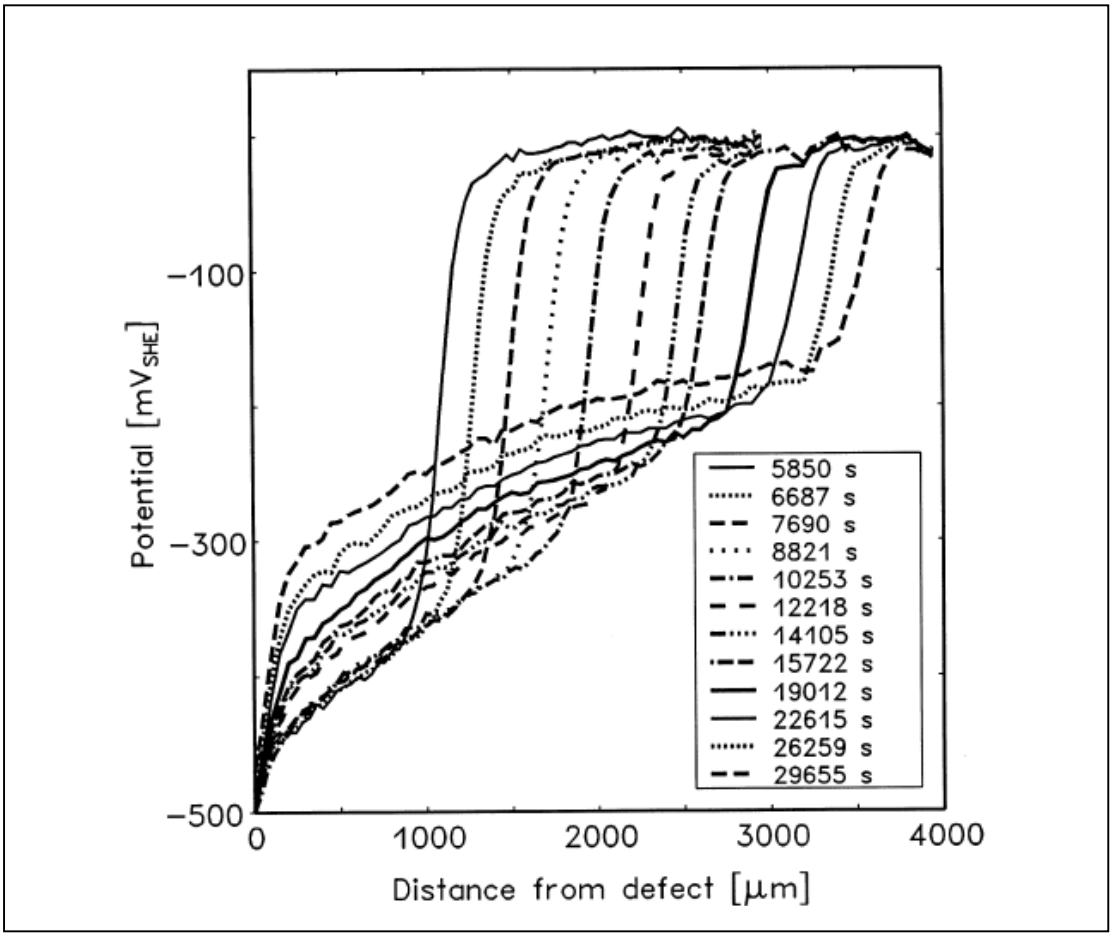


Fig.1.4 Typical potential distribution (measured by SKP) in air for different disbonding times (An unpigmented epoxy-ester coating on cold rolled steel with the defect covered with 0.5M KCl solution). [56]

Fürbeth and Stratmann [57-59] examined the delamination of amine-modified epoxy-ester films on zinc galvanised steel substrates both from a defect with intact zinc layer and from a defect down to steel. By using SKP, the disbonding kinetics and influence of CO_2 were successfully studied by following the progress of the delamination front as described above.

Following the method of Stratmann *et al.* [45, 55, 57, 60], Williams and McMurray [61] employed SKP to carry out a study on mechanism of corrosion-driven disbonding process affecting polyvinyl butyral (PVB) coatings adherent to the intact zinc surface of hot-dip galvanised (HDG) steel. It was found that an electrochemical

delamination cell was established after placing aqueous sodium chloride solution onto the coating defect. Also it was observed that the delamination of unpigmented PVB coatings follows parabolic kinetics (disbonding distance is linearly increased with $\sqrt{t}$) with cation migration in the interface electrolyte layer being the rate-determining step. They also reported that the pH of the underfilm electrolyte is ≥ 10 and failure of the polymer/metal bond results from a combination of base-catalyzed PVB hydrolysis, dissolution of a zinc (hydr)oxide film, and electro-osmotic pressure.

Reddy *et al*. [62, 63] and Doherty and Sykes [64] conducted studies on the mechanism of degradation of organic coatings by using SAM and SKP together. They reported that the combination of the SKP measuring the electrochemical activity with the SAM measuring the physical change is a powerful way to get better understanding of coating breakdown.

1.4.1.2 Factors affecting cathodic disbonding

- **Disbonding Kinetics (Time Dependence)**

Several researches [65, 66] have shown that for a circular defect, there is a linear relationship between the disbonded area and exposure time, or for a linear defect, a linear relationship between disbonding distance and $\sqrt{time}$ was found, indicating a parabolic relationship between the disbonded distance and the exposure time. When plotting the disbonded area versus time, a "delay time" which is derived from the intercept with the time axis is usually found before the initiation of the disbonding. The slope of the linear line is the "disbonding rate constant". The delay time is usually

attributed to the ingress of water, oxygen or ions into the coating for corrosion to start. Leidheiser and Wang used tape to remove the coating that had disbonded before making their disbonded area measurements [67] and observed a linear relationship between the disbonded area and time for the cathodic disbonding of an alkyd coating on steel [65].

Sharman *et al*. [68] examined cathodic disbonding of both unpigmented and pigmented chlorinated rubber coatings from steel under free corrosion conditions. When the disbonded distance was plotted against the square root of the exposure time, a linear relationship was found. Here the tests clearly measured only areas of complete adhesion loss (*i.e.* with unpigmented chlorinated rubber coatings, disbonding was measured at intervals by visual observation based on the subsequent examination showing the light region around the exposed metal corresponding to a zone of total adhesion loss; for the pigmented coating, "zig-zag" defects were prepared to determine the distance to which adhesion had been lost). The delay time was shortened after exposure to distilled water, so they conclude that water uptake controls delay time.

Skar [69] and Knudsen [70] studied cathodic disbonding of two model epoxy coatings and it was found that both of these two coatings showed a linear relationship between the disbonded area and exposure time. These results are in accordance with the results reported by Leidheiser *et al*. [65] and Addison, Kendig and Jeanjaquet [51].

Leng *et al.* [55] studied cathodic disbonding of an unpigmented epoxy-ester on cold rolled steel using a SKP. The disbonding front was determined as previously

described (See Page.20) for the SKP potential profile results, Fig.1.4 [56] and it was found the disbonding distance followed a $\sqrt{time}$ dependence, Fig.1.5.

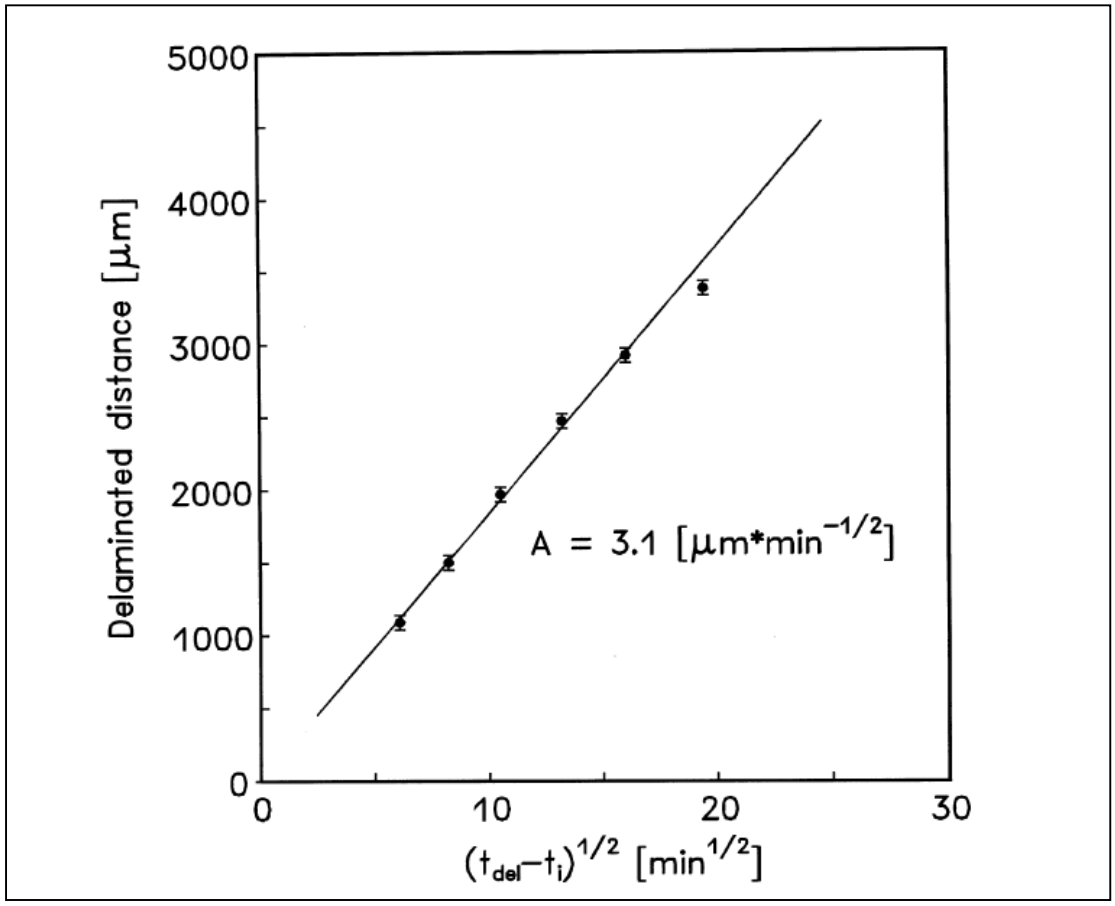


Fig.1.5 Plot of the delaminated distance *vs.* $\sqrt{t}$. Where t_{del} is the time passed after addition of the electrolyte to the defect; t_i is the incubation time and A is the slope of the plot for $t \gg t_i$. [55]

Fig.1.5 shows that the progress of the disbonding front is linearly proportional to $\sqrt{t}$. It was therefore suggested by Leng *et al.* that diffusion perpendicular to the coating cannot be the rate-determining step for the delamination reaction for the reason that this diffusion path does not depend on the distance to the defect. And it was proposed that the transport of ions parallel to the interface from the defect to the delamination front is most likely to be the rate-determining step.

However, Watts and Castle [71] in an earlier study on the kinetics of cathodic

disbonding of epoxy powder coatings on steel substrates with different surface finishes observed a logarithmic relationship between disbonded area and time rather than a linear dependence on time during an initial exposure period which shifted to a linear fit after this period, see Fig.1.6.

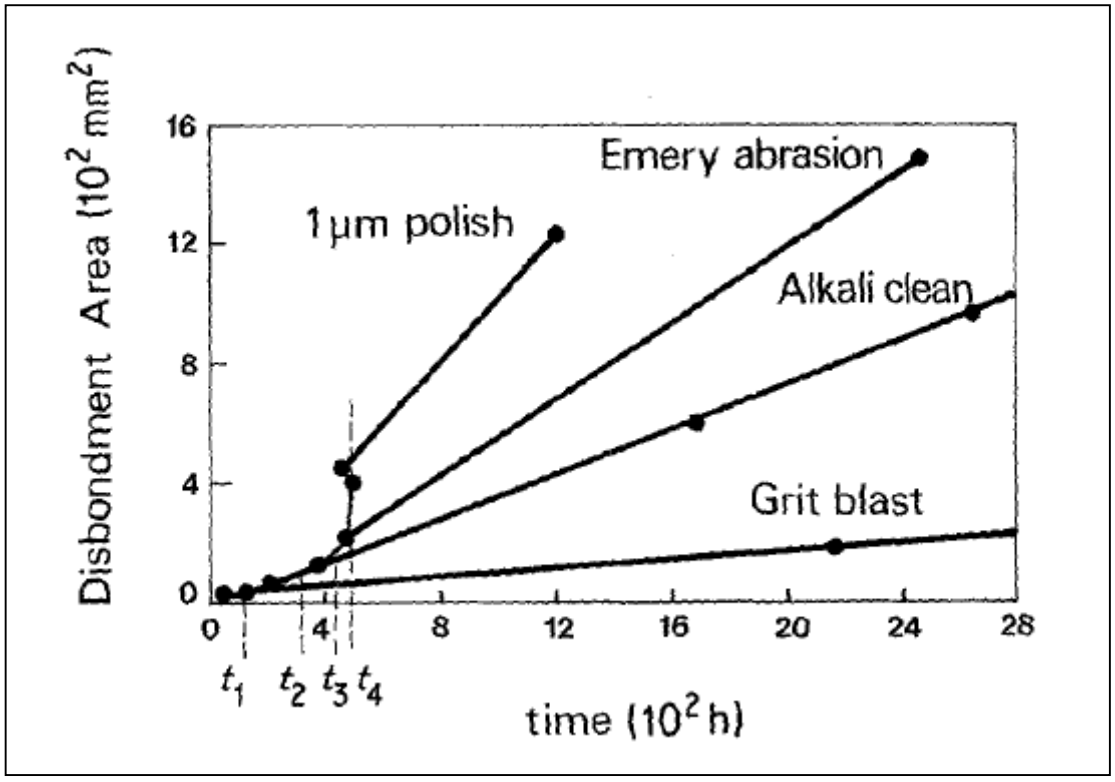


Fig.1.6 Overall scheme for the kinetics of cathodic disbonding. t1, t2, t3 and t4 represent the times at which the change from logarithmic to linear rate occur, for in turn, grit-blasted, alkali-cleaned, emery-abraded and polished substrate. [71]

It can be seen from Fig.1.6 that there is a marked difference in disbonding rate depending on the substrate surface profile. The overall model for delamination proposed [71] is that the rate-controlling step passes from oxide reduction to the geometric area of the cathode (corresponding to the logarithmic part in Fig.1.6) and finally to coating/metal interface diffusion.

- **Dry Film Thickness (DFT)**

Jin *et al*. [72] studied the cathodic disbonding of a chlorinated rubber lacquer of

different film thicknesses and reported that the disbonding rate decreased linearly with increasing DFT when the DFT increased up to 100 μm but if the coating is above 100 μm thick, the disbonding rate is independent of the DFT.

Skar and Steinsmo [73] studied cathodic disbonding of an epoxy-polyamide coating from steel and found that the disbonding rate decreased linearly with increasing film thickness in the range of 80 – 300 μm. While Sharman *et al*. [68] investigated the effect of film thickness on cathodic disbonding of an unpigmented chlorinated rubber coating from steel under free corrosion condition and observed that the disbonding rate constant decreased very little with the film thickness.

Leidheiser *et al.* [74] reported that the rate of cathodic disbonding of polyurethane decreased with increasing coating thickness in the range of 10 – 20 μm. While in a later paper [65], Leidheiser *et al.* studied the disbonding of an alkyd coating (142 μm thick) on steel and observed that the disbonding rate dropped to a low value when the thickness of the topcoat exceeded 90 μm. Whereas, the disbonding rate of the primer plus topcoat did not change much with film thickness for thicknesses > 50 μm. Fig.1.7 shows the results.

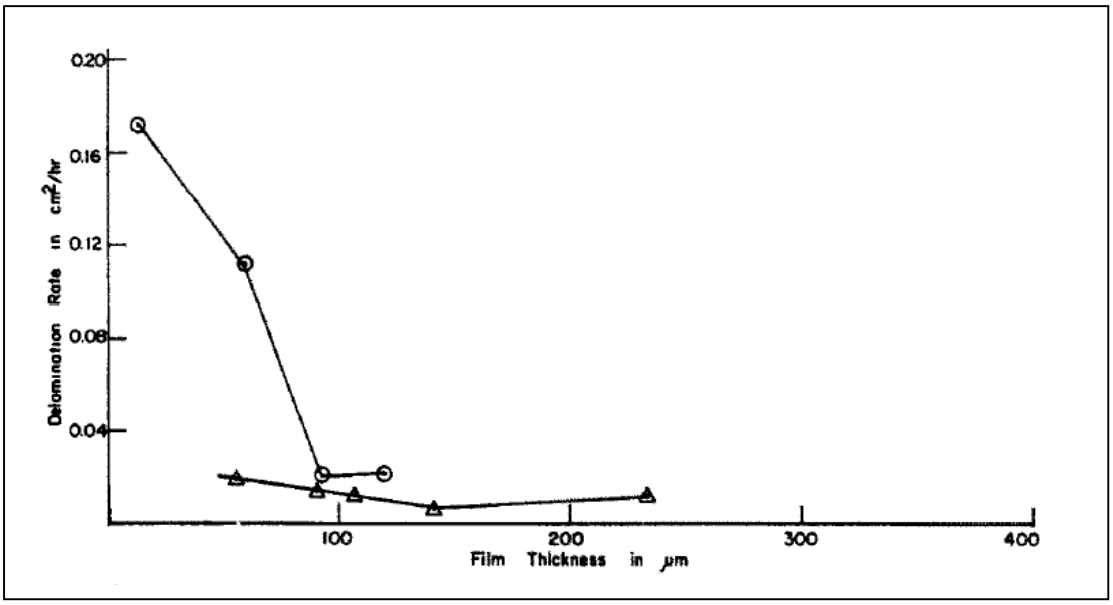


Fig.1.7 The delamination rates of an alkyd coating on steel polarised at -0.8V in aerated 0.5M NaCl as a function of film thickness. o – Topcoat only and Δ - Primer plus topcoat. [65]

- **Effect of Cations**

Several studies have been dedicated to the study of the effect of cations. Leidheiser *et al*. [65] reported that the disbonding rate of polybutadiene coatings on steel increases with the cation type in the sequence of LiCl < NaCl < KCl < CsCl and is linearly related to the diffusion coefficient of these chlorides in solutions.

Mcleod [75] has conducted cathodic disbonding tests of uniformly cross scratched coated steel panels, both with and without the application of cathodic polarisation. Unpigmented chlorinated rubber, unpigmetned epoxy, unpigmented vinyl and alkyd finish coatings have been investigated. It was stressed that the processes that occur under both testing conditions are similar. He also found that the speed of delamination of the unpigmented coatings in 0.5M alkali metal chloride solutions follows the sequence of LiCl < NaCl < KCl < CsCl. This observation is in agreement with earlier work of Leidheiser *et al.* [65].

Sharman *et al*. [68] examined cathodic disbonding of an unpigmented chlorinated rubber and a primer containing iron oxide pigment from steel which was exposed to NH_4Cl, LiCl, NaCl, KCl, CsCl or $SrCl_2$ solutions. It was found that $SrCl_2$ and NH_4Cl solutions only produced slow disbonding rates, unrelated to cation mobility or coating type; while for the alkali metal chlorides, it was reported that the rate of disbonding of unpigmented lacquer showed a strong dependence on cation mobility, but the pigmented coating did not, as shown in Fig.1.8. Thus, it was proposed that the controlling process changes from ion transport along the interface to oxygen diffusion along the same path when pigment is added. This corresponds well with the Guruviah's conclusion [16].

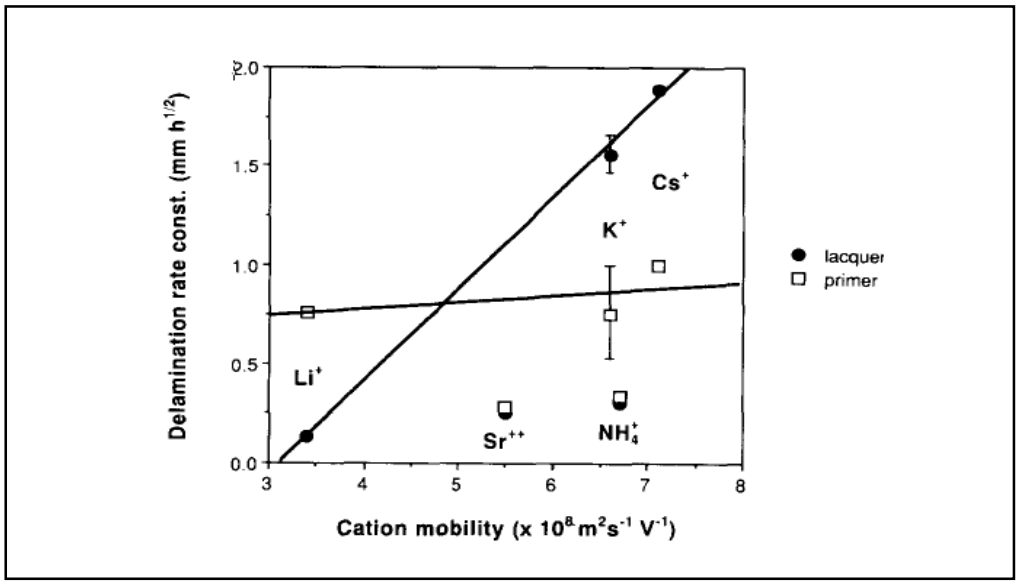


Fig.1.8 Influence of cation mobility on the rate of disbonding from mild steel for lacquer and primer coatings in 0.5M chloride solutions. (Duplicated tests-no error bar if results coincide.) [68]

Note that the y axis of Fig.1.8 does not truly give a "rate" as units are not in time^{-1}. If the disbonding is controlled by ion transport, then a linear relationship between the "disbonding rate constant" (mm·h$^{-1/2}$, as shown in Fig.1.8) with $\sqrt{mobility}$ is what

would be expected.

Leng *et al.* [55] studied the effect of type of cations on cathodic disbonding of an unpigmented epoxy-ester on cold rolled steel and found that the larger the hydrated cation, the slower the observed delamination rate, *i.e.* in the sequence of $Li^+ < Na^+ < K^+ < Cs^+$. The effect of anion type on the delamination kinetics was also studied with the defect covered by a 0.5M solution of NaBr, NaCl, NaF and $NaClO_4$. It was found that the type of anion does not significantly affect the disbonding which suggests the anion does not play any essential role within the mechanism of cathodic disbonding, provided corrosion occurs.

Knudsen and Skar [70] investigated the cathodic disbonding of an epoxy coating, 250μm thick, in LiCl, NaCl and CsCl solution and reported that the disbonded area was linearly increased with the molar conductivity of the cation.

- **Effect of Electrolyte Concentration**

Leidheiser and Wang [67] have studied the effect of electrolyte concentration (0.125M, 0.5M and 1.0M NaCl solutions) on cathodic disbonding of a polybutadiene film. It was found that the disbonding rate *decreased* with increased electrolyte concentration (0.125M > 0.5M > 1.0M), which was attributed to the decreased water activity and oxygen solubility in the more concentrated electrolyte.

Leng *et al.* [55] studied the influence of electrolyte concentration on the delamination rate of an unpigmented epoxy-ester (50 – 60 μm thick) on cold rolled steel using a SKP. The defect was covered by different NaCl-containing solutions of 0.1M, 0.5M and 1.0M, with deionized water as a comparison. The disbond was determined as

previously described from Volta-potential profile (like Fig.1.4). It was observed that the concentration of cations has a remarkable influence on the disbonding rate and the disbonding rate *increases* with the increased ionic strength of cations within the solution, which is in the sequence of 1M > 0.5M > 0.1M > Deionized water (=0, there is no disbonding in deionized water). It was also reported that there is no disbonding observed when the concentration of cations are below 0.05M, which was explained by a threshold concentration of ions at the coating/metal interface required for a galvanic element to be established. For the very dilute solution, not enough ions are incorporated into the interface to initiate the disbonding.

Sørensen *et al*. [76] studied the effect of the concentration of cations in the bulk solution on the extent of cathodic disbonding of epoxy coatings in solutions of potassium chloride ranging from deionised water to 2M. It was observed that no disbonding occurred when the concentration of the solution was below 0.005M which is explained by the fact that the corrosion rate will be low when the ionic strength is low and the resistance of the aqueous solution towards transfer of galvanic current is high. In the range of 0.01 to 0.5M, the extent of cathodic disbonding is proportional to the concentration, while from 0.6 to 2M, the disbonding rate *decreases* with the increasing concentration, which is ascribed to the lower oxygen concentration in the more concentrated salt solution. Fig.1.9 shows the disbonding distance as a function of salt concentration in the range of 0 - 2M.

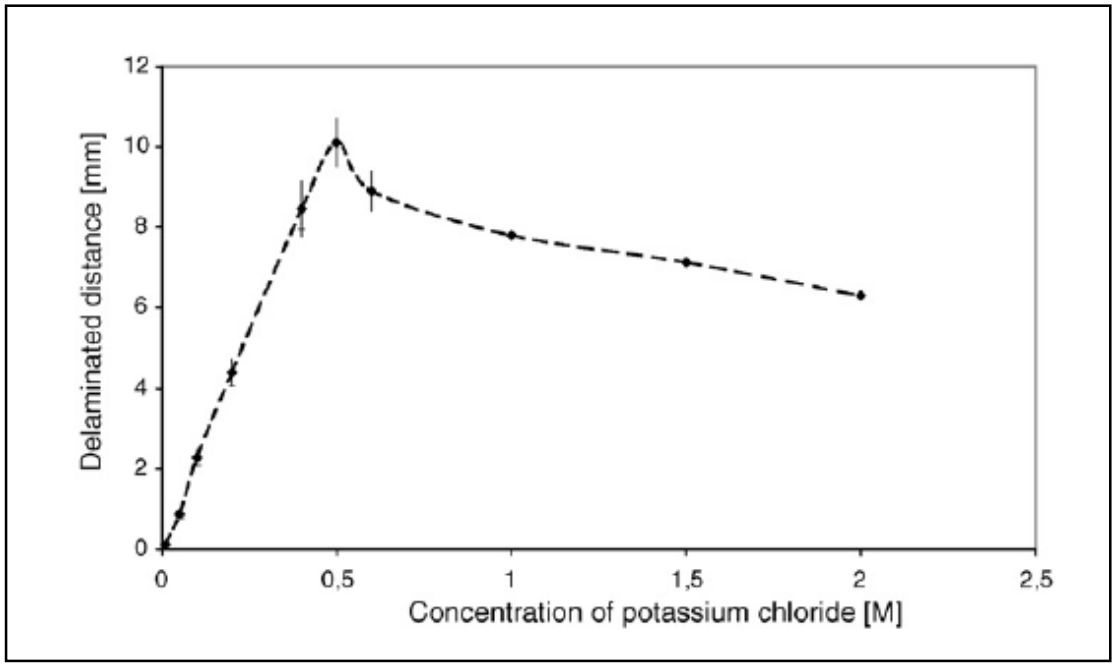


Fig.1.9 Delamination as a function of concentration of potassium chloride solutions after 9 weeks of exposure at free corrosion potential and 18℃. [76]

Apparently, there is a transition from control by ion transport to control by oxygen diffusion.

- **Effect of Temperature**

Leidheiser *et al*. [77] have studied the effect of temperature on the cathodic disbonding of polybutadiene coatings on a galvanized steel substrate immersed in 0.5M NaCl and reported that the activation energy for the disbonding process is 39.7 kJ/mol, which they concluded is consistent with a rate-controlling step that involves diffusion.

Skar and Steinsmo [73] studied the effect of temperature on cathodic disbonding of an epoxy-polyamide coating and an activation energy of 33 ± 5 kJ/mol was found for the cathodic disbonding process which corresponds to E_A values for *D*-type conductivity.

- **Cathodic Polarisation**

When a cathodic potential is applied, the more negative the potential, the slower the anodic reaction but the faster the cathodic reaction. Though corrosion at the anode is prevented, the cathodic reaction is accelerated, leading to more severe disbonding.

Jin *et al*. [72] studied the cathodic disbonding of chlorinated rubber lacquer coatings on mild steel under cathodic polarisation and reported a linear relationship between applied potential and the disbonding rate.

Steinsmo and Skar [78] conducted a study on the cathodic disbonding of an epoxy coating, 255 ± 12 μm thick, immersed in 0.5M NaCl solution with potential applied. The results showed that the disbonded area increased more quickly as the potential decreased.

More recently, Sørensen *et al*. [76] investigated the effect of cathodic polarisation on the cathodic disbonding of epoxy coatings immersed in seawater and reported that the disbonding distance increased linearly with the increasing applied potential, ranging from -745 mV to -1400 mV, when ions can penetrate the coating from solution, but cathodic polarisation does not affect cathodic disbonding when potential is controlled only at the defect site (by creating a separate compartment) so that ionic transport is restricted to the coating/steel interface.

- **Transport Path and Rate-limiting factor**

Many researches have been carried out to study the transport path during cathodic disbonding.

Leidheiser [79] reported that for a thin polybutadiene system, the pathway for the cation transport was through the coating and ion transport was the rate-controlling

step.

Skar and Steinsmo [73] studied several factors affecting the cathodic disbonding of an epoxy-polyamide coating on steel and found that the disbonding rate decreased linearly with increasing dry film thickness (80 – 300 μm) and was dependent on the cation type in the electrolyte. Three possible routes were proposed as the transportation routes for the cation species. Fig.1.10 gives the illustration of these routes. Route 1 is laterally along the coating/metal interface; Route 2 is through the coating which has already disbonded and Route 3 is through the intact coating which is in advance of the disbonding front. It was suggested that Route 1 is unlikely to be the main transportation path due to the strong dependence on film thickness; Route 3 is excluded after comparison of the charge transport and disbonded area which showed that these two processes have different cation dependence, dry film dependence and temperature dependence, and therefore, it was suggested that migration along Route 2 is the remaining path.

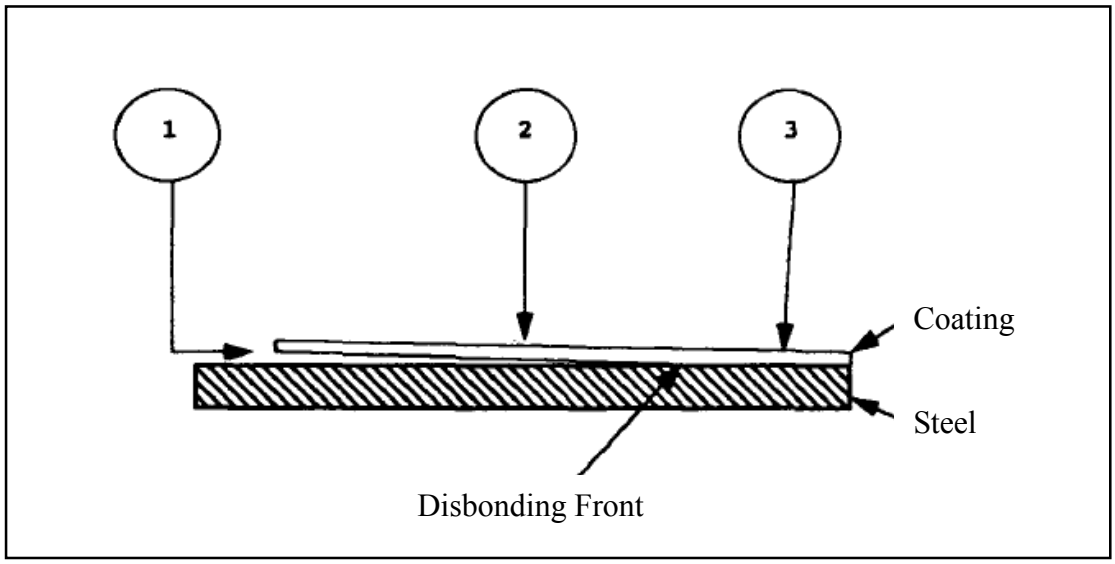


Fig.1.10 Possible migration routes on a coated specimen with a defect. [73]

Luo *et al*. [80] studied the cathodic disbonding of a 500 μm thick pigmented polyurethane coating from steel in 3.5% NaCl solution using Electrochemical Impedance Spectroscopy (EIS). To separate the measurements of the cathodic disbonding process from the influence of the impedance of the artificial defect, double-cylinder electrolyte cells were designed. It was reported that for a thick pigmented polyurethane coating, the more important transport pathway for reactive species is along the coating/steel interface rather than through the coating.

Deflorian and Rossi [81] investigated the transport mechanism through polyester coatings on phosphatised steel during cathodic disbonding by using EIS. A double electrochemical cell was applied in order to separate the solution in contact with the defect and the solution in contact with the rest of the intact organic coating. It was found here that Li^+ and Na^+ diffuse mainly through the defect whereas the smaller hydrated ions K^+ and Cs^+ diffuse through the coating. The proposed reason for the different behaviours is the different dimensions of the hydrated cations, with K^+ and Cs^+ being smaller.

1.4.1.3 Mechanism of Cathodic Disbonding

The mechanism of cathodic disbonding of organic coating has been extensively studied for several decades. It is apparent from examination of the literature that cathodic disbonding, like many other phenomena observed with protective organic coatings, varies from system to system. Therefore, no one model is up to now universally applicable to explain the mechanism of cathodic disbonding.

It is generally believed [14, 15, 82] that the major driving force for cathodic disbonding in corrosion processes in the presence of air is the cathodic reaction, which is the cathodic reduction of oxygen,

$H_2O + 1/2\ O_2 + 2\ e^- = 2\ OH^-$ (the predominant reaction)

Or possibly the evolution of hydrogen,

$2\ e^- + 2\ H_2O = 2\ OH^- + H_2$

if the driving force is enough.

Leidheiser *et al*. [65] concluded that the occurrence of the cathodic disbonding process is because of the high pH generated by the cathodic reaction, with $H_2O + 1/2\ O_2 + 2\ e^- = 2\ OH^-$ as the dominant reaction for cathodic disbonding. They also reported that in the absence of oxygen, no disbonding occurred. Oxygen reduction occurs under the paint, giving rise to a significant increase in the pH in the interfacial region between the paint and the metal substrate if alkali metal cations are available. This can be supported by Ritter and Kruger [83], who reported that the pH is greater than 14 as measured at the delaminated edge from underneath the organic coating where the cathodic reaction occurs.

Koehler [84] presented that the root cause for cathodic disbondment of protective organic coatings was the displacement of the coating by a high pH aqueous film between the coating and the substrate.

However, Leng *et al.* presented an idea that reactive intermediates formed at the coating/metal interface during oxygen reduction are more destructive than OH^-. They studied the disbonding rate of an unpigmented epoxy-ester (50 – 60 μm thick) on cold

rolled steel using a SKP and proposed that the polymer, which is chemically destroyed during oxygen reduction, forms a gel-like structure that severely limits the mechanical adhesion to the substrate and also acts as a pathway for diffusion at the interface [55]. In a later paper [85], they reported that the reason for the loss of adhesion is due to the reactive intermediates formed during oxygen reduction. The reactions that results in the intermediates are as follows,

$$O_2 + e^- \rightarrow O_2^{-\cdot},$$

$$O_2^{-\cdot} + H^+ \rightarrow O_2H^{\cdot},$$

$$O_2H^{\cdot} + e^- \rightarrow O_2H^-,$$

$$O_2H^- + H^+ \rightarrow H_2O_2,$$

$$H_2O_2 + e^- \rightarrow OH^{\cdot} + OH^-$$

$$\text{and } OH^{\cdot} + e^- \rightarrow OH^-$$

The disbonding rate in an alkaline environment (NaOH solution) in the absence of oxygen was compared with the disbonding rate in the presence of oxygen but with the defect covered with NaCl solution. It was observed that the disbonding rate in the former condition was considerably slower than the latter one. Thus, it is suggested that OH^- is not rate-determining for the overall disbonding reaction. This has been confirmed by studies carried out by Grundmeier and Stratmann [86], which proved that the coating/metal interface is destroyed by a strong oxidative attack that can only be caused by the intermediates of the oxygen reduction reaction rather than by an alkaline attack.

A recent study by Sørensen *et al*. [87] investigated the influence of free radicals and

peroxides on the rate of cathodic disbonding by incorporating free radical scavengers and peroxide decomposers into various generic types of coatings. It was found that the addition of free radical scavengers led to a significant reduction in the extent of cathodic delamination of epoxy and coal-tar epoxy coatings, a limited effect on bituminous coatings and limited or no improvements for the acrylic, chlorinated rubber and polysiloxane coatings, which was believed to be the free radicals being engaged in the mechanism of cathodic delamination. The different behaviour of the various types of coatings was explained by the ranking of the stability of the hydrogen atoms in the polymer toward reaction with free radicals.

Sharman *et al*. [68] conducted a study on the cathodic disbonding of chlorinated rubber coatings from steel under free corrosion conditions and proposed that migration of cations along the coating/substrate interface controls the disbonding for lacquer coatings, whereas for pigmented coatings, it is oxygen-diffusion controlled. This agrees with Sørensen *et al*. [87] that the mechanism of the cathodic disbonding of chlorinated rubber can not be explained by the free radicals due to the limited influence of the addition of free radical scavengers into the coating on the disbonding rate as described above.

Skar and Steinsmo [73] tested several factors affecting the cathodic disbonding of epoxy films and concluded that the transport of cations through the film where the film is already disbonded is the rate controlling factor for the disbonding process.

Stratmann *et al.* [21, 45, 55, 56, 85] suggested that during cathodic delamination, a galvanic element forms between a defect in the polymer acting as the local anode and

the defect border acting as local cathode. As a consequence, oxygen reduction takes place at the intact metal oxide/polymer interface next to the defect, leading to the destruction of the interface and loss of adhesion of the polymer. In a recent work, Hausbrand *et al.* [88] also proposed that cathodic disbonding is the fastest mechanism causing the destruction of the metal oxide/polymer interface. A key parameter that controls the formation of the local galvanic element at the disbonding front is the potential gradient between the defect and the intact metal oxide/polymer interface, as it constitutes the driving force for the galvanic coupling and the potential gradient falls (the potential at the disbonding tip, E_{tip}, increases) as delamination progresses, leading to slower disbonding and parabolic kinetics as seen.

1.4.2 Blistering

Blistering is one of the first visible signs to show insufficient protection by organic coatings during corrosion. It is reported [89] that corrosion underneath an organic coating will be almost inevitably accompanied by blistering.

The mechanism of blister formation during the corrosion process has been widely studied and four main mechanisms have been proposed:

- Blistering by volume expansion due to swelling [90, 91];
- Blistering due to gas inclusion or gas formation [92];
- Osmotic blistering [93, 94];
- Electroosmotic blistering [95, 96].

Blistering by volume expansion due to swelling. It has been suggested that when

swelling of the coating occurs because of water absorption, blisters may form and water may collect at the coating/metal interface. Prosser and Bullett [97] doubted whether this is really a common mechanism for blister formation. Funke [98] also doubted it and states that "Considering the viscoelastic properties of paint films it is hard to understand why stresses arising from the absorption of such small amounts of swellant should not be relieved by relaxation processes before local detachment and blister formation may occur. Moreover it would be expected that by volume expansion due to swelling wrinkling would result rather than blister formation, as is observed when paint films are exposed to suitable organic solvents. There is also no reason why stresses due to volume expansion by swelling should not result in a delamination of the whole film rather than in the formation of discrete local blisters."

Blistering due to gas inclusion or gas formation. Blisters may develop due to the incorporation of air bubbles or volatile components in the film on paint preparation or application. These blisters are not necessarily confined to the interface, but when they are, they can cause corrosion to occur.

Osmotic blistering. For osmotic processes to take place the film must be semi-permeable, *i.e.* permeable to water but impermeable or at least strongly permeation-retardant to dissolved, osmotically active substances [98]. The driving force for osmotic blistering is the presence of a soluble species, typically a salt at the coating/substrate interface. Salts may be present on contaminated substrate or generated (as above) by the corrosion process. A concentrated solution is created with the penetration of water from the coating to the interface, and the difference in

concentration of the soluble salt between inside and outside provides osmotic pressure to drive water from the coating surface to the interface and thus a blister is formed. The osmotic mechanism is considered to be the most important mechanism responsible for the blister formation of organic coatings on steel substrates [99] and may explain most cases of blistering.

Van der Meer-Lerk and Heertjes [100], who compared permeation rates measured by the rate of volume increase on blistering with those obtained directly from permeation experiments, suggested that the osmotic mechanism is probably the most common mechanism by which blisters form, especially where the metal is contaminated by salt before painting.

An outstanding example of osmotic blistering was cited by an unidentified discussion participant at the Corrosion 81 meeting in Toronto [101]. A ship was painted in Denmark and made a voyage immediately thereafter across the Atlantic and into the Great Lakes. When it reached port, a blister pattern in the form of a handprint was observed above the water line. Apparently, the paint was applied over a handprint. No blistering occurred during exposure to seawater because of the high salt content of the water, but when the ship was exposed to fresh water (the Great Lakes), the osmotic forces became significant and blistering occurred.

Three different ways for osmotic blistering occurring have been raised by Funke [98]. These are: blistering due to phase separation during film formation; blistering due to paint defects, and blistering adjacent to scribes. But basically for most of the cases, these blisters are cathodic blisters. In electrochemical corrosion, oxygen supplies as a

cathodic reactant with formation of OH^- anions. For the balance of the ionic charges, cations may migrate to the cathodic areas (or OH^- anions) and on exposure to salt solutions, like NaCl solutions, NaOH will be formed, which is responsible for the alkaline aqueous solution present in blisters. An increase of osmotic pressure in the blistering area may result in a rapid dilution with water and the growth of the blister.

Whereas it is widely agreed that the osmotic mechanism is by far the most important one for blistering of paint films observed during practical performance, it is often highly speculative what type of osmotic active substance is present at the coating/substrate interface [98].

Electroosmotic blistering. This has been proposed as a possible mechanism of blistering [95, 96]. Under the influence of a potential gradient, water may move through a membrane or capillary system, resulting in blisters.

Mayne [102] conducted a research on blistering (anodic or cathodic) on a corroding metal substrate and proposed that the type of blisters depended on the permselectivity of the coating. He also analysed the blister fluid under polystyrene films and concluded that only 6 percent of the fluid accumulated because of osmosis, 4 percent as a consequence of the hydration of ions and the remaining 90 percent was due to electroosmosis, *i.e.* diffusion of liquid through the film towards a region, where the water concentration is higher, driven by an electrical potential difference.

Castle and Watts [103] suggested that the polymer-metal bond is attacked by the highly alkaline solution accumulated at the metal surface which is formed by hydroxyl ions generated by the cathodic reduction of oxygen under the coating

combining with cations that carry the ionic current. For blistering to proceed, the delaminating site requires water, oxygen for the cathodic reaction, and cation migration.

1.4.3 Filiform Corrosion

Sharman [104] firstly used the term filiform corrosion (FFC) in 1944 to describe filamentary trails of corrosion product forming on organic-coated steel surfaces at high relative humidity in air. Filiform corrosion is a thread-like, superficial corrosion which advances on metal surfaces underneath coatings [105]. The filaments consist of an actively corroding head followed by an inactive tail. Filament heads are electrolyte-filled, containing metal cations and aggressive anions, such as Cl^-, and exhibit a low pH towards their leading edge caused by cation hydrolysis; filament tails are filled with dry, porous corrosion product. On steel, the head of the filament is usually blue, blue-green, or gray, and the tail is rusty red, indicating the head is deaerated while the tail is aerated.

The appearance of FFC varies as a consequence of several factors including: high relative humidity [98], coating defects where salts may come into contact with exposed metal [105], the presence of intermetallic particles (IMPs) [106, 107], the presence of oxygen [108] and the permeability of the coating to allow for water diffusion to the active head [108, 109]. Leth-Olsen and Nisancioglu [110] studied the filiform corrosion behaviour of aluminium sheet and suggested that surface processing, including rolling and annealing, which plays a critical role in the surface

composition and structure, in turn, greatly affected the alloy susceptibility to FFC.

The mechanism of coating disbondment in iron filiform corrosion have been discussed in a number of publications, nevertheless, it still remains unclear.

Williams and McMurray [111] investigated the initiation and propagation of filiform corrosion on PVB-coated iron following contact with aqueous group (I) chloride salts by using in-situ SKP and ex-situ SIMS measurements. Because of the similarity of filament propagation velocities observed beneath cathodically delaminated and intact PVB coatings, it was concluded that cathodic delamination cannot be a rate determining step in the propagation of FFC on PVB-coated iron.

Filiform corrosion will not be expected under the immersion condition of this work.

Chapter 2 Experimental Method

2.1 Introduction

This chapter is to introduce the system studied and the techniques used in this work. Basically, the system studied here is epoxy coatings on mild steel and three techniques are mainly used to conduct this study: Scanning Acoustic Microscopy (SAM), Scanning Kelvin Probe (SKP) and Electrochemical Impedance Spectroscopy (EIS). They are also backed up by the traditional technique: Optical Microscopy. The preparation of test specimens along with the principles of operation, theory behind those three techniques and experimental set up are discussed here.

2.2 Materials

2.2.1 Substrate

Cold rolled mild steel Q-panels, from Q-Lab Corporation, ground on one side, 0.8 mm thick, 102 mm wide and 152 mm long are used in this work. These panels are made from standard low-carbon, cold-rolled steel complying with ASTM A-366 and QQS-698 and have a roughness of 20 – 50 micro-inches (0.51 – 1.27 μm) for the ground surface, 1/4 hard temper and 372.3 MPa tensile strength.

2.2.2 Organic Coatings

Most experiments in this work have been performed with an unpigmented epoxy coating. The detailed information about this coating is as following: epoxy resin

DER660-X80 ex Dow chemicals EEW 397 supplied as 80% solution in xylene. The amine curing agent is a proprietary in-house phenalkamine epoxy adduct with an equivalent weight of 291 and stoichiometry 71%. The solvent is a mixture of xylene and butanol, 3:1 by volume. Unpigmented epoxy and curing agent are mixed in the proportion of 2.42:1 by weight.

For some experiments, pigmented epoxy coatings have also been used. For pigmented epoxy (Epoxy/Talc and Epoxy/Talc/Zinc Phosphate), the curing agent is added at 3.99:1 by weight.

Paint	**Vol % Solid**	**Wt % Solid**	**PVC**	**Wt % Pigment**	**Specific Gravity**	**Fillers/Extenders/ Pigments**
Unpigmented Epoxy (EC)	54	60.92	0	0	1.007	-
Epoxy/Talc (ET)	54	66.73	20.87	25.68	1.1823	Talc (Tixogel)
Epoxy/Talc/ Zinc Phosphate (ETZ)	54	66.97	20.88	26.2	1.1906	Talc (Tixogel)- Zinc Phosphate Dihydrate

Table.2.1 Details of pigment content (Talc: Average particle size 12.8 μm, Zinc Phosphate Dihydrate: Average particle size 7.5 μm).

All coatings in this work are provided by International Paint Ltd..

2.3 Sample preparation

Cold rolled mild steel Q-panels with a ground surface were degreased with acetone and dried. An epoxy coating was applied with a steel rod (7 mm in diameter) using the draw-down method with gaffer tape acting as a gauge that controlled wet-film thickness (2 layers of gaffer tape gave a dry film thickness of 40 ± 10 μm), Fig.2.1. The coating was cured at ambient temperature in a dust free environment for at least 2 weeks before testing. After drying, the dry film thickness (DFT) of the coatings was measured by a SHEEN SS. 1200 film thickness gauge. Samples with particular thicknesses were selected as required and cut to the size of 7 cm [L] × 5 cm [W]. An electrical wire was soldered to the sample to allow tests with SKP, Fig.2.2. The back and the edges were sealed with a hot mixture of beeswax/colophony (4:1 by weight) and a layer of gaffer tape on the top (to avoid breaking of the mixture of beeswax/colophony). For disbonding tests, a linear defect (10 mm [L] × 1.5 mm [W]) was created at the centre of each sample in a direction parallel to its shorter side using a sharp chisel-edged cutter. A downward force was applied to penetrate the coating until the bare substrate steel was exposed. All defects were visually inspected for cleanness and uniformity.

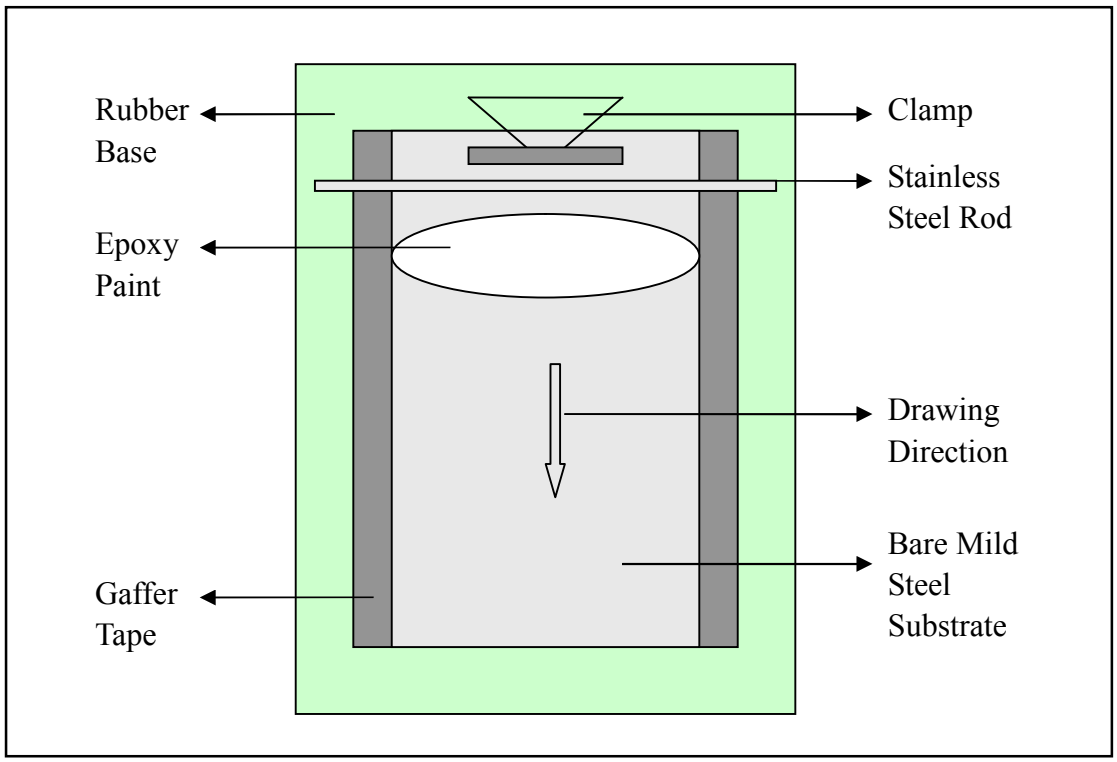


Fig.2.1 Schematic diagram of the draw-down application

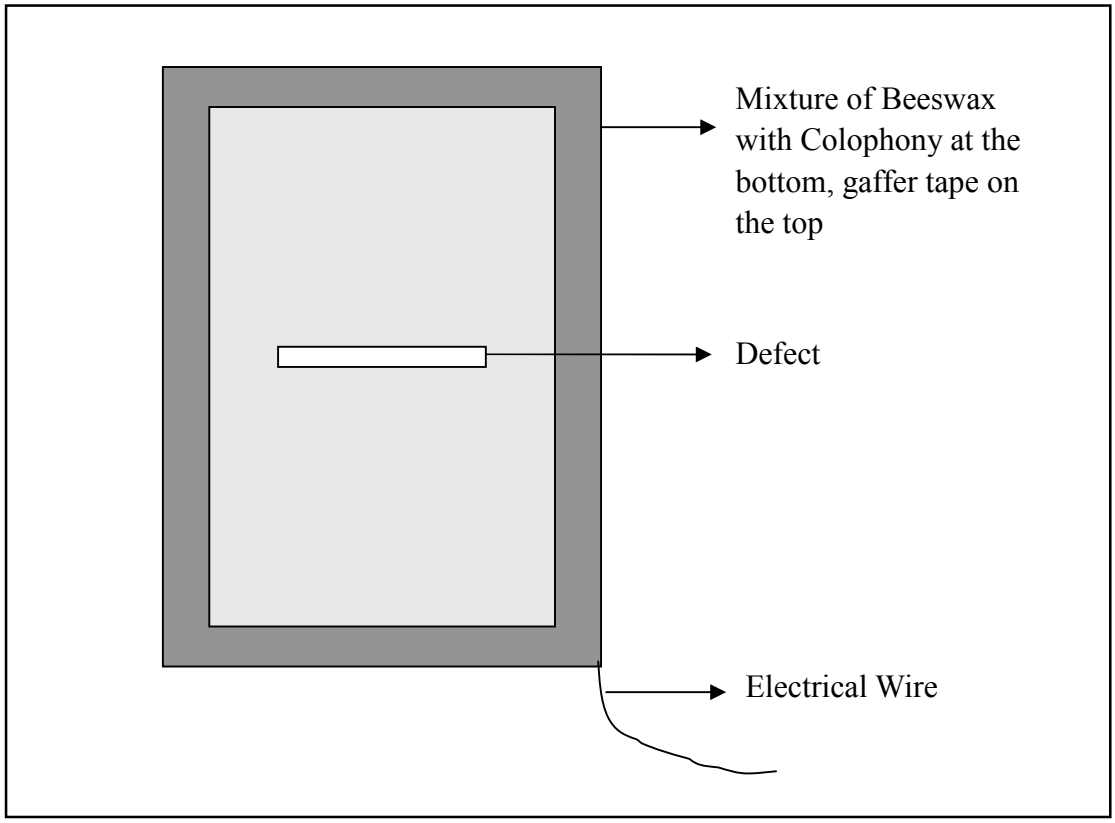


Fig.2.2 Schematic diagram of coated sample with defect

2.4 Techniques

2.4.1 Scanning Acoustic Microscopy (SAM)

2.4.1.1 Introduction

The first SAM was developed in 1974 by Lemons and Quate [112]. It has wide applications in biological and medical research, the semi-conductor industry, and in ceramic and polymer studies. One of the great advantages of the scanning acoustic microscope lies in the ability to penetrate through materials which are optically opaque and produce contrast which arises from variation in elastic properties. In this work, SAM is used to monitor the propagation of disbonding and the growth of blisters underneath the organic coating. By studying the coating/metal interface with SAM, we could learn more about the early stage of disbonding of the coating and corrosion process of the metallic substrate.

2.4.1.2 SAM Theory

The functioning principle of SAM is as shown in Fig.2.3.

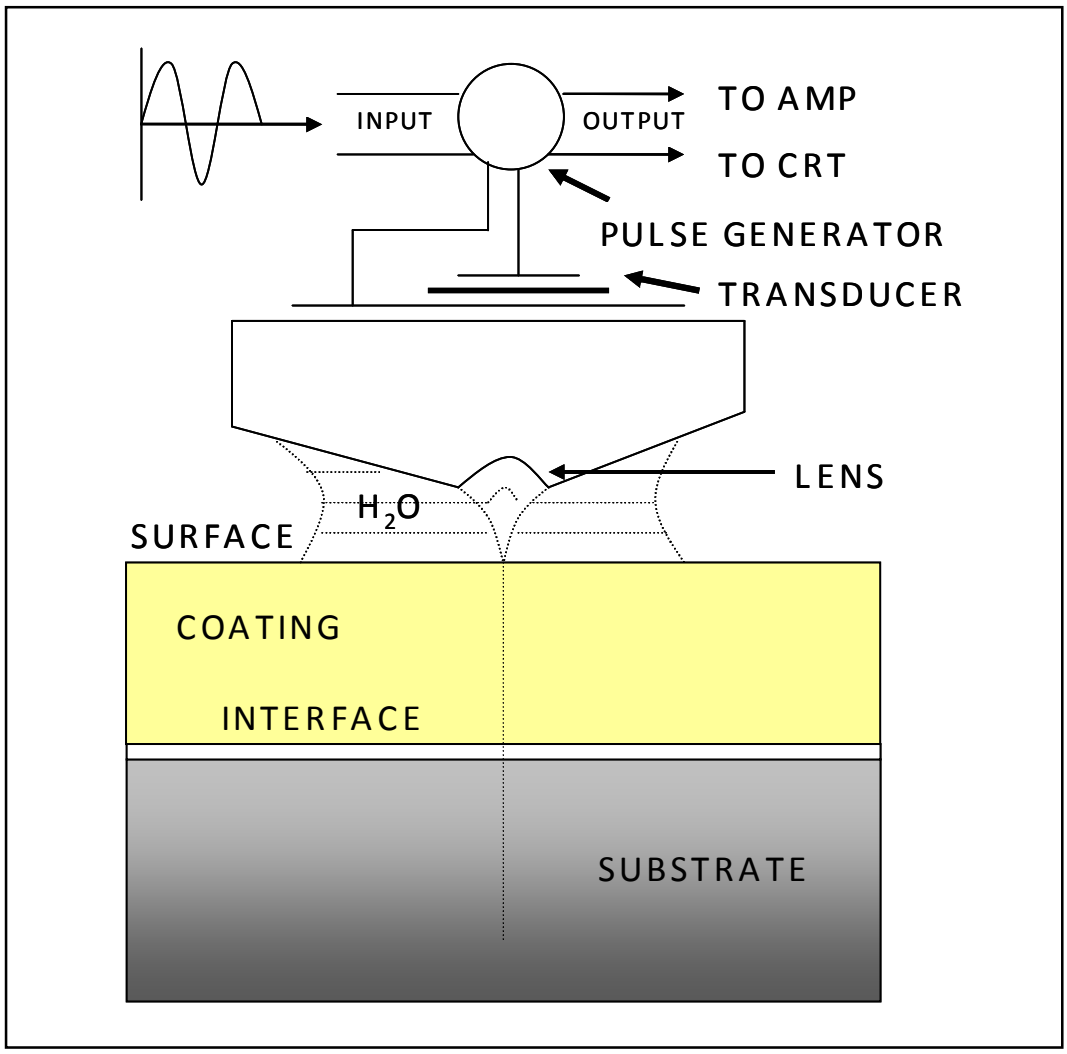


Fig.2.3 SAM schematic diagram

Acoustic waves are generated by a piezoelectric transducer which is typically made of crystals of lithium niobate, quartz or ceramic for frequencies under 100 MHz. The transducer is stimulated to oscillate at its own frequency by an intermittent electronic pulse (or for narrow-band lenses, a forced oscillation is effected via a high frequency electromagnetic field). The acoustic signal is then transmitted via a sapphire cylinder to the lens integrated inside it. After interaction of the acoustic field with the object the system works in the reverse order. It collects the reflected, now diverging acoustic waves and converts them back into flat waves and then into an electric signal.

Sapphire is generally chosen as the lens material due to the fact that the acoustic waves can transmit effectively and without severe attenuation in it. It works as both a transmitter and receiver of acoustic pulse with the pulse echo technique, in which case the acoustic energy reflected from the sample can be re-focused by the lens and transmitted to the transducer which generates a voltage output.

SAM is an in-situ technique that makes use of acoustic waves and senses the differences in acoustic impedance, Z, between different phases at the coating/metal, coating/water or water/metal interfaces to create images of microscopic objects. Z is given by:

$$Z = \rho \bullet \upsilon \qquad \textit{[Equation 2.1]}$$

Where ρ is the density of the material and v is the acoustic wave velocity.

Due to the poor propagation of acoustic waves in air, it is necessary to have an aqueous coupling medium to transmit the signal. For most fluids, the attenuation varies as the square of the ultrasonic frequency. Generally, the higher the frequency is, the shorter the pulses (in time and space), but the higher the attenuation. To minimise the attenuation, distilled water is most commonly used as the coupling medium. The acoustic wave propagates through an organic coating or metal and is focussed at the coating/metal interface.

When an acoustic wave passes through an interface between two phases, with acoustic impedances Z_1 and Z_2, the ratio of the reflected amplitude to the incident amplitude is given by the reflection coefficient, R:

$$R = \frac{Z_2 - Z_1}{Z_2 + Z_1} \qquad \textit{[Equation 2.2]}$$

The fraction of the power reflected is proportional to the square of R. A detectable reflection will occur due to the differences in the acoustic impedances generated by the sudden changes in density or stiffness.

The resolution of a microscope, ω, can be defined as the minimum size of a feature that can be determined. The resolution of the conventional optical microscope is determined by the Equation 2.3 which is based on the Rayleigh criterion.

$$\omega = \frac{0.61\lambda}{N.A.} \qquad \textit{[Equation 2.3]} \text{ [113]}$$

The practical resolution of the reflection acoustic microscope is somewhat better than the resolution based on the Rayleigh criterion and is given by the equation:

$$\omega = \frac{0.51\lambda}{N.A.} \qquad \textit{[Equation 2.4]} \text{ [113]}$$

Where λ is the wavelength of the acoustic wave ($\lambda = \frac{v}{f}$ *[Equation 2.5]*) and N.A. is the numerical aperture of the lens which is equal to sin θ (θ is the semi-angle of the lens aperture subtended at the focus).

The frequency of the transducer used in these experiments is 80 MHz (KSI WINSAM 100) and the acoustic wave speed, v, of a typical epoxy coating is 2650 m·s^{-1} [114] (In this work, it has been tested by measuring the dry films with known film thicknesses of 28 ± 2 μm and 55 ± 2 μm, the corresponding film thicknesses obtained from SAM by setting the acoustic wave speed of 2659 m·s^{-1} are 30 μm and 57 μm, respectively, which are within the acceptable error range. Thus, for this coating system, 2650 m·s^{-1} was used as the acoustic wave speed.), giving a wavelength of about 33 μm. Estimating θ to be between 5° to 10° from the typical working distance, the lens gives a resolution of about 100 μm to 200 μm (Because the size of the features observed

during disbonding are normally bigger than this range, this SAM is suitable to characterise disbonding).

For any wave motion, the wavelength is equal to the wave speed divided by the frequency. Therefore, the higher the lens frequency is, the smaller the wavelength, and the higher the resolution. Though a better resolution is achieved at a higher frequency, attenuation in the sample will be more pronounced.

2.4.1.3 Functioning Principles

The KSI WINSAM can be operated in several modes: A-, B-, C-, D-, X- and G-scan modes. Here in this work, A-, B-, C-, G-scan modes are used to characterise the disbonding.

A-scan: The time of flight information (echo signal, amplitude *vs.* time) can be displayed continuously, Fig.2.4. By monitoring the A-scan, the focus of the microscope can be adjusted by moving the transducer with the Z-handwheel until the chosen echo signal gives a maximal signal in the A-scan. The A-scan mode can be used to characterise reflections of a single point of interest in a specimen and also used to set the 'gate' which detects the signal for image formation. Time difference between peaks can be used to calculate distance if the acoustic wave speed is known.

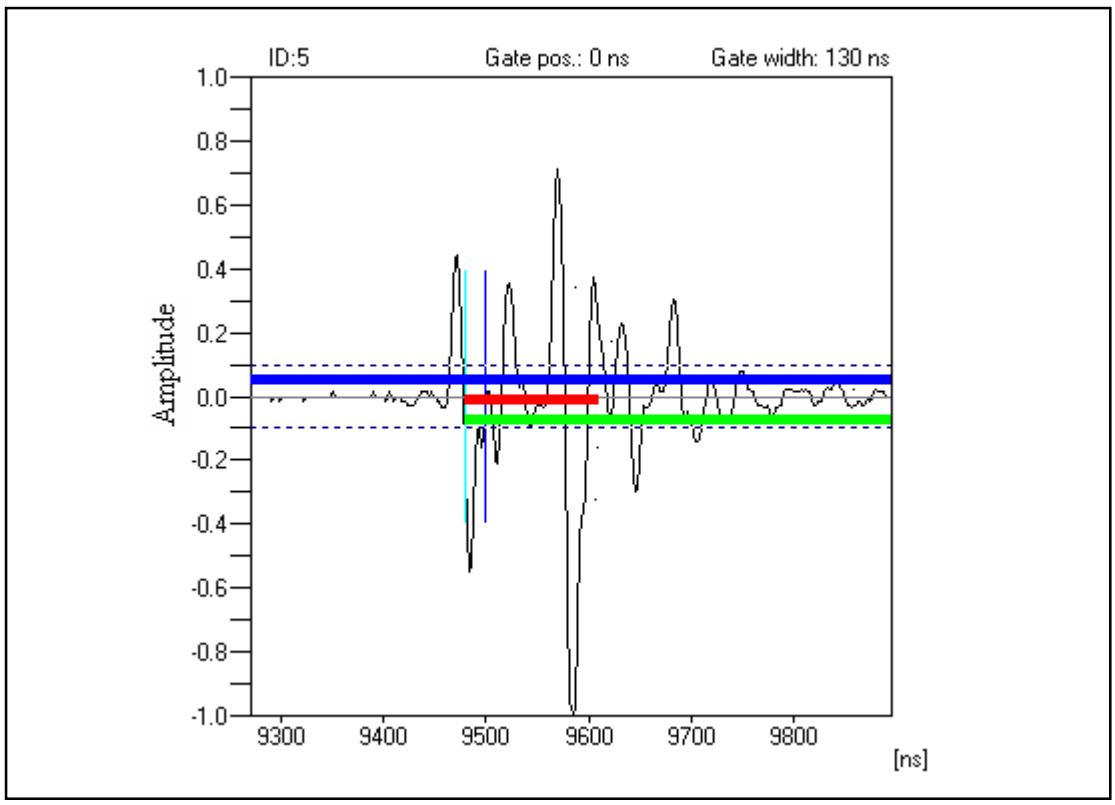


Fig.2.4 A-scan window showing acoustic signal, B-scan gate (green), C-scan gate (red), surface trigger (thick blue). Amplitude in arbitrary units.

A-scan Signal Formation Theory

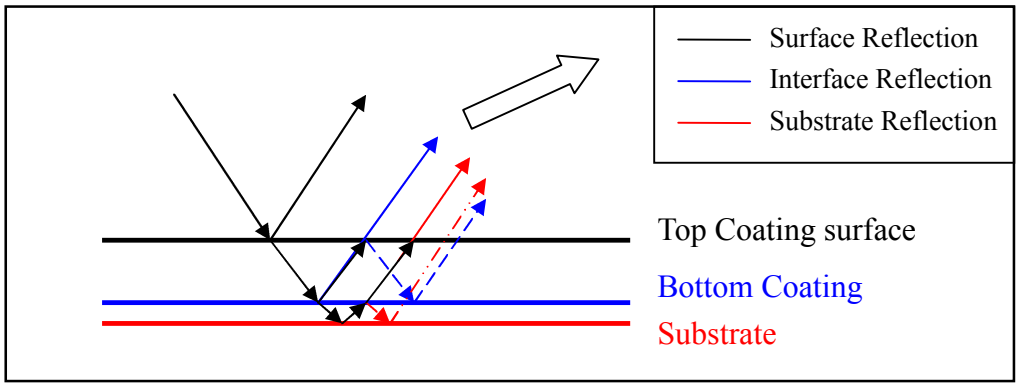


Fig.2.5 Schematic diagram showing acoustic wave reflection in a detached organic paint coated mild steel.

Fig.2.5 gives a diagram showing a simplified reflection process of the acoustic waves in organic paint on mild steel, in the real case, it may be more complicated than this and multiple reflections may exist.

Ultrasonic waves are reflected at the interfaces where the acoustic impedance changes and the intensities of these reflection signals are influenced by the values of impedance possessed by the materials that form these boundary surfaces. An intact coating/metal interface gives the same phase as the top coating surface because impedance increases across the boundary. However, the phase of reflected waves from a greater-impedance substance to a smaller-impedance substance is reversed. During disbonding, the phase of the reflected waves penetrate from the bottom coating surface to coating/water interface which is of low impedance is reversed. These signals will increase with the acceleration of disbonding.

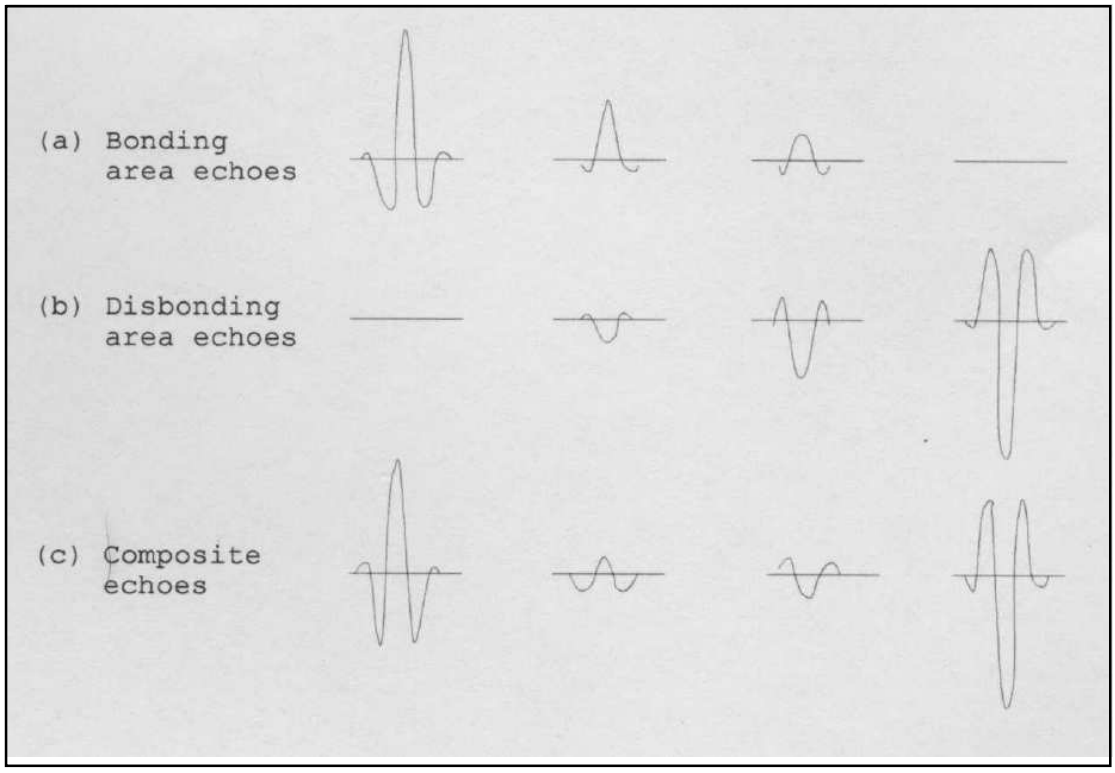


Fig.2.6 Typical SAM signals showing waves reflected from (a) Bonding area; (b) Disbonding area and (c) Composite echoes of (a) and (b). [After KSI]

Fig.2.6 (a) shows the typical SAM waves reflected from the bonding area and the intensity of which decreases with the reduction of the degree of bonding. Fig.2.6 (b)

gives the signals reflected from the disbonding area whose phase is reversed to the incident-wave phase. These signals become more dominant with the acceleration of disbonding. Fig.2.6 (c) shows the composite signals of (a) and (b) when the superstition of signals occurs.

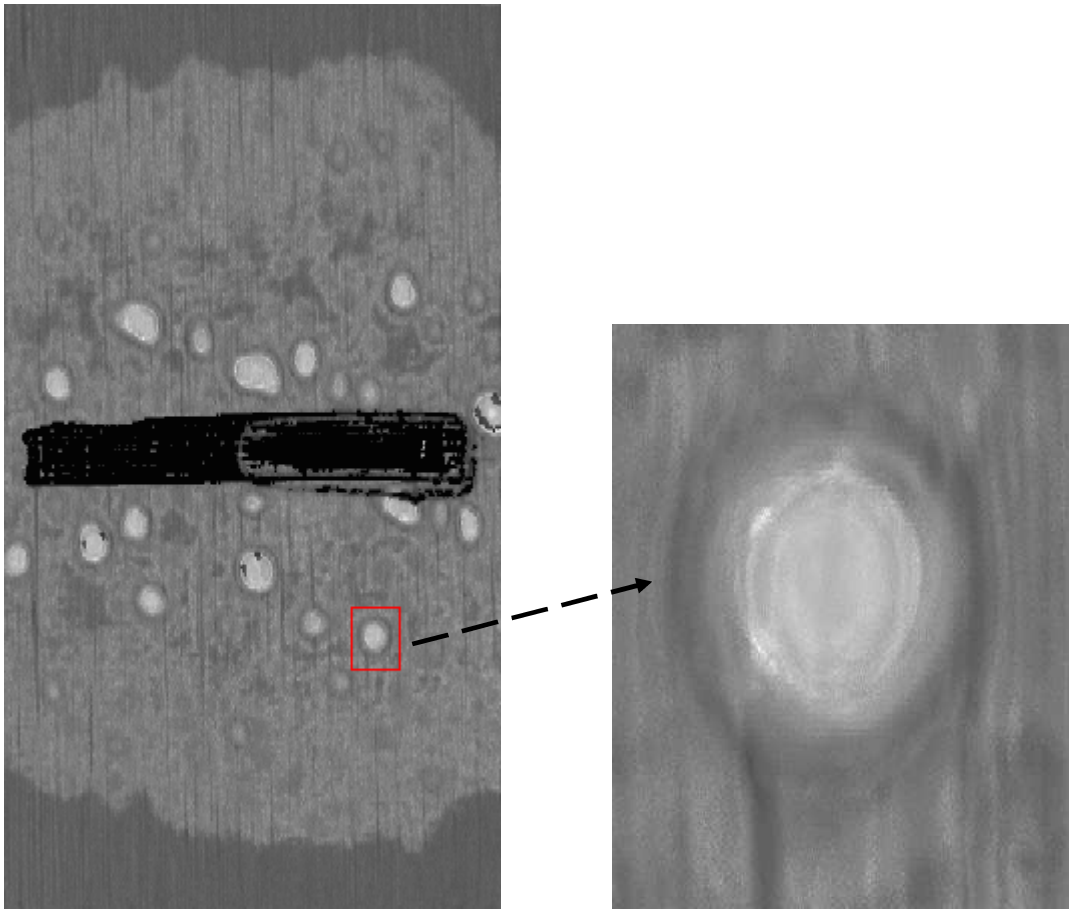
Gate: The green line and the red line in Fig.2.4 represent the B-scan gate and the C-scan gate respectively. These select the portion of the signal used to form the image. B-scan and C-scan images will be created with the selected time regions corresponding to a particular interface, for instance, the coating surface or coating/metal interface.

Surface Trigger: The surface trigger system is employed in this work to minimise the effect caused by non-flatness of the specimen and to avoid the need for precise levelling. The lens is moved parallel to the specimen during scanning. When the surface trigger on, the echo signal from the specimen top surface will serve as the reference marker and the selected signals are then captured after a fixed time delay after this reference. In this case, even though the surface topography changes, the gate will remain at a fixed relative depth in the specimen regardless of the surface topography. However, the focus of the microscope is not adjusted during scanning, hence any severe tilt or large change in the surface topography will not be compensated by the surface trigger system, resulting in part of the image becoming out of focus. This usually does not happen due to the large depth of field of the SAM lens.

C-scan: This mode moves the scanner in a meander pattern over the sample resulting

in a planar view image at a specific depth. Images of disbonding and blisters formation can be generated. Fig.2.7 gives a typical C-scan image.

Fig.2.7 (b) shows a C-scan image of a blister which corresponds to the circled region in Fig.2.7 (a). For a blister, with the surface trigger on, the image will be gated at the metal surface and the different contrast in Fig.2.7 (b) showing the different height of the blistered area.



(a) (b)

Fig.2.7 A typical C-scan image of EC after immersed in 3.5% NaCl solution for 7 days showing (a) disbonding and blisters; (b) close up of the selected blister in (a).

B-scan: A cross-sectional view through the sample, which is known as the B-scan image, is generated by moving the scanner in the X-direction only with signals

selected by the B-scan time gate in the A-scan window. This can include several peaks from the A-scan. The surface trigger is not used when obtaining the B-scan image.

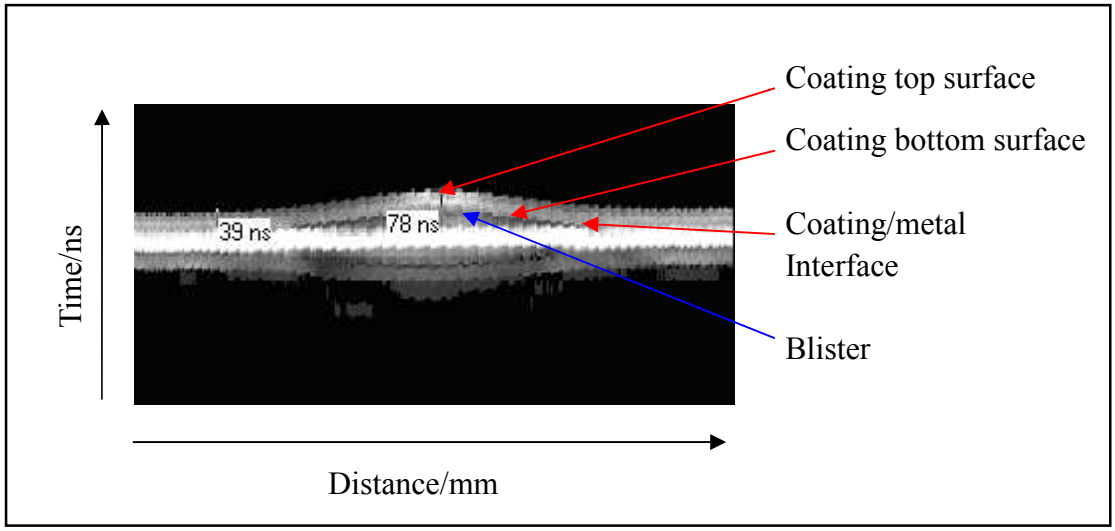


Fig.2.8 B-scan image of a blister, showing the cross-sectional view

Fig.2.8 gives a typical B-scan image showing a blister formed on a disbonded EC sample. The white line in the middle is the metal surface and the curved part represents the blistering area. It is apparent that at the blister there are three sets of signals representing reflections from the coating top surface, bottom surface and coating/metal interface respectively. Through measuring the time interval between the reflections, the information about wet/dry coating thickness can be obtained by calculating with $d = \frac{v \bullet t}{2}$ *[Equation 2.6]*, where d is the distance between the coating surface and the substrate; v is the acoustic velocity in the coating and t is the time interval. Similarly, the separation between coating and substrate within a water-filled blister can readily be calculated from the known velocity of sound in water.

G-scan: By selecting G-scan, more than one C-scan image from different reflections

corresponding to different depths in the specimen can be produced simultaneously based on separate gate settings for each depth, which is time-saving and allows the characterisation of both the polymer surface and the polymer/metal interface features at the same time. In this work, this mode is normally combined with the "Pre-scan" to get a general idea about the features of the surface and the interface, C-scan follows.

2.4.1.4 SAM Examination Setup and Operation

The specimen, mounted on a glass slide with plasticine for levelling, was placed in distilled water (approximately 3 cm deep) in a reservoir underneath the lens. The distilled water acts as the coupling medium for the propagation of the acoustic waves. The disbonded samples were examined by several lenses with different frequencies, 20 MHz, 50 MHz, 80 MHz and 150 MHz, in the preliminary work and it was found that the one with the frequency of 80 MHz was the most appropriate one to examine the coating system studied here.

In the scan parameter set up section, 80 MHz was selected with the wave speed set as 2650 $m \cdot s^{-1}$ which is the typical value for epoxy coating [114] as mentioned above in Section 2.4.1.2 when estimating the resolution of the lens.

The lens was placed directly above the centre of the sample and by using the Z-handwheel, it was lowered into the distilled water. Air bubbles on the lens, if there were any, were removed with a soft brush.

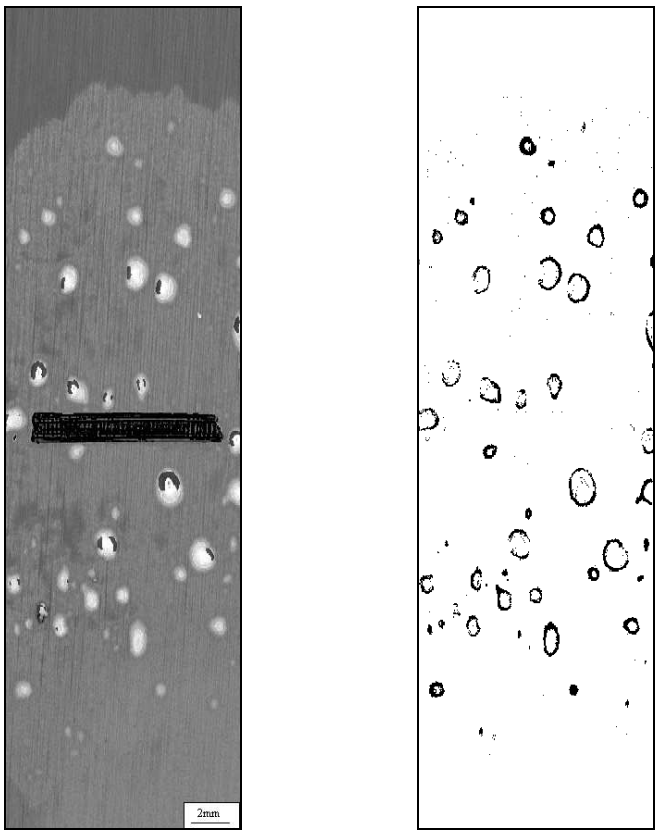
Surface trigger was enabled and the focus of the microscope was adjusted until the echo signal corresponding to the part of interest (coating/metal, coating/electrolyte or

electrolyte/metal interface) gave a maximum signal in the A-scan. Then the C-scan or B-scan (disable the surface trigger) gate was set accordingly.

The size and the quality of the scan were set through the "Scanner" window. It allows the user to define the scanning parameters such as Scan mode (Scan, Prescan, Fast prescan); Scan quality (Normal and High quality) and Resolution (less to more). Once the Surface Trigger was enabled and the Scan Field, Speed and an estimated gate were set, a prescan were conducted to get an overview of the sample. Normally the Speed was firstly set as 50% and it took about 20 seconds to complete scanning for a scan field of 30 mm [L] × 30 mm [W]. By reducing the Speed (to 10% in this work), increasing the Resolution (to more) and adjusting the gate, a SAM image of high quality then formed. It took 5 to 30 minutes to acquire the image depending on the size of the scanned area. It was also possible to zoom in by circling a particular area of interest on the acquired SAM image (with bigger scanning area) and scan again to get possibly more detailed and much clearer information about it. The exported SAM images were in the format of *.sam files, which is a unique file format used by KSI. By saving images with this format and opening by the KSI SAM software, scanning parameters were kept for future reference. The A-scan of the acquired image was also retained through this format of image. In addition, the SAM images can be exported as Windows Bitmap Files, which facilitates file opening, but one disadvantage of this format is that it does not save the scan parameter information. Therefore, SAM images were normally saved as *.sam files first, then converted into *.bitmap files for use in other programs.

2.4.1.5 SAM Image Analysis

SAM C-scan images are exported from the WINSAM software as bitmap images. Image analysis software, ImageJ 1.43u (National Institute of Health, USA, http://rsb.info.nij.gov/ij) is used to analyse the blistering on the SAM images. First open a SAM image and convert it to 8-bit greyscale by Image → Type → 8-bit. Then create a "thresholded" binary image by adjusting threshold through Image → Adjust → Threshold and Process → Binary → Make Binary, see Fig.2.9 b) for an example of the "thresholded" binary image. Before analysis, set the measurement scale (Analyze → Set Scale). In the *Set Scale* window, type the "Distance in Pixels" and the "Known Distance" with the "Unit of Length". When counting blisters and measuring area, select the Analyze → Analyse Particles, the lowest size limit constituting a blister can be defined either in pixel^2 or mm^2. This analysis gives the information about the blistering, including the number, size, and area of the blisters.



a) b)

Fig.2.9 Images showing the SAM image analysis for blistering, a) SAM C-scan image; b) "thresholded" binary image converted by ImageJ.

2.4.2 Scanning Kelvin Probe (SKP)

2.4.2.1 Introduction

The Scanning Kelvin Probe (SKP) is a non-contact, non-destructive vibrating capacitor device measuring the work function (WF) difference between a conducting specimen and a vibrating tip. The WF is the (least) amount of energy required to remove an electron from the surface of a conducting material to a point just outside the metal with zero kinetic energy, usually expressed in V. The physical form of a SKP is a head unit containing a voice coil driving system and an integral amplifier suspended above a sample. The vibrating tip and the sample form a capacitor, having

(in principle) parallel-plate geometry. The difference in work function creates a charge displacement causing electron flow in and out of the external circuit as the tip vibrates. Leng *et al.* [56] suggested that the Volta-potential measured by SKP, exactly follows the changes of the electrode potential at the inner interface (coating/metal interface or electrolyte/metal interface). They also reported that only at highly alkaline pH, does a Donnan-potential, a potential across the coating, makes some small contributions to the measured potential, which can probably explained by a decomposition of the coating under those conditions. However, the Donnan-potential is small enough comparing to the delamination potential, thus it is normally ignored.

The SKP has several advantages over other electrochemical techniques for the corrosion study. One of the most significant features of the SKP is that it allows measuring the local electrode potential with high accuracy even below highly insulating polymer layer close to a coating defect where the bare substrate metal is exposed to the testing environment – even though the impedance of the defect is low, as this technique requires no electrolyte contact between the reference electrode and the working electrode [45]. It only requires very weak electric fields, which are not likely to influence the electrical or chemical structure of the specimen.

2.4.2.2 SKP Operation Principles

Principles of operation talked about in this section will be based on the SKP system employed in this work, which is from KP Technology Ltd.. Unique features of Off-Null Measurement and Height Regulation invented by Prof. Baikie [115] have

been incorporated in this system. Fig.2.10 gives a schematic view of this SKP system.

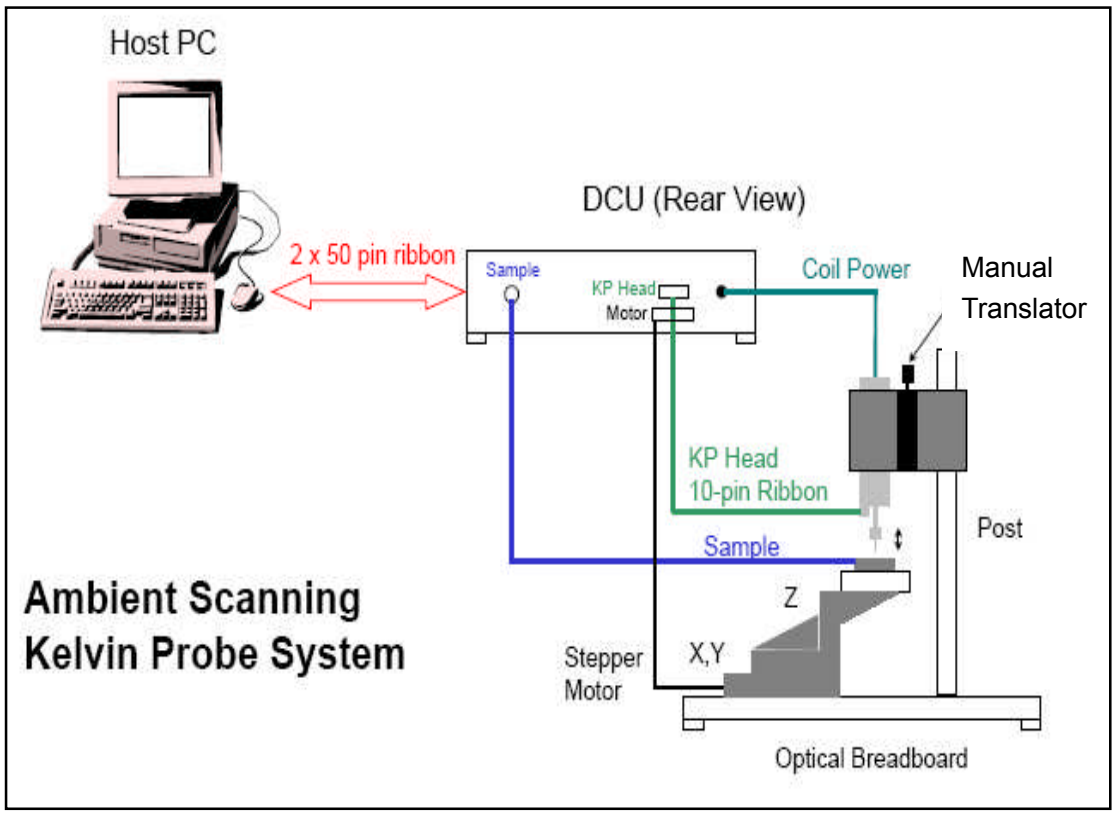


Fig.2.10 Schematic SKP System (After KP Technology Ltd.).

The Kelvin Probe is mounted on a 2.5 cm manual translator which is mounted on a 36 cm centrally located optical post. To keep the humidity high, a metal chamber is attached to the sample holder to control the humidity. It is placed right underneath the Kelvin Probe tip. The 3-axis stepper motor is mounted onto the optical breadboard with X, Y in the plane of the surface and Z positioned vertically. The movement of these stepper motors are controlled by the SKP 3.66 software. Fig.2.11 and Fig.2.12 show the operating windows.

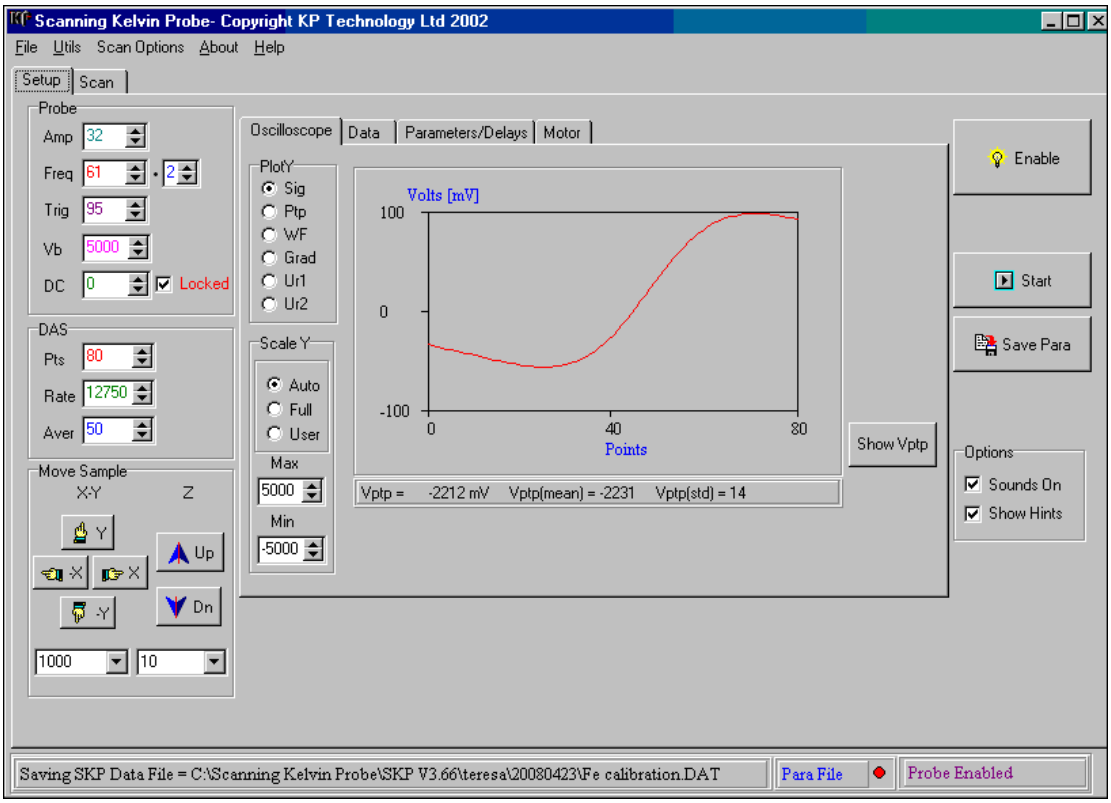


Fig.2.11 SKP set-up screen

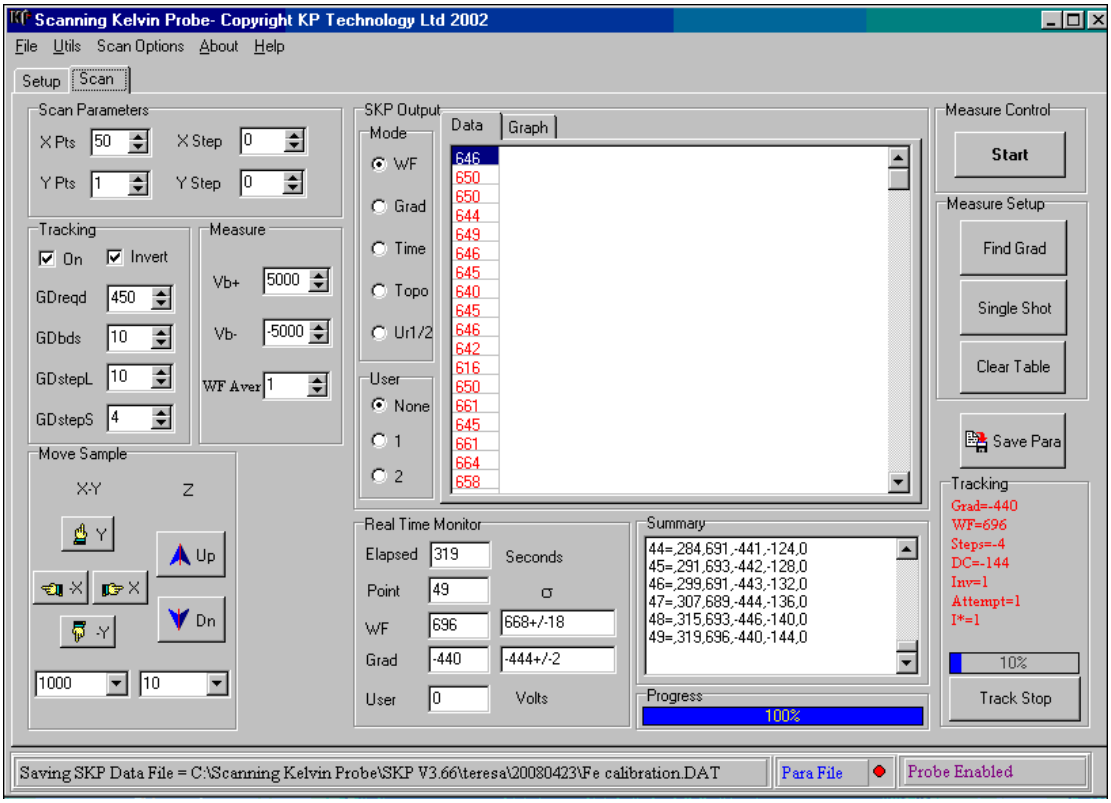


Fig.2.12 SKP scan screen shot

- **Off-Null**

To get good Kelvin Probe measurements, noise reduction is important. Significant improvement can be obtained by putting a Faraday cage as a shield system. While in the KP Technology SKP system, an "Off-Null" technique developed by Baikie [116] is involved to minimise the influence of noise.

Theory of Off-Null Technology

There are two capacitances formed when the coated metal system is measured by a SKP, with one air-filled capacitance (C_{Air}) between the polymer surface and a flat circular ended SKP tip which is positioned close above the specimen, and a coating capacitance (C_C) across the polymer in series, see Fig.2.13.

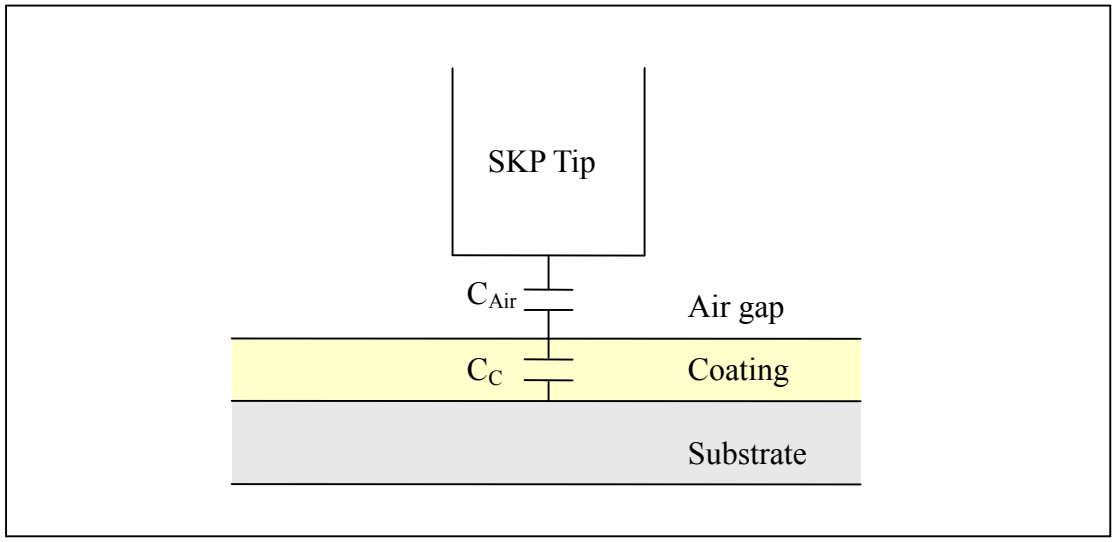


Fig.2.13 Schematic diagram of capacitors formed in SKP measurement of a coated metal.

The total capacitance of the whole system, C, is given by

$$\frac{1}{C} = \frac{1}{C_{Air}} + \frac{1}{C_C} \qquad \textit{[Equation 2.7]}$$

The capacitance is usually expressed as,

$$C = \frac{\varepsilon_0 \varepsilon_R A}{x} \qquad \textit{[Equation 2.8]}$$

Where ε_0 is the permittivity of free space; ε_R is the relative permittivity of the medium; A is the tip area and x is the plate (tip sample or gap air) separation.

Because ε_R is higher for wet coating and spacing, x, is usually less, it is apparent from the Equation 2.7 that C_C will be a lot bigger than C_{Air}. Therefore, $C \approx C_{Air}$, suggesting that the C_{Air} is the dominant capacitance.

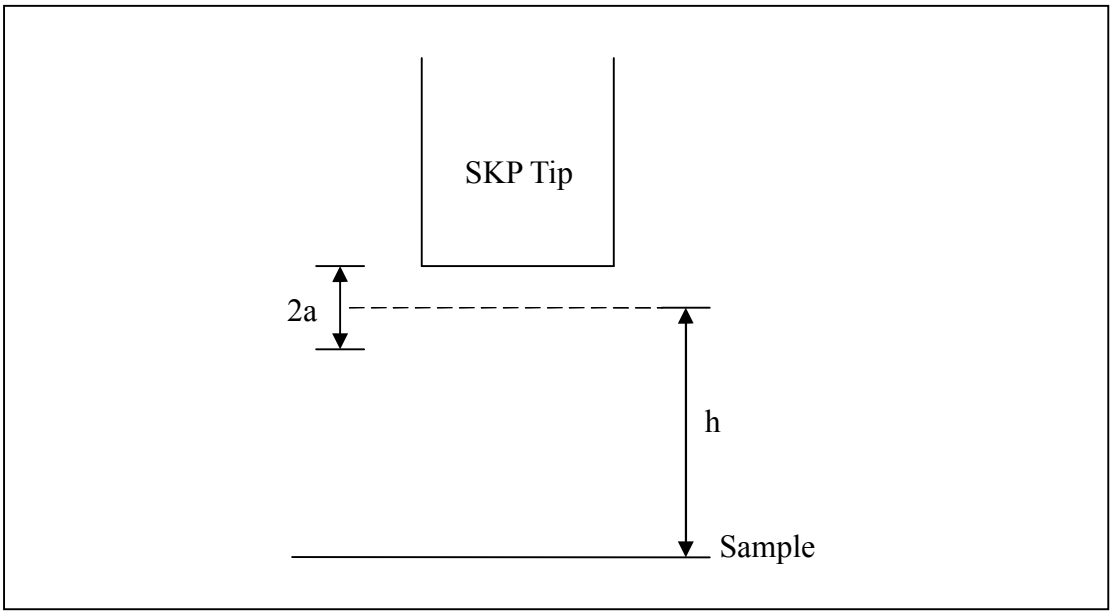


Fig.2.14 Schematic diagram of the tip-sample spacing during tip oscillation.

Fig.2.14 gives a schematic diagram of the tip-sample spacing during tip oscillation where the tip vibrates normal to the sample surface. h is the mean spacing between the tip and the sample and a is the amplitude of the tip motion (half the total displacement). Treating the tip-sample gap as a simple parallel-plate capacitor (an approximation), when the tip is vibrated, a varying capacitance is produced.

$$C_t = \frac{\varepsilon_0 A}{x_t} \qquad \textit{[Equation 2.9]}$$

Where C_t is the Kelvin capacitance which is the time-varying tip-specimen capacitance; ε_0 is the permittivity of air (8.8542×10^{-12} $C^2\cdot N^{-1}\cdot m^{-2}$); A is the surface area of the tip and x_t is the time-dependent tip-sample separation.

The position of the SKP tip changes with time,

$$x_t = h + a\sin\omega t \qquad \textit{[Equation 2.10]}$$

Where ω is the frequency at which the tip vibrates expressed in radians.

Assuming a homogeneous electric field between the tip and sample, the current flowing across the capacitor, i, can be expressed as:

$$i = \Delta E \cdot \frac{dC}{dt} \qquad \textit{[Equation 2.11]}$$

$$\Delta E = V_c + V_b \qquad \textit{[Equation 2.12]}$$

Where V_c represents the voltage difference between probe tip and sample and V_b is the external voltage applied to balance the circuit.

Substituting Equations 2.9, 2.10 and 2.12 in Equation 2.11, the current signal i_t can be expressed as:

$$i_t = (V_c + V_b)\varepsilon_0 A \cdot [-\frac{a\omega\cos\omega t}{(h + a\sin\omega t)^2}] \qquad \textit{[Equation 2.13]}$$

According to the Ohm's law, the output voltage, V, can be expressed as:

$$V = (V_c + V_b)R\varepsilon_0 A \cdot [-\frac{a\omega\cos\omega t}{(h + a\sin\omega t)^2}] \qquad \textit{[Equation 2.14]}$$

Where R is the I/V converter feedback resistance.

This gives the SKP voltage output signal which is asymmetric as shown in Fig.2.14. The asymmetry is induced by the position dependency of the Kelvin capacitance, C_t, as Equation 2.9 indicates.

The peaks are located where the change of capacitance is at its maximum and they are occurring close to the lowest tip position. At these points, $i_t = i_{max}$, the output signal reaches the peak-to-peak voltage, V_{ptp}. The voltage passes through zero at the highest and the lowest tip positions because there is no capacitance change due to the tip being stationary at these points.

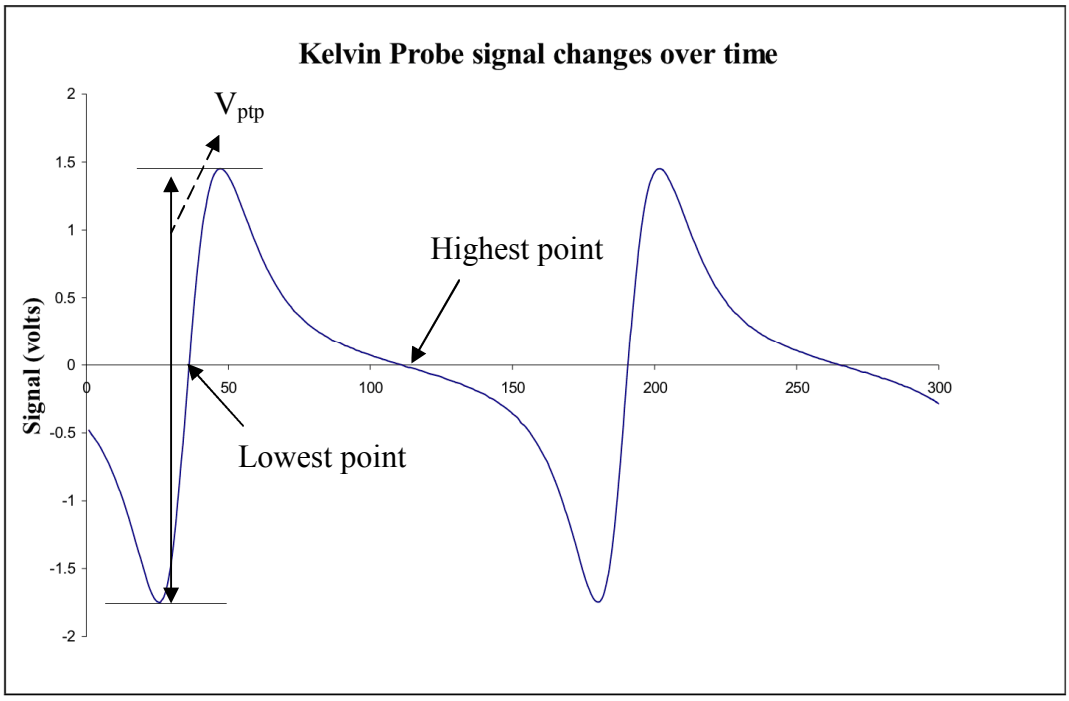


Fig.2.15 SKP output signal (After KP Technology Ltd.)

As Equation 2.14 suggests, if V_{ptp} is plotted versus V_b, a straight line which intersects the origin of the V_b axis at the point where $V_b + V_c = 0$ is obtained. KP Technology measures the V_{ptp} corresponding to the applied backing potential of 5 V and -5 V and with these two points, V_c is determined by plotting the line between them. This is termed as the "Off-Null" signal detection. Fig.2.16 gives the V_{ptp} output versus V_b plot used to determine V_c.

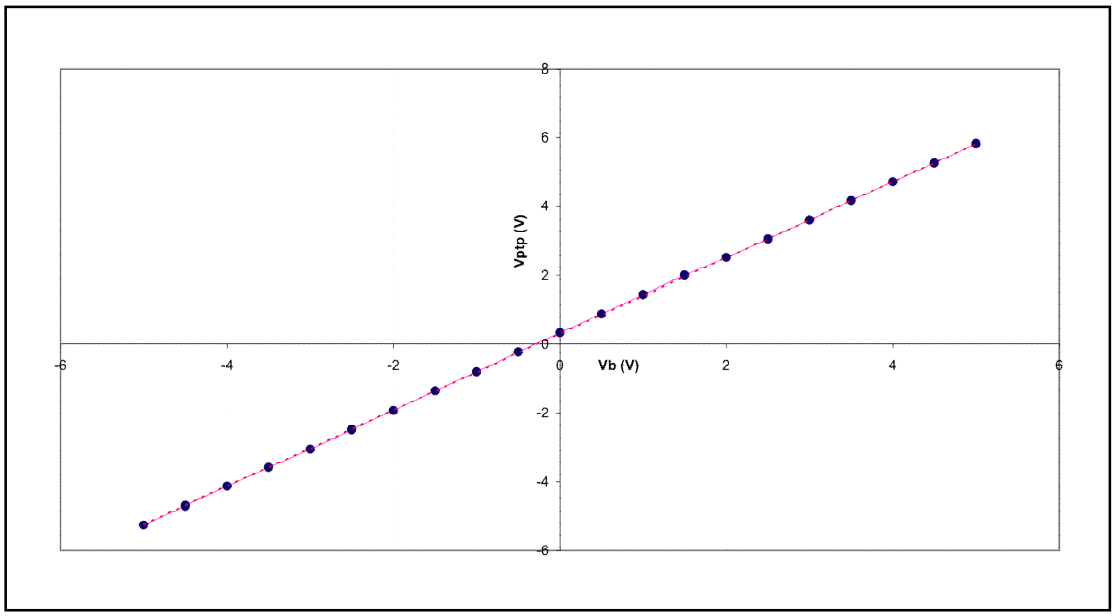


Fig.2.16 Peak-to-Peak Output versus Backing Potential (After KP Technology Ltd.)

The Off-Null method makes the work function difference measurement less likely to be affected by noise due to the small size of noise relative to the large signal used.

- **Height Regulation**

Another feature of the KP Technology SKP system is the "Height Regulation". By controlling the height of the instrument tip from the specimen, the scanning measurements can be automatically performed under identical experimental parameters. Without this technique, the work function measurements will be different unless the separation can be kept constant.

A gradient value (slope of the line in Fig.2.16) and allowed error in the required gradient are set before measurements. During measurement, gradient is measured at each point to check the tip-sample separation and the stage height controller responds accordingly, so that the height of the tip is adjusted until the gradient falls within the pre-defined range. Bigger allowed error in the required gradient allows a faster scan.

On the other hand, if the error is small, the gradient may still be out of the pre-set range after 20 times of iteration, in which case, the probe takes measurement at the current height without more iteration. With proper operation and relatively flat sample, this usually does not happen and error in WF will in any case normally be small.

In principle, WF should not depend on height, while in practise, it does. This difference between theory and practice is not up to now fully explained.

The incorporation of Off-Null and Height Regulation method in this SKP system produces stable high signal levels, repeatable high-resolution measurements. By moving the tip in a meander movement above the specimen surface, it is possible to obtain a distribution of the surface work function. Simultaneously, the topography gradient and time data are recorded by the SKP.

2.4.2.3 SKP Experimental Setup

2.4.2.3.1 Examination Details

Several circular flat ended tips including Gold tip: 500 μm; Silver tip: 1.0 mm, 500 μm and 250 μm in diameter were tried in the preliminary work. The 500 μm silver tip was selected from those tips to conduct this study. It gives a larger current signal than 250 μm, but the resolution is more limited. As we usually scan large areas, it does not matter. Silver was chosen because it showed a more stable calibration than gold.

The tip oscillation frequency was set as 61.2 Hz (corresponding to the resonant frequency of the driver), with an amplitude of 32 μm. A backing potential, Vb, of ±5 V was applied. The required gradient, GD Reqd, was usually set as 100 – this

determines the tip-sample separation. Xstep (see Fig.2.12) is the steps in the x-direction taken between each two measuring points. The distance between every two measuring points, d = Xstep × 0.4 μm. Normally, Xstep is set as 1000, corresponding to 0.4 mm between each two measuring points which is less than the tip size to get better resolution. Ystep is similar to Xstep but in the y-direction. It is normally set as 1000 as well.

The SKP tests were carried out in a metal chamber which controlled the relative humidity (RH) to about 75% by pumping air via two flasks with distilled water inside. The relative humidity is monitored by a humidity meter during measurement. Also the defect was filled with a droplet of 3.5% NaCl solution to keep it wet and topped up as necessary while doing the SKP measurements.

2.4.2.3.2 SKP Tip Resolution Test

A cylindrical aluminium stub with a 750 μm thick mild steel insert, Fig.2.17, as used by Doherty [117] was used to test the 500 μm silver tip resolution. The sample surface was degreased by using acetone and ethanol before testing.

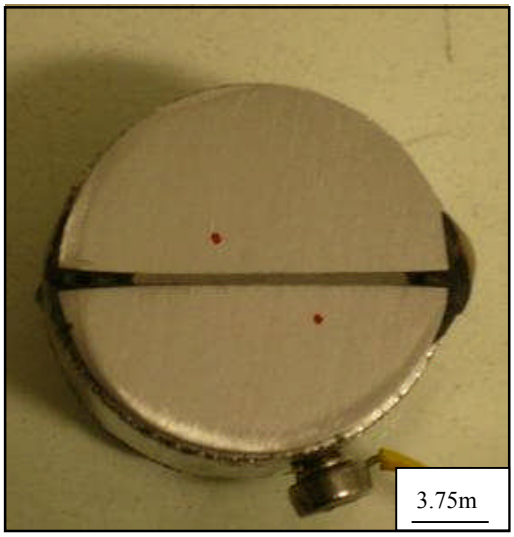


Fig.2.17 Optical image of the sample for the resolution test

The tip scanned across the steel insert and an area of 5 mm × 5 mm with the step size (distance between two measuring points) of 100 μm was mapped and the WF map is shown in Fig.2.18.

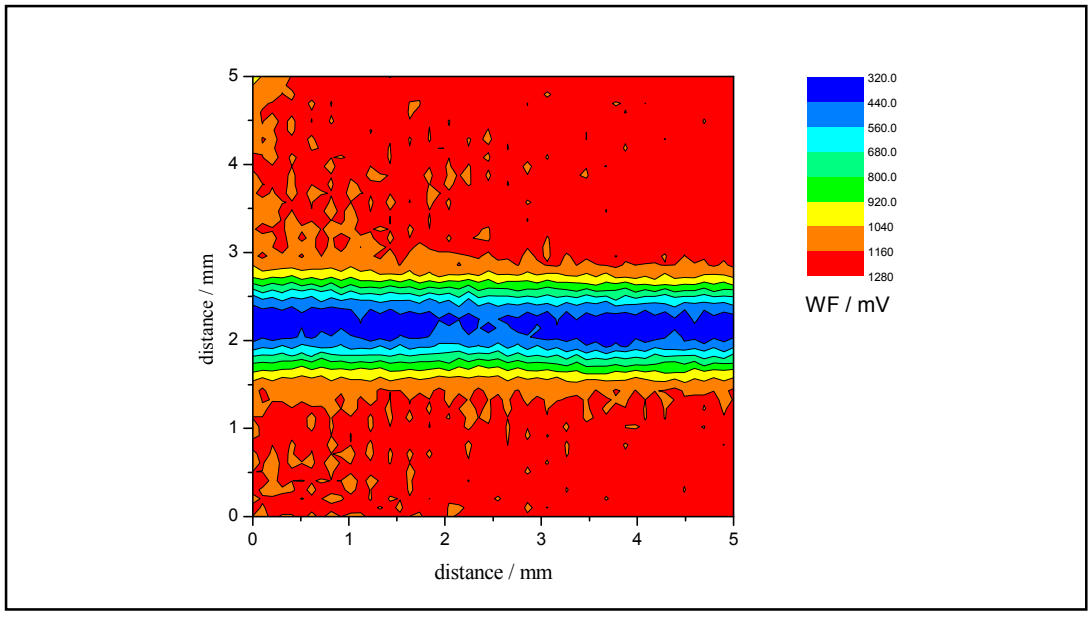


Fig.2.18 SKP WF map for the tip resolution test

A line scan was also performed across the steel insert with different gradient, G, values, Fig.2.19.

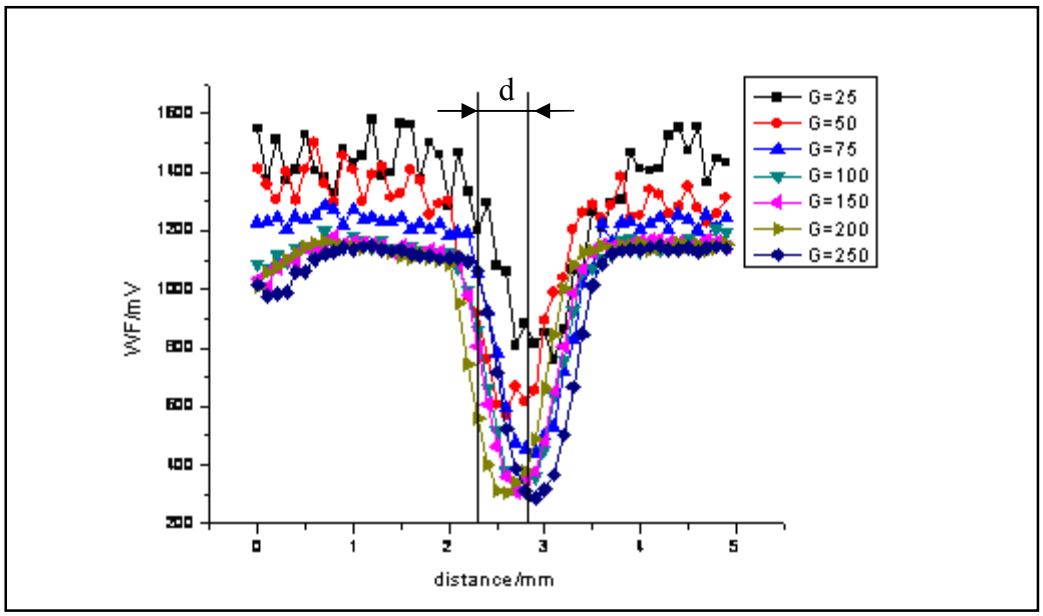


Fig.2.19 SKP line scan for tip resolution test

This shows that for G = 100 - 250, the WF values are essentially the same, but change if tip-sample distance is increased further. The profile width, d, as labelled in Fig.2.19, is similar to the tip diameter.

2.4.2.3.3 SKP Calibration

- Height Calibration

It is useful to calibrate gradient settings in term of "height" of the probe above the sample. This calibration will depend upon the bias signal settings and size of tip. When the effective height is zero, the corresponding current is infinite. Height dependence of the gradient can be calculated.

Treating the tip-sample gap as a simple parallel-plate capacitor (an approximation), the capacitance can be described as Equation 2.9.

$$C_t = \frac{\varepsilon_0 A}{x_t} \qquad \textit{[Equation 2.9]}$$

If the charges on the plates are +Q and –Q, and the voltage between the plates is expressed as V, then the capacitance is given by,

$$C = \frac{Q}{V} \qquad \textit{[Equation 2.15]}$$

Also, for a steady flow of charge through a surface, the current I can be expressed as the electric charge transfer through the surface over some time and can be calculated with the following equation,

$$I = \frac{Q}{t} \qquad \textit{[Equation 2.16]}$$

More generally, electric current can be represented as the rate at which charge flows through a given surface as,

$$I = \frac{dQ}{dt} \qquad \textit{[Equation 2.17]}$$

Substituting Equation 2.15 into 2.17 gives,

$$I = V\frac{dC}{dt} \qquad \textit{[Equation 2.18]}$$

And substituting Equation 2.9 into 2.18 gives,

$$I = -V\varepsilon_0 A\frac{dx}{x^2 dt} \qquad \textit{[Equation 2.19]}$$

I is proportional to G, thus,

$$x_t^{-2} \propto G$$

If we plot 1/G *vs.* x^2, it should give us a straight line. While in practice, a straight line of 1/G *vs.* x rather than 1/G *vs.* x^2 was found (Fig.2.20). The different behaviour between the ideal parallel capacitor ($x_t^{-2} \propto G$) and the real SKP ($x_t^{-1} \propto G$) is believed to be due to the geometric effect of the tip and the sample surface [118].

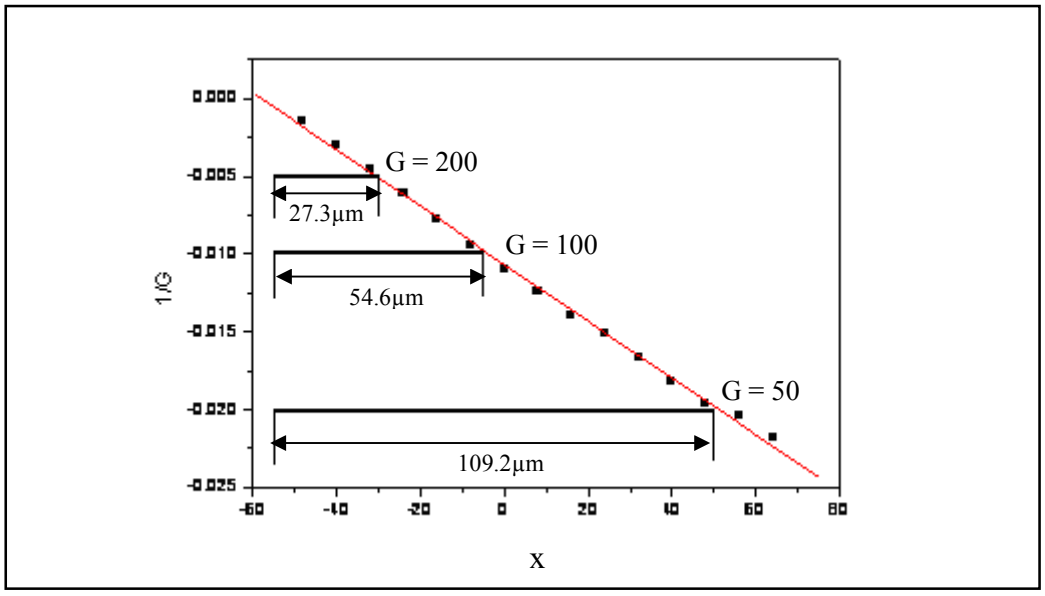


Fig.2.20 SKP Height Calibration Graph, x is the arbitrary displacement.

It can be seen from Fig.2.20 that 1/G is linearly proportional to x, which can be expressed as $\frac{1}{G}$ = -1.83E-4 x - 0.01 with the correlation coefficient of R = 0.999. Note, x shown here is the relative distance from the tip to the initial tip position. The initial measuring point for Fig.2.20 is under the GD Reqd of 100, which is the same as the one used for the sample measurements. When $\frac{1}{G}$ reaches 0, G = ∞, corresponding to zero separation (C = ∞), i equals to i_{max}, which means the tip-sample separation at the peak current should be zero. In this case, it is at the point where a distance of 54.64 μm below the initial measuring point, the current reaches the peak current. Fig.2.20 has shown some effective heights corresponding to different gradients. Therefore, an effective height (at position of peak current) can be deduced directly from gradient for 'peak' operating conditions.

- Electrochemical Calibration

To convert the work function (WF) data acquired from the SKP to electrochemical potential, electrochemical calibration was conducted.

Three cylindrical pieces of metal, Cu, Fe and Zn, with a hole drilled from the top surface of each piece to act as a reservoir containing an appropriate electrolyte were used to carry out the electrochemical calibration. The WF and the potentials, E, of these three electrochemical standards: Cu / sat. $CuSO_4$, Fe / sat. $FeSO_4$ and Zn / sat. $ZnSO_4$ were measured by the SKP and a voltmeter attached to the saturated calomel electrode (SCE) at the same time. This has been done similarly in other work [56, 61, 117, 119]. The settings of the SKP during calibration were the same as those used for the sample measurements.

Table.2.2 has listed a typical SKP electrochemical calibration result for three standards showing the potential values measured by a voltmeter with the SCE as a reference and the WF values measured with the SKP.

Standards	Potential / mV (*vs.* SCE)	WF / mV (SKP)
Cu / sat. $CuSO_4$	298	-114.9
Fe / sat. $FeSO_4$	-398.8	703.6
Zn / sat. $ZnSO_4$	-785.8	1046.1

Table.2.2 Typical SKP calibration standards

If WF (SKP) is plotted versus E (*vs.* SCE), Fig.2.21 is obtained.

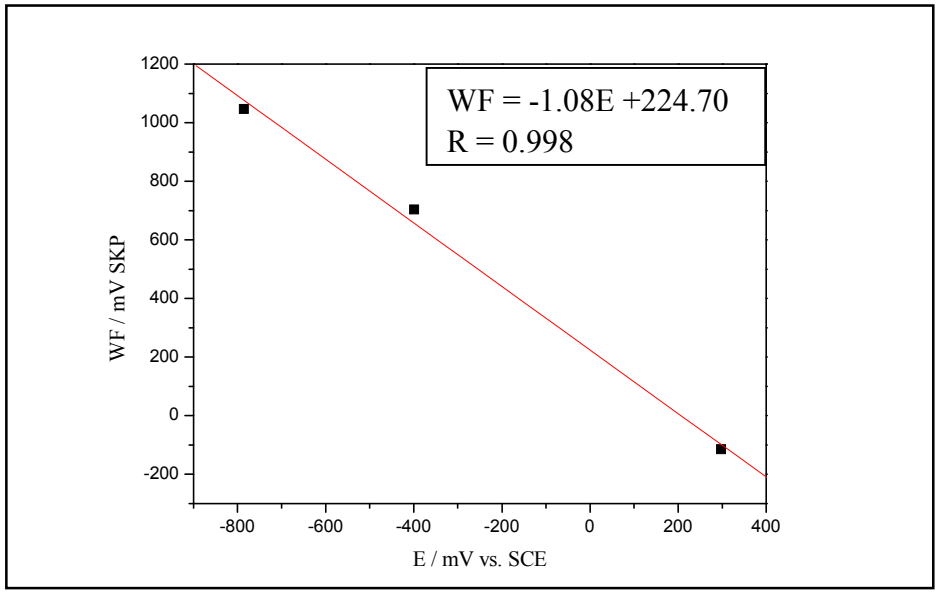


Fig.2.21 Typical SKP electrochemical calibration graph

As shown in Fig.2.21, a linear line of WF (SKP) versus E (*vs.* SCE) resulted and within the experimental error, the slope is 1.0, which shows it is possible to convert the WF data measured by the SKP to electrochemical potentials. And in this case, the SKP would operate as a reference electrode with a potential of 225 ± 0.5 mV *vs.* SCE. All the WF data obtained from SKP in this work were converted to electrochemical potentials through this electrochemical calibration method. And the potential data were saved as *.dat files, processed with OriginPro 7.5 and presented as contour maps. See the Appendix for detail.

2.4.3 Electrochemical Impedance Spectroscopy (EIS)

2.4.3.1 Introduction

Electrochemical Impedance Spectroscopy (EIS) is a non-destructive technique used to track the condition of a coated metal sample as it changes. In EIS, an AC voltage of

varying frequency is applied to the sample. It offers several advantages: 1) it uses very small excitation amplitudes, which cause only minimal perturbation to the electrochemical testing system; 2) it is possible to take measurements as a function of frequency and the analysis of the response can provide important information regarding the corrosion process occurring.

Here EIS is used to characterise an intact organic coating painted metal substrate either coupled or not coupled with a bare metal, it can measure 1) the deterioration of the organic coating caused by exposure to an electrolyte, shown by a decrease in resistance and 2) the increase in corrosion rate of the metallic substrate due to the degradation of the coating and subsequent attack by the electrolyte shown by falling charge transfer resistance, R_{ct}.

2.4.3.2 EIS Equipment

An ACM instruments Gill AC potentiostat is used to acquire the EIS results in this work. The input impedance needs to be significantly higher than the coated sample, so an optional paint buffer is used with the potentiostat to offer ultra-high input impedance and to minimise leakage current.

A three-electrode cell is used, which consists of a test sample as a working electrode (WE), a saturated calomel electrode (SCE) as a reference electrode (RE) and a platinised titanium counter electrode (AE). Fig.2.22 shows a schematic diagram of the setup of the cell for the EIS measurements in this work.

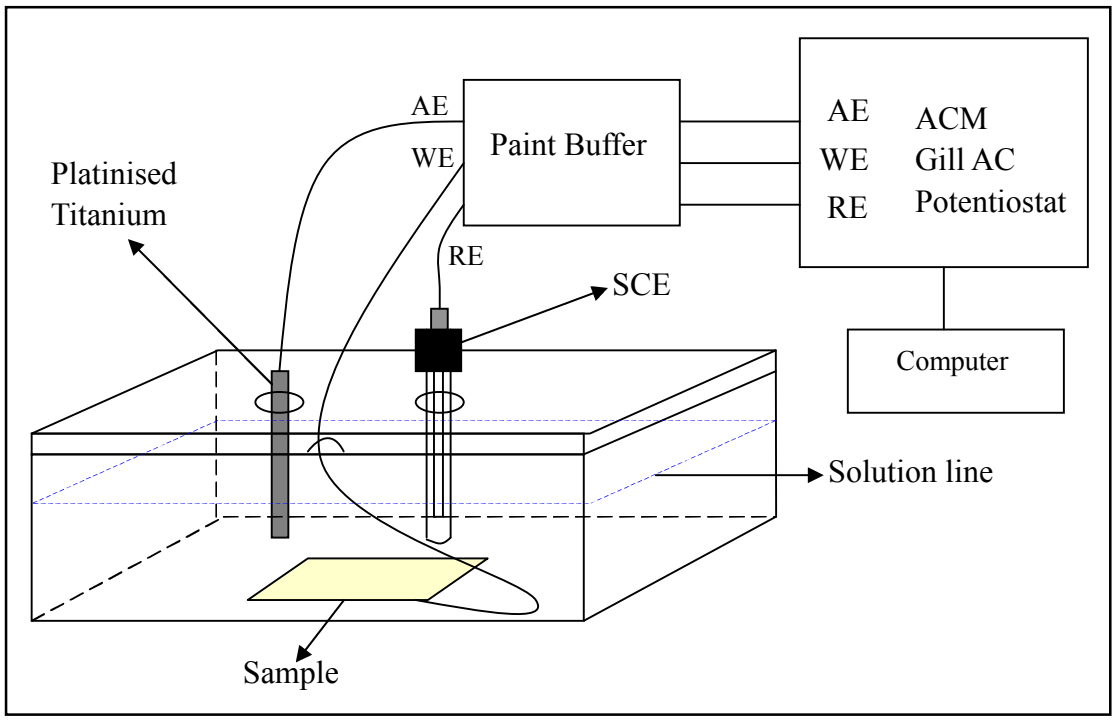


Fig.2.22 Schematic diagram of the cell used for EIS measurement

A Faraday cage which is a grounded conductive enclosure (*i.e.* steel box) is always used to enclose the cell and the electrodes during the EIS measurements due to the small measured cell currents. It reduces the current noise picked up by the working electrode and the voltage noise picked up by the reference electrode.

2.4.3.3 AC Circuit Theory

Impedance is a measurement of the ability of a circuit to resist the flow of electrical current. Electrochemical impedance, $Z(\omega)$, is usually measured by applying a sinusoidal AC potential to an electrochemical cell and measuring the current through the cell. $Z(\omega)$ is often expressed as a complex number consisted of a real and an imaginary part, which is given by,

$$Z(\omega) = Z_0 e^{(j\phi)} = Z_0(\cos\phi + j\sin\phi) \qquad \textit{[Equation 2.34]}$$

Where Z_0 is a magnitude, ω is the radial frequency and ϕ is the phase shift.

If the real part is plotted on the X-axis and the imaginary part is plotted on the Y-axis of a chart, a "Nyquist Plot" is produced, Fig.2.23. On the Nyquist plot, the impedance can be represented as a vector (arrow) of length $|Z|$ and the angle between the vector and the X-axis, commonly called the phase-angle, which is ϕ = arg Z. High frequency data are on the left side of the plot and low frequencies are on the right.

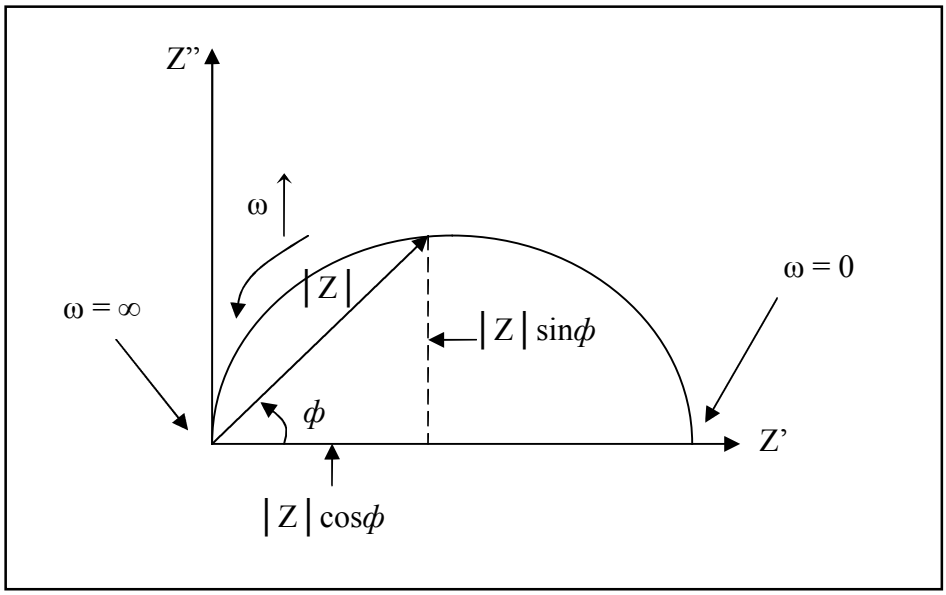


Fig.2.23 Nyquist Plot with Impedance Vector

"Bode Plot" is another popular presentation method. This consists of two graphs where the modulus of the impedance, $|Z|$, versus the frequency is plotted on a log-log scale, and phase angle, ϕ, against log frequency.

Fig.2.24 and Fig.2.25 give a typical Nyquist and a Bode plot respectively of an unpigmented epoxy coated mild steel immersed in 3.5% NaCl solution for 14 days.

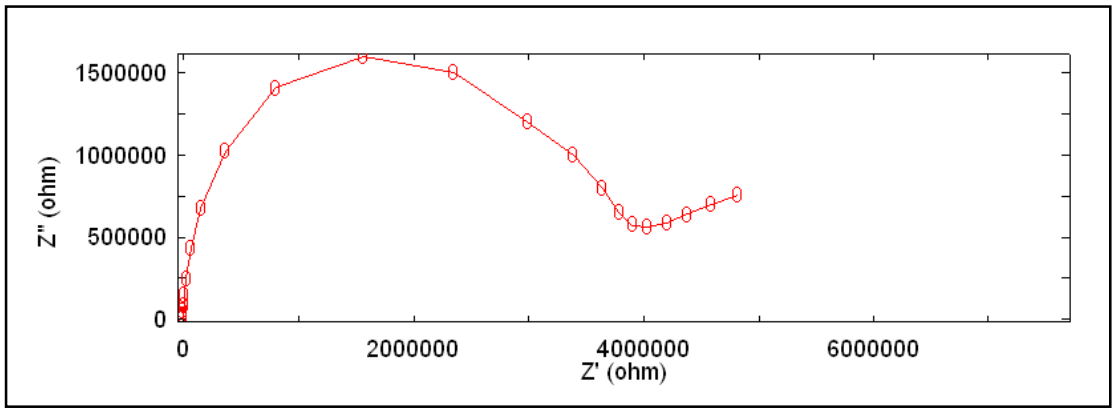


Fig.2.24 A typical Nyquist plot from the data points measured by EIS.

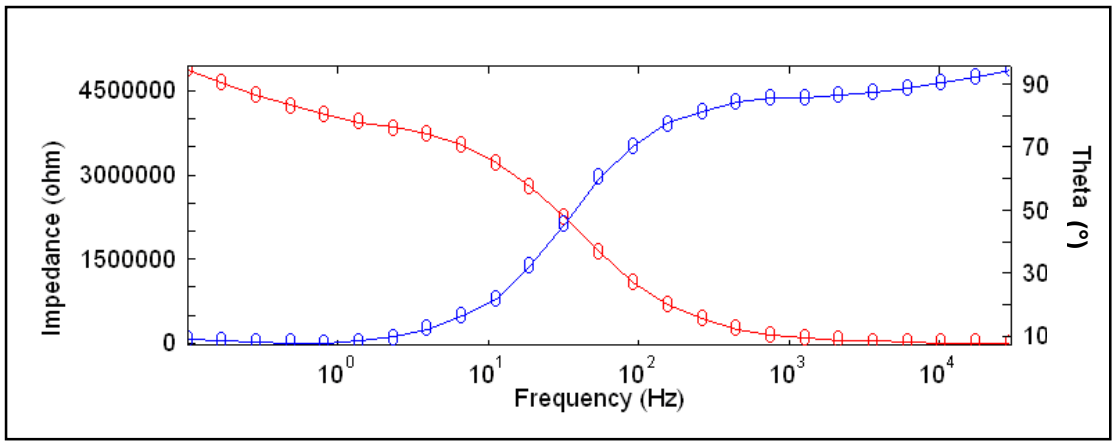


Fig.2.25 A typical Bode plot corresponding to the data points shown in Fig.2.29.

Equivalent Circuit Model

To quantify the physical and chemical processes, EIS data is commonly analysed by fitting an appropriate equivalent electrical circuit by using non-linear least squares regression software (e.g. ZSimpWin). EIS equivalent circuit models usually consist of a number of common electrical elements, such as resistors, capacitors and inductors in a network where both serial and parallel combinations of elements occur.

Each of the circuit elements in the equivalent circuit models a specific function of the sample. The equivalent circuit in Fig.2.26 is generally used to describe a failed organic coating on a metallic substrate.

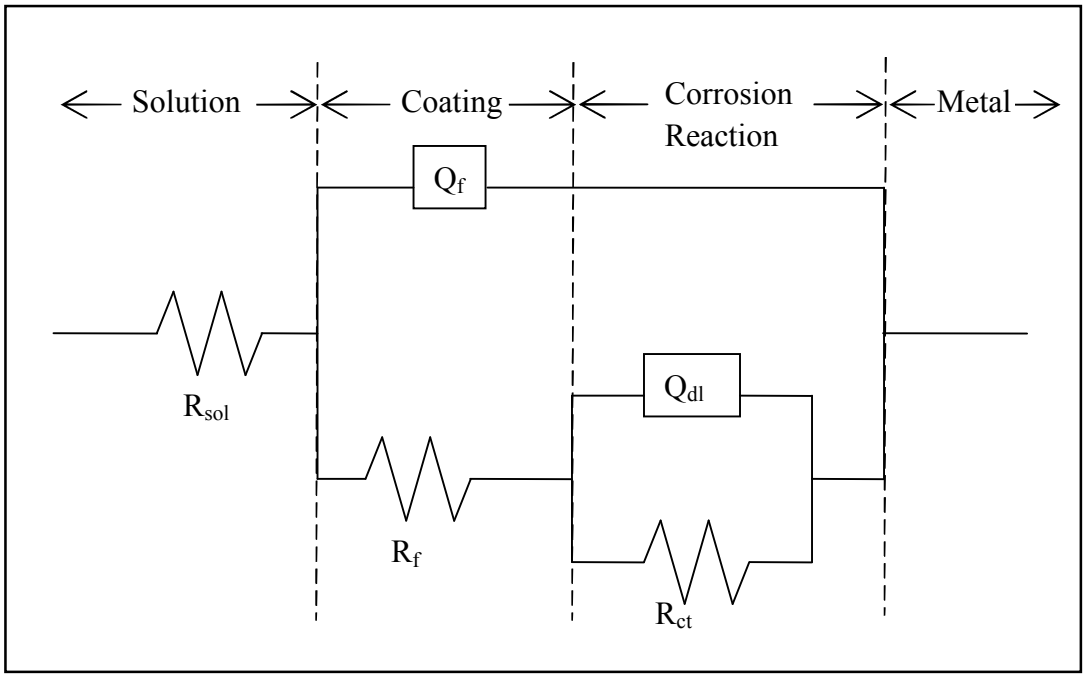


Fig.2.26 Equivalent circuit model, R(Q(R(QR))), for a failed organic coating on a metallic substrate.

R_{sol} is the solution resistance, Q_f is the constant phase element (CPE) of the coating (here CPE rather than capacitance is used and this will be discussed later), R_f is the film resistance, Q_{dl} is the double layer constant phase element and R_{ct} is the charge transfer resistance.

For an organic coating on a metallic substrate immersed in a salt solution, as time goes on, the value of the electrical elements changes, which leads to different EIS responses. Due to the nonconductive nature of an organic coating, when initially immersed in an electrolyte, coated metal samples typically exhibit very high impedance. With increasing immersion time, the impedance of the coating decreases gradually because of the uptake of water and ions during immersion and often the degradation of the polymer.

Equivalent Circuit Elements

Solution Resistance, R_{sol}: It represents the resistance of the solution between the reference electrode and the working electrode included in the equivalent circuit model though it is usually very small and not important. This resistance can be determined by fitting the experimental data to the circuit model and will be the (real) resistance at the high frequency intercept.

Film Resistance, R_f: The resistance of the coating changes during exposure to the penetration of electrolyte into the coating. It usually decreases with time of exposure and falls more quickly once corrosion begins [26, 64]. However, it is not unusual for R_f to increase after long exposure time which is typically attributed to corrosion products formed within the coating or on the metal substrate blocking the coating pores.

Charge Transfer Resistance, R_{ct}: Polarisation resistance, R_P, is a measure of the corrosion rate of the metal substrate underneath a coating. It is inversely proportional to the corrosion rate. For an activation controlled system, R_P is also known as charge transfer resistance, R_{ct}. The relation between R_{ct} and the corrosion current, i_{corr}, is as shown in Stern-Geary equation [120], Equation 2.35.

$$R_{ct} = \frac{dE}{di} = \frac{B}{i_{corr}} \qquad \textit{[Equation 2.35]}$$

Where B is determined from a Tafel plot.

For anode and cathode reactions under activation control, the current is given by the Tafel equation. It was shown by Fig.2.27 that under these conditions, the slope $\frac{dE}{di}$ at E_{corr} is inversely proportional to i_{corr}. The polarisation curve tends towards linearity

at this essential point.

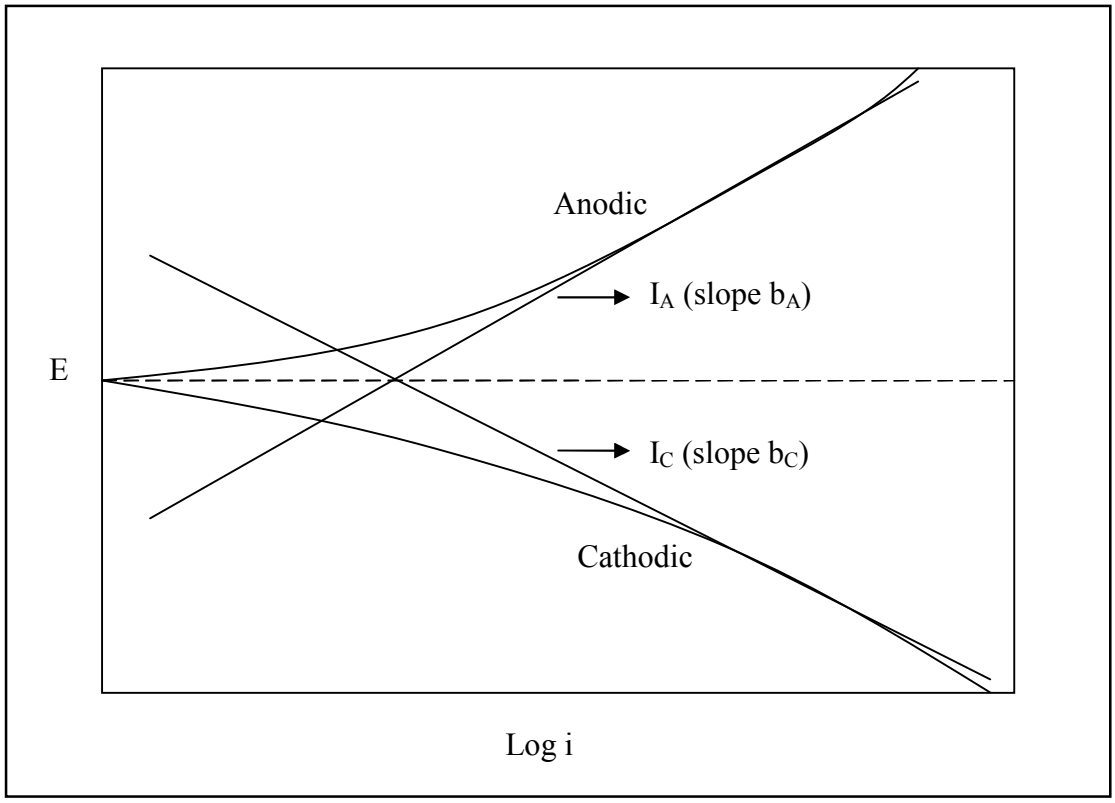


Fig.2.27 Tafel plot for a reversible electrode

Fig.2.27 shows a schematic illustration of a Tafel plot of potential, E, against the logarithm of the current density, log i, where the anodic and cathodic constant are b_A and b_C. They are determined from the slopes of the anodic and cathodic lines.

$$B = \frac{b_A b_C}{2.3(b_A + b_C)} \qquad \textit{[Equation 2.36]}$$

Coating Capacitance, C_f: The capacitance of an organic coating is a very important parameter to measure during coating failure.

$$C_f = \frac{\varepsilon_0 \varepsilon_r A}{d} \qquad \textit{[Equation 2.37]}$$

Where ε_0 is the permittivity of free space, $\varepsilon_0 = 8.85\times10^{-12}$ F·m^{-1}; ε_r is the relative permittivity of the coating; A is the area, m^2 and d is the thickness, m.

The relative permittivity, ε_r, depends on the material. For a vacuum, $\varepsilon_r = 1$; water at 20℃, $\varepsilon_r = 80.1$ and an organic coating, $\varepsilon_r = 4 - 8$.

As water ingresses into the coating, the capacitance of an organic coating coated metallic substrate will change due to the large difference in the relative permittivity between water and organic coating. The most widely used equation relating capacitance to water content was proposed by Brasher and Kingsbury [121], which is known as the Brasher-Kingsbury equation:

$$V_W = \frac{\log(C/C_0)}{\log K_W} \qquad \textit{[Equation 2.38]}$$

Where V_W is the volume fractions of water; K_W is the relative permittivity of water and C and C_0 are the capacitances measured at any time and at zero time respectively.

While in a later paper, Sykes [122] revisited the deviation of this equation and proposed an alternative form which is more sensible.

$$V_W = \frac{\log(C/C_0)}{\log(K_W/K_P)} \qquad \textit{[Equation 2.39]}$$

Where K_P is the relative permittivity of the dry coating.

EIS can be used to measure the capacitance change and therefore water content.

Double layer capacitance, C_{dl}: The coating is not the only feature of the sample that gives rise to a capacitance. At the corrosion site, there is a charge on the metal electrode and an ionic charge in the solution that are separated at the metal/solution interface which is commonly known as the "double layer" in electrochemical theory. The capacitance is called the Double Layer Capacitance, C_{dl}. The value of C_{dl} is usually in the range of 0.1 – 0.4 F/m^2 which is a lot higher than that of C_f (10^{-5} F/m^2).

Impedance of C_{dl} falls as frequency increases, so that R_{ct} becomes shorted out; the smaller C_f only shorts R_f at very high frequency, thus difference in C values leads to 2 semi-circles with the one at the low frequency representing electrode reactions and the high frequency representing the coating.

Constant Phase Elements (CPE), Q: Capacitors in EIS experiments often show non-ideal behaviour so that "Constant Phase Elements" are usually used to model the experimental data, rather than capacitance. The impedance of CPE is given by,

$$Z = \frac{1}{Q(j\omega)^n} \qquad \textit{[Equation 2.40]}$$

This expression is similar to the equation describing the impedance response of capacitor ($Z = \frac{1}{j\omega C}$ *[Equation 2.41]*), but includes the exponent n (0 – 1). The value of n is ≤ 1 and is adjusted by the curve fitting software to give a good fit to the real data. The closer the value of n to 1, the more "ideal" the capacitor. This model element deals simply with Bode plots that do not show slope = -1 (ideal capacitor, C).

Warburg Impedance, Z_W: In some cases, an impedance called Warburg Impedance is generated at the electrode by concentration polarisation (*i.e.* diffusion). This element can be deduced by solving Fick's second law (a partial differential equation solution) for a sinusoidal signal. Fig.2.28 shows an equivalent circuit model with a Warburg Impedance.

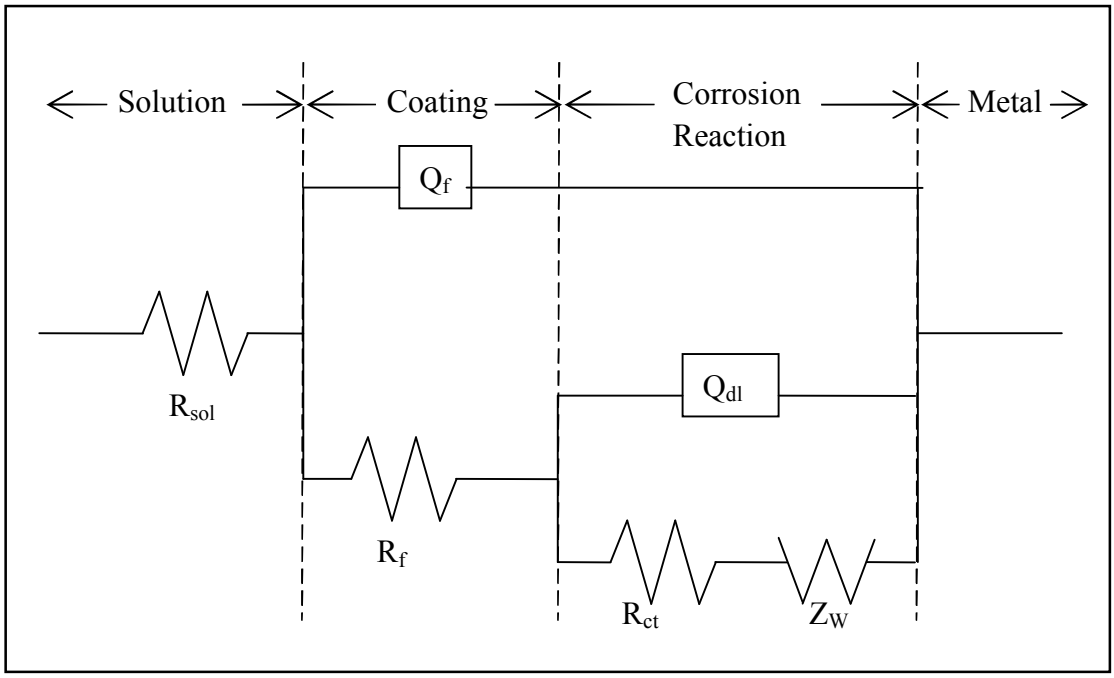


Fig.2.28 Equivalent circuit model, R(Q(R(Q(RW))))

The Warburg impedance depends on the frequency of the perturbation signal and has both real and imaginary components. At high frequency, the diffusing reactants only diffuse a short distance which results in the small Warburg impedance; while at low frequency, the reactants travel further which causes bigger Warburg impedance. Z_W tends to a limit in the presence of convection which limits diffusion layer thickness.

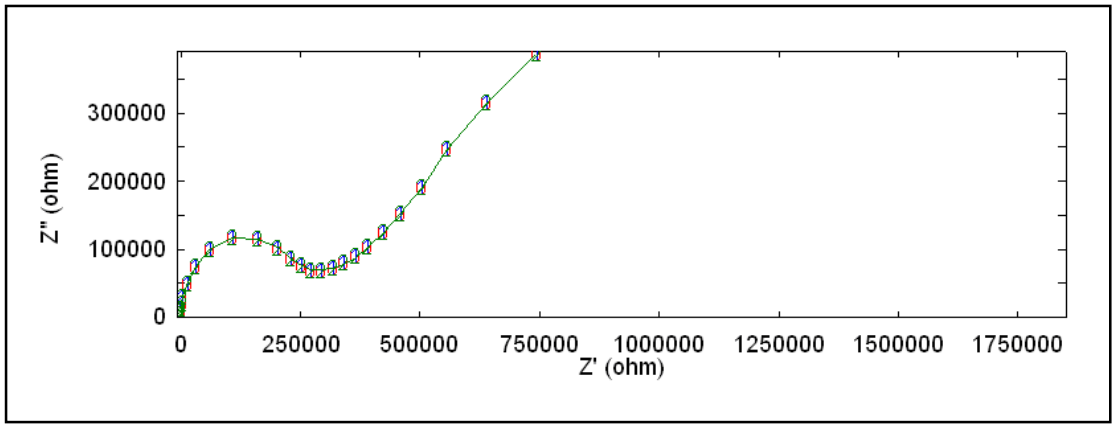


Fig.2.29 A typical Nyquist plot showing the Warburg impedance

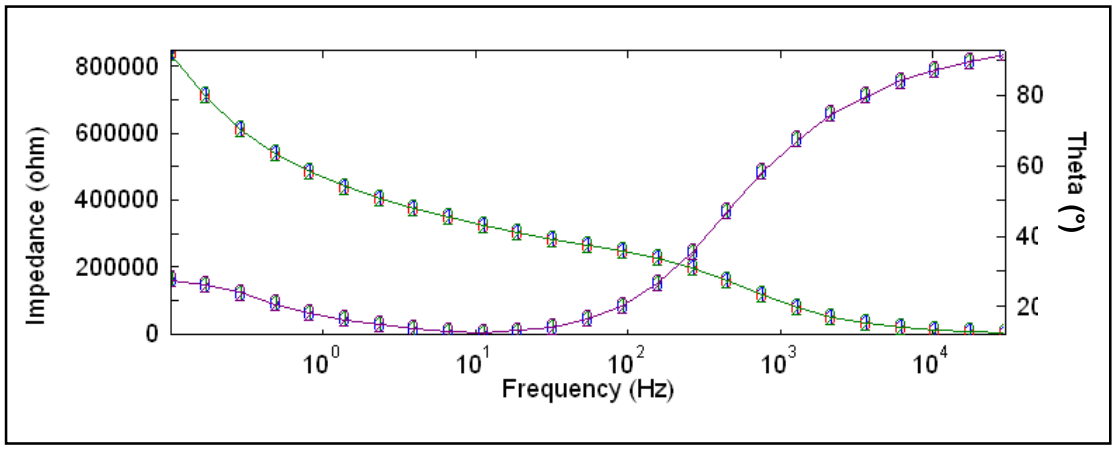


Fig.2.30 A Bode plot corresponding to Fig.2.34.

Fig.2.29 and Fig.2.30 show a Nyquist and a Bode plot including a Warburg impedance. On the Nyquist plot, the Warburg impedance appears as a diagonal line with a slope of 45°. On the bode plot, it should show a phase shift of 45° and a slope of $-\frac{1}{2}$ for lnZ/lnf. If fitting the data obtained from the EIS of Fig.2.34 into the equivalent circuit model R(Q(R(Q(RW)))) by ZSimpWin, Fig.2.31 is obtained.

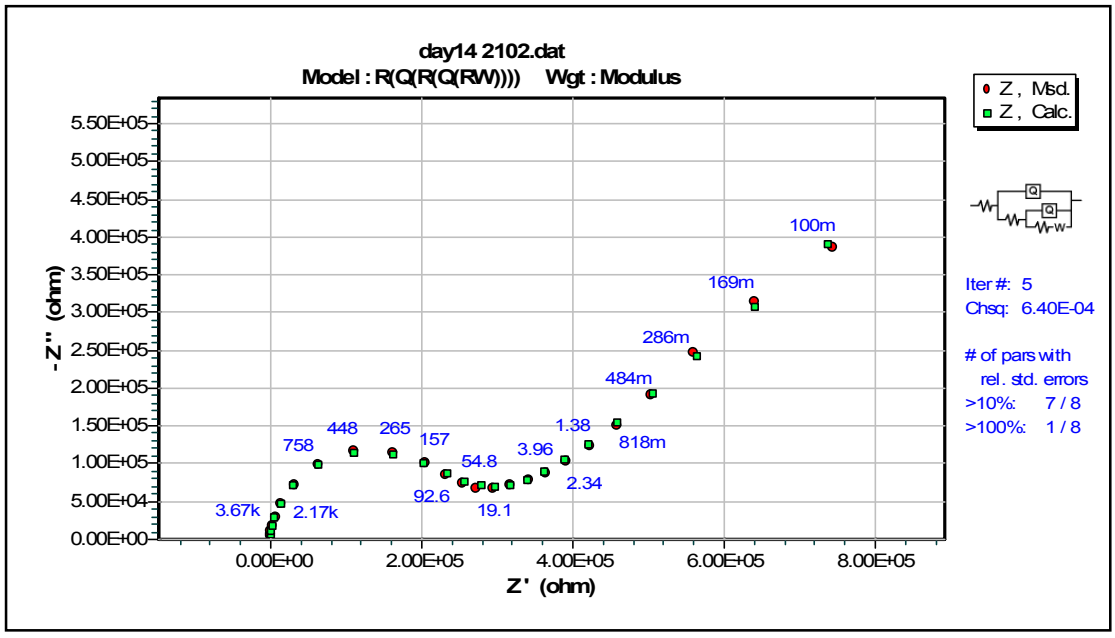


Fig.2.31 Data obtained from the EIS (Red) and the simulated results from ZSimpWin (Green).

It can be seen from Fig.2.31 that the EIS data (red points) and the fitting data (green points) correlate well with each other.

Chapter 3 Cathodic Disbonding Characterisation

3.1 Introduction

Many cathodic disbonding studies have been carried out over the past years [53, 55-59, 65, 68, 75, 85, 123]. Nevertheless, the complex mechanism of cathodic disbonding of organic films on steel is not yet fully understood. In order to get a further understanding of the mechanism of cathodic disbonding, two types of tests: full-immersion tests and semi-immersion tests were designed in this part of work. The aim of the full-immersion tests was to characterise the cathodic disbonding of an unpigmented epoxy on mild steel under the normal immersion condition. The semi-immersion tests were designed so that the coatings below the defect are compeletely immersed in 3.5% NaCl solution, but above the defect, the coating is exposed to water saturated air. There are three reasons for this design: 1) it can provide a critical comparison between two testing conditions (full-immersion *vs.* exposure to water-saturated air) on the same sample; 2) it helps to distinguish the route for ion transport or current flow: if there is a big difference in the disbonding rates between above and below the defect, then transport through the coating is playing a part; if there is no significant difference, then the most likely explanation is that transport is mainly along the coating/metal interface; 3) it can determine whether the SKP experiments [45, 55-59, 85] that only immerse the defect, while exposing the remainder of the panel to humidity will actually replicate normal cathodic disbonding

(samples fully-immersed in the solution). All the experiments in this chapter were performed with the unpigmented epoxy coated mild steel, EC samples, under free corrosion conditions. Scanning Acoustic Microscopy (SAM) and Scanning Kelvin Probe (SKP) were mainly employed to conduct this study. They are also backed up by the traditional Optical Microscopy. Adhesion tests were carried out to explain the "blister" formation within the "disbonded area".

3.2 Cathodic Disbonding Characterisation

3.2.1 Experimental

Samples used in experiments in this chapter are the unpigmented phenalkamine cured epoxy coated mild steel, EC samples (DFT: 45 ± 5 μm), which were prepared as described in Chapter 2. They were tested both fully- and semi-immersed in 3.5 wt.% NaCl solution at room temperature. Fig.3.1 gives a schematic diagram of the semi-immersion test setup. The water level was in line with the middle of the defect so that the part below the defect was completely immersed with the defect wet, while the part above the defect was exposed to water-saturated air. SAM and SKP examinations were carried out at regular intervals after immersion. The experimental settings of SAM and SKP are the same as described in Chapter 2.

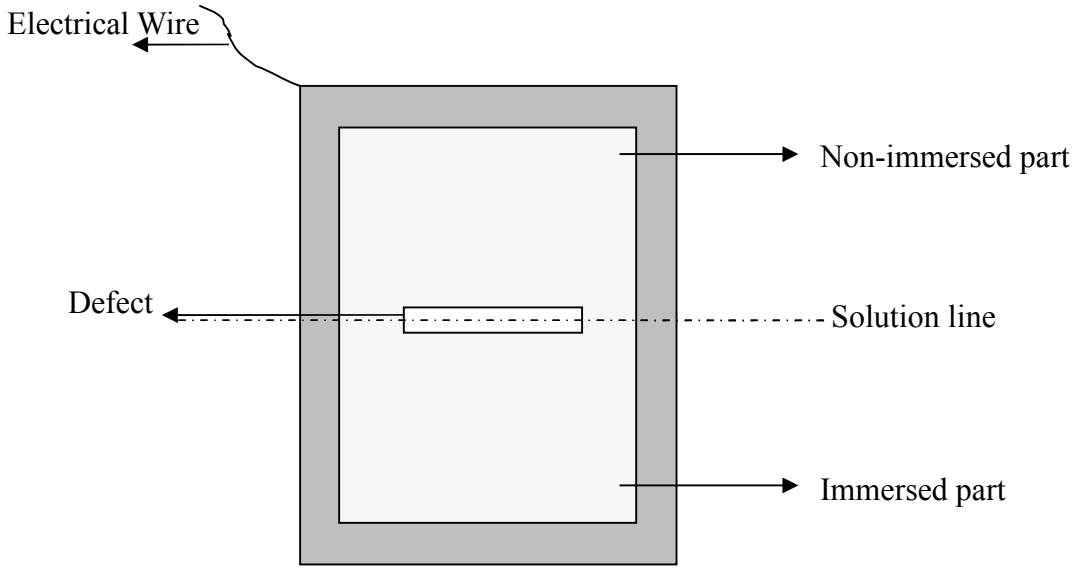


Fig.3.1 Schematic diagram of the semi-immersion test (Not to scale)

3.2.2 Results and Discussion

3.2.2.1 Full-immersion Tests

3.2.2.1.1 SAM and SKP Characterisation

Fig.3.2 - Fig.3.6 give a series of optical and SAM images, some SKP potential maps are also presented here, showing the cathodic disbonding of the unpigmented epoxy coating fully immersed in 3.5% NaCl solution for 5 days.

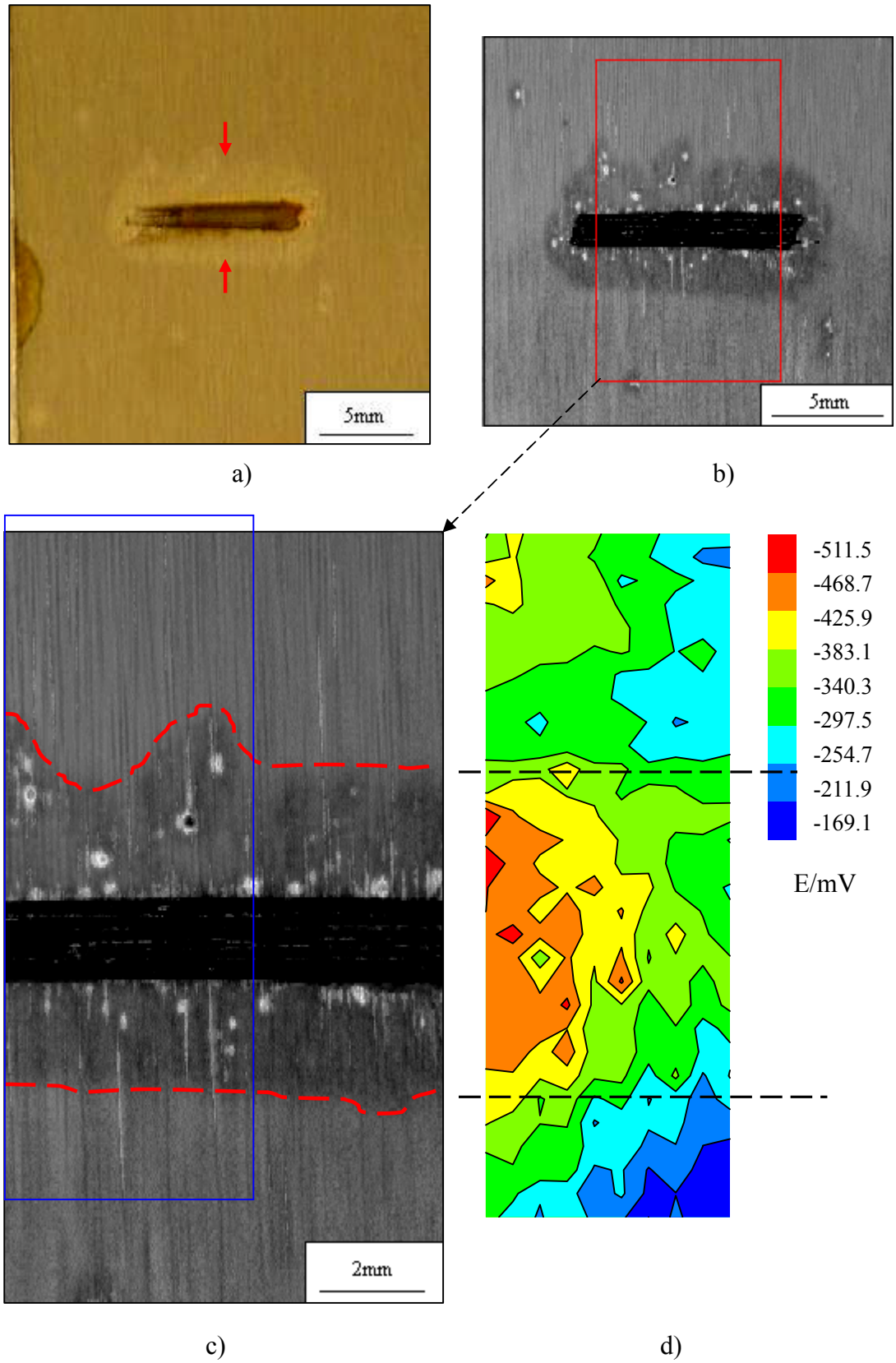


Fig.3.2 EC fully-immersed in 3.5% NaCl solution, day 1, a) optical image; b) SAM image; c) SAM image corresponding to close up of the circled area in b); d) SKP potential map corresponding to the circled region in c).

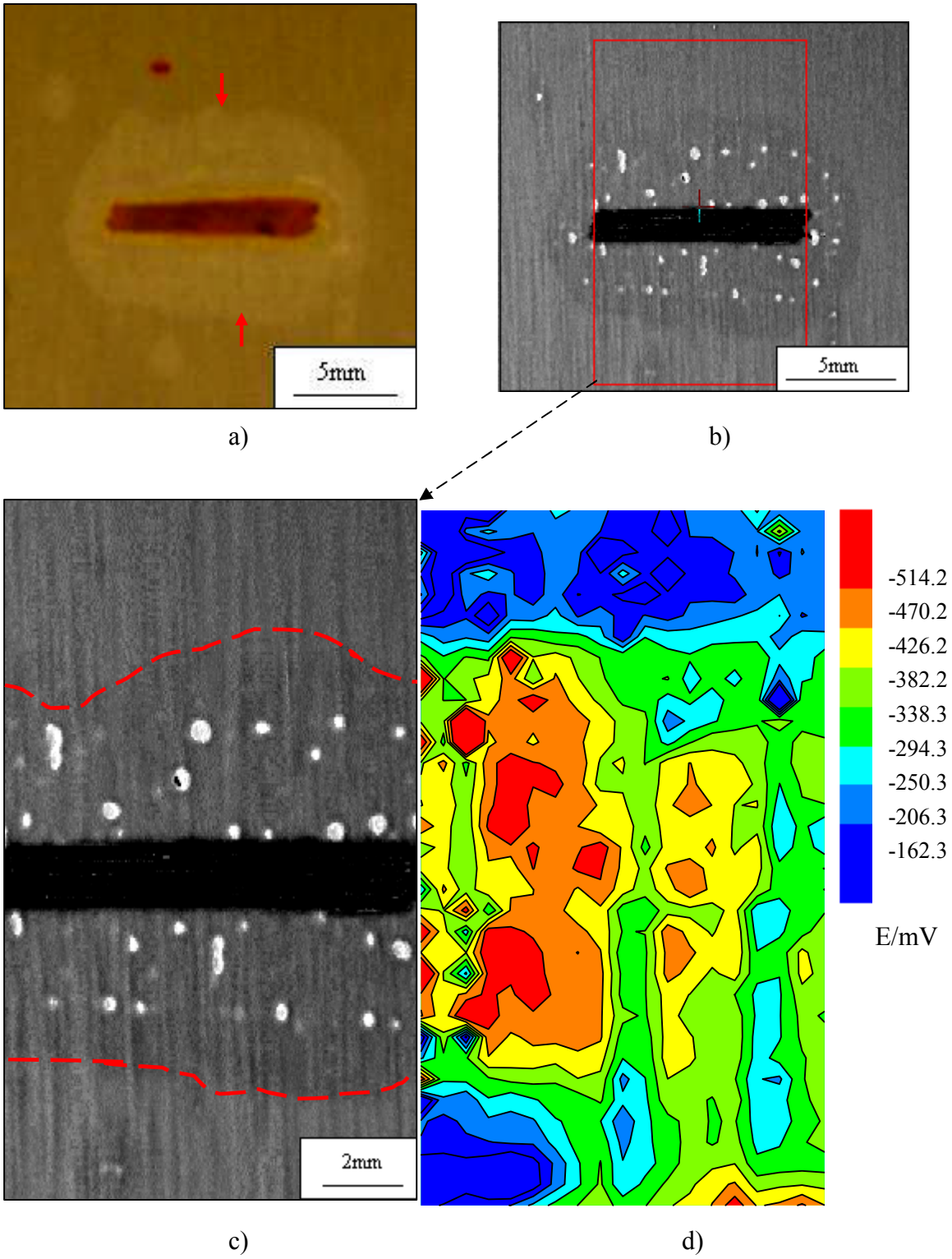


Fig.3.3 EC, full-immersion, day 2, a) optical image; b) SAM image; c) SAM image corresponding to close up of the circled area in b); d) SKP potential map corresponding to c).

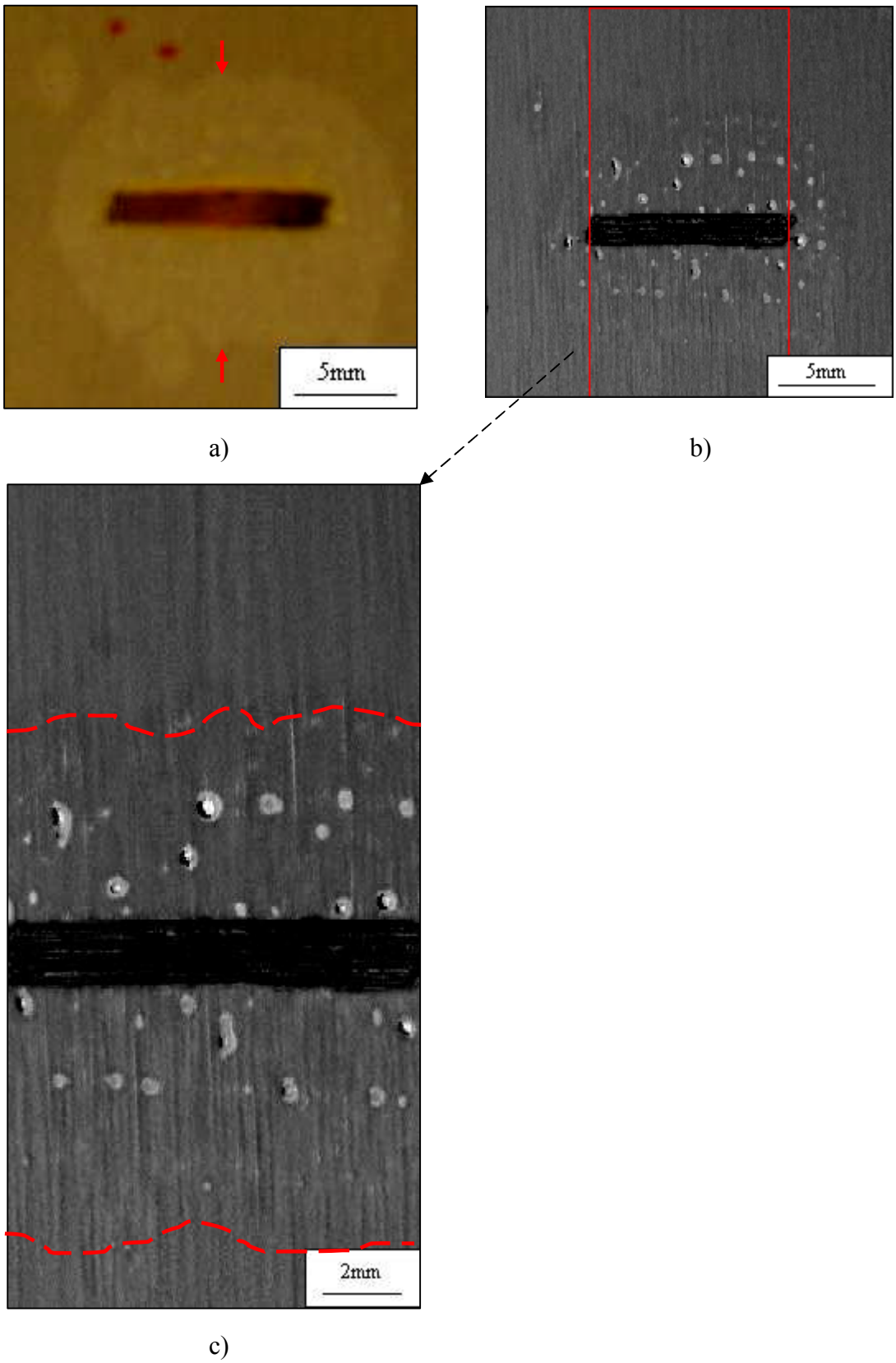
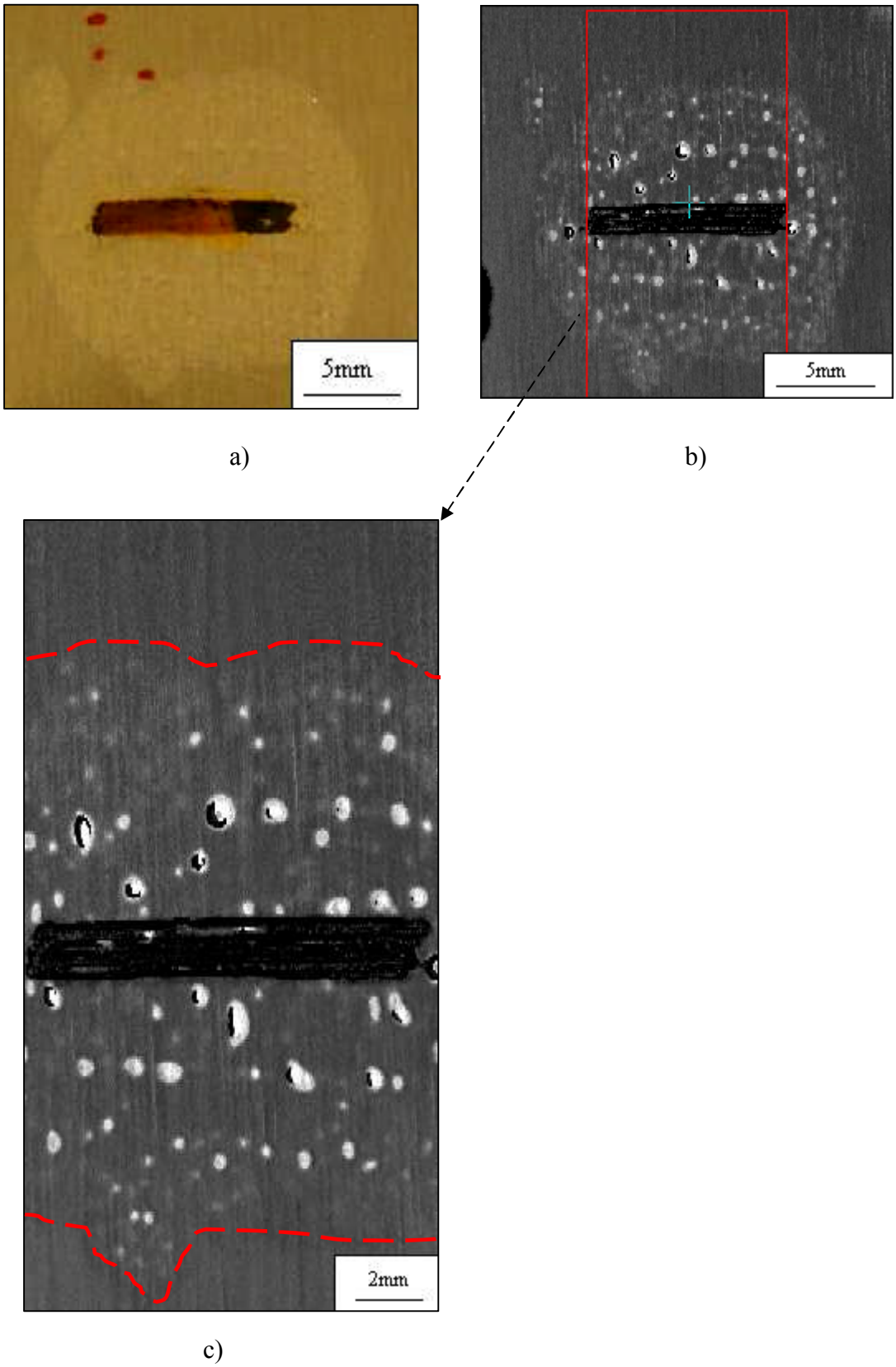


Fig.3.4 EC, full-immersion, day 3, a) optical image; b) SAM image; c) SAM image corresponding to close up of the circled area in b).



a) b)

c)

Fig.3.5 EC, full-immersion, day 4, a) optical image; b) SAM image; c) SAM image corresponding to close up of the circled area in b).

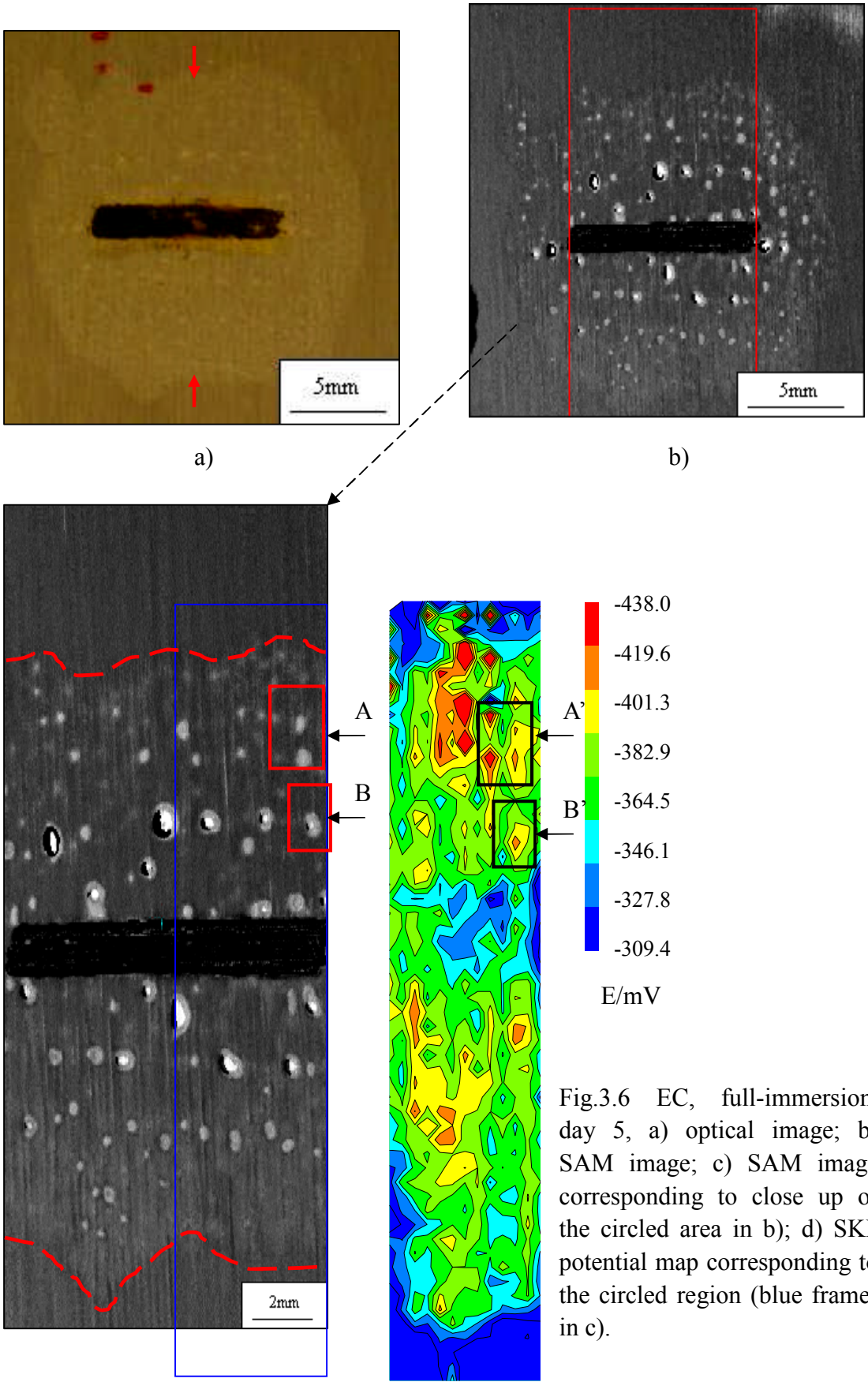
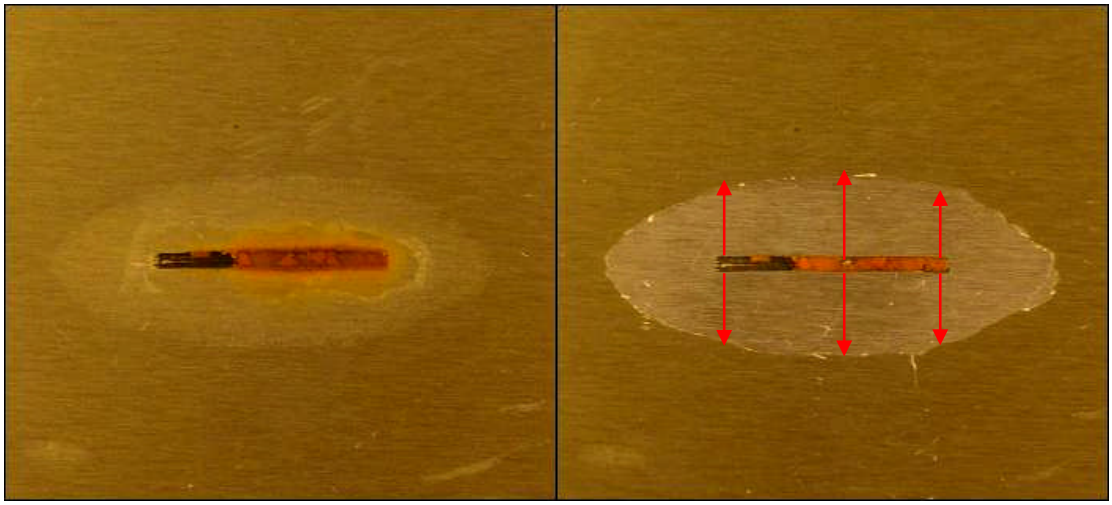


Fig.3.6 EC, full-immersion, day 5, a) optical image; b) SAM image; c) SAM image corresponding to close up of the circled area in b); d) SKP potential map corresponding to the circled region (blue frame) in c).

As shown in the optical images, Fig.3.2 a) – Fig.3.6 a), a lighter "halo" around the defect is clearly distinguished. We believe the area in the "halo" is disbonded (Here "disbonded" does not mean total adhesion loss. This will be discussed later.). The red arrows mark the disbonding front. This is supported by the preliminary work, in which a scalpel was applied to remove the coating within the disbond and it was found that the border of the disbonded region and the intact region is quite distinct - it was easy to remove the coating within the disbonded area, while beyond the border, the coating could not be easily peeled off. Fig.3.7 gives two optical images: one before coating removal (Fig.3.7 a)) and the other after the removal of the coating in the disbonded area (Fig.3.7 b)). The average of three distances from either side was defined as the cathodic disbonding distance. While in this work, disbonding distances of both sides along the defect have been measured and recorded.

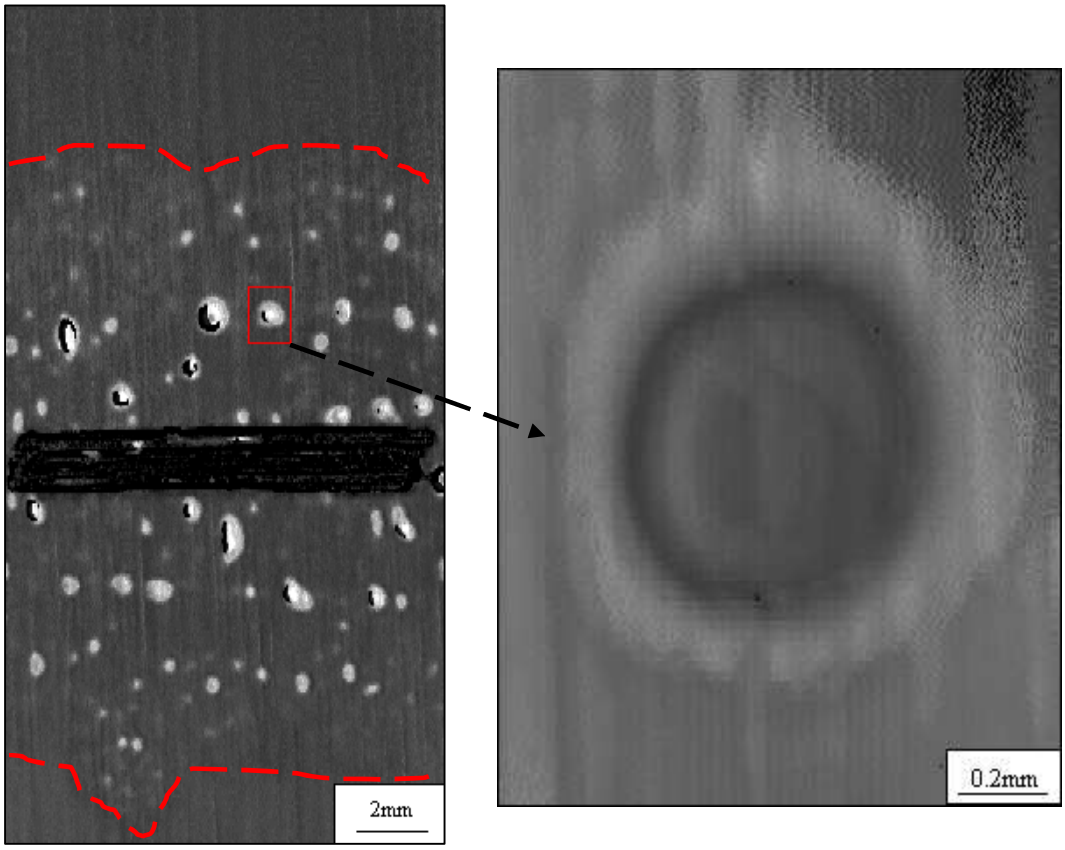


a) b)

Fig.3.7 Optical images showing the peel-off test for the disbonding distance determination, a) before coating removal; b) after coating removal.

The black feature in the centre of the SAM image corresponds to the linear defect created on the sample. The darker areas are the disbonded region with the red lines

marking the disbonding front. SAM examinations show that disbonding spreads outwards from the defect forming a roughly elliptical patch corresponding to the "halo" shown in the optical images around the linear scribe mark, but within which, brighter areas, circular in shape, *e.g.* Fig.3.8 b) shows a typical circular feature (about 1mm in diameter) corresponding to the circled area in a), are blisters. It showed different contrasts over the whole blister, which was due to the changing distances of the polymer from the substrate. This could be explained by the A-scan and B-scan of the SAM. These circular features increase in number and size as exposure time with fresh ones forming close behind the disbonding front. The presence of similar circular features was previously reported by Kendig and Addison [50, 52].



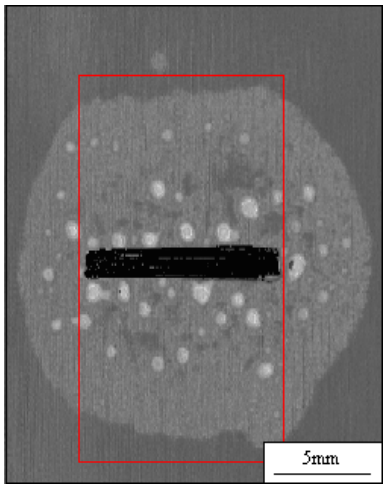
a) b)

Fig.3.8 EC, full-immersion, day 5, a) SAM image; b) circular feature corresponding to the circled area in a).

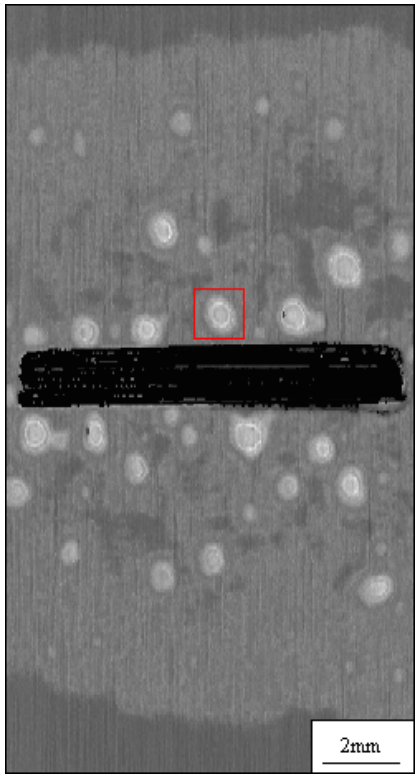
The following section will show these brighter circular features to be blisters. Some SKP potential maps with corresponding SAM images are presented in Fig.3.2 e) and f), 3.3 e) and f) and 3.6 e) and f) showing the measurements of the electrochemical potential underneath the coating correlate quite well with the SAM images. The orange and red patches are with more negative potentials, corresponding to anodes; while the blue and green ones with more positive potentials correspond to cathodes. Fig.3.6 e) and f) display a typical matching of the SKP potential map with the SAM image. Boxes A′ and B′ in Fig.3.6 f) identify anodes, which correspond to the "blisters" in boxes A and B in Fig.3.6 e), suggesting that the "blisters" have formed at the local anodes within the disbonded region which help the propagation of the disbonding.

3.2.2.1.2 Circular Feature and Blister Discussion

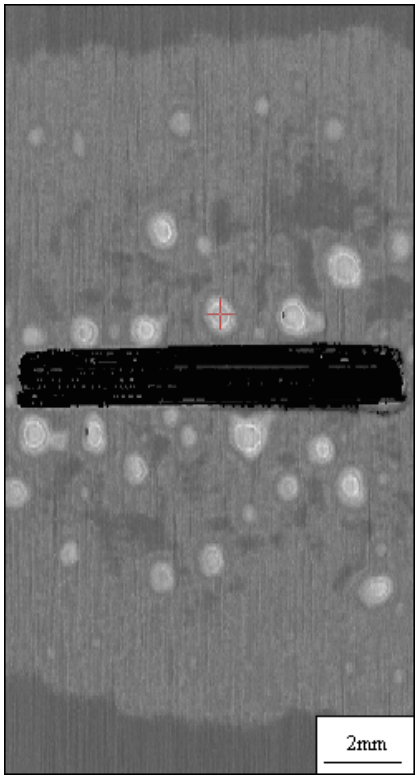
To explain the circular features occurring within the disbond to be blisters, SAM A-scan, B-scan and C-scan results are shown here for illustration.



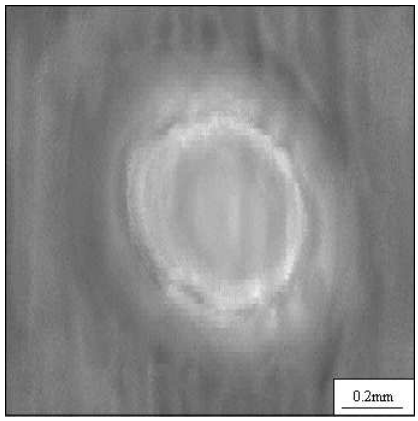
a)



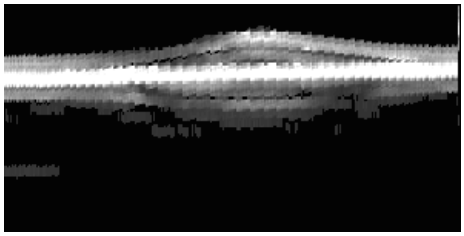
b)



c)

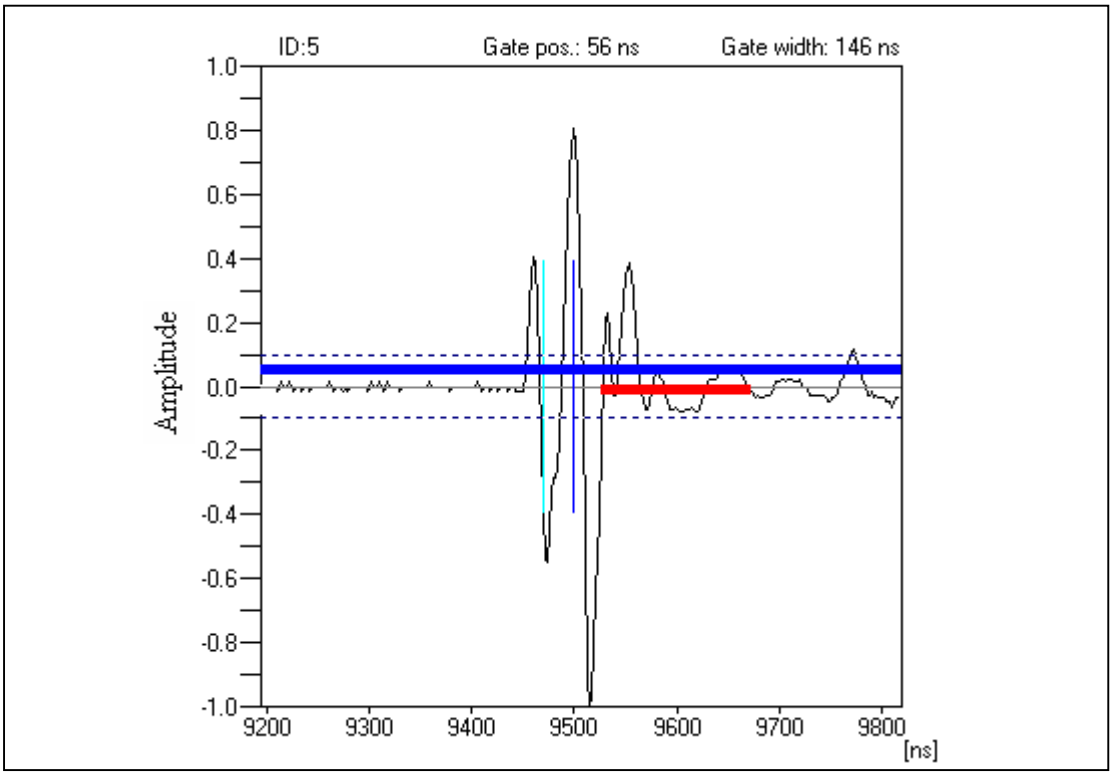


d)

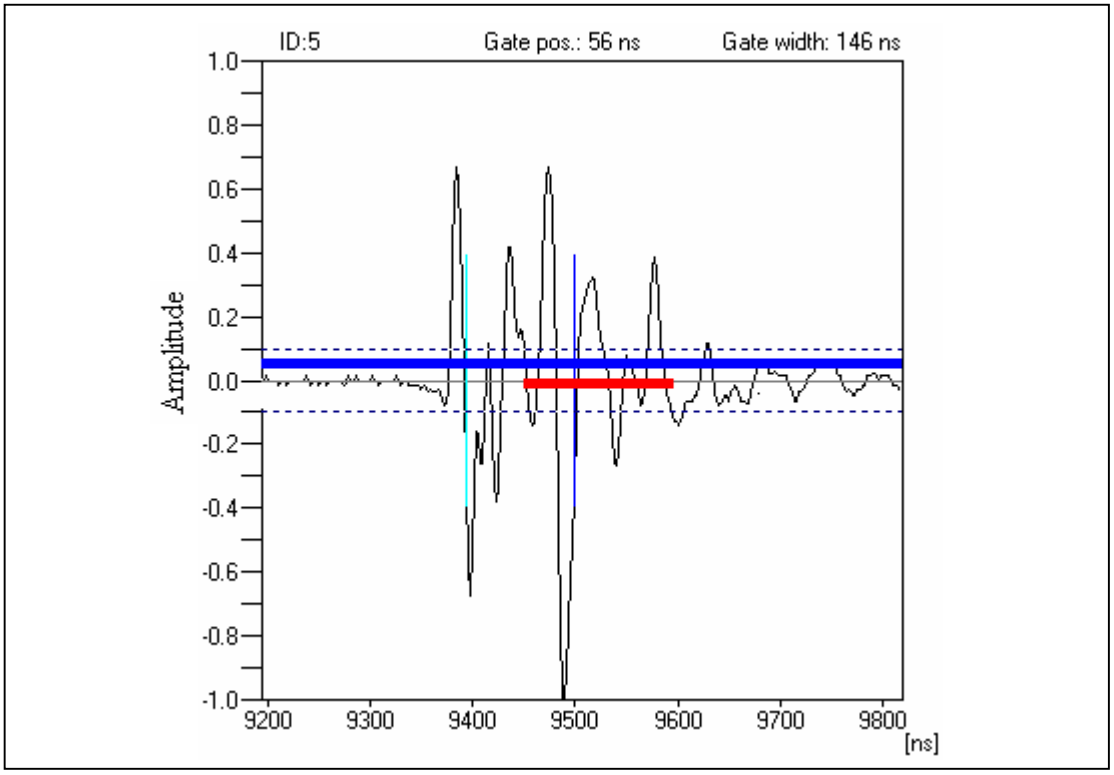


e)

Fig.3.9 SAM results showing circular features occurring within the disbond, a) C-scan of the disbond; b) and c) close up of the circled area in a); d) close up of the circular feature circled in b): e) B-scan centred with the "cross" in c).



a)



b)

Fig.3.10 A-scan window showing received acoustic signal of EC fully immersed in 3.5% NaCl solution, day7, a) “intact area”; b) “blistering”. Amplitude in arbitrary units.

The reflected signal in Fig.3.10 a) shows the echo train of the "intact area" within the disbond and in Fig.3.10 b) represents the echo train of the "circular features". There are mainly three reflection echoes in Fig.3.10 b). The first echo is attributed to the reflection from the coating surface; the second corresponds to the reflection from the coating/metal interface and the third from the substrate with subsequent peaks arise from the multi-reflections from coating/metal interface or super-position of the peaks from the coating/water and water/metal interfaces.

The time lag between the first and the second echo in Fig.3.10 a) corresponds to a coating thickness of 54 μm (1/2 * (41 ns * 2650 $m \cdot s^{-1}$ [114])), while the dry film thickness measured by the thickness gauge is about 42 μm. The increase is probably due to the water uptake after immersion in the NaCl solution and the modification of the acoustic velocity by water uptake. In Fig.3.10 b), the time difference between the first peak and the second peak (which is now inverted due to phase reversal) again represents the coating thickness of 49 μm (1/2 * (37 ns * 2650 $m \cdot s^{-1}$)) and the first and the third peak represents the distance between the coating surface and the metal: 98 μm (1/2 * (74 ns * 2650 $m \cdot s^{-1}$)). Obviously, reflections from the metal within the circular feature have a longer delay than for the "intact area", which is consistent with bulging of the coating and presence of a slower medium (water) and additional interfaces. This supports our assumption that those circular features are blisters.

However, this raises the question: how can blisters form within a region that is already disbonded? Is it possible that adhesion is still present? To answer this, adhesion tests were carried out.

3.2.2.1.3 Adhesion tests

3.2.2.1.3.1 Introduction

This part of work aims at the explanation of the blister formation within the disbond. In light of the previous work carried out by Crossen [124] in Oxford, the 90° peel testing method was applied to test the adhesion.

Peel testing is a destructive method frequently used to assess the adhesion of coatings. It is simple, easy to operate, and the adhesion force can be acquired quickly after removal from solution before the interface begins to dry. Bullet and Prosser [40] reported that the major drawback of the peel testing method to examine the adhesion is the dependence of the results on the peel rate, which gives an empirical value rather than an absolute value of the adhesion force. Only qualitative adhesion measurements are needed in this work which aim at testing whether there is any adhesion remained in the "disbonded area" of the sample after being immersed in the 3.5% NaCl solution for a couple of days.

3.2.2.1.3.2 Experimental

90º peel testing was conducted after the SAM and SKP tests on a 5 mm wide strip which was cut into the coating by a scalpel perpendicular to the defect with the samples still in the solution. Fig.3.11 shows the setup constructed for measuring the peel force.

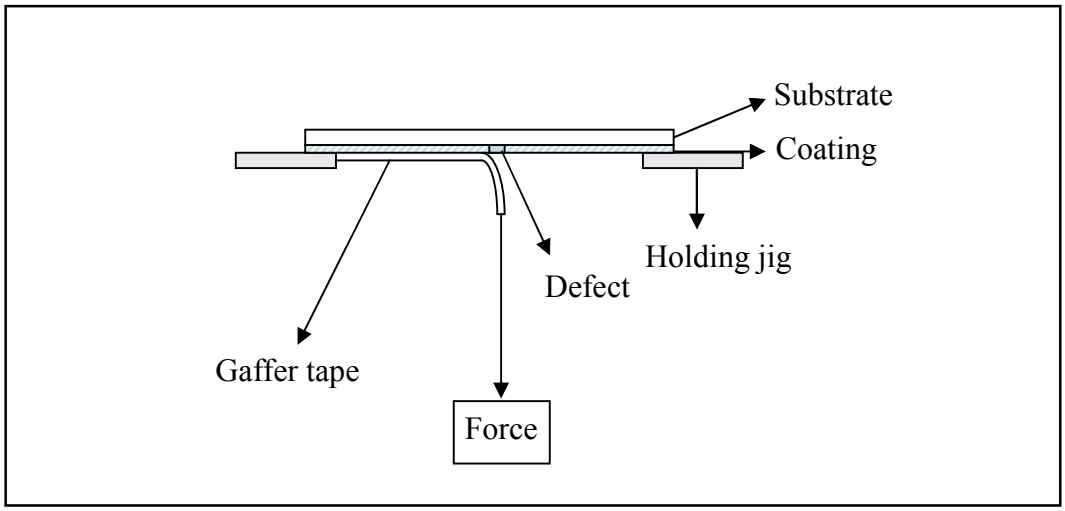


Fig.3.11 Schematic diagram of peel testing

The film is lifted off by applying force (Mass was added in small increments until the coating just started to peel off from the substrate.) to a strip of adhesive gaffer tape starting from the coating edge at the defect. The angle between the coating film detached by the adhesive tape and the substrate was kept at a constant value of 90º. The mass applied was determined with a chemical balance and converted to a peel force (F = mg).

The same procedure was repeated for other strips cut from the opposite side to check the reproducibility of the results.

3.2.2.1.3.3 Results and Discussion

Table.3.1 shows the mass applied on the 5 mm wide adhesive tape strip to remove the disbonded coating from mild steel (an EC sample which has been fully immersed in 3.5% NaCl solution for 7 days).

Tests	Mass applied/g
1	9.6
2	10.1
3	10.9
4	9.7

Table.3.1 Mass applied to peel off the disbonded EC coating immersed in 3.5% NaCl solution for 7 days. Results of the repeated tests have been shown.

The mass applied on the 5 mm wide strip of tape to peel off the coating from the substrate is 10.1 ± 0.8 g, therefore the adhesion force is about 0.2 $N \cdot cm^{-1}$. Though the adhesion strength is heavily degraded by exposure to the salt solution and the products of the cathodic oxygen reduction, which agrees well with the documented work of Walker [47], Ruggeri and Beck [125], Graham and Emerson [126], Leidheiser and Wang [67], Funke [43] and Crossen [124, 127], application of force is still required to remove the coating from the substrate.

Leidheiser and Wang used tape to remove the coating that had disbonded before making their disbonded area measurements [67], but no quantitative data of adhesion was given, so we cannot be sure whether the coating was already completely detached or not.

Funke [99] suggested that during blistering, the organic coating should still adhere to the substrate beyond the periphery of the blistered region. The tests were carried out by applying adhesive tape to samples of various organic coatings which had been exposed to liquid water at ambient or elevated temperatures for some time. It was

shown that the adhesion of the wet coating had substantially decreased before blistering occurred, and blisters grow within this low adhesion region.

Residual adhesion within the disbonded area has also been reported in a recent study on the cathodic disbonding of polyurethane films on oxide-covered steel by Wielant *et al.* [128], in which to further evaluate whether the higher ion mobility was correlated to the interfacial adhesion strength, 90º peel-off tests were carried out to measure the remaining adhesion of the polyurethane based lacquer within the disbonded area. It was reported that the polymer could be easily lifted off, and that force needed to remove the coating was near the detection limit of the equipment available [55], demonstrating that the existence of some remaining adhesion was possible.

Changes must occur at the coating/metal interface or in the surface layer of the polymer that weaken adhesion between the coating and the substrate and also resulted in the generation of SAM contrast. The incomplete detachment of the coating from the substrate is linked to production of alkali by the reduction of oxygen at the coating/metal interface or possibly generation of free radicals which can destroy the chemical bonds or result in the degradation of the coating [87, 129]. But at some local sites, adhesion is not completely lost and blisters form.

3.2.2.1.4 Disbonding Kinetics

As exposure continues, the disbonded area propagates and the increase of the disbonding distance follows parabolic kinetics with exposure time, as shown in Fig.3.12.

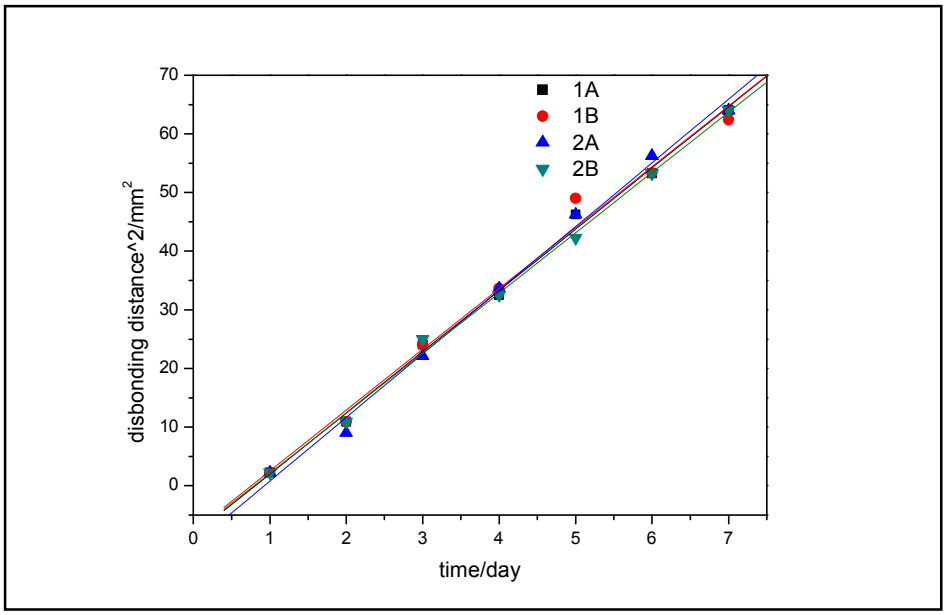


Fig.3.12 Disbonding of EC immersed in 3.5% NaCl solution. Duplicate panels were tested, 1A: sample1 + sideA; 1B: sample1 + sideB; 2A: sample2 + sideA and 2B: sample2 + sideB.

Sample	**Disbonding Rate Constant ($mm^2 \cdot day^{-1}$)**		**Correlation Coefficient R**	
	Side A	Side B	Side A	Side B
1	10.4	10.4	0.998	0.994
2	10.9	10.3	0.997	0.998

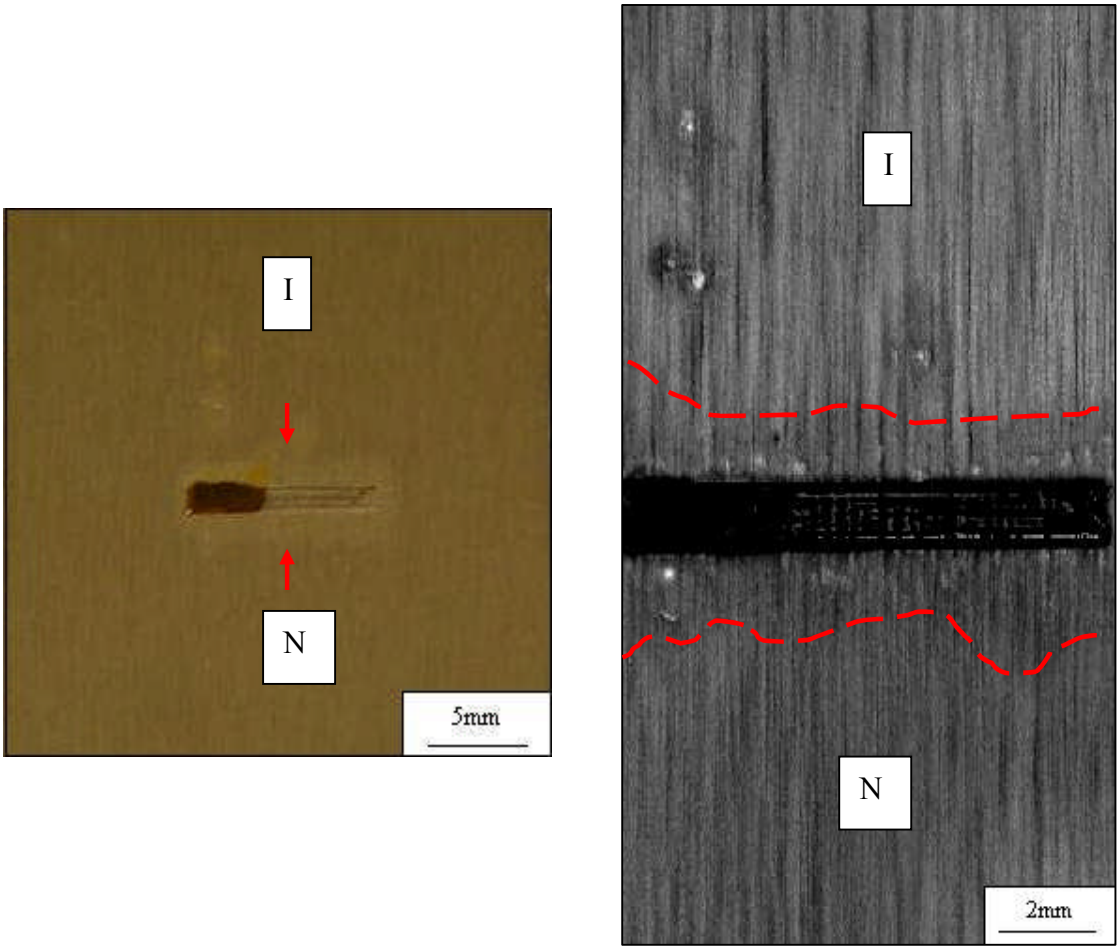
Table.3.2 Disbonding rate constants and the correlation coefficients.

Table.3.2 gives a summary of the disbonding rate constants of duplicate EC samples which were exposed to 3.5% NaCl solution for 7 days. It is apparent that the disbonds of both sides along the defect have similar rates. And all the correlation coefficients of the linear fit for the disbonding distance ^ 2 *vs.* time are > 0.99, which suggests that the cathodic disbonding of unpigmented epoxy coated mild steel immersed in 3.5% NaCl solution follows parabolic disbonding kinetics, generally implying a mechanism

involving diffusion of ions, water or oxygen along the coating/metal interface.

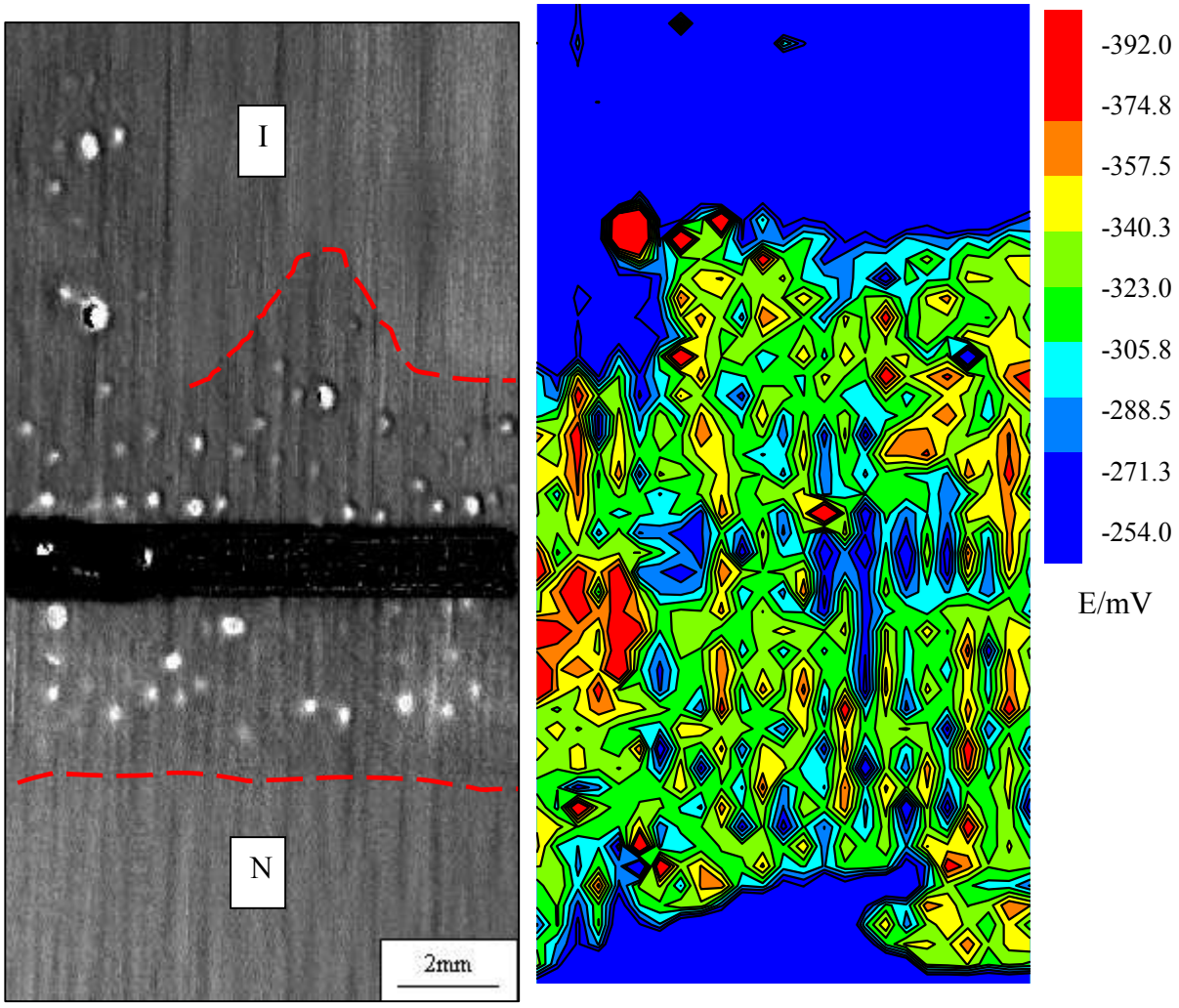
3.2.2.2 Semi-immersion Tests

3.2.2.2.1 SAM and SKP Characterisation

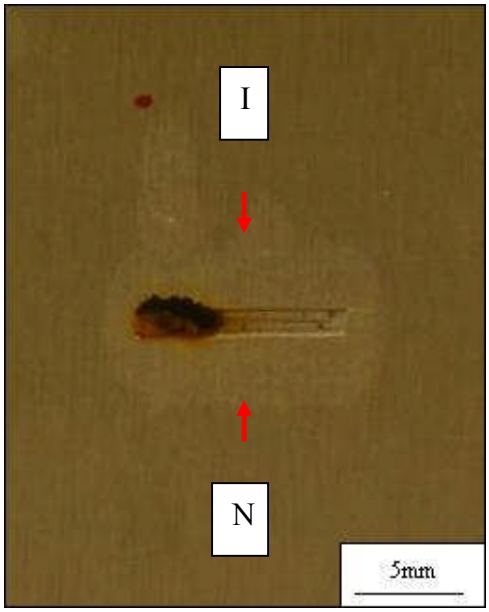


a) b)

Fig.3.13 EC semi-immersed in 3.5% NaCl, day 1, a) optical image; b) SAM image. I - Immersed part; N - Non-immersed part.

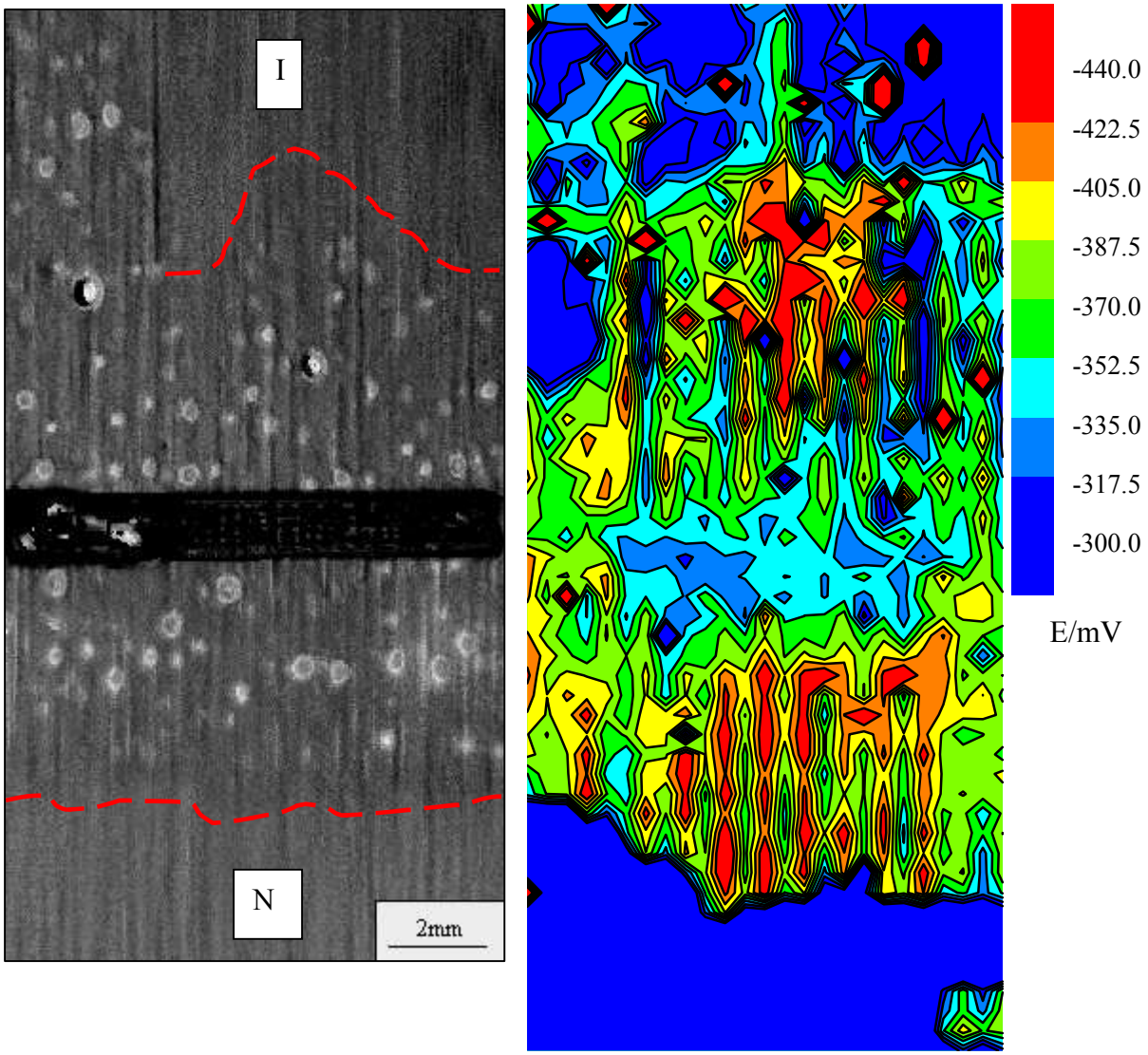


a) b)

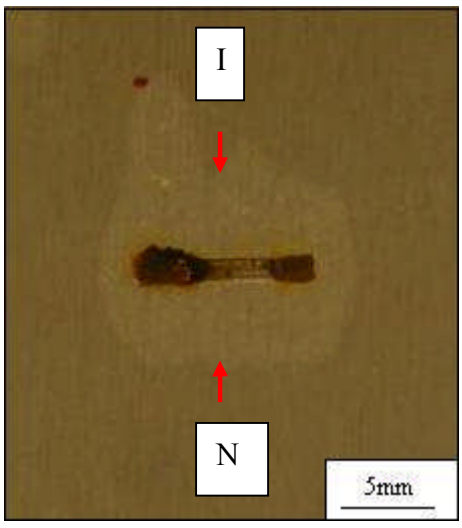


c)

Fig.3.14 EC semi-immersed in 3.5% NaCl solution, day 2, a) SAM image; b) SKP potential map corresponding to the area scanned by SAM in a); c) optical image. I - Immersed part; N - Non-immersed part.



a) b)



c)

Fig.3.15 EC semi-immersed in 3.5% NaCl, day 3, a) SAM image; b) SKP potential map corresponding to a); c) optical image. I - Immersed part; N - Non-immersed part.

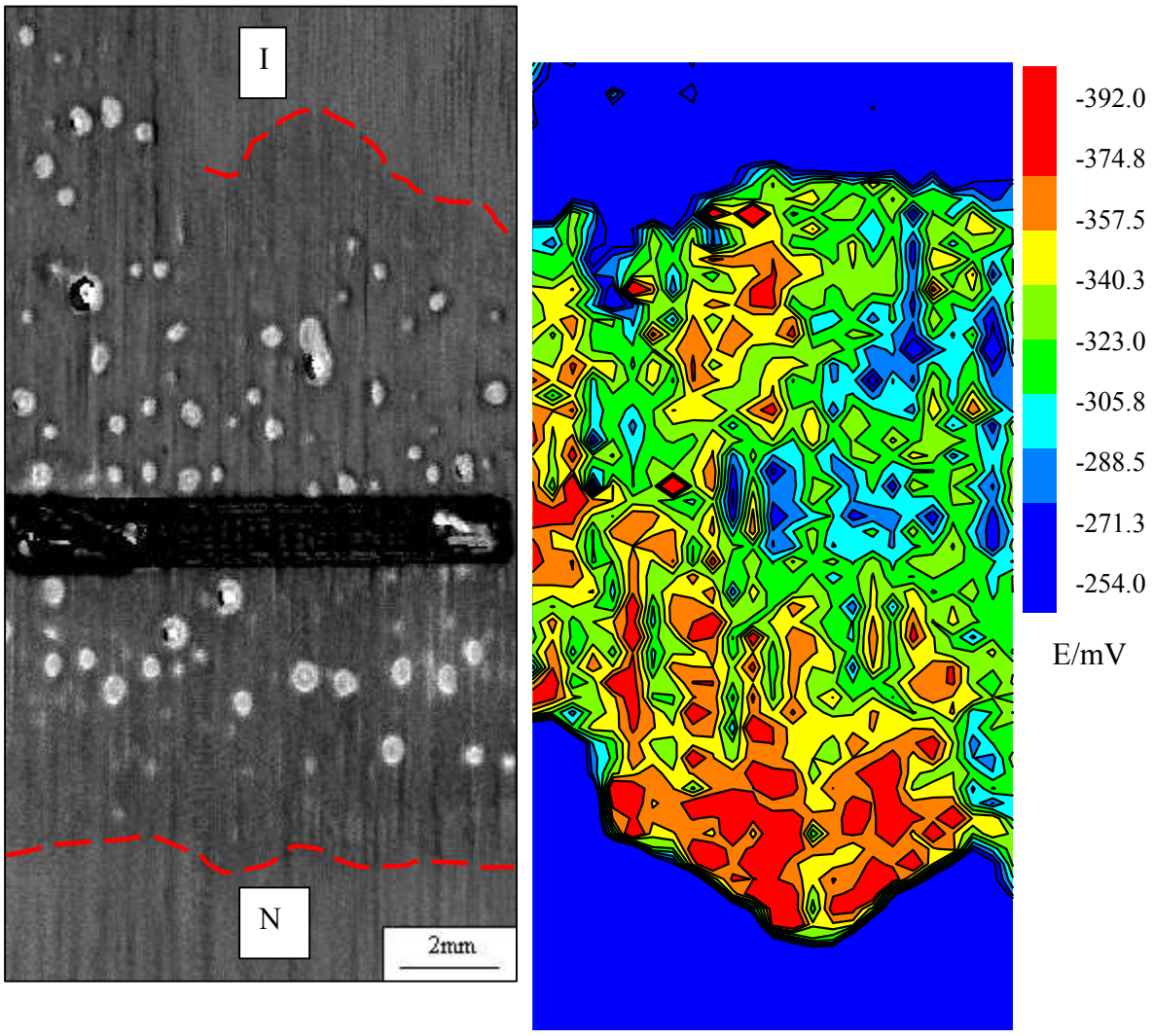
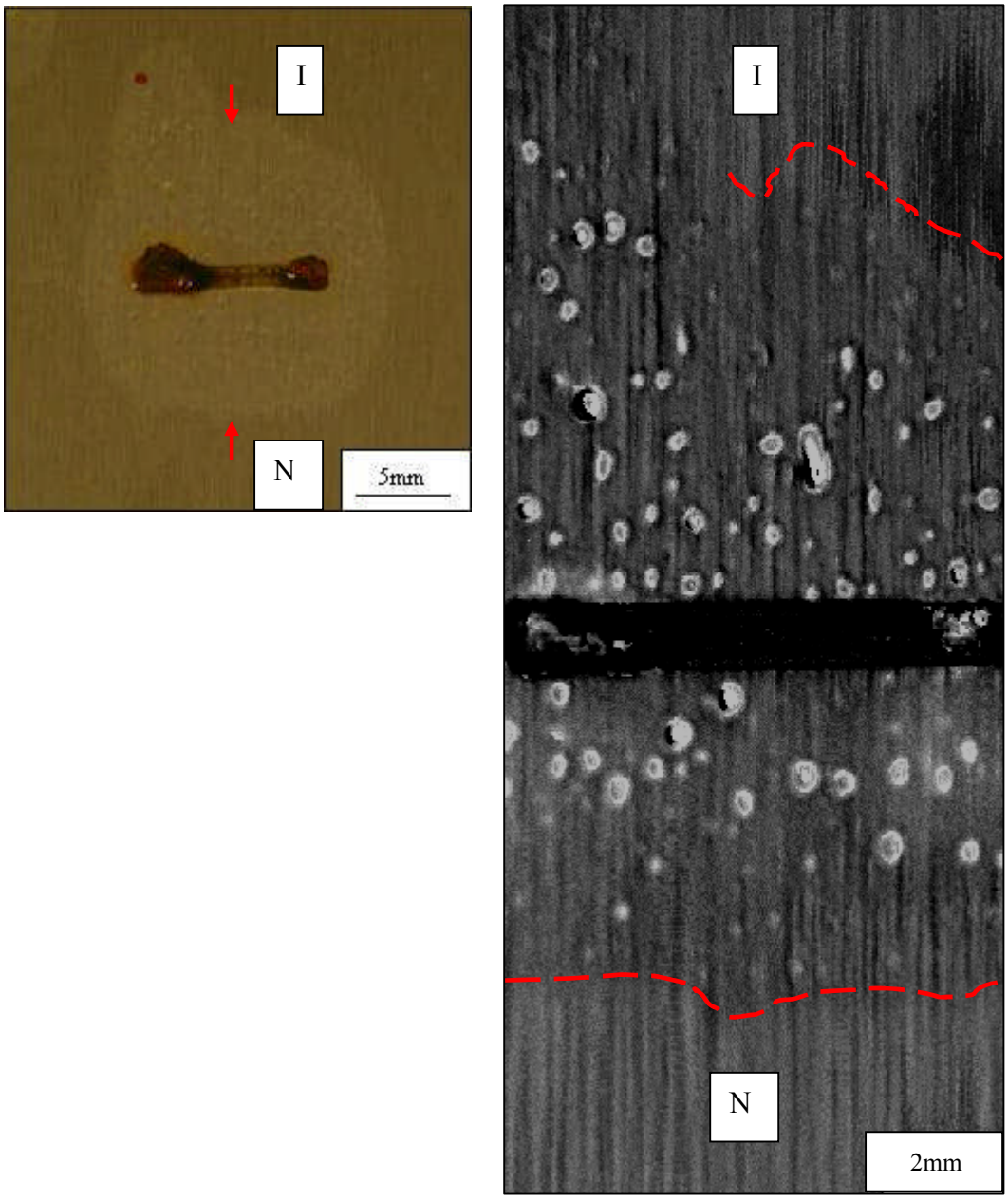


Fig.3.16 EC semi-immersed in 3.5% NaCl, day 4, a) SAM image; b) SKP potential map corresponding to a); c) optical image. I – Immersed part; N – Non-immersed part.

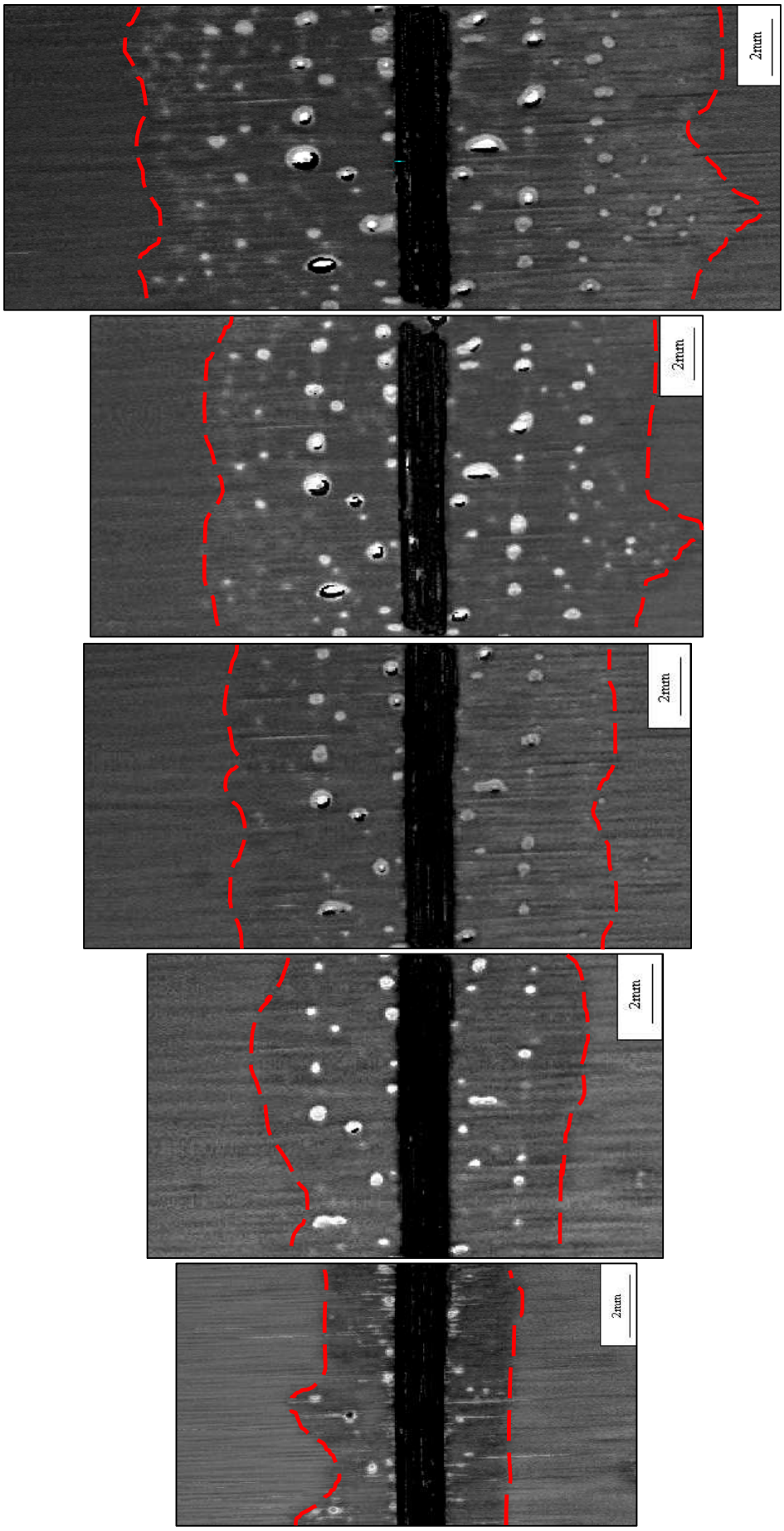


a) b)

Fig.3.17 EC semi-immersed in 3.5% NaCl solution, day 5, a) optical image; b) SAM image. I – Immersed part; N – Non-immersed part.

Fig.3.13 – 3.17 show the optical and SAM images of the EC samples semi-immersed in 3.5% NaCl solution along with the SKP potential maps. For comparison purpose, Fig.3.18 and Fig.3.19 give a summary of the SAM images under full- and semi-immersion conditions for 5 days. It can be seen that cathodic disbonding of EC

under semi-immersion condition shows similar behaviour to that under full-immersion condition. For the semi-immersed samples, both the immersed and the non-immersed parts disbonded outwards from the defect and the extents of disbonding of these two parts are quite symmetrical. Blisters occurred within the disbonded area with number and size growing as time increased as under full-immersion. The symmetry of disbonding of the immersed and non-immersed parts shows that the passage of current or ions through the coating below the waterline does not affect the progress, or nature of disbonding.



a) b) c) d) e)

Fig.3.18 A summary of the SAM images of EC fully-immersed in 3.5% NaCl solution. a) day1; b) day2; c) day3; d) day4 and e) day5.

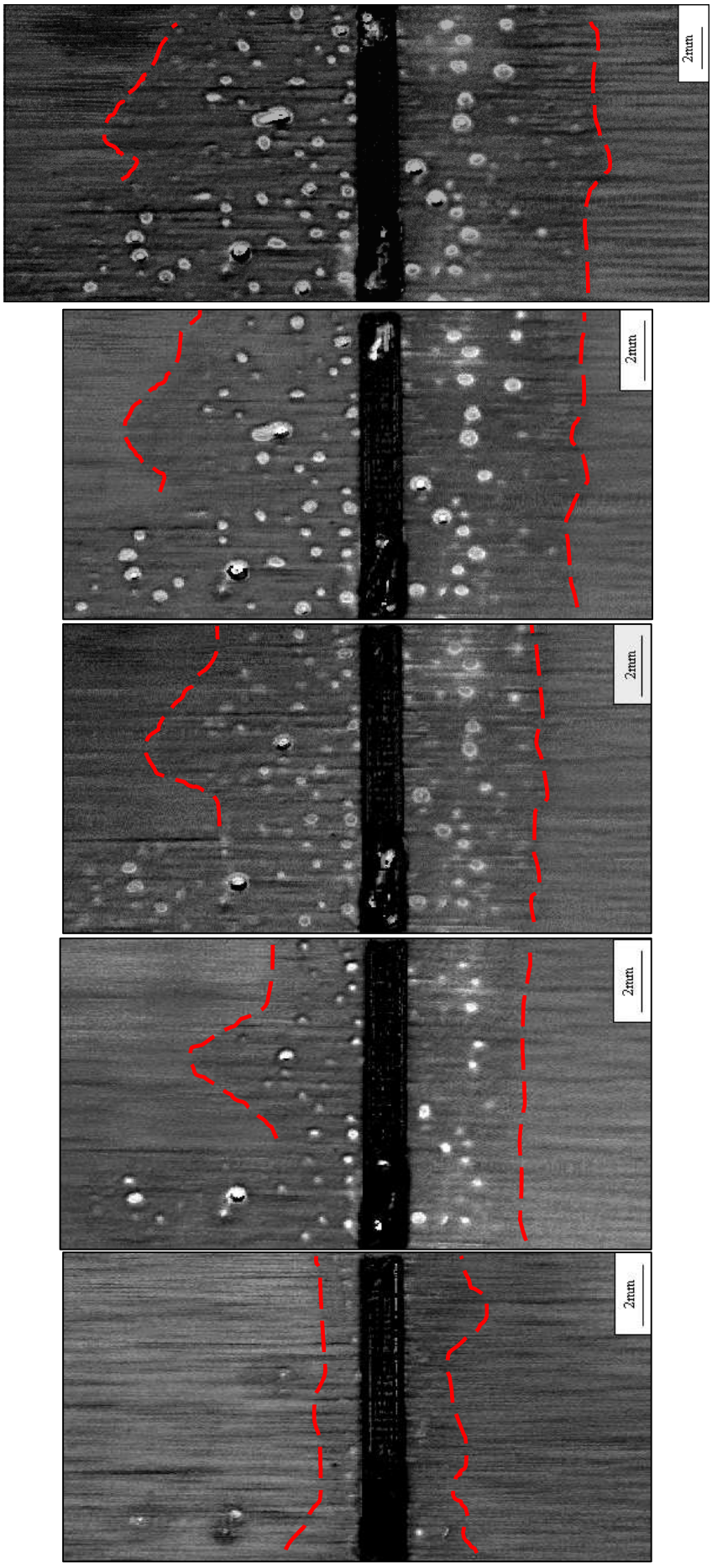


Fig.3.19 A summary of the SAM images of EC semi-immersed in 3.5% NaCl solution. a) day1; b) day2; c) day3; d) day4 and e) day5.

Fig.3.13 d), 3.14 d) and 3.15 d) show the SKP potential maps corresponding to the SAM images Fig.3.13 c), 3.14 c) and 3.15 c). There are some stripes on these potential maps which are most likely artefacts caused by the small height differences that arise where the SKP is tracking down a slope in one direction and up a slope in the other between two lines when scanning. Table.3.3 gives a set of typical gradient data recorded by SKP when scanning across the sample surface. This shows one track is close to the lower set limit while the other is at the upper limit.

-92	-107	-108	-110	-110	-107	-108	-110	-107	-107
-92	-92	-90	-92	-92	-92	-90	-90	-90	-93
-92	-109	-106	-110	-107	-110	-107	-109	-106	-110
-92	-92	-93	-93	-93	-90	-90	-91	-91	-92
-90	-108	-107	-110	-107	-110	-106	-108	-108	-109
-91	-92	-92	-91	-92	-90	-91	-91	-90	-90
-90	-107	-109	-106	-108	-106	-108	-110	-107	-107
-91	-90	-90	-92	-90	-90	-90	-91	-93	-92
-91	-108	-107	-107	-109	-107	-108	-110	-105	-107
-92	-90	-90	-90	-90	-92	-91	-92	-90	-91

Table.3.3 Typical gradient data recorded by SKP, ↓ shows the data recording sequence.

The SKP potential maps for the semi-immersion tests show similar behaviour to the full-immersion tests. The orange and the red patches are with more negative potentials, while the blue and the green ones with more positive potentials. It is therefore clear

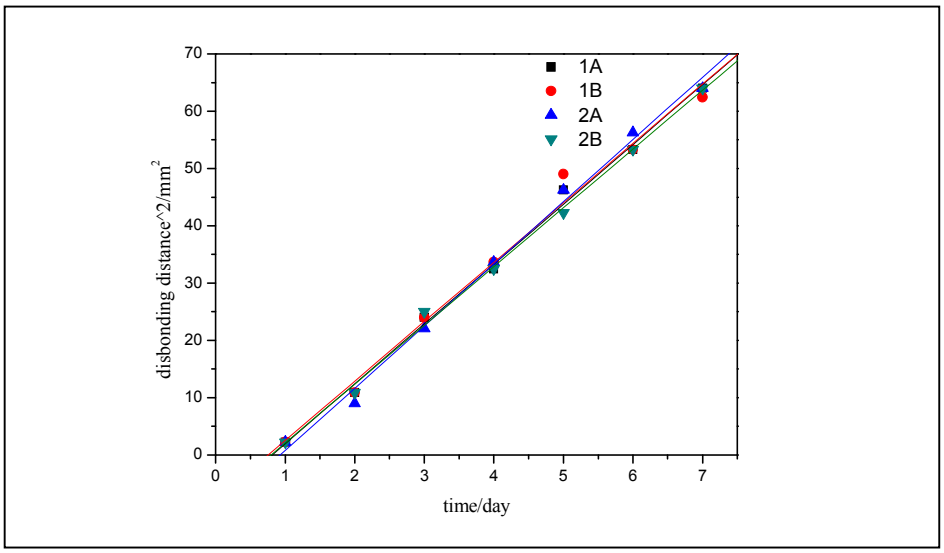
that the potential of the defect is more positive, indicating cathodic behaviour; the blisters have more negative potential, indicating anodic blistering. These results are in line with the ones obtained under full-immersion conditions in the previous section. The blisters are located at the anodic sites within the disbonded region where ions accumulate and lead to osmotic blisters. Similar behaviours have been reported by Reddy [62, 63] and Doherty [64]. The likely explanation for the formation of anodic sites within the disbonded region is that initially, Fe^{2+} is generated due to the anodic attack at the defect with alkali formed beneath the coating by the cathodic reduction of oxygen. Then the oxidation of $Fe(OH)_2$ within the defect results in the deposition of rust FeOOH. Once the rust in the defect makes contact with the steel, it becomes the cathodic reactant and reduced to black magnetite which leads to the development of new anodes as seen here. A possible reaction is:

$$8\ FeOOH + Fe^{2+} + 2\ e^{-} \rightarrow 3\ Fe_3O_4 + 4\ H_2O$$

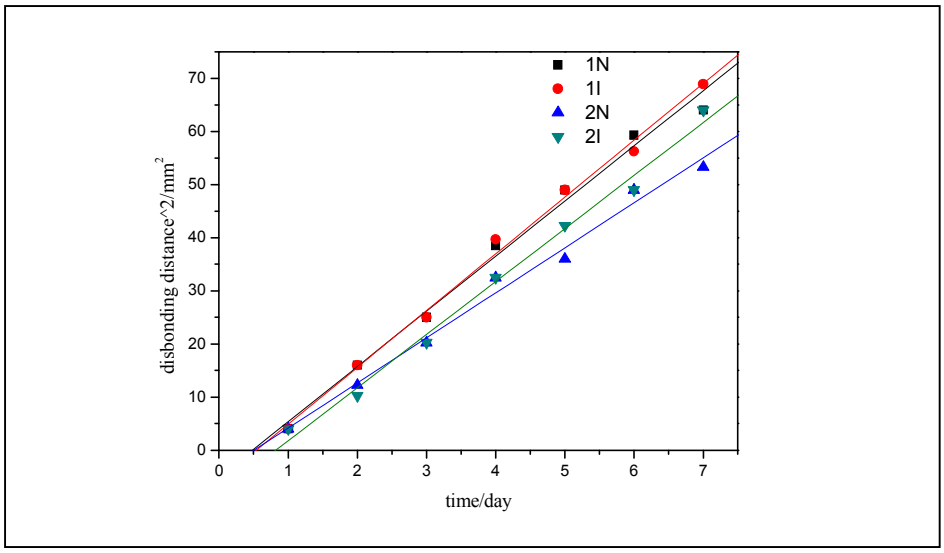
However, results of disbonding both under full- and semi-immersion conditions in this work are very different from others' [45, 129] in which the potential at the defect is most negative then increases steadily towards the tip of the disbond which may be explained by the difference in experimental setup - in this study, the samples were either fully-immersed which the whole scribed samples were horizontally immersed in the solution and when conducting the SKP measurements, they were taken out of the solution and exposed to humid air within a chamber but with the defect kept wetted in solution or semi-immersed in the solution which the scribed samples were vertically immersed into the NaCl solution with the solution line in line with the

middle of the defect so that the part below the defect was totally immersed in the solution and the part above was exposed to humid air, and when conducting the SKP measurements, the procedures are the same as the ones for full-immersion tests; while in other work, a typical one is Stratmann's work [45, 55, 56, 129], only the defect of the sample is wet with the rest of the coating exposed to high humidity so that the transport of ions only can along the coating/metal interface. Though the design of the setup of the semi-immersion test was trying to simulate Stratmann's setup, the results obtained are still different.

3.2.2.2.2 Disbonding Kinetics



a)



b)

Fig.3.20 Cathodic disbonding (distance^2 *vs.* time) of EC under full- and semi-immersion conditions, a) full-immersion; b) semi-immersion. Two panels were tested under each condition. (1, 2: Sample 1,2; A, B: Side A, B around the defect; N, I: Non-immersed, Immersed part).

Immersion condition	**Disbonding rate constant/mm^2·day^{-1}**			
	1A/N	**1B/I**	**2A/N**	**2B/I**
Full-	10.4	10.4	10.9	10.3
Semi-	10.4	10.7	8.5	10.0

Table.3.4 Disbonding rate constants of EC under full- and semi-immersion conditions, A and B represent side A and B of fully-immersed sample; N and I represent non-immersed and immersed parts of semi-immersed sample.

Fig.3.20 shows the square of cathodic disbonding distance of EC both fully- and semi-immersed in 3.5% NaCl solution increased linearly with exposure time, indicating that the disbonding under both conditions follows a parabolic disbonding kinetics. Several authors [55, 68-70] have found the same result, but may describe it in different ways, either as the disbonded area increases linearly with the exposure time or the disbonded distance increases linearly with the square root of time.

Table.3.4 gives the disbonding rates of EC calculated from the plots as shown in Fig.3.20. It can be seen there is not much difference. The parabolic relationship between the disbonding distance and time is generally taken to mean that the disbonding is controlled by a diffusion process along the coating/metal interface.

Also, as Fig.3.20 shows, the disbonding needs some time to be initiated, which is usually known as the delay time. It is usually determined by the intercept of the linear fit with the abscissa (time-axis).

3.3 Conclusions

For the system studied in the current part of work, the following conclusions can be obtained:

1) The disbonded region which is visible both by eye and in the SAM propagates away from the defect as exposure time increases, but does not correspond to complete adhesion loss, as verified by peel-testing experiments.
2) Blisters form within the disbond which can be attributed to the formation of local anodes as shown in the SKP potential maps which leads to local accumulation of ions that then generate blisters by osmosis.
3) Disbonding under the full- and semi-immersion conditions shows similar behaviours.
4) Semi-immersion tests show that the disbonding of the part which was below the defect (immersed in solution) and the part which was above the defect (exposed only to water vapour) follow parabolic kinetics with time and the disbonding rates

of these two parts are the same, which suggests that the disbonding of the unpigmented epoxy on mild steel is likely to be controlled by a transport process along the coating/metal interface as proposed by [55, 68, 80].

Chapter 4 An Investigation of Factors Affecting Cathodic Disbonding

4.1 Introduction

Cathodic disbonding has been studied extensively, however, the mechanism is not yet fully understood up to now, which is partly due to the variety of the results obtained when tested under different conditions. Here in this chapter, several factors affecting the cathodic disbonding process have been investigated and discussed. These factors are Film Thickness; Cation Mobility; Electrolyte Concentration; Temperature; Paint Composition, Polarisation and Open Circuit Potential. Samples tested in this chapter were prepared as described in Chapter 2 and at least two samples were tested for each experiment. But for some experiments, results of only one sample (typical) are shown.

4.2 Factors Affecting Cathodic Disbonding

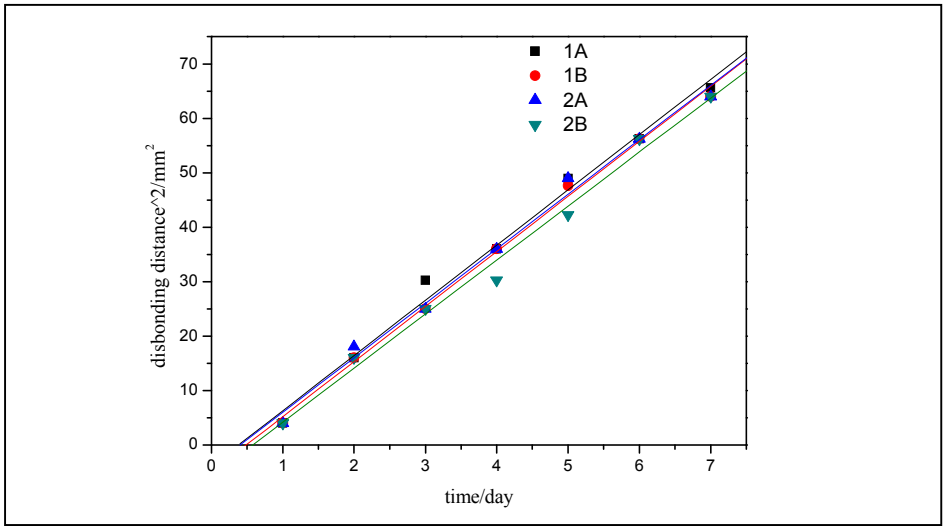
4.2.1 Effect of Film Thickness

4.2.1.1 Introduction

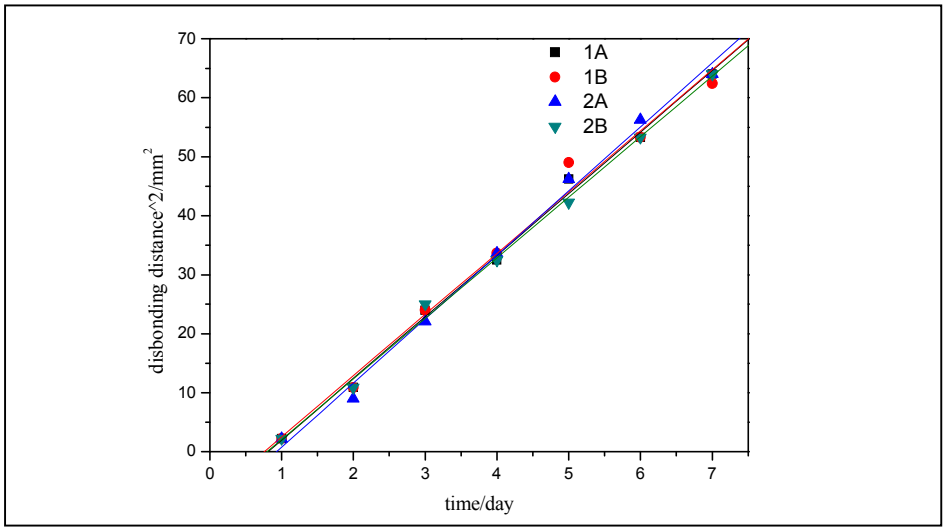
Examination of the effect of film thickness is another way to learn about the transportation path. It has been widely investigated by several groups [65, 68, 72-74]. This part of work aims to find out the effect of film thickness on cathodic disbonding of the unpigmented epoxy, EC, coatings on mild steel and help determine the transport path for the cathodic disbonding process. If not via coating, we should

expect the disbonding rate to be independent of thickness, or if via coating, we should expect that the rate is proportional to $\frac{1}{thickness}$. Panels coated with unpigmented epoxy films of different dry film thickness (DFT), 30 ± 5 µm, 45 ±5 µm, 60 ± 10 µm, 85 ± 10 µm were prepared and tested under the full-immersion condition (immersed in 3.5% NaCl solution contained plastic boxes which a lid was on to prevent evaporation) at room temperature.

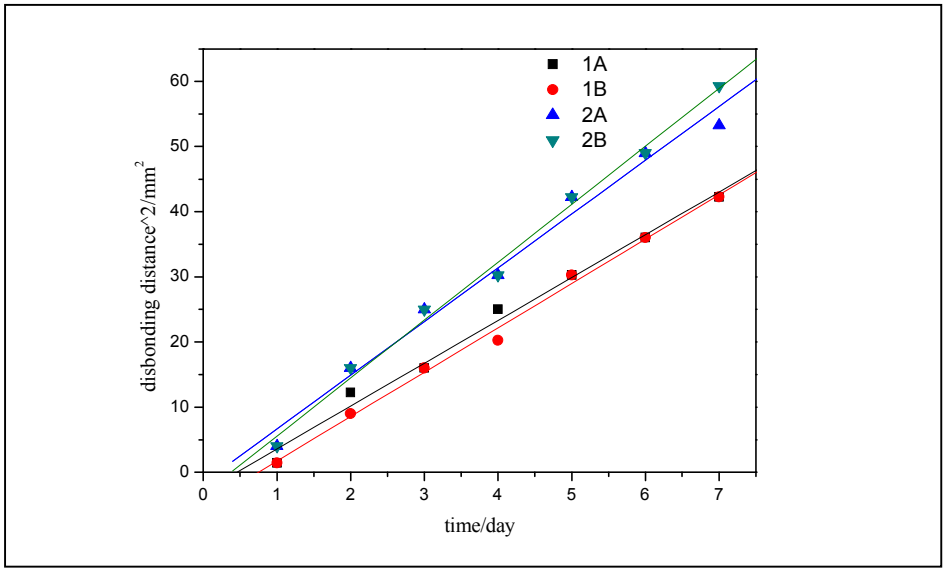
4.2.1.2 Results and Discussion



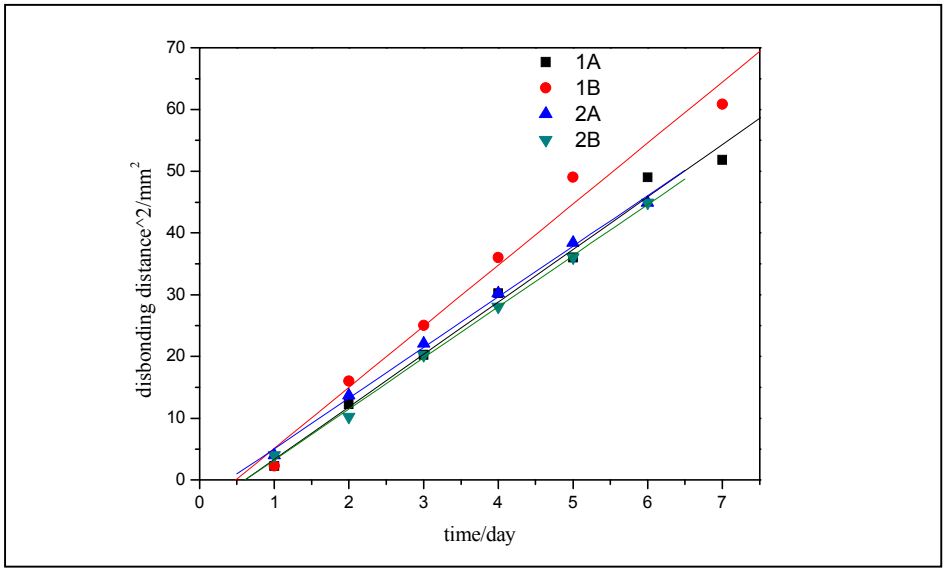
a)



b)



c)



d)

Fig.4.1 Disbonding of EC with different DFT, a) 30 ± 5 µm; b) 45 ± 5 µm; c) 60 ± 10 µm; d) 85 ± 10 µm. Two panels of each thickness were tested. 1, 2: Sample 1 and 2; A, B: Measurements on opposite sides of the same defect (Side A and B).

Fig.4.1 shows the typical disbonding behaviour of the panels as a function of coating thickness. The tests lasted for 7 days. It is clear that the disbonding distance^2 *vs.* time plots give linear lines with a correlation coefficient over 0.99 indicating the disbonding of all the panels follows parabolic disbonding kinetics.

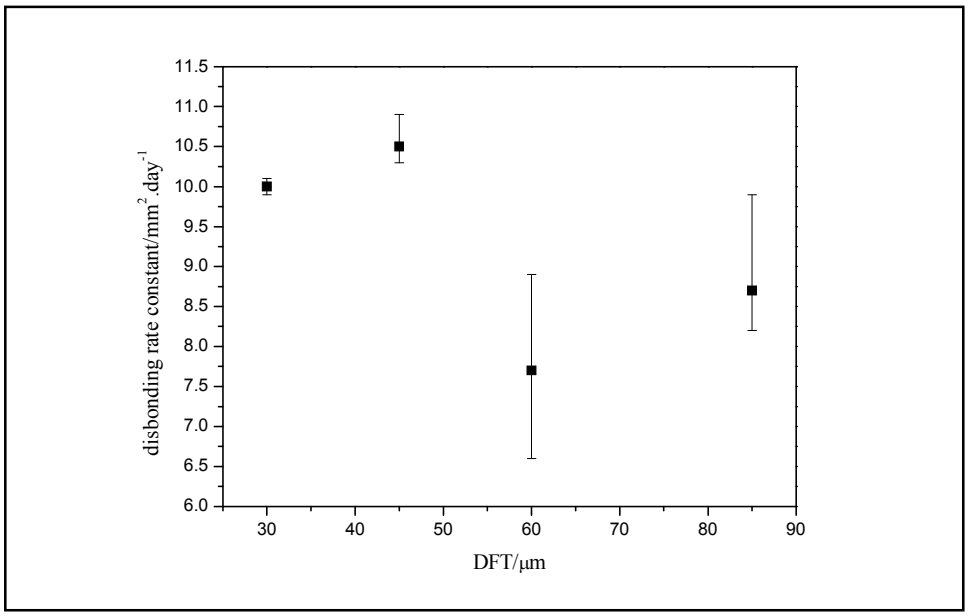


Fig.4.2 Disbonding rate constants of EC of different DFT.

Fig.4.2 summarises the results of the disbonding rate of EC samples with different film thickness. They were determined from the disbonding distance^2 *vs.* time plots as shown in Fig.4.1. It shows that increasing the film thickness of the EC coating only caused a slight decrease in the disbonding rate indicating that there is only a small influence of the film thickness on the disbonding rate. Similar results have been obtained before by Sharman *et al.* and Knudsen [68, 130]. If reactions at or transport along the coating/metal interface completely determine the disbonding rate, then the film thickness should not be expected to affect the disbonding rate at all. However, for this system, it is likely that the main transport route is along the coating/metal interface as argued in Chapter 3.

Now since the transport route of the cathodic disbonding, which is mainly along the coating/metal interface, is clear, we want to know what species controls the disbonding rate.

To solve this, based on the previous work [55, 65, 68, 70], the investigation on the cathodic disbonding of EC in different alkali metal chloride solutions has been carried out.

4.2.2 Effect of Cations

4.2.2.1 Introduction

Four solutions were examined to assess the effect of cations on cathodic disbonding, they were 0.5M LiCl, NaCl, KCl and CsCl. The EC (DFT: 45 ± 5 μm) coated mild steel panels were immersed in these solutions for 7 days in a closed solution-containing box to prevent solution evaporation.

If transport of cations were the rate-limiting factor for the cathodic disbonding of the system studied, a linear relationship would be expected between the disbonding rate (distance^2/time) and the cation mobility.

4.2.2.2 Results and Discussion

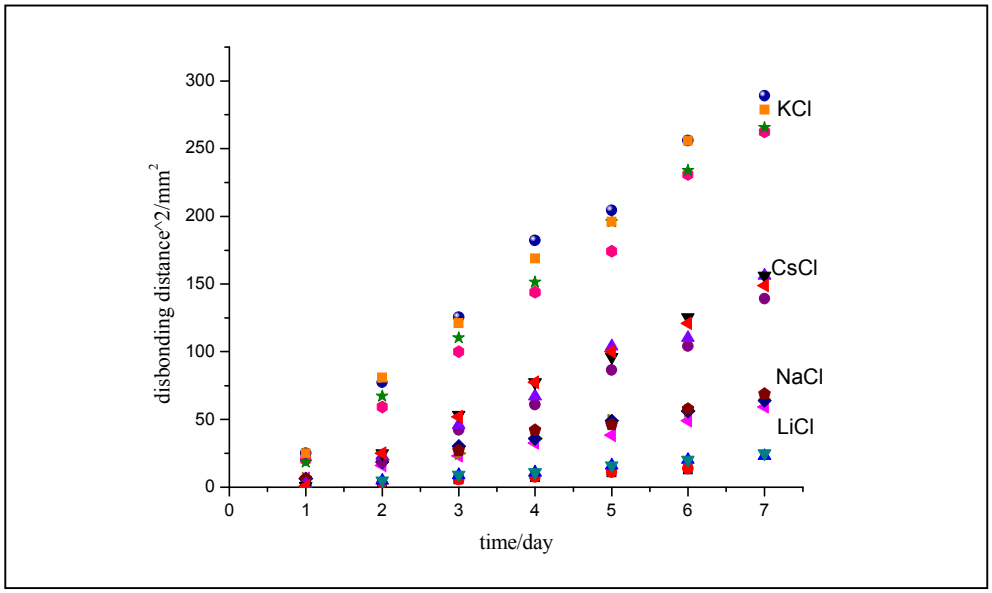


Fig.4.3 Disbonding (disbonding distance^2 *vs.* time) of EC immersed in 0.5M alkali metal chloride solutions. Duplicate samples were tested.

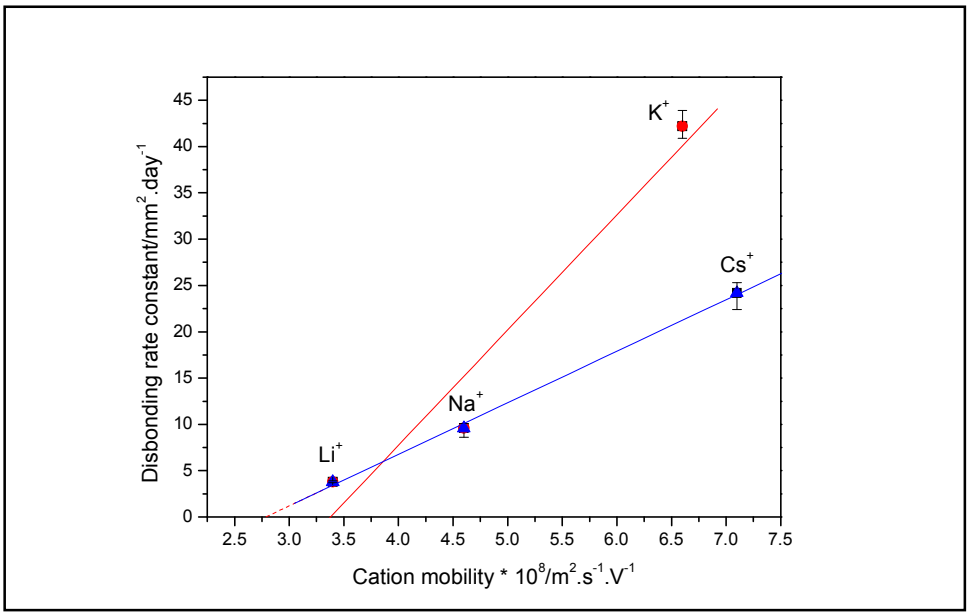


Fig.4.4 Disbonding rate constant *vs.* cation mobility: effect of cation mobility.

Fig.4.3 gives a summary and comparison of disbonding distance^2 versus time of EC in among 0.5M LiCl, NaCl, KCl and CsCl solutions. They all show a linear relationship. It is of particular interest to notice that the disbonding distance^2 versus

time line for disbonding in KCl is steeper than that for CsCl, indicating that the disbonding rates in the four solutions are in the sequence of $K^+ > Cs^+ > Na^+ > Li^+$. This result is somewhat surprising (not as what we expected), since most of the disbonding rate results obtained from other work [55, 65, 68, 75] are in the sequence of $Cs^+ > K^+ > Na^+ > Li^+$, which agrees with the ranking of the mobility of these ions in aqueous electrolytes. It is clear that the general trend is for faster disbonding with more mobile cations, as shown in Fig.4.4 (disbonding rate *vs.* cation mobility [131, 132]), which gives two regression fits, one is for Li^+, Na^+, K^+ (the red line) and the other is for Li^+, Na^+, Cs^+ (the blue line). The linear regression fit for Li^+, Na^+, Cs^+ apparently correlates better, which gives an intercept with the x-axis of 2.8, indicating the critical mobility needed to start disbonding is 2.8×10^8 $m^2 \cdot s^{-1} \cdot V^{-1}$ (if the Cs^+ behaves normally), but we are not sure whether K^+ or Cs^+ is out of sequence yet. It is not known why the results of the present work should have shown this anomaly. However, some other work did show similar behaviour, but no proper explanation has been put forward.

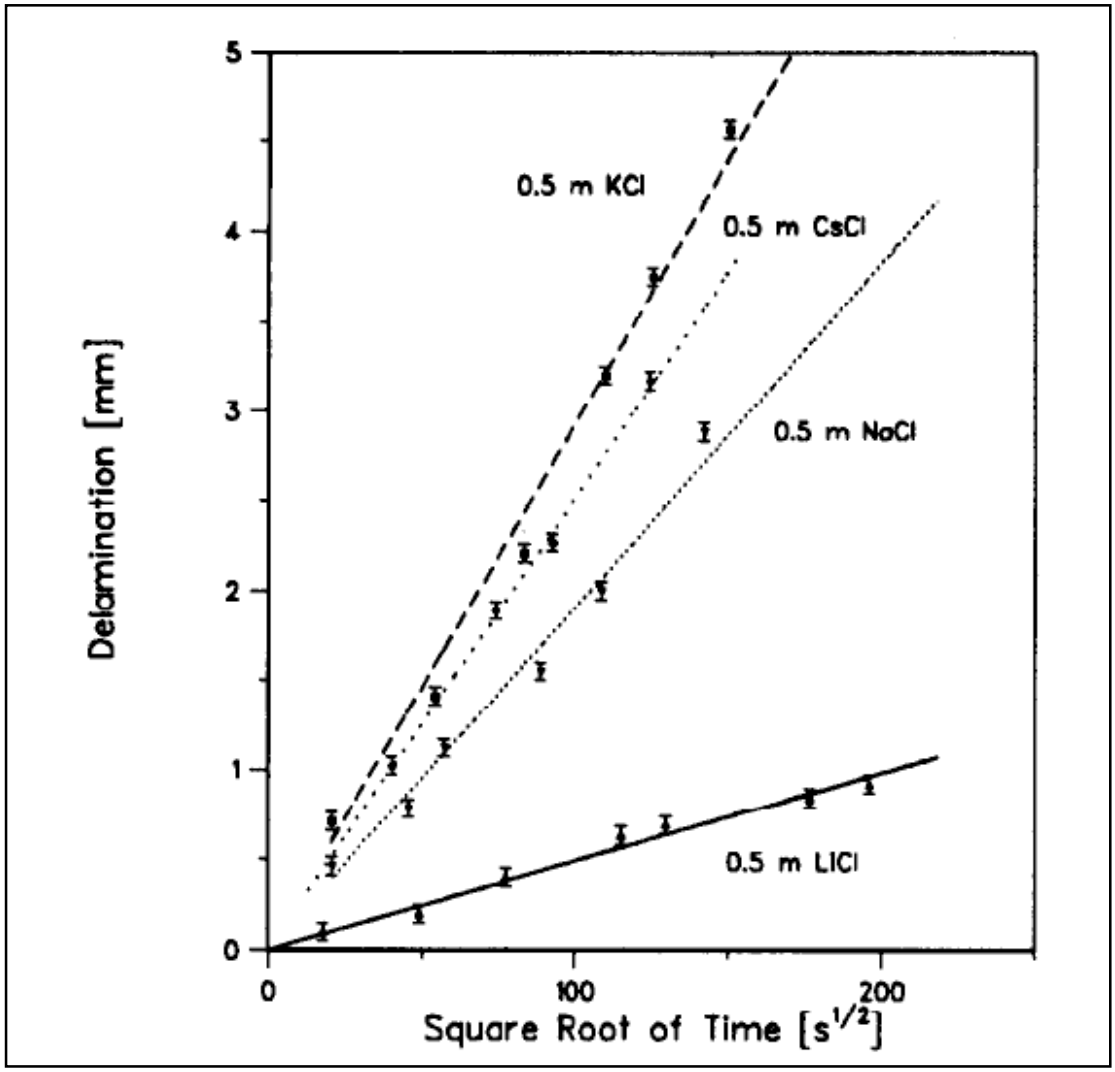


Fig.4.5 Delamination as a function of the square root of the corrosion time. [45, 60]

Fig.4.5 gives a figure from Stratmann's work [45, 60] showing the effect of cations on disbonding. This figure appeared twice in these two papers. However, the strange behaviour in CsCl was not addressed and their explanation for the effect of cations is "Perfect linear behaviour is observed, which demonstrates that the diffusion of cations from the local anode (defect) to the local cathode is rate-determining. The delamination rate depends on the nature of the cation: the larger size of the cation, the faster the observed delamination rate. This is in agreement with the known dependence of the diffusion coefficient on the size of the alkali ions in aqueous

electrolytes." The figure does not in fact show this.

One of Leidheiser's work [65] also showed similar behaviour. See Fig.4.6.

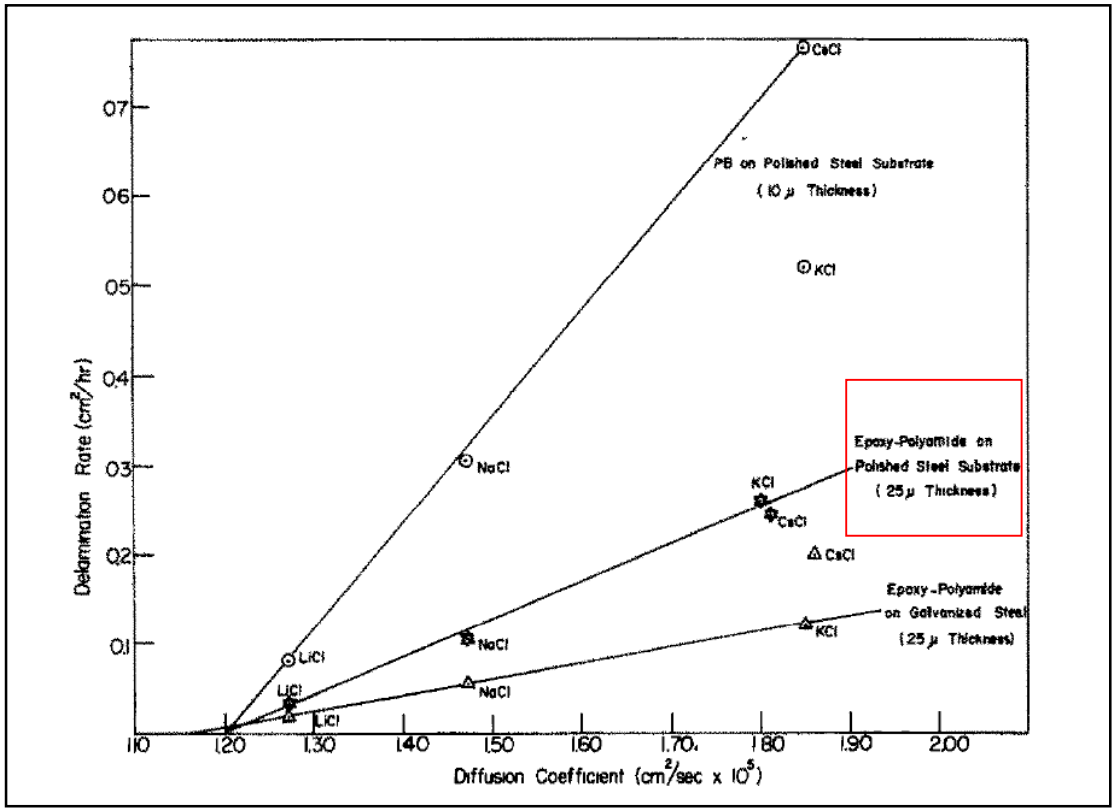


Fig.4.6 Cathodic delamination rate *vs.* the diffusion coefficient of four electrolytes and three different substrate/coating systems. [65]

It can be seen from Fig.4.6 [65] that for the epoxy-polyamide (25 μm) on polished steel substrate (the red line circled testing system), the disbonding rate as a function of diffusion coefficient of aqueous solutions of LiCl, NaCl, KCl and CsCl follows the sequence of LiCl < NaCl < CsCl < KCl, which agrees with the results obtained by Stratmann and us.

For the system studied in the current work, it is quite obvious that the disbonding depends on the cation type though they all follow the same disbonding kinetics. A possible explanation for the anomalous behaviour observed is because of the property difference in between KCl and CsCl. A survey of relevant parameters (mobility,

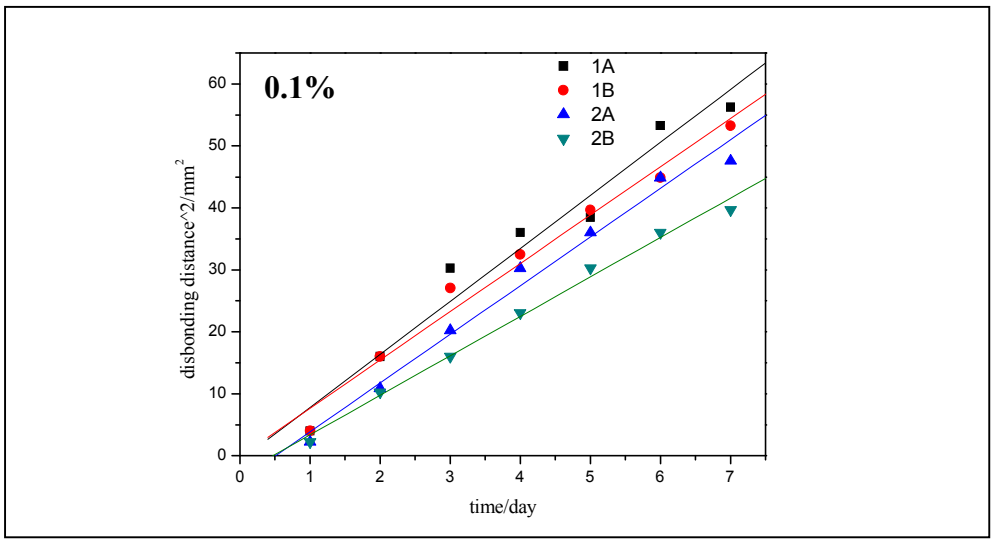
oxygen solubility in solution, pH of salt hydroxide *etc.*) shows a systematic trend Li^+ → Na^+ → K^+ → Cs^+, which is in line with our expectations from the periodic table. It should be remembered however that we are not, apparently, dealing with migration in bulk solutions [55], a weak layer of degraded coating resulted by the chemical attack of the free radicals or alkali generated during oxygen reduction which affects the transport of the cations along the coating/metal interface and therefore perfect correlation with mobilities in aqueous solution should not necessarily be expected.

4.2.3 Effect of Solution Concentration

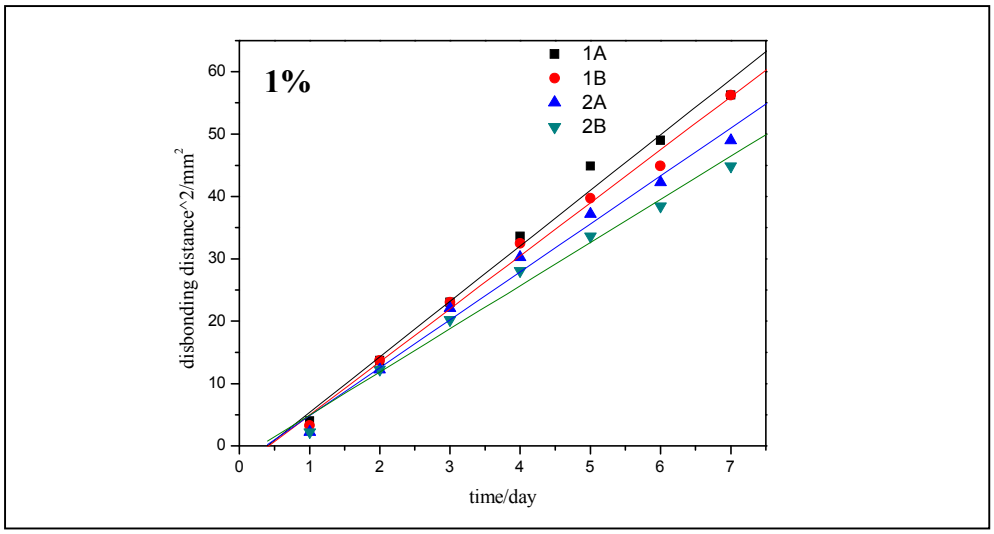
4.2.3.1 Introduction

To study the effect of ionic strength on cathodic disbonding, EC samples exposed to NaCl solutions of different concentrations: 0.1%, 1%, 3.5% and 5% (by weight) were tested.

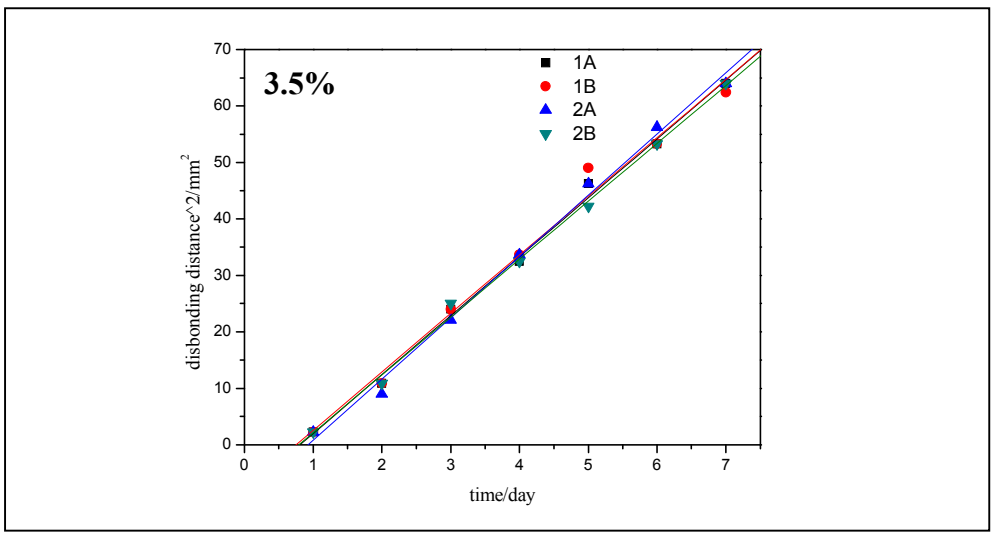
4.2.3.2 Results and Discussion


0.1%
1A
1B
2A
2B
disbonding distance^2/mm^2
time/day
0
10
20
30
40
50
60
0
1
2
3
4
5
6
7

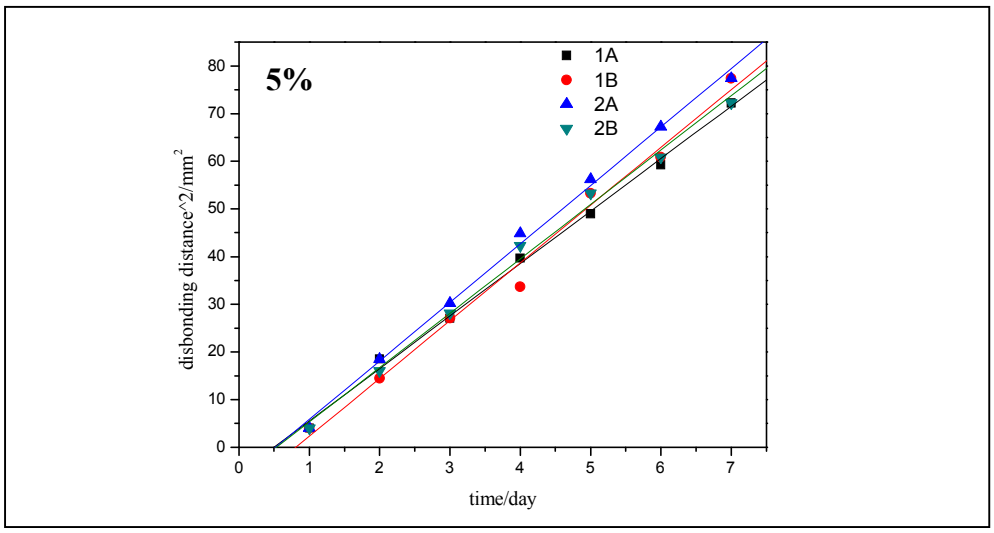
a)


1%
1A
1B
2A
2B
disbonding distance^2/mm^2
time/day
0
10
20
30
40
50
60
0
1
2
3
4
5
6
7

b)


3.5%
1A
1B
2A
2B
disbonding distance^2/mm^2
time/day
0
10
20
30
40
50
60
70
0
1
2
3
4
5
6
7

c)



d)

Fig.4.7 Disbonding of EC immersed in NaCl solutions of different concentrations, a) 0.1%; b) 1%; c) 3.5%; d) 5%. Two panels under each concentration were tested. (1, 2: Sample 1 and 2; A, B: Measurements on opposite sides, side A and B, of the same defect).

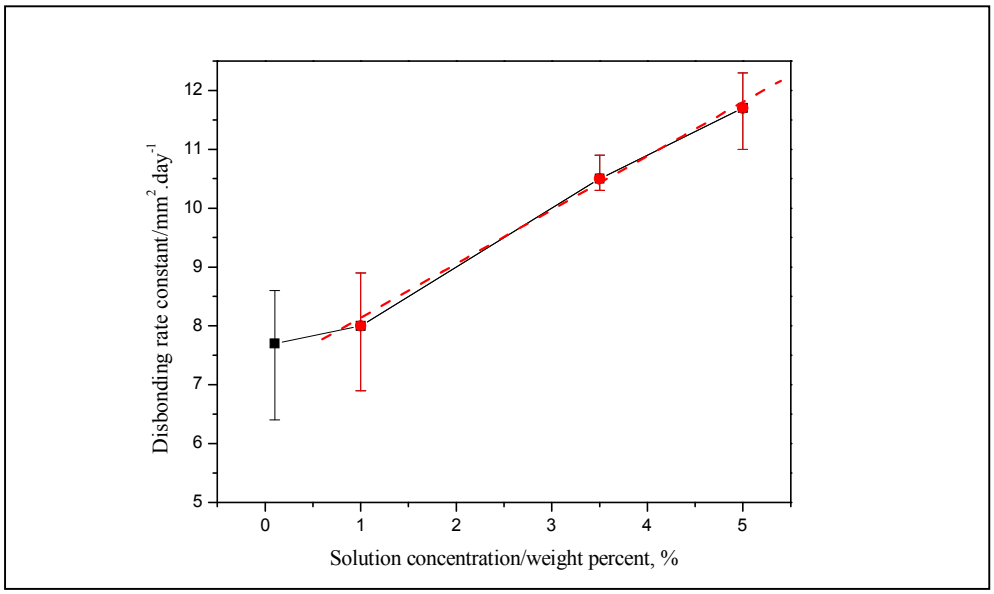


Fig.4.8 Disbonding rate constant *vs.* Solution concentration

Above 1% NaCl, the positive influence of salt concentration is quite clear (It seems there is a linear relationship between the disbonding rate and the solution concentration when it is more than 1%, as shown by the red line in Fig.4.8, the

correlation coefficient of the linear fit is more than 0.99.), but the disbonding in 0.1% NaCl solution is faster than we would expect from the regression fit. A possible explanation for the increase of the disbonding rate with the increasing solution concentration is that in the more concentrated NaCl solution, there is a greater inwards migration of Na^+ ions compared to the outwards migration of OH^- generated by the cathodic reaction at the coating/metal interface, so that a higher concentration of alkali (or free radicals) is generated, which will accelerate the disbonding (or the degradation of the coating). While at 0.1% (≈0.02M), the disbonding rate is not significantly less than that in 1% (≈0.2M) NaCl solution, which indicates that there is some "critical point" between these two concentrations. If the concentration is above that value, the disbonding will increase linearly with the solution concentration; while the cathodic disbonding behaviour of coatings immersed in solutions with the concentration below 1% needs further testing (in the future work).

Fig.4.7 and Fig.4.8 demonstrates that the disbonding can not be treated as a simple diffusion process. This agrees with Leng *et al.* [55] that the disbonding rate can not be explained only by the mobility of the cation due to the independence of the mobility on the concentration (Fig.4.9) and the ions move along a gel-like polymer layer, though they reported that the concentration of cations has a remarkable influence on the delamination rate and below a concentration of cations of 0.05M inside the defect, no delamination could be observed which was explained by a minimum concentration of ions at the coating/metal interface necessary for establishing a galvanic element.

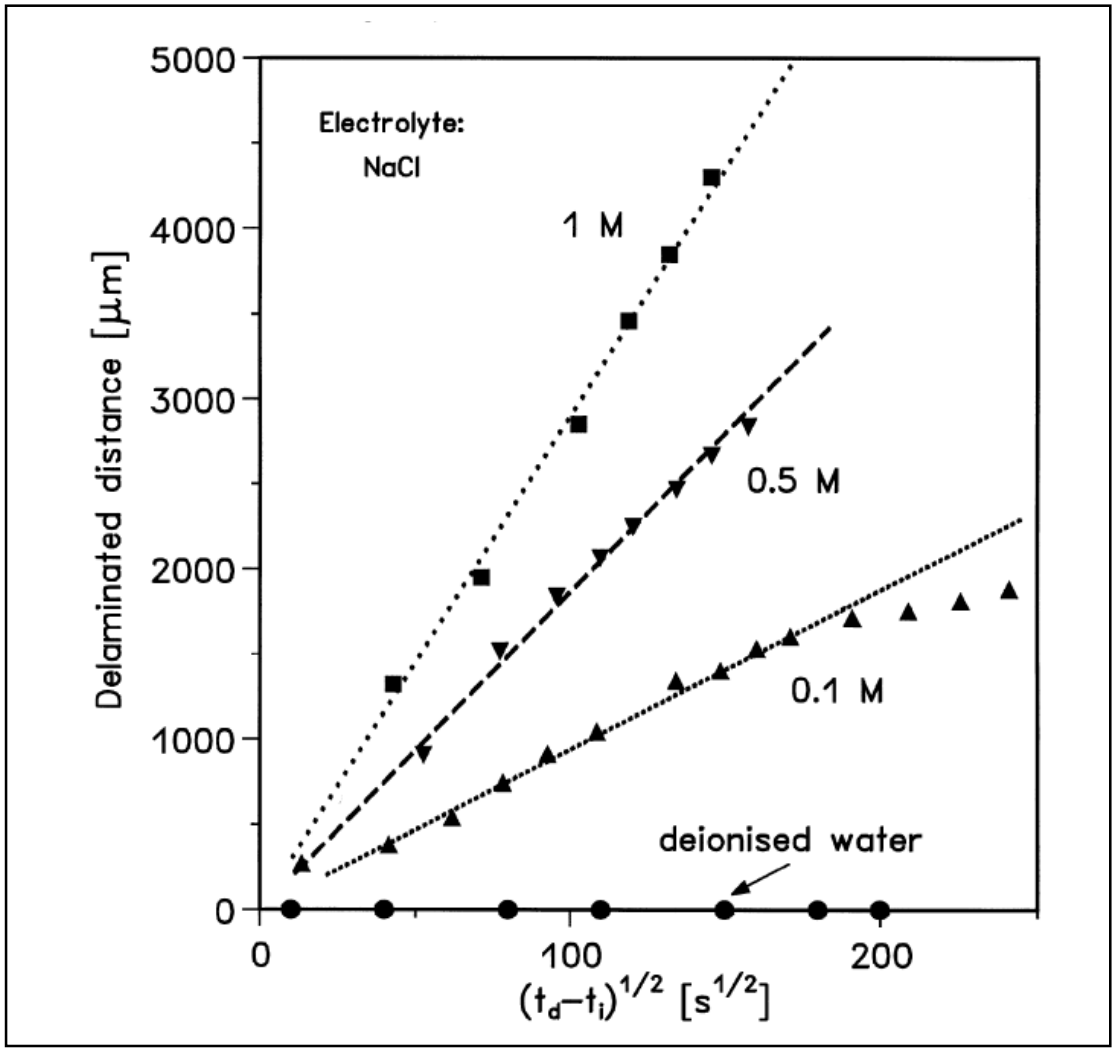


Fig.4.9 Delamination kinetics as a function of the ionic strength of NaCl within the defect [55].

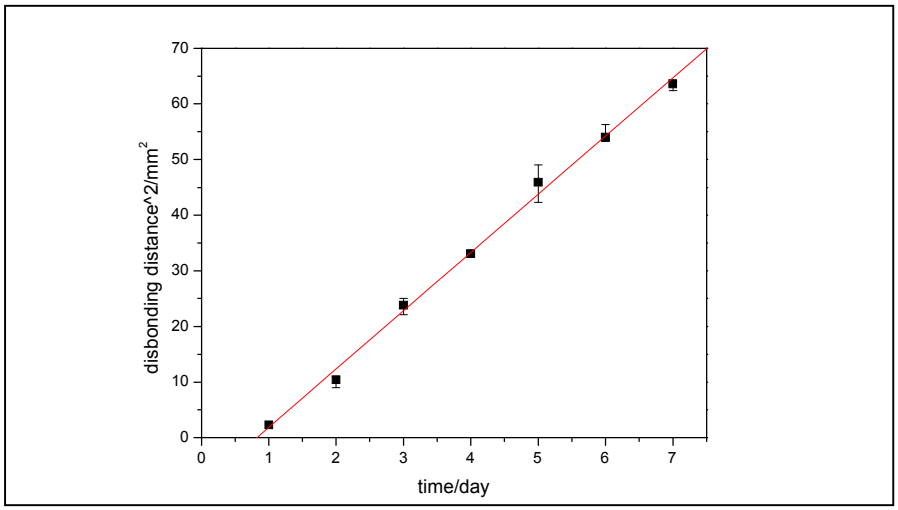
This analysis by Leng *et al.* did not discuss how concentration affects potential, but here we see it as an important parameter. SKP measurements show that potential gradients exist beneath the coating and Crossen [53] argues that electro-migration is more important than diffusion. For electro-migration, the flux of cations will depend upon the concentration present: this upsets the balance between ions migration in and diffusion out.

4.2.4 Effect of Temperature

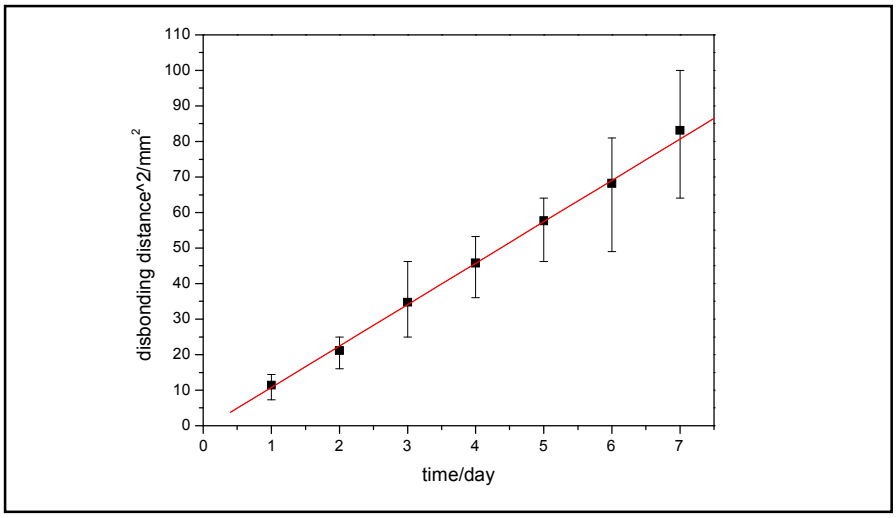
4.2.4.1 Introduction

EC coated mild steel samples exposed in duplicate to 3.5% NaCl solutions at 22℃, 30℃, 40℃ and 50℃ were studied. 30℃ and 40℃ tests were conducted in a temperature-control box (self-built, a 100W bulb controlled with a digital thermostat (RS Components Ltd., Accuracy: ±1℃) within a perspex box). Due to the temperature-control limit, 50℃ tests were carried out in a thermostat bath, SUB Aqua 26L (Grant Instruments Ltd) with samples enclosed in 3.5% NaCl solution contained boxes and horizontally positioned.

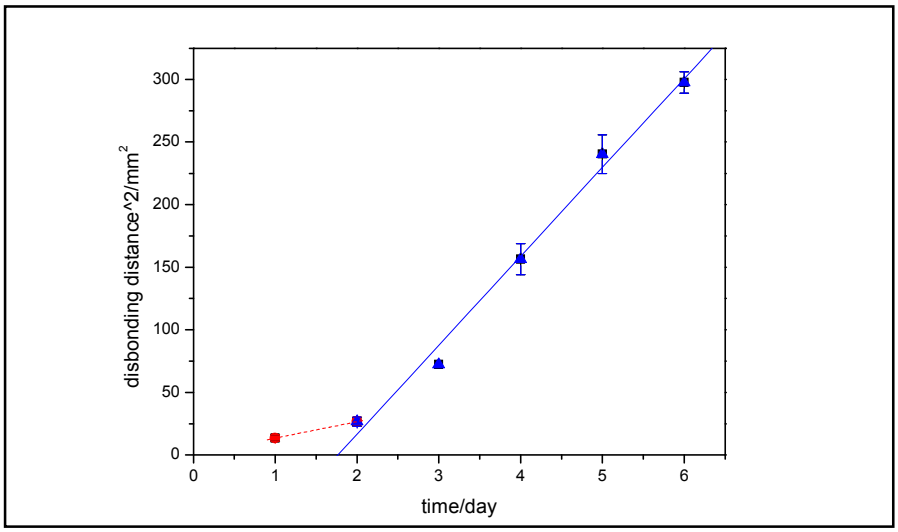
4.2.4.2 Results and Discussion



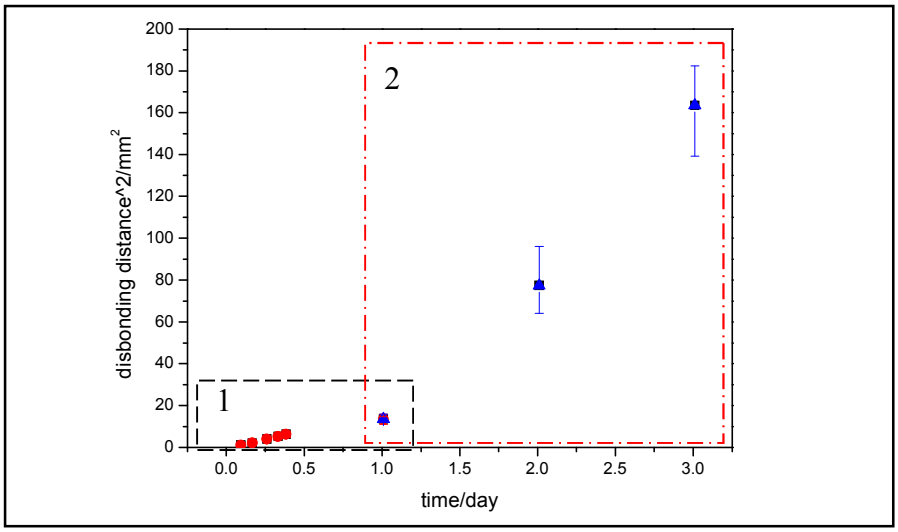
a)


disbonding distance^2/mm^2
time/day
0
10
20
30
40
50
60
70
80
90
100
110
0
1
2
3
4
5
6
7

b)


disbonding distance^2/mm^2
time/day
0
50
100
150
200
250
300
0
1
2
3
4
5
6

c)


disbonding distance^2/mm^2
time/day
1
2
0
20
40
60
80
100
120
140
160
180
200
0.0
0.5
1.0
1.5
2.0
2.5
3.0

d)

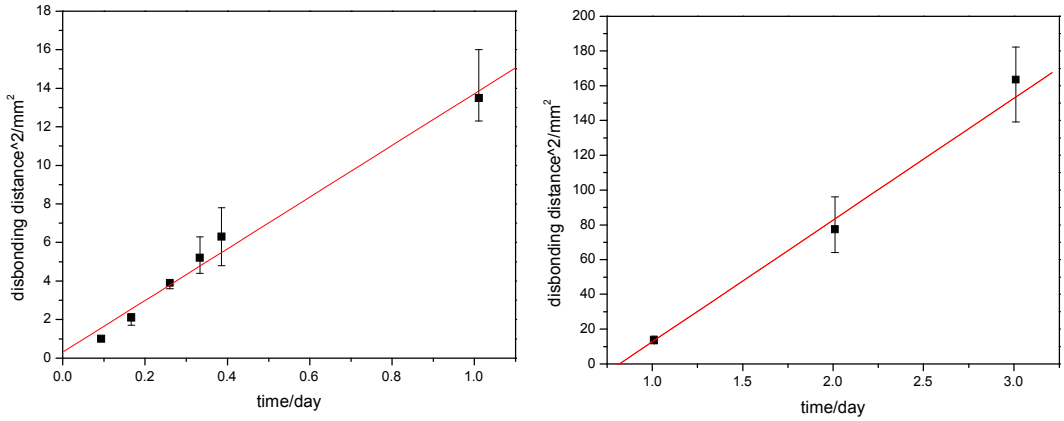


Fig.4.10 Disbonding of EC under different temperatures, a) 22℃; b) 30℃; c) 40℃; d) 50℃; d1) corresponding to the circled zone 1 in d) and d2) corresponding to the circled zone 2 in d). Two panels were tested under each temperature.

As shown in Fig.4.10 a) and b), cathodic disbonding of EC under 22℃ and 30℃ gives a linear relationship between disbonding distance^2 and time, and the delay time for the disbonding at 30℃ is shorter than at 22℃. While at higher temperatures of 40℃ and 50℃, similar disbonding behaviours were found, see Fig.4.10 c) and d). Only the data of the first three days were used to give the plot for 50℃, because it had already disbonded over the whole panel after three days immersion. The disbonding rate is much slower at first (the first 2 days for 40℃, Fig.4.10 c) and the first day for 50℃, Fig.4.10 d)). This is probably attributed to the initiation of disbonding.

If disbonding is controlled by a thermally-activated process, such as ion diffusion, the dependence of cathodic disbonding rate on temperature should in principle given by the Arrhenius Equation, Equation 4.1, provided the same kinetics operates across the whole temperature range, where the activation energy which characterises the rate-controlling process is given by,

$$k = Ae^{-E_a / RT} \qquad \textit{[Equation 4.1]}$$

Where k is the disbonding rate constant, T is the absolute temperature (K), R is the gas constant (8.314 $J \cdot mol^{-1} \cdot K^{-1}$) and E_a is the activation energy ($J \cdot mol^{-1}$).

If we plot ln (cathodic disbonding rate) *vs.* 1/T, a linear line is expected with the slope equal to $-\frac{E_a}{R}$.

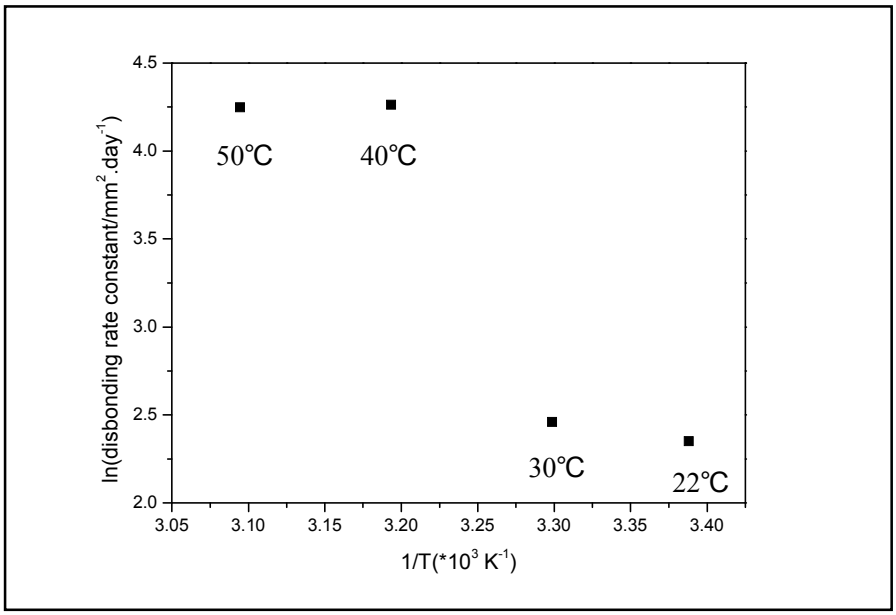


Fig.4.11 ln (disbonding rate) *vs.* 1/T of EC immersed in 3.5% NaCl solution

However, for the system studied in the current work, we do not get a straight line for ln (disbonding rate) *vs.* 1/T (Fig.4.10), with a sudden increase in disbonding rate between 30℃ and 40℃. There is no significant difference between the disbonding rates at 40℃ and 50℃ but they are much faster than those at 22℃ and 30℃, which indicates there may be a critical point between 30℃ and 40℃ where a transition takes place in the presence of the weak layer bonding the coating to the metal.

4.2.5 Effect of Polarisation

4.2.5.1 Introduction

All the experiments carried out above were under free corrosion conditions. In this part, a controlled potential was applied. When a cathodic potential is applied, the defect will be under cathodic protection (corrosion may be prevented) at the negative potentials, but the cathodic reaction is accelerated, leading to more severe disbonding. This section investigates the effect of applied potential on disbonding, which is known from work on cathodic protection to produce faster disbonding [72, 78]. Here we examine this to quantify the role of potential in free corrosion tests. Potential is allowed to change over time in these tests, so that rate is likely to be influenced by changes in potential as the tests progress. Free corrosion potential, Ecorr, has not generally been reported in earlier studies.

-800 mV and -1000 mV potentials were applied on EC both fully and semi-immersed in 3.5% NaCl solutions. To conduct the investigation, a cell was set up where a piece of platinum-coated titanium acted as a counter electrode, a saturated calomel electrode (SCE) was used as a reference electrode and the coated sample (EC) itself was the working electrode. A potentiostat (H. B. Thompson & Associates) was used to apply the potential. Fig.4.12 gives a schematic diagram of the experimental set up. The samples were exposed to 3.5% NaCl solution and polarised with different potentials for 7 days at room temperature. Free corrosion potential was measured using a Pico-Log system (ADC-16, pico Technology) with a SCE as a reference electrode.

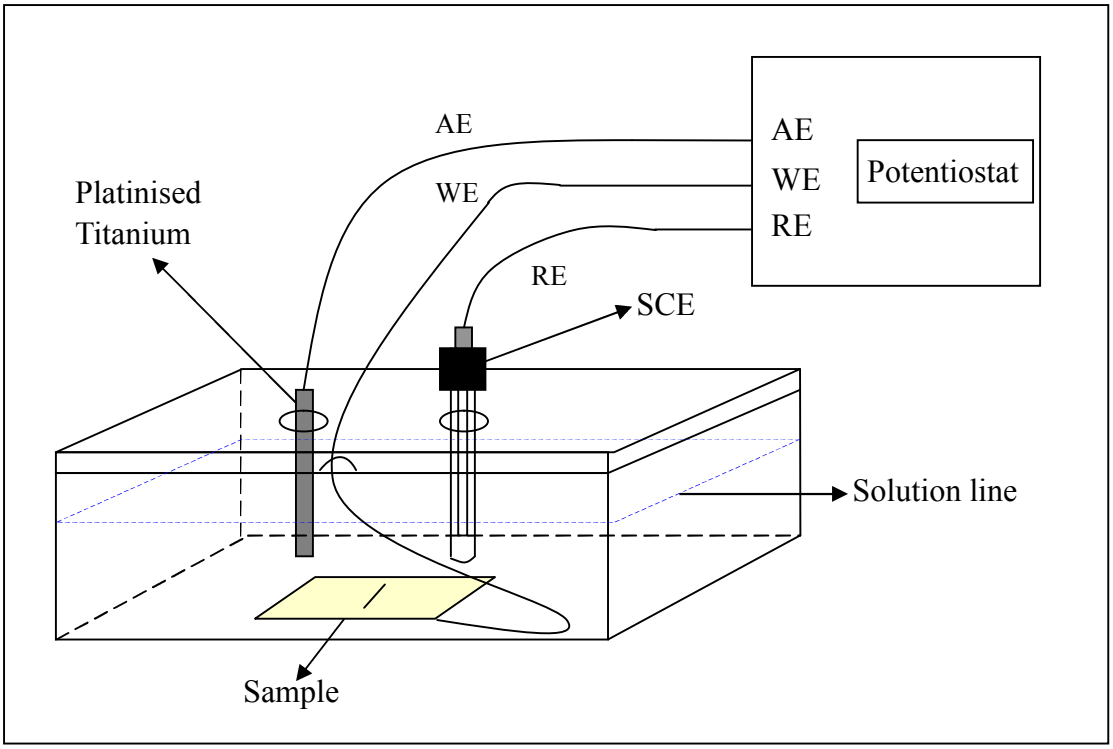
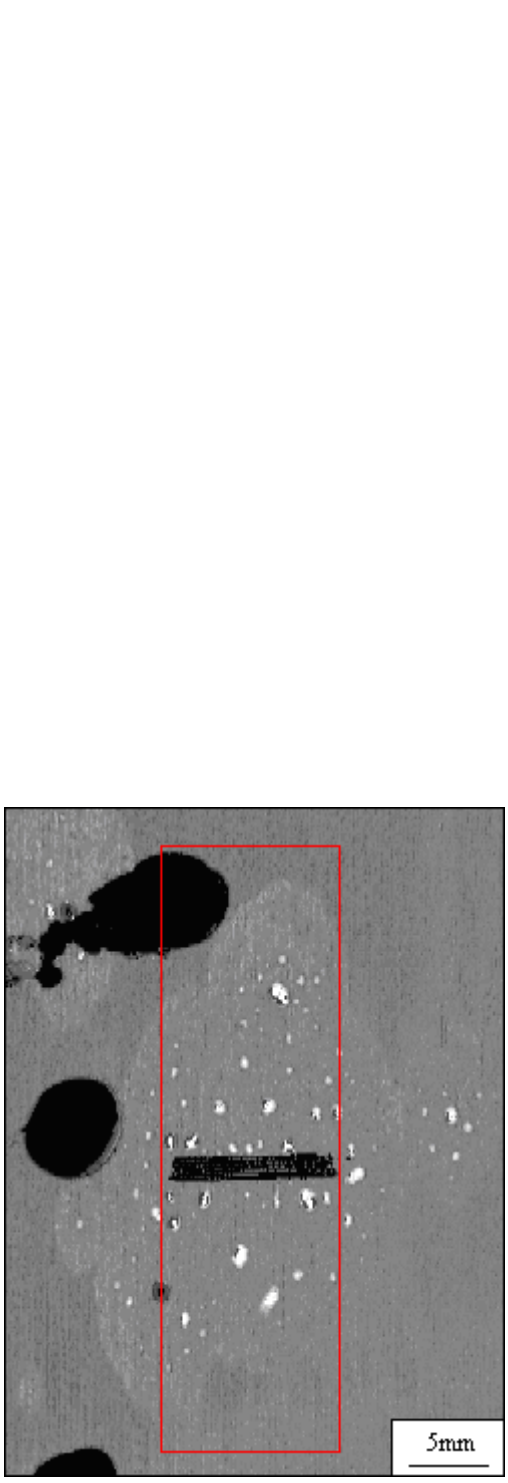


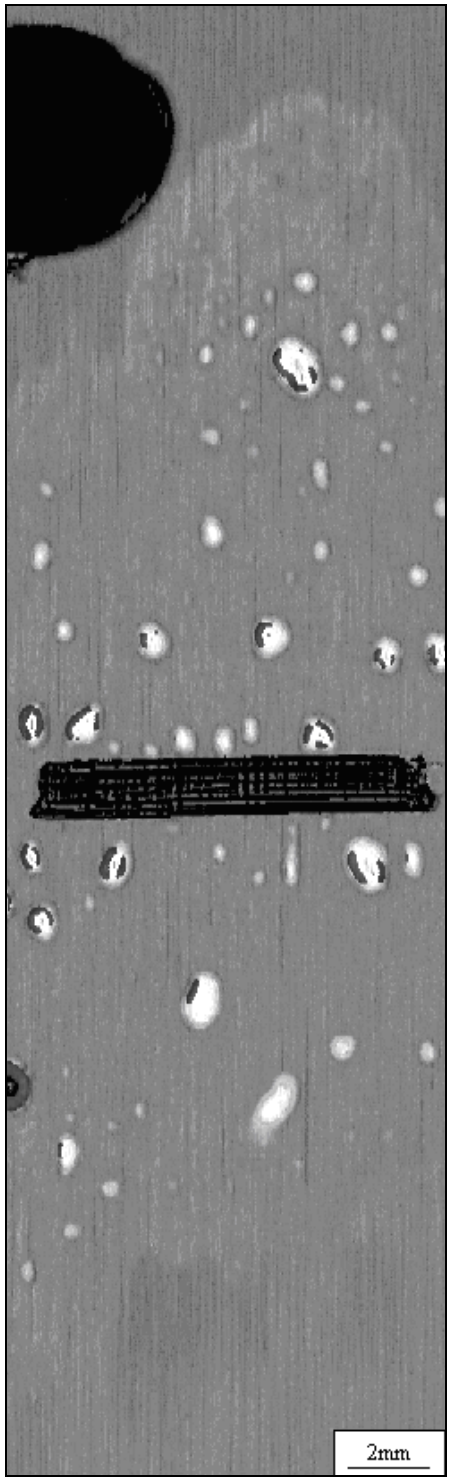
Fig.4.12 Schematic diagram of polarisation set up.

4.2.5.2 Results and Discussion

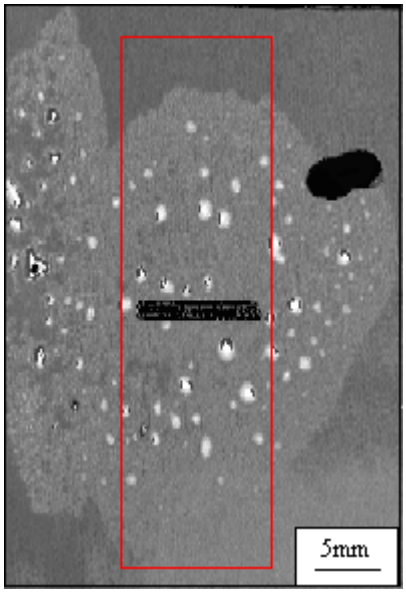
Fig.4.13 and Fig.4.14 give the SAM images of EC samples after fully- and semi-immersion tests in 3.5% NaCl solution with potential (-800 mV or -1000 mV) applied for 7 days.



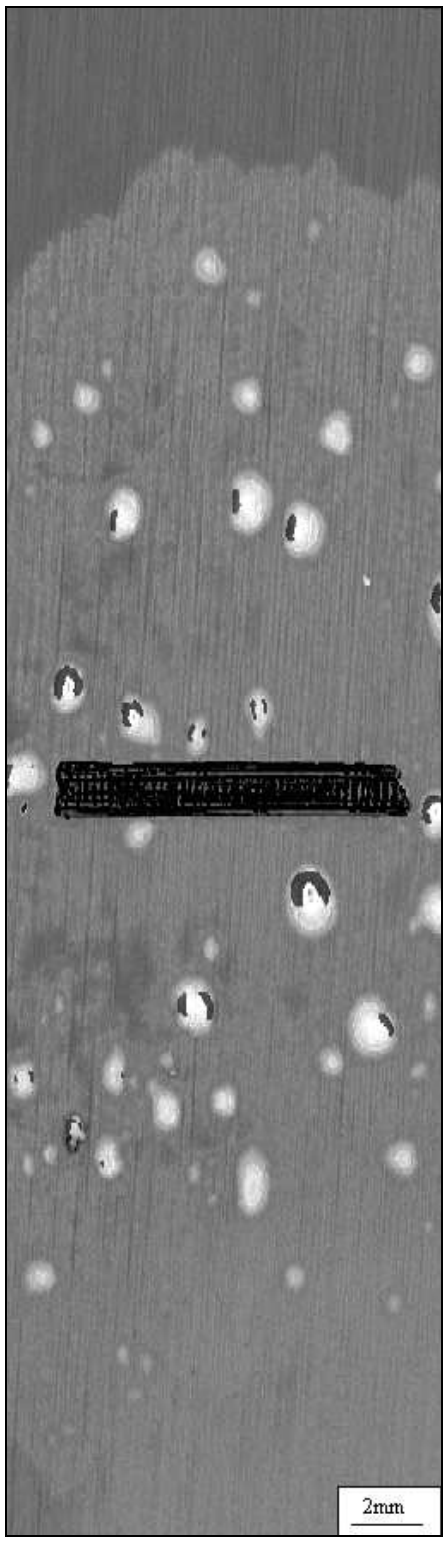
a)



b)

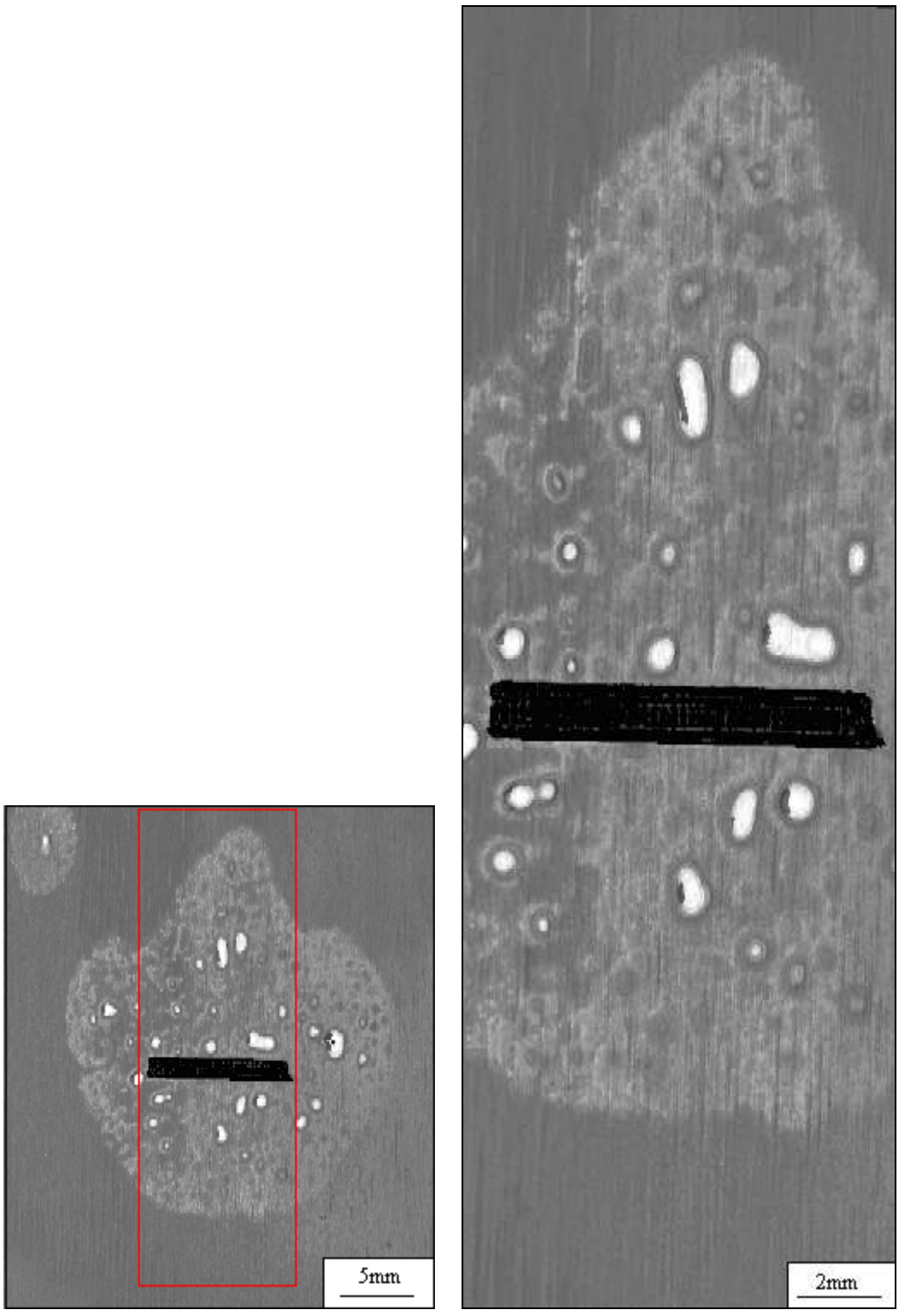


c)

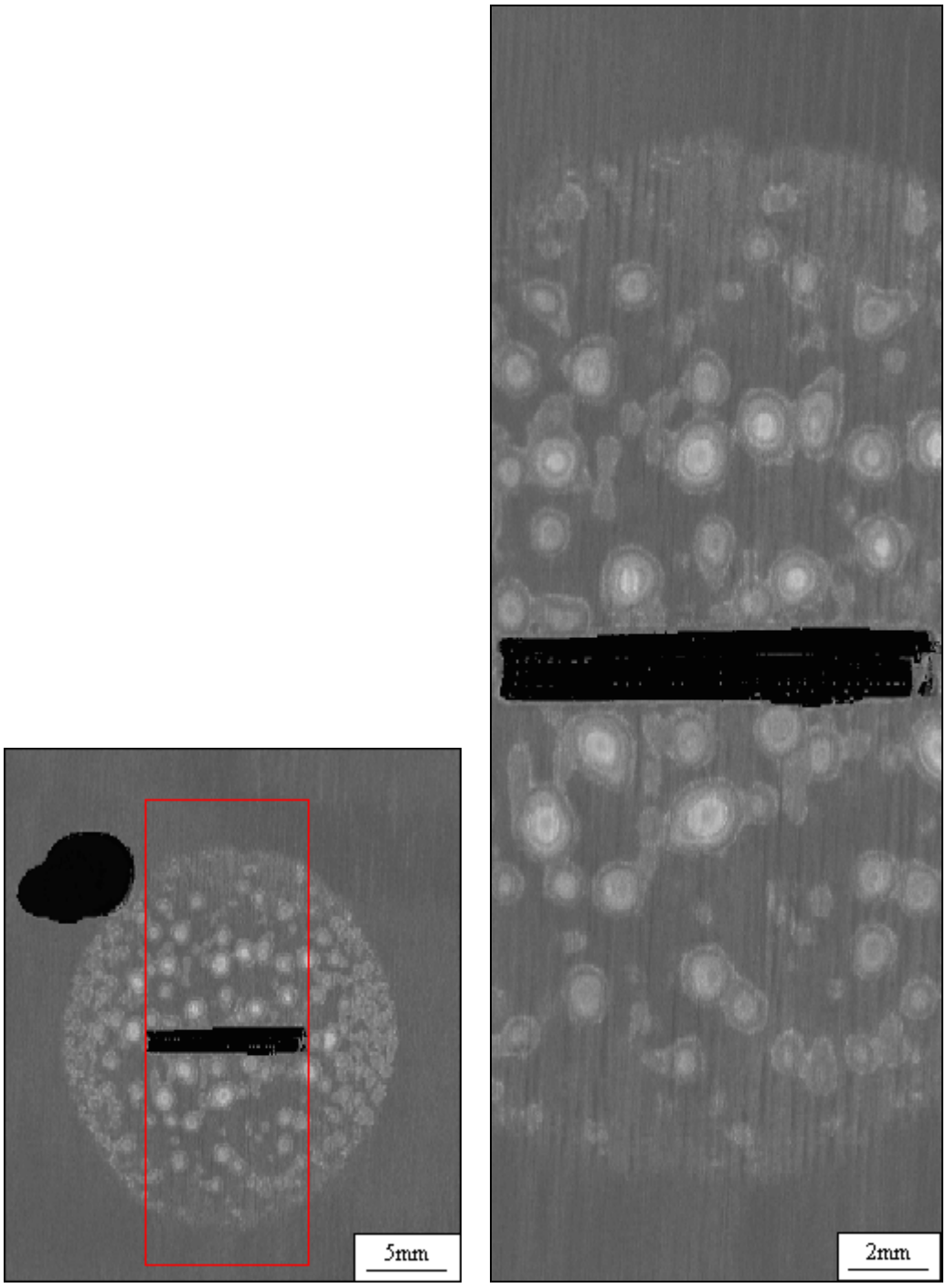


d)

Fig.4.13 SAM images of EC fully-immersed in 3.5% NaCl solution with potentials applied, day 7. a) -800 mV; b) close up of a); c) -1000 mV; d) close up of c). The black features in a), b) and c) are the wax on the sample surface which was used to seal the defect in the coating (excluding the artificial linear defect created) to prevent corrosion starting at those defects.



a) b)



c) d)

Fig.4.14 SAM images of EC semi-immersed in 3.5% NaCl solution with potentials applied, day7. a) -800 mV; b) close up of a); c) -1000 mV; d) close up of c). The black feature in c) is the wax on the sample surface.

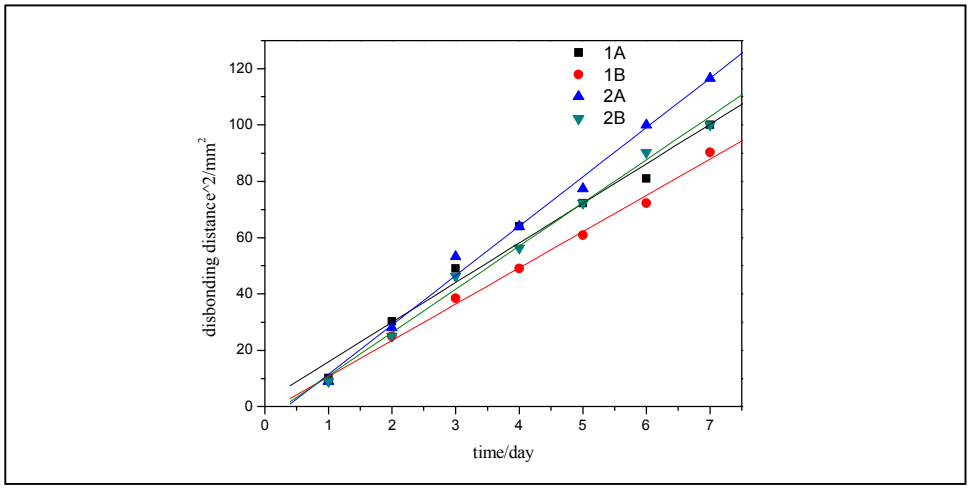
The dark line across the centre of each image is the scribe (artificial defect) in the coating. It can be seen from these images that more and bigger blisters occurred with

a cathodic potential applied and that the disbonding extent is wider with the more negative potential applied, indicating faster disbonding rates. Table.4.1 gives the blistering area data analysed by image analysis software – ImageJ to give an idea about the number and size of blisters occurring under cathodic polarisation in full- and semi-immersion conditions. The details of SAM image analysis by ImageJ have been described in Chapter 2. In this work, an area of 0.2 mm^2 was defined as the lowest size limit constituting a blister (relatively big blister). Features exceeding this size were countered and measured by the software.

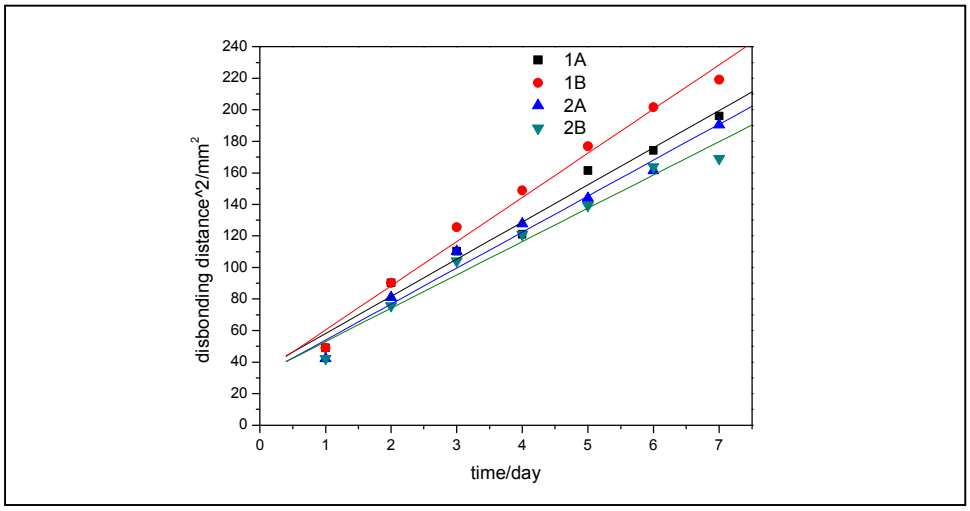
	Full-immersion		**Semi-immersion**	
	-800 mV	**-1000 mV**	**-800 mV**	**-1000 mV**
Count	3	27	27	38
Total Area (mm^2)	0.826	11.482	13.855	24.970
Average Size (mm^2)	0.275	0.425	0.513	0.657
Area Fraction (%)	0.3	2.2	3.8	7.6

Table.4.1 SAM Image analysis data for the blistering area from ImageJ.

If we plot the disbonding distance^2 as a function of time for EC under full- and semi-immersion condition with potential applied, Fig.4.15 and Fig.4.16 are obtained.

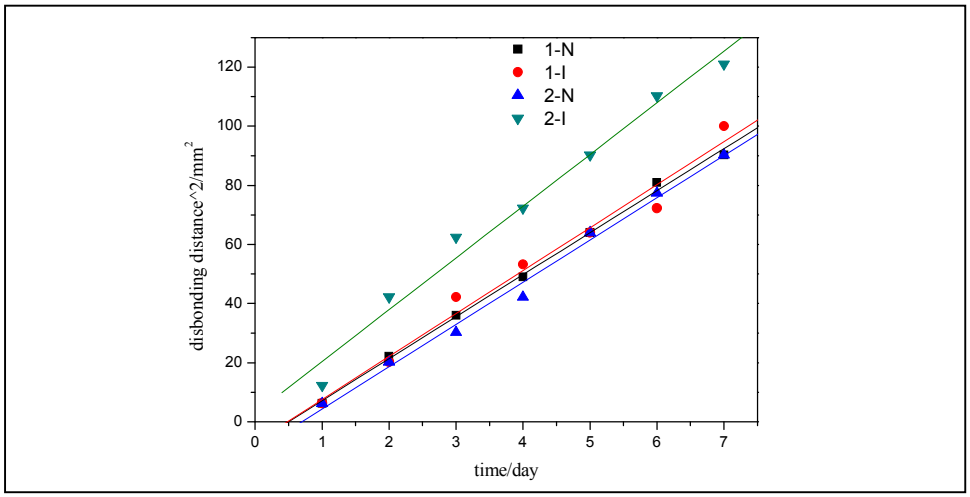


a)

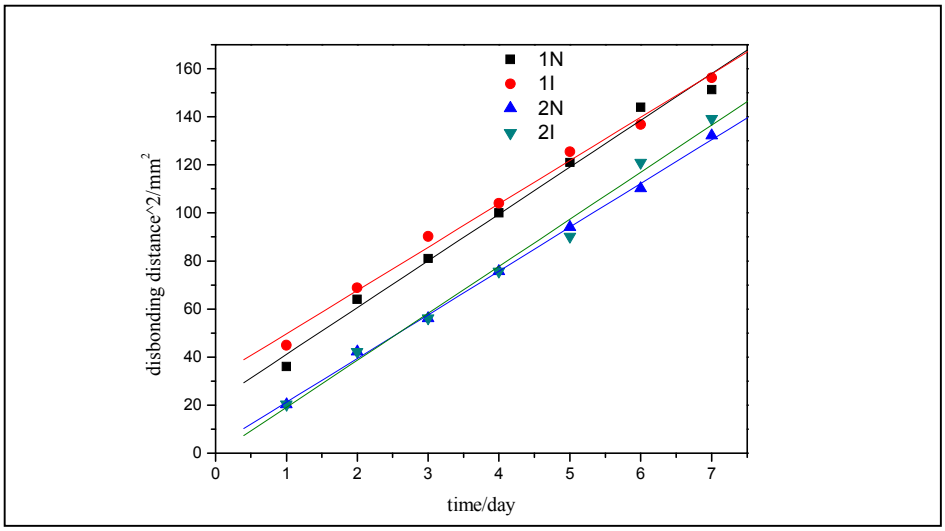


b)

Fig.4.15 Disbonding of EC fully-immersed in 3.5% NaCl solution with different potentials applied, a) -800 mV; b) -1000 mV. Two panels under each potential were tested. 1, 2: Sample 1 and 2; A, B: Measurements on the opposite sides of the same defect, side A and B.



a)



b)

Fig.4.16 Disbonding of EC semi-immersed in 3.5% NaCl solution with different potentials applied, a) -800 mV; b) -1000 mV. Two panels under each potential were tested. 1, 2: Sample 1 and 2; N, I: Non-immersed, Immersed part.

Linear lines were found to correlate the plots in Fig.4.15 and Fig.4.16 with the correlation coefficient over 0.99, indicating parabolic kinetics for widening of disbonding under both cases. It is clearly shown in Fig.4.15 a) and b) that the disbonding distance^2 of fully-immersed EC samples after polarisation with -1000 mV for 7 days (240 mm^2) is about double that under -800 mV polarisation (120 mm^2). The free corrosion potentials measured for full- and semi-immersion tests are about -685 mV and -680 mV, respectively. It is interesting to note that as shown in Fig.4.15 b) and Fig.4.16 b) that when polarised at -1000 mV, the delay time is < 0 (if we calculate it as usual). This supports Doherty's [133] argument that the delay time is for initiation of corrosion which a cathodic polarisation is applied to the coated metal; in these experiments (polarisation at -1000 mV), cathodic reaction starts at once and solution has immediate access to interface, so disbonding begins at once. Indeed it seems that disbonding proceeds more rapidly than predicted at relatively short times.

Fig.4.17 summarises the disbonding rates of EC polarised at different potentials both under full- and semi-immersion conditions.

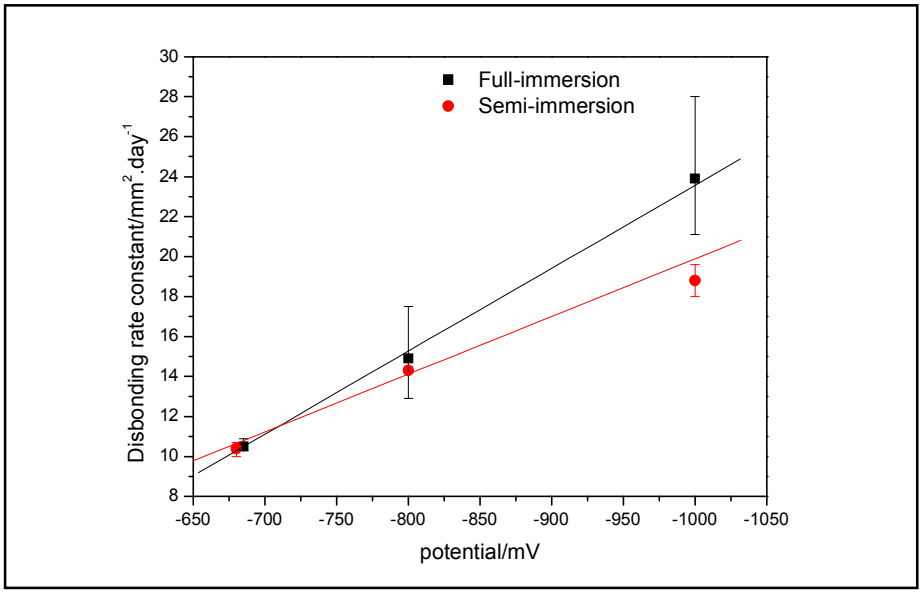


Fig.4.17 Disbonding rate constant *vs.* potential applied: effect of polarisation.

It is clearly shown that the disbonding rate increases linearly with the increasingly negative potential applied which is attributed to more rapid cathodic reaction (O_2 reduction) or faster ion migration resulting from the bigger potential difference between the defect and the intact coating. Also, the disbonding rate under full-immersion condition with potential applied is faster than that under semi-immersion conditions, yet is still symmetrical in the latter case (Fig.4.16). See Fig.4.17.

The effect of polarisation shown here correlates well with Stratmann's results. We have analysed Stratmann's potential profile (a typical one), Fig.4.18 [56], to see the change of disbonding rate as potential. Taking the potential difference at the active zone as marked, which is from the disbonding tip to the intact coating area, and calculating the disbonding rate at each disbonding time, Fig.4.19 is obtained.

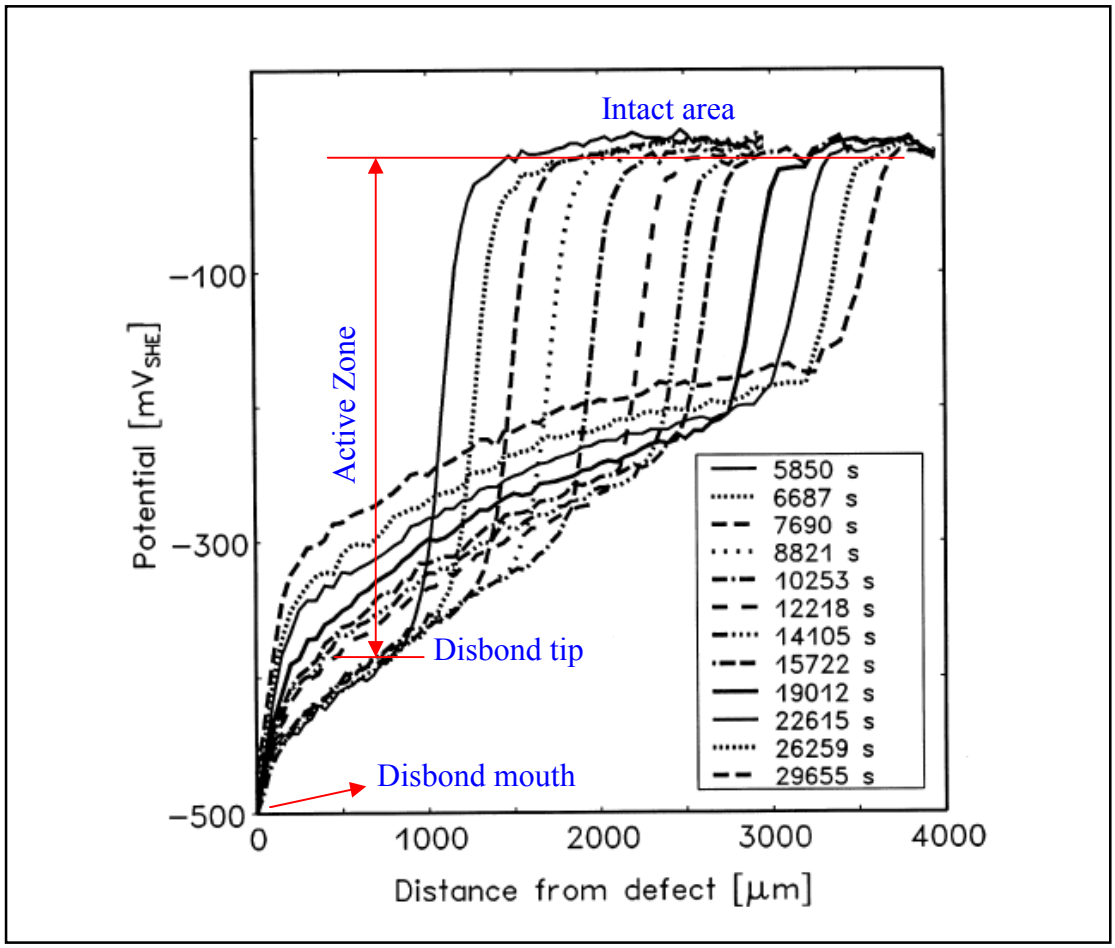


Fig.4.18 Typical potential distribution (measured by SKP) in air for different disbonding times (An unpigmented epoxy-ester coating on cold rolled steel with the defect covered with 0.5M KCl solution). [56] *(the same as Fig.1.4)*

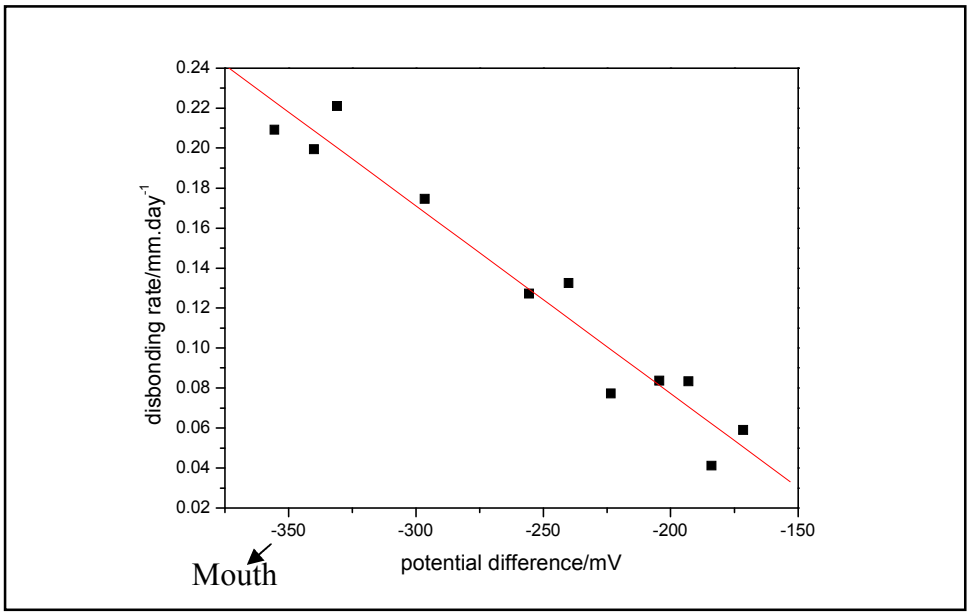


Fig.4.19 Potential difference *vs.* disbonding rate calculated from Fig.4.18.

It showed that the disbonding rate decreases with the decreasing potential difference of the active zone and a quite good linear relationship was found to correlate them. As the tip potential, E_{tip}, becomes less negative, the disbond growth slows. This suggests that in these experiments, the most important factor affecting the disbonding process is the potential difference between the disbond tip and the intact coating. This seems to offer an important insight into the nature of the disbonding process.

In this work, however, it does not actually show that it is the potential difference between the disbond tip and the intact coating that drives the disbonding since the potential difference between the disbond tip and the intact coating does not give a systematic change over time.

4.2.6 Free Corrosion Potential in the Defect

4.2.6.1 Introduction

Due to the lack of information from the previous studies on the potential change over immersion time under free corrosion condition, here in this part, the free corrosion potential, Ecorr, was monitored over time.

Any electrical measurements on the coated samples should be made with negligible current flow, otherwise, the flow of current may introduce damage to the coated sample which is not what we expected. Therefore, a potential voltmeter with a very high impedance is an absolute necessity for the corrosion potential measurements. Here the Pico-Log system (ADC-16, pico Technology) with buffer built inside was used to measure the free corrosion potential of the EC sample with a linear defect on

it immersed in 3.5% NaCl solution with time. A SCE reference electrode was attached to the Pico-Log system when recording.

4.2.6.2 Results and Discussion

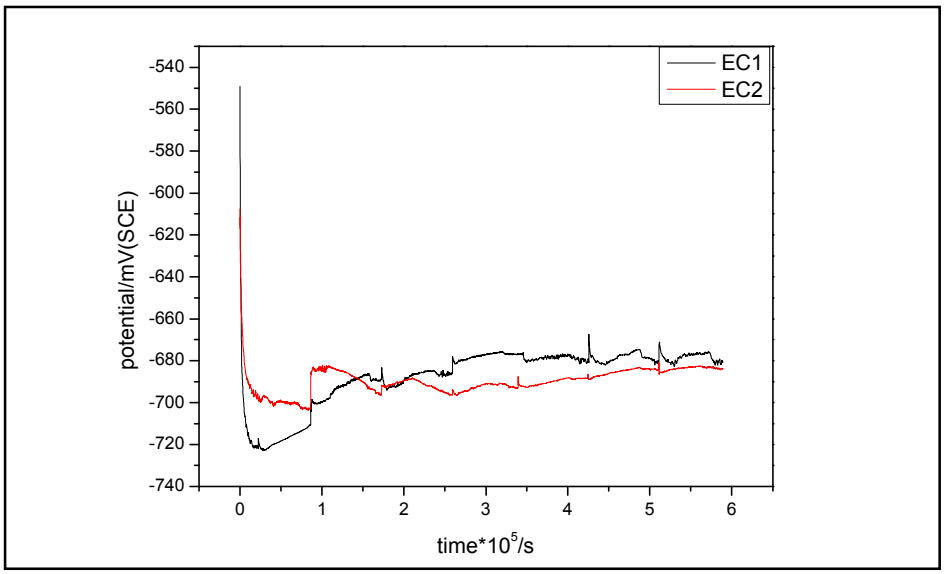
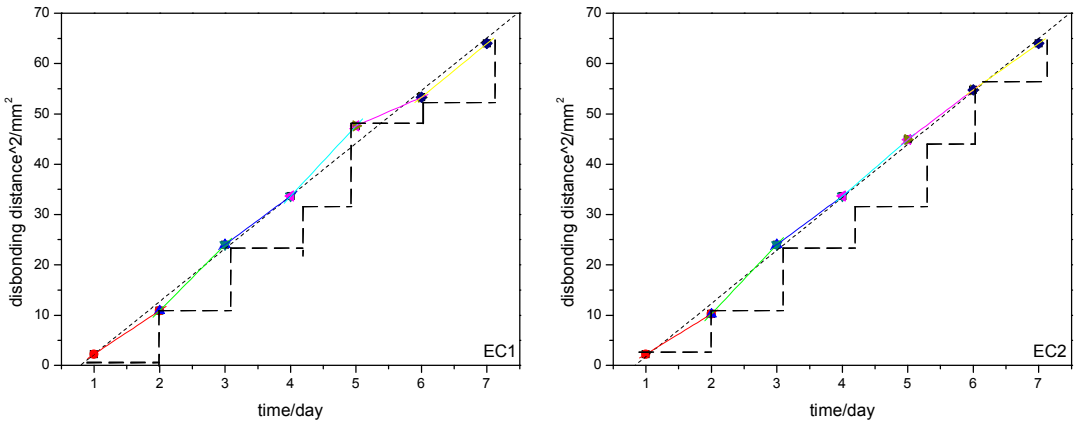


Fig.4.20 Potential *vs.* time recorded by Pico-Log, EC fully-immersed in 3.5% NaCl solution. Two panels were tested.

As shown in Fig.4.20, the free corrosion potential decreased significantly in the first 2000s and a relatively larger variation occurred during the first day, but was quite constant afterwards. The big drop of the potential corresponds to the initiation of corrosion. From controlled potential tests (Section 4.2.5), we should expect any change in potential versus time to influence the rate as disbonding proceeds. The small change in E seen here (28 ± 5 mV) will have a minimal effect on rate.

If we plot the disbonding distance^2 versus time for EC1 and EC2 which have been used for Fig.4.20, Fig.4.21 is obtained.



a) b)

Fig.4.21 Disbonding distance^2 *vs.* time results of duplicate EC fully-immersed in 3.5% NaCl solution for 7 days, a) EC1; b) EC2.

It is shown in Fig.4.21 that the disbonding of EC fully immersed in 3.5% NaCl solution follows parabolic disbonding kinetics as discussed in previous sections though there are small variations in disbonding rates when calculated from the slopes of the coloured lines connecting individual points as shown in Fig.4.21 which correspond well with the small variations of free corrosion potential as shown in Fig.4.20. Therefore, it can be concluded that there will be little effect of the free corrosion potential on disbonding rate over time, which rules out the possibility that the retardation over time is due to the free corrosion potential change.

4.2.7 Effect of Paint Composition

4.2.7.1 Introduction

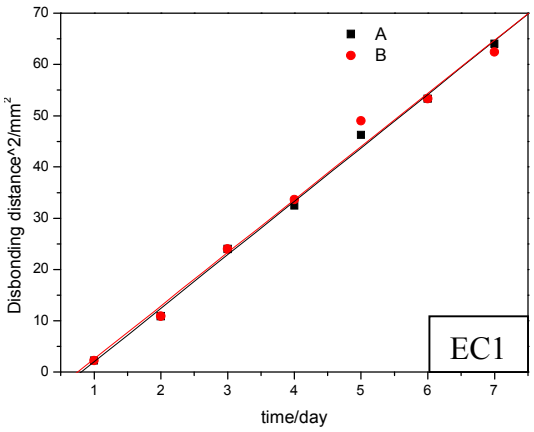
In this part of work, the effect of added pigments, including an inhibitive pigment, was explored. Cathodic disbonding of unpigmented epoxy (EC) and pigmented epoxy (epoxy with talc, ET; epoxy with talc and zinc phosphate, ETZ) were studied. Details

of pigment content are shown in Table.2.1. Disbonding kinetics of each coating were obtained and SAM was applied to characterise the coating/metal interface after fully-immersed in 3.5% NaCl solution for 7 days.

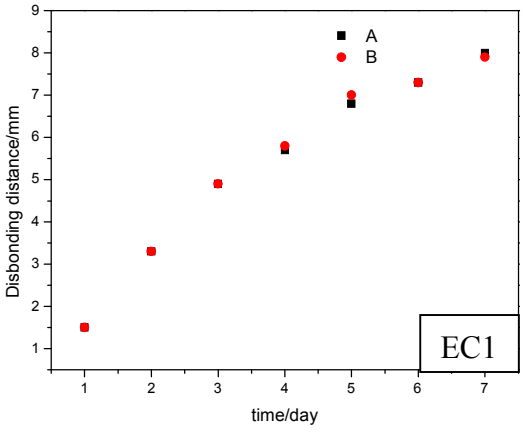
4.2.7.2 Results and Discussion

The disbonding results obtained make it difficult to distinguish a relationship between the disbonding distance and exposure time of the pigmented coatings. In these samples, it seems they could either be linear or parabolic. To show the relationships clearly, plots of disbonding distance *vs.* time and disbonding distance^2 *vs.* time have been plotted separately for the duplicate samples.

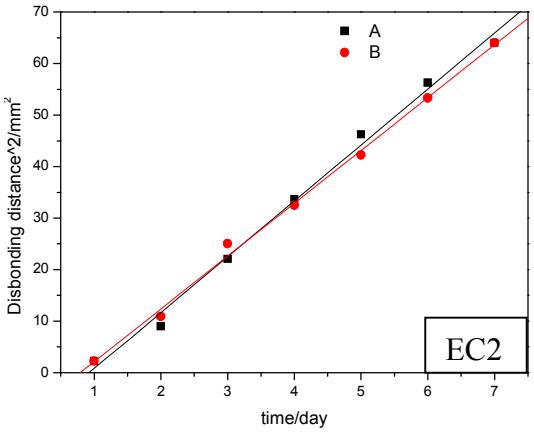
Parabolic **Linear**



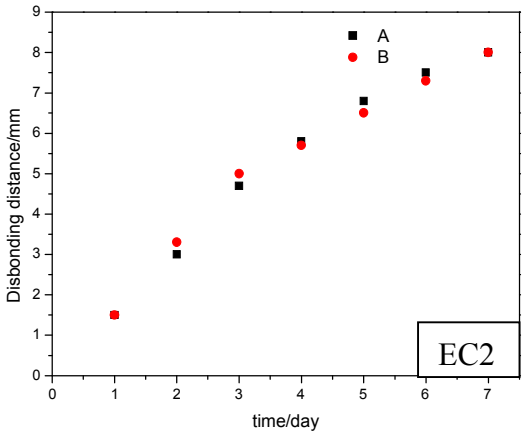
a)



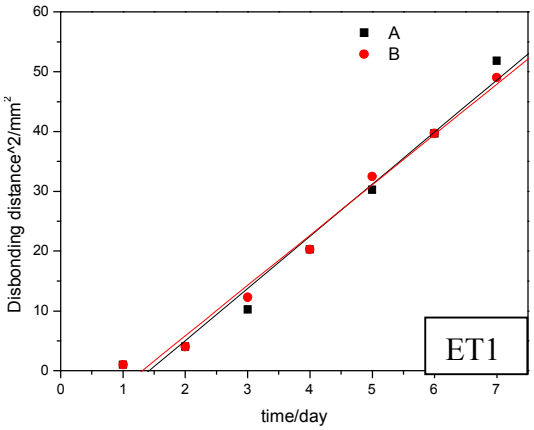
a')


Disbonding distance^2/mm^2
time/day
A
B
EC2

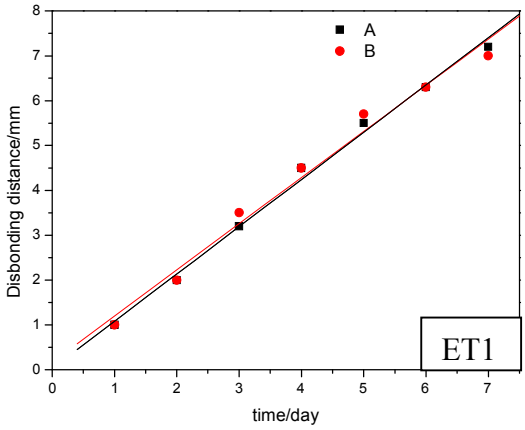
b)


Disbonding distance/mm
time/day
A
B
EC2

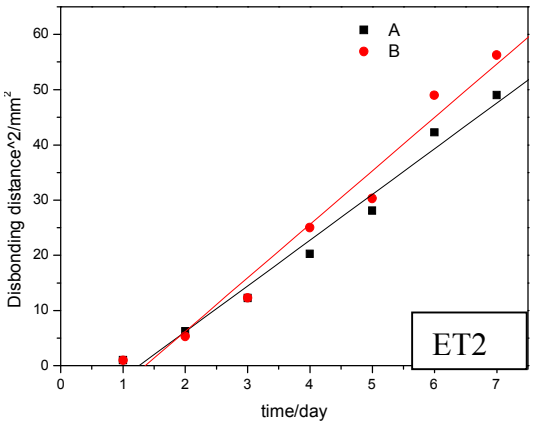
b')


Disbonding distance^2/mm^2
time/day
A
B
ET1

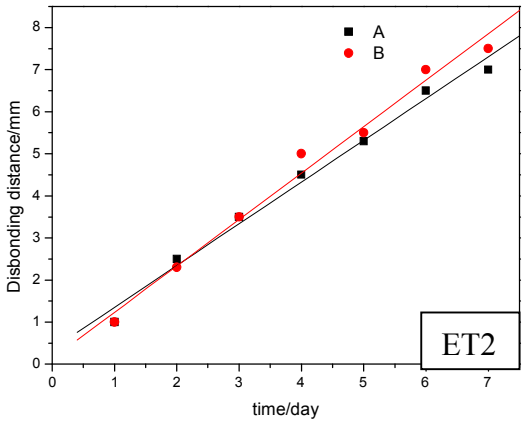
c)


Disbonding distance/mm
time/day
A
B
ET1

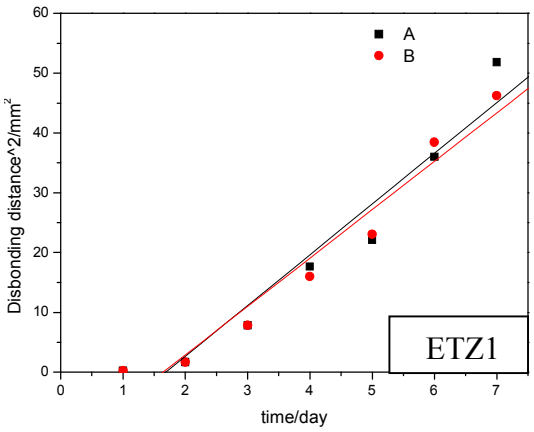
c')


Disbonding distance^2/mm^2
time/day
A
B
ET2

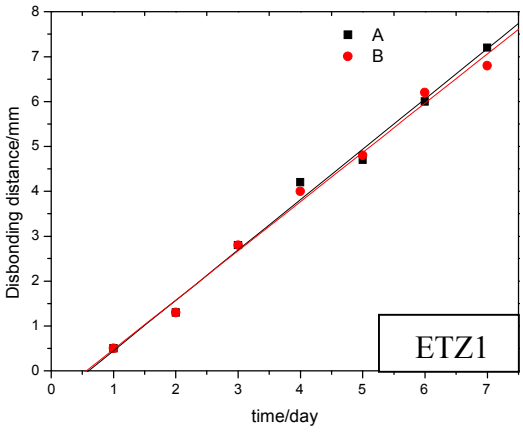
d)


Disbonding distance/mm
time/day
A
B
ET2

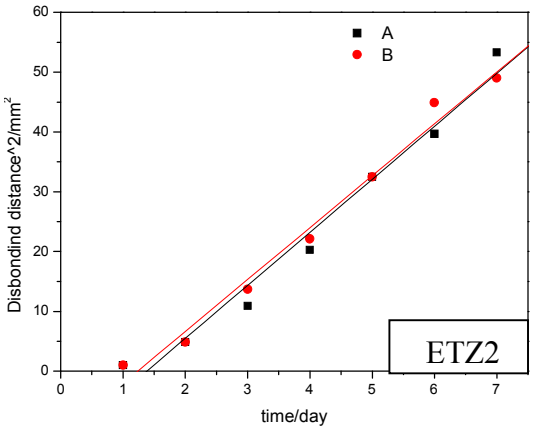
d')



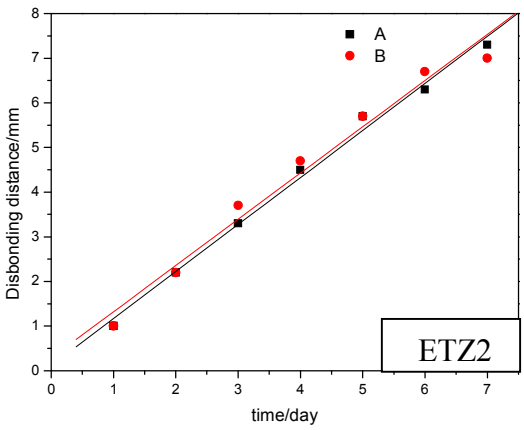
e)



e')



f)



f')

Fig.4.21 Disbonding distance^2 *vs.* time (a) - f)) and disbonding distance *vs.* time (a') – f')) for duplicate samples of EC, ET and ETZ fully-immersed in 3.5% NaCl solution for 7 days. A, B: Measurements of the opposite two sides of the same defect, side A and B.

Paint	Disbonding kinetics / disbonding distance (d/mm) *vs.* time (t/day)							
	Liner (d *vs.* t) & Correlation Coefficient (R)				Parabolic (d^2 *vs.* t) & Correlation Coefficient (R)			
	1A	1B	2A	2B	1A	1B	2A	2B
EC	-	-	-	-	10.4 & 0.998	10.4 & 0.994	10.9 & 0.997	10.3 & 0.998
ET	1.1 & 0.997	1.0 & 0.992	1.0 & 0.994	1.1 & 0.993	8.7 & 0.988	8.4 & 0.993	8.3 & 0.990	9.7 & 0.985
ETZ	1.1 & 0.996	1.1 & 0.996	1.1 & 0.997	1.0 & 0.989	8.5 & 0.968	8.1 & 0.977	8.9 & 0.988	8.7 & 0.992

Table.4.2 Cathodic disbonding of EC, ET and ETZ fully-immersed in 3.5% NaCl solutions. Slopes of both d *vs.* t and d^2 *vs.* t plots have been given.

It can be seen from Fig.4.21 and Table.4.2 that for the unpigmented epoxy, it is very certain that the disbonding follows parabolic kinetics; while for the pigmented epoxy coatings, it is not as clear whether the disbonding kinetics are linear or parabolic. But based on the correlation coefficient of the regression fit, the linear relationship fits better for the pigmented samples. Table.4.2 also shows that ET and ETZ have similar disbonding rates which are slightly slower than that of EC.

Sharman *et al.* [68] investigated cathodic disbonding of an unpigmented and an iron-oxide pigment containing chlorinated rubber from steel and reported that the rate of disbonding of the unpigmented chlorinated rubber showed a strong dependence on cation mobility, but the pigmented coating did not. However, if we re-plot their data [132], Fig.4.22 and Fig.4.23 are obtained.

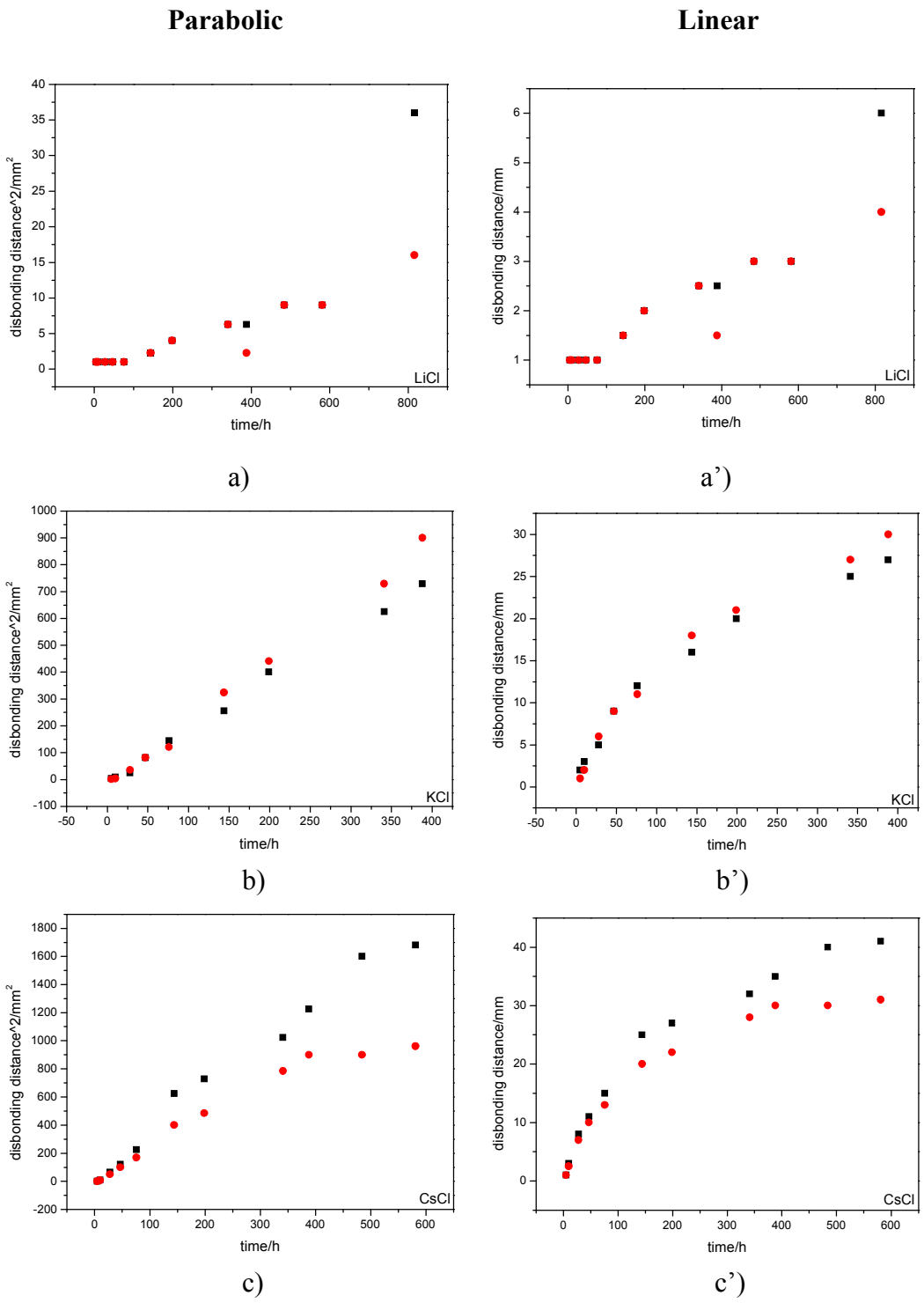


Fig.4.22 Disbonding distance ^2 *vs.* time (a) – c)) and disbonding distance *vs.* time (a') – c')) for unpigmented chlorinated rubber immersed in 0.5M LiCl, KCl and CsCl solutions.

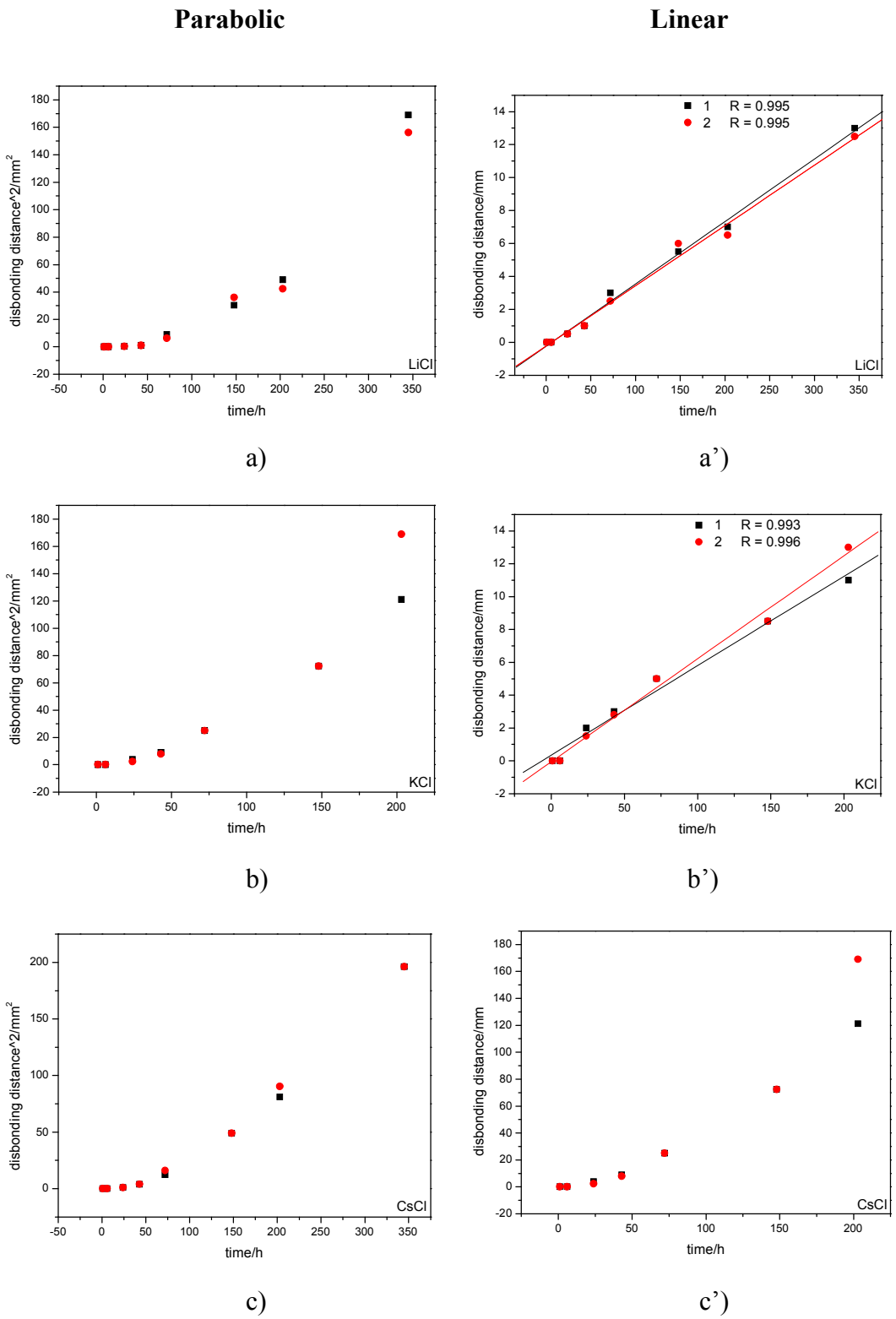


Fig.4.23 Disbonding distance ^2 *vs.* time (a) - c)) and disbonding distance *vs.* time (a') – c')) for pigmented chlorinated rubber immersed in 0.5M LiCl, KCl and CsCl solutions. R is the correlation coefficient for the regression fit.

As shown in Fig.4.22, it is clear that for the unpigmented chlorinated rubber,

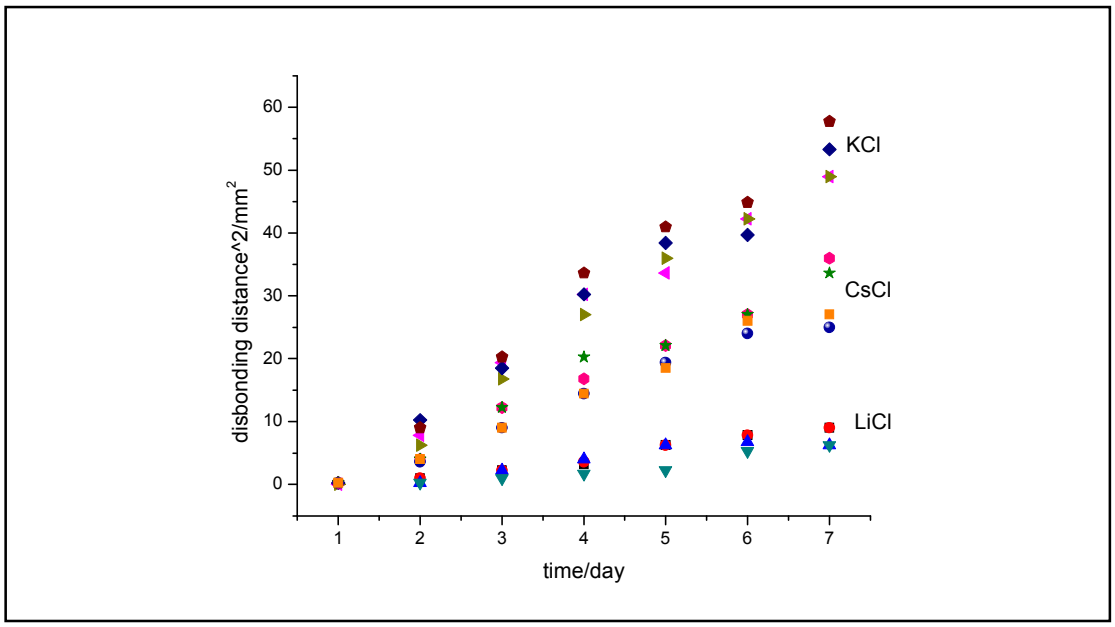
parabolic kinetics fits better; however, for the pigmented chlorinated rubber (Fig.4.23), it is apparent that linear kinetics fits better for cathodic disbonding in LiCl and KCl solution, but in CsCl solution, it is not clear whether the linear or parabolic kinetics fits better. These results of disbonding kinetics for unpigmented and pigmented chlorinated rubber are the same as found here for epoxy coatings.

In this work, the disbonding of unpigmented epoxy coated mild steel follows parabolic kinetics; frequent linear kinetics is seen for the pigmented coatings. Several possible simple mechanisms have been analysed to illustrate the difference in the disbonding kinetics.

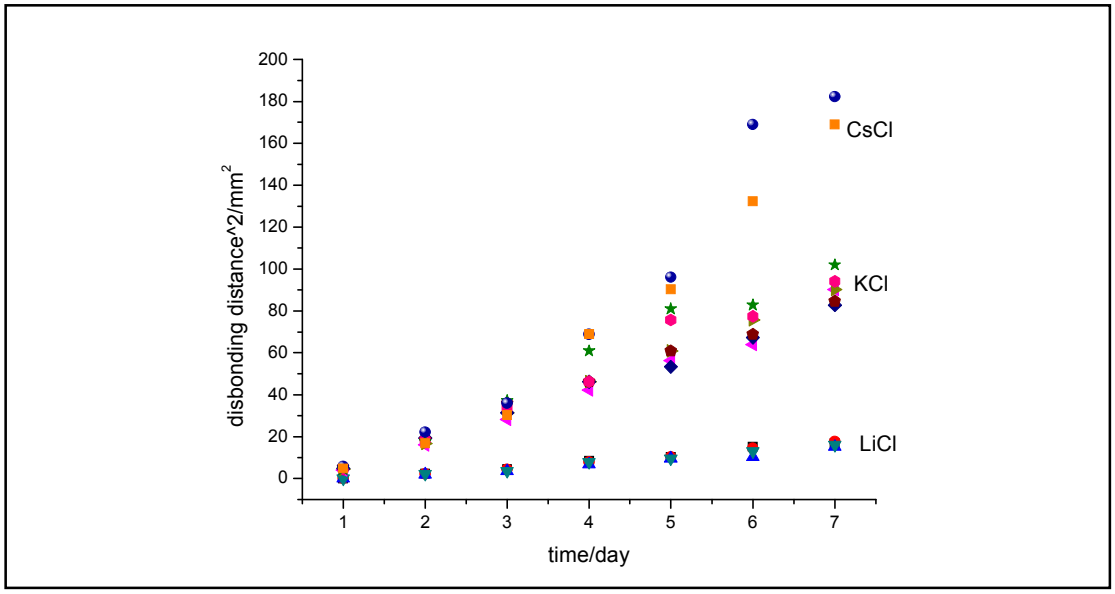
In terms of simple mechanisms, the rate-controlling process can be ion or oxygen transport with two possible transport routes, (vertically) through the coating or (horizontally) along the coating/metal interface.

The parabolic disbonding kinetics of the unpigmented coatings can be explained by the ion transport along the coating/metal interface as the rate-controlling process. This is supported by: 1. results of effect of cations, Fig.4.3: the disbonding rates are in the sequence of KCl > CsCl > NaCl > LiCl though the reason for why the rate in KCl is faster than in CsCl has not been fully understood yet; 2. the effect of film thickness (results as shown in Section 4.2.1): slightly slower rate with increased film thickness, which ruled out the possibility of ion transport through the coating as the main rate-determining process and 3. semi-immersion tests results as shown in Section 3.2.2.2: symmetrical disbonding of the immersed and the non-immersed parts, which again ruled out the possibility of ion transport through the coating; while the

pigmented coatings showed linear disbonding kinetics, based on the simple mechanisms, transport through the coating which gives linear kinetics should be the main rate-determining process. Then the question is whether ion or oxygen transport controls the rate. In presence of pigment, the permeabilities of oxygen and water are decreased [68], thus oxygen transport through the coating is now likely to be much slower. If oxygen transport through the coating is the rate-controlling process, disbonding of pigmented coatings in different cation chloride solutions should not have much difference. However, if we examine the effects of cations on disbonding of pigmented coatings, Fig.4.24 is obtained. (Note that the pigmented coatings used for Fig.4.24 are an old batch of samples results of which are not used in this work due to the inappropriate curing agent used which is very viscous and may affect the cross-linking process of the paint. Results of other parts in this work are all based on a new batch of samples which the curing agent is appropriately mixed with epoxy.)



a)

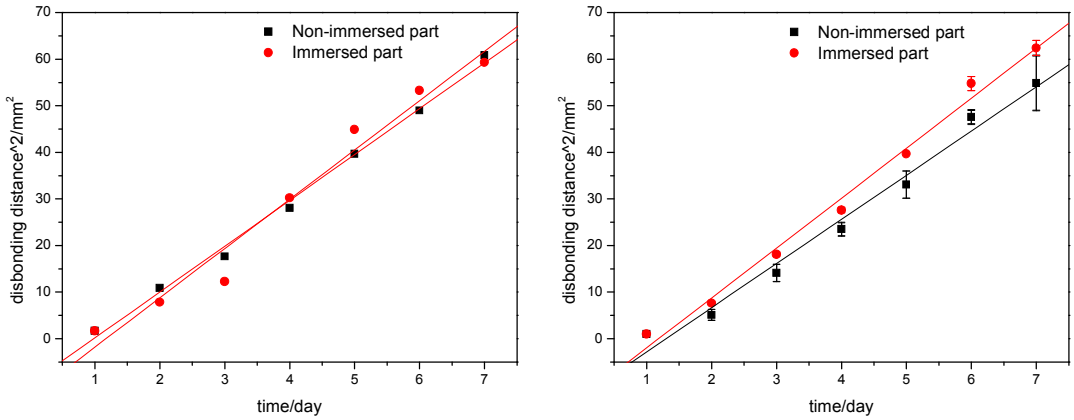


b)

Fig.4.24 Effect of cations on disbonding of pigmented coatings (the old batch), a) ET; b) ETZ.

The use of the results of the old batch of samples shown here supports the point that the disbonding rates of the pigmented coatings are different in different alkali metal chloride solutions, suggesting ion transport plays an important part. However, we should notice that the disbonding rates of the old batch of samples are much smaller than the new batch and fails to test the reason for the linear kinetics because the disbonding of the old batch of samples here show a parabolic kinetics. Therefore, these tests should be repeated with samples of the same batch as the ones used to obtain Fig.4.21.

If ion transport through the coating is the rate-controlling process for the pigmented coatings, then for the semi-immersion tests, the disbonding of the immersed and the non-immersed parts should show significant difference. However, it is not the case here. See Fig.4.25.



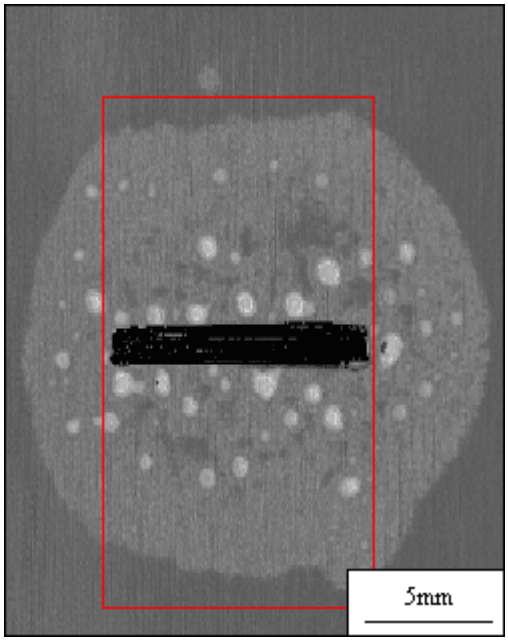
a) b)

Fig.4.25 Disbonding of pigmented coatings semi-immersed in 3.5% NaCl solution, a) ET and b) ETZ.

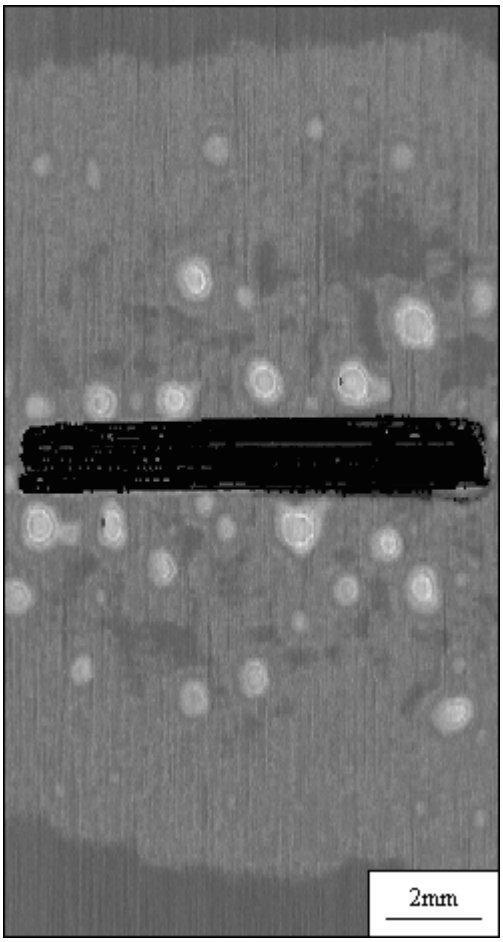
It is shown in Fig.4.25 that there is no significant difference in the disbonding rates of the immersed and the non-immersed parts of the pigmented coatings, suggesting ion transport through the coating can not be the rate-determining process.

From the above analysis, the possibilities based on the existing simple mechanisms have all been excluded, which leads to a conclusion that the simple models can not account for the behaviour seen here. Therefore, a more complex model, possibly a combination of several mechanisms may exist which however, has not been setup in this work yet.

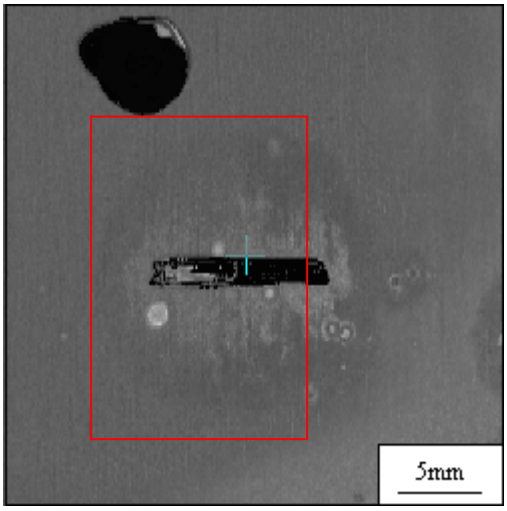
To help understand the difference between cathodic disbonding of EC, ET and ETZ, SAM was applied to characterise the coating/metal interfaces of these samples. See Fig.4.26 for the SAM images. Images of only one sample for each coating are displayed because of the similarity of the duplicate samples tested.



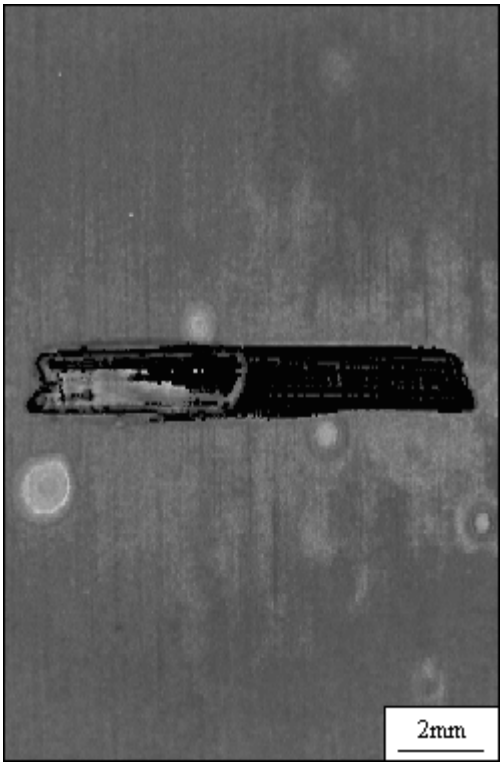
a)



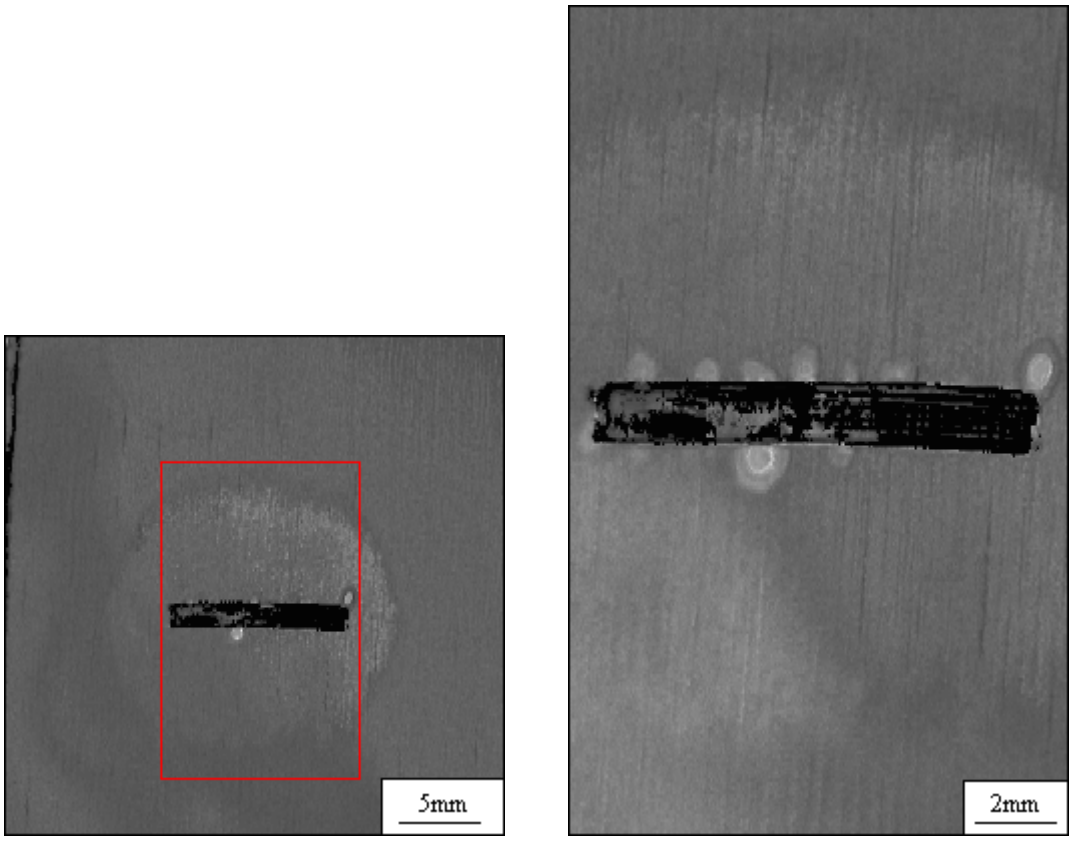
b)



c)



d)



e) f)

Fig.4.26 SAM images of EC, ET, ETZ immersed in 3.5% NaCl solution, day 7. a): EC; b) magnified view of the circled region in a); c): ET; d) magnified view of the circled region in c); e) ETZ; f) magnified view of the circled region in e).

Fig.4.26 b), d) and f) present a clear view of the disbonding around the defect, which correspond to the circled areas in Fig.4.26 a), c) and e). The boundary between the disbonded and non-disbonded region is well distinguished for EC, as Fig.4.26 a) and b) show. While for ET and ETZ, they are less well defined than for EC.

Blisters occurring at the disbonding front help the propagation of disbonding. Many blisters are visible within the disbonded area of the EC samples, but fewer ones (mainly close to the defect) are found for ET and ETZ. If blisters form at anodes, then it seems that pigments inhibit the development of new anodic sites. Zinc phosphate is an inhibitive pigment, so this is what we expect, but the influence of talc is more

surprising.

4.3 Summary of Conclusions

For the system studied, the following conclusions can be drawn from the current work.

- **Effect of Film Thickness**

Cathodic disbonding of EC samples slows only slightly with increased film thickness, suggesting that transport through the paint is not the main transport route for cathodic disbonding process.

- **Effect of Cations**

The disbonding rates of EC are in the sequence of KCl > CsCl > NaCl > LiCl when immersed in these four solutions, which is surprising and the anomalous behaviour of K^+ or Cs^+ (KCl > CsCl) has not yet been fully understood.

- **Effect of Electrolyte Concentration**

Higher flux of Na^+ ions in the more concentrated solution results in a faster disbonding rate which can be attributed to a higher Na^+ flux in compared to OH^- flux out, thus a higher pH generated at the coating/metal interface that can lead to more severe disbonding due to the lager cathodic currents caused.

- **Effect of Temperature**

There is no significant difference between disbonding rates at 40℃ and 50℃, but they are faster than those under 20℃ and 30℃, which can be explained by the existence of some critical point between 30℃ and 40℃ where a transition takes place

in the presence of a weak layer (resulted by the attack of hydroxide ions or free radicals during oxygen reduction process) bonding the coating to the metal substrate.

- **Effect of Polarisation**

Cathodic disbonding rate increased with the more negative potential applied which is attributed to the bigger cathodic current caused by the larger potential gradient between the defect and the intact coating, or the ability to sustain a bigger potential difference between the disbond tip and the undisbonded region.

- **Free Corrosion Potential in the Defect**

The free corrosion potential dropped about 100 mV in the first 2000s and a relatively larger variation (28 ± 5 mV) occurred during the first day, then kept relatively constant afterwards, so it should not significantly affect rate for most of the time.

- **Effect of Paint Composition**

Unpigmented and pigmented coatings show different disbonding kinetics, which the unpigmented epoxy follows parabolic disbonding kinetics with ion transport along the coating/metal interface as the rate-determining process, while linear kinetics for the pigmented coatings without known rate-controlling process. Also, there is a small reduction in disbonding rate of pigmented coatings comparing to unpigmented coatings. SAM examinations showed that there were less blisters around the defect for the pigmented coating which can be explained by the ability of zinc phosphate to suppress the formation of anodes, but it is not clear why talc produces a similar effect. However, we should remember that it is very unlikely that only single mechanism exists during cathodic disbonding. It is more possible that several mechanisms occur

in combination depending on the nature of the coating system. Changes of factors affecting the cathodic disbonding process may affect a particular mechanism thus result in the reduction (or increase) of cathodic disbonding rate but may not prevent it completely due to the existence of other mechanisms.

Chapter 5 Corrosion Properties of Intact Coatings

5.1 Introduction

Cathodic disbonding of coating with an artificial linear defect has been discussed in the previous chapters which mainly focused on studying the reaction or process occurred through the defect and along the coating/metal interface. To characterise the cathodic reaction underneath the paint and study the change in properties of the coatings while exposed to the product of the cathodic reactions, here in this chapter, a coated panel (without defect created) is coupled with a bare metal so that it acts as a cathode, but without direct access for the solution to the coating/metal interface. The coupled bare metal replaces the bare metal exposed at the defect (like the one on the samples used in Chapter 3 and 4) to drive the cathodic reaction underneath the paint but without transport of species along the interface from the defect. A stepwise potentiostatic method was employed to characterise the cathodic reactions beneath the paint and the current was allowed to achieve a steady state at each potential. Electrochemical Impedance Spectroscopy (EIS) has also been applied to assess the ion transport through the intact coating at regular time intervals.

5.2 Experimental

Sample

Unpigmented epoxy coated mild steel samples (DFT: 55 ± 5 μm) were prepared as

previously described. However, no artificial defect was created. A piece of bare mild steel of the same size as the coated panel was cut from the Q-panel described in Chapter 2. The specimens used for this part of study were made by connecting wires of the coated panel and the bare metal together which allowed anode and cathode to be electrically coupled during exposure. All specimens were immersed in 3.5% NaCl solution at room temperature.

Polarisation Measurements

The polarisation measurements were taken by a Gill AC Potentiostat (ACM Instruments), using a three-electrode cell with just the coated specimen as the working electrode, a saturated calomel electrode (SCE) as the reference electrode and platinised titanium the counter electrode. Before the potentiostatic measurements, the rest potential of the coupled samples was measured. A series of downwards potential steps (-100 mV to -700 mV) from the rest potential were applied afterwards. The current was measured every 1 second and 300 ~ 420 readings were taken for each test to achieve a steady current.

EIS

EIS measurements on the coupled samples or just the coated specimen were taken periodically using the Gill AC Potentiostat (ACM Instruments) with a high-impedance paint buffer. The impedance was measured across frequency range of 30 kHz to 0.1 Hz using an excitation signal of 20 mV amplitude. The EIS data obtained was fitted with an equivalent circuit model using the ZSimpWin 3.22d software, which fits the model circuit by non-linear least squares regression. The EIS results allow

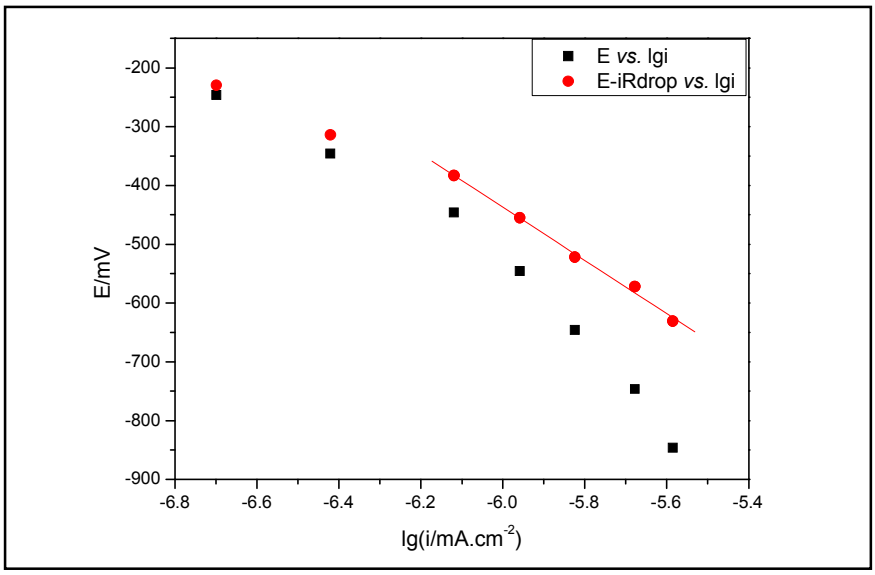
polarisation measurements to be corrected for "iRdrop", using the film resistance value.

5.3 Results and Discussion

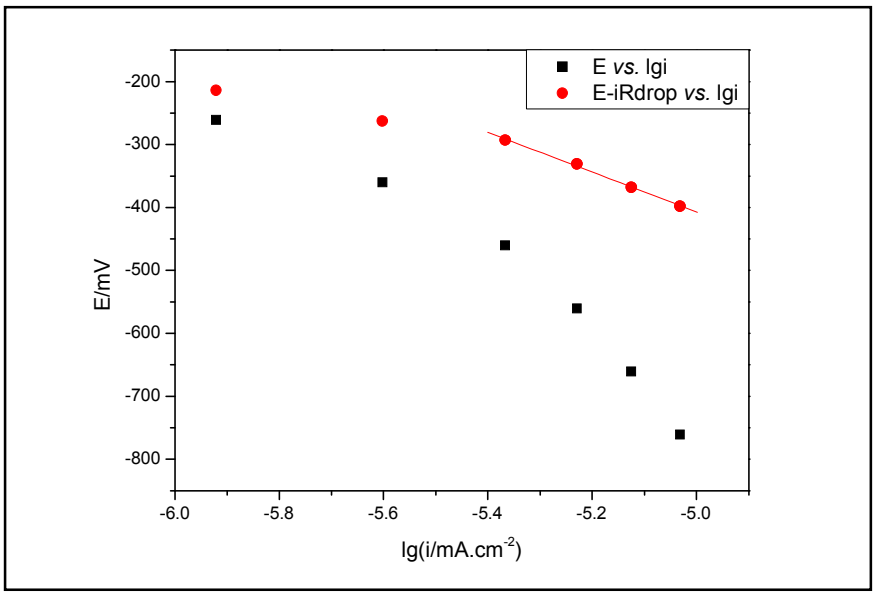
Here in this part, results of duplicate samples (Sample Ⅰ and Sample Ⅱ) are shown.

- **Potentiostatic Measurement Results**

The polarisation result for a coated panel after being coupled with a piece of bare mild steel and exposed to 3.5% NaCl solution for 7 days is shown in Fig.5.1, a) for Sample Ⅰ and b) for Sample Ⅱ, as E *vs.* lgi (Tafel plot). However, because the polarisation curve was measured through the high - resistance coating, the measurements contain a large iRdrop associated with current flowing through the paint. Therefore, the potential, E, has been corrected for ohmic potential drop in the coating (E-iRdrop *vs.* lgi) by adding the applied overpotential to the rest potential and subtracting the iRdrop (steady state current multiplied by the film resistance). Film resistance values were given by the EIS measurements (The following section will give the details about the film resistance determination.). After correction, we see the true electrode behaviour.



a)



b)

Fig.5.1 Polarisation results of EC coated mild steel after being coupled with bare mild steel and exposed to 3.5% NaCl solution, day 7: a) Sample Ⅰ; b) Sample Ⅱ.

The polarisation curves after correction for the "iRdrop" have been shown. It is apparent that though there is difference between these two panels, the cathodic reactions of them both obey Tafel law (the red lines), with the Tafel slopes of -453 mV for Sample Ⅰ and -316 mV for Sample Ⅱ.

- **EIS Results**

Fig.5.2 gives the Nyquist plots of the coated panel of Sample I after being coupled with bare mild steel for 3 days, 4 days and 7 days. All measurements were taken at the coupled potential.

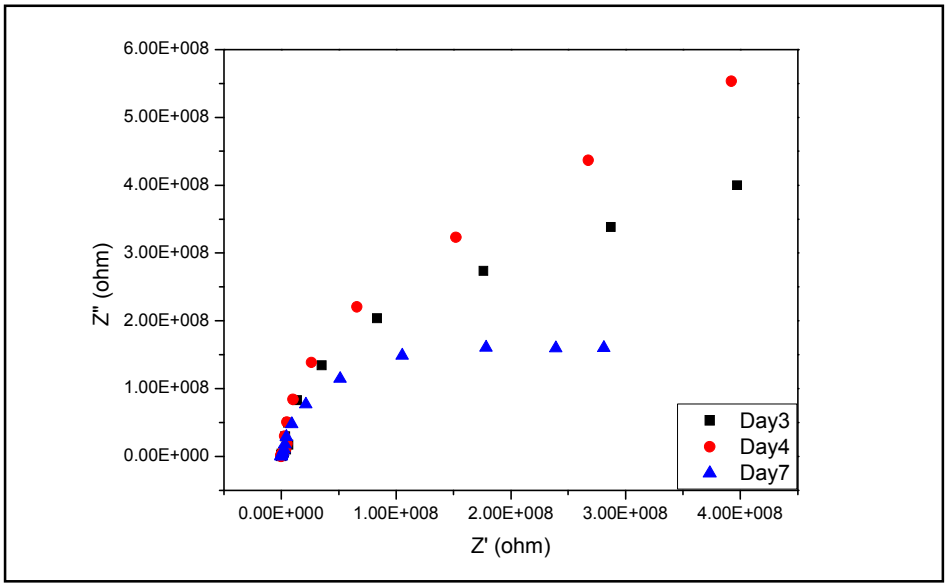


Fig.5.2 Nyquist plots for the coated panel of Sample I.

As demonstrated in Chapter 2, the high frequency semi-circle, which is the left part on the Nyquist plot, is the impedance response of the coating and the low frequency semi-circle gives information about the corrosion reaction. An equivalent circuit model of R(Q(R(QR))) (Fig.5.2) was used to fit the data.

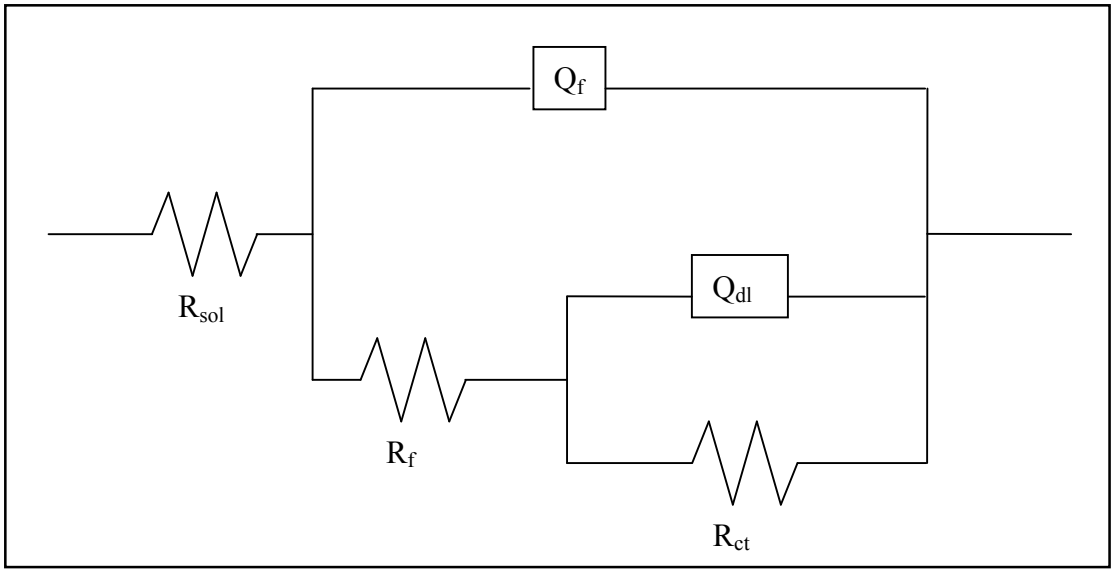


Fig.5.2 R(Q(R(QR))) model. R_{sol} is the solution resistance; R_f is the film resistance; R_{ct} is the charge transfer resistance; Q_f is the constant phase element (CPE) corresponding to film capacitance and Q_{dl} is the CPE corresponding to double layer capacitance.

The fitting results of Sample Ⅰ are presented in Table.5.1.

Time/day	$R_{sol}/\Omega\cdot cm^2$	Q_f (F)	n	$R_f/\Omega\cdot cm^2$	Q_{dl}/F	n	$R_{ct}/\Omega\cdot cm^2$
3	0.03873	1.25E-9	1	8.463E7	4.349E-10	0.8491	6.694E8
4	2.911E-6	1.261E-9	1	9.993E7	5.371E-10	0.7581	1.317E9
7	0.03519	1.295E-9	1	8.254E7	5.858E-10	0.7581	2.737E8

Table.5.1 EIS fitting data R(Q(R(QR))) for the coated panel of Sample Ⅰ immersed in 3.5% NaCl solution.

As Sample Ⅰ, fitting results for EIS measurements of Sample Ⅱ are shown in Table.5.2.

Time/day	R_{sol}/Ω	Q_f (F)	n	R_f/Ω	Q_{dl}/F	n	R_{ct}/Ω
3	0.009999	1.148E-9	1	3.317E7	2.996E-9	0.7081	2.949E7
4	0.04639	1.161E-9	1	3.322E7	1.512E-9	0.818	3.716E7
7	0.01516	1.181E-9	1	3.896E7	3.138E-9	0.8643	2.502E7

Table.5.2 EIS fitting data R(Q(R(QR))) for the coated panel of Sample II immersed in 3.5% NaCl solution.

Table.5.1 and Table.5.2 show that the coating resistances of the coated panels of these two samples were of the order of $10^7\ \Omega$ throughout the measuring period, suggesting that over the time scale of a typical disbonding test, the barrier properties of the coating remain good. Film resistance (R_f) values as shown in Table.5.1 and Table.5.2 were used for the correction of "iRdrop" for the polarisation curves.

5.4 Conclusions

The cathodic reaction of a coated panel coupled with a bare metal immersed in NaCl solution is not controlled by the high coating resistance (the response is not ohmic), nor do we find that the reaction controlled by oxygen transport through the coating, but obeys Tafel law.

If an intact coating does not control the cathodic reaction through control of the ionic current, or oxygen transport, it is reasonable to suppose that with a defect where ions and O_2 have easier access that the cathodic reaction will be under activation control, obeying the Tafel law as seen here.

Chapter 6 Mathematical Model for Cathodic Disbonding

6.1 Introduction

One important conclusion from Chapter 5 is that the cathodic reduction of oxygen within the disbond should be under activation control, rather than diffusion control. Here we explore the consequence through a mathematical model of the current flow beneath the paint. The model is based on the prevalent view that the anode is at the defect, with only cathodic processes beneath the paint.

6.2 Mathematical model for potential and current within the disbond

6.2.1 Model development

A crevice-like solution- (or gel-) layer (possibly degraded coating) is found at the coating/metal interface during cathodic disbonding. Fig.6.1 gives a simplified schematic diagram showing an idealised corroding “crevice” for a disbonded system.

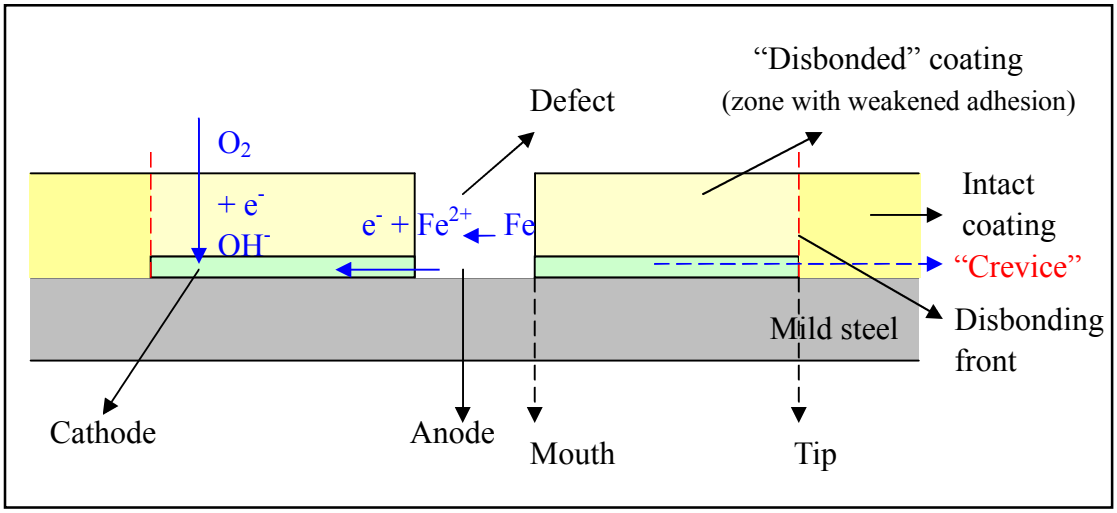


Fig.6.1 Schematic diagram of an idealised corroding "crevice" for a disbonded system

Mathematical models help understand the fundamental mechanisms underlying the cathodic disbonding and make predictions about conditions beneath the coating. A mechanistic model describing the electric potential profile and corrosion current within a corroding "crevice" is presented here. This model couples the anodic area within the defect with cathodic areas in the disbonded region and is based on the assumption that a uniform conducting layer forms along the coating/metal interface during disbonding. The thickness of the layer and its conductivity are treated as constant with position and time.

Nomenclature

x: distance measured from the crevice mouth;

t: crevice gap (taken to be uniform across the length of the "disbonded" region), m;

l: length of crevice (from mouth to tip), m;

w: width of crevice, m;

i_x: cathodic current density within the disbond (at position x), $mA \cdot m^{-2}$;

E_M: the boundary potential at the mouth (the open end) of the crevice, mV;

E_T: the potential at the crevice tip, mV;

κ: conductivity of the "solution"-layer within the crevice, $\Omega^{-1}\cdot m^{-1}$, (taken to be uniform as a first approximation);

A: A = wt, cross-section area of the disbond, m^2;

β: $\beta = \frac{b}{2.3}$, Tafel slope, b, of the Tafel equation for the cathodic reaction of oxygen, $\eta = a + b \lg i$, where η is the surface overpotential, mV;

i_M: cathodic current density at the crevice mouth, $mA\cdot m^{-2}$;

i_T: current density at the crevice tip, $i_T = 0$.

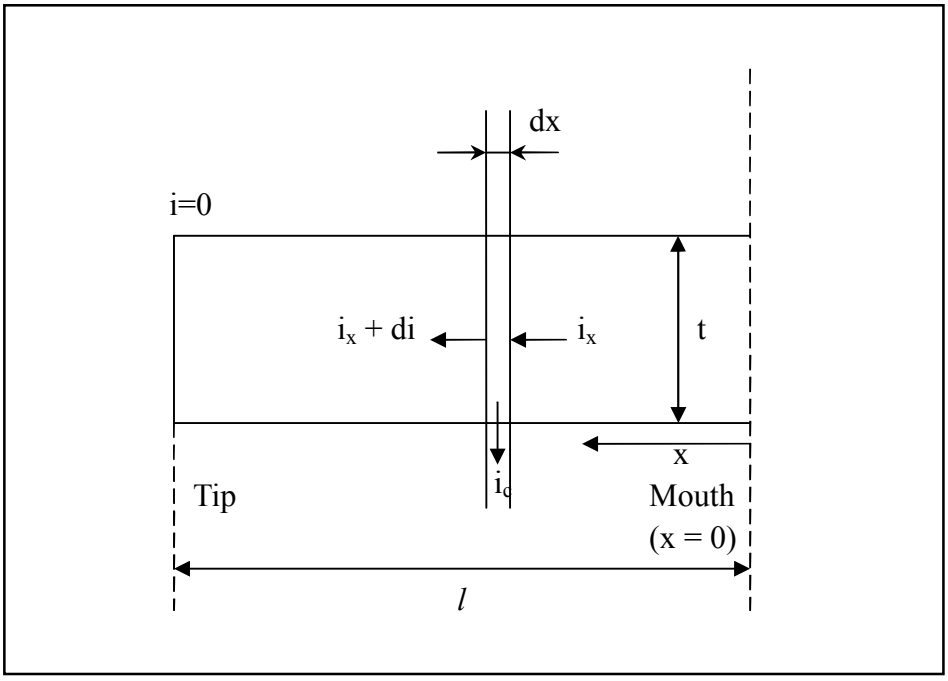


Fig.6.2 Schematic illustration of the crevice model.

The current density i passing through the cross-sectional area perpendicular to the direction of current can be calculated directly from the electric field, $\frac{dE}{dx}$, using ohm's law [134].

$$i = \kappa \frac{dE}{dx} \qquad \textit{[Equation 6.1]}$$

Because the cathodic reaction beneath the coating follows Tafel law,

$E - E_M = \beta \ln \frac{i}{i_M}$, where β and i_M are found from experiment and E_M is the rest potential measured during EIS experiments.

The cathodic current density at the electrode surface can be expressed as a function of x,

$$i_c = i_M \exp\left(\frac{E_x - E_M}{\beta}\right) \qquad \textit{[Equation 6.2]}$$

Thus the current density in the crevice increases across an element dx from i_x to $i_x + di$, defined by,

$$wtdi = i_M \exp\left(\frac{E - E_M}{\beta}\right) wdx \qquad \textit{[Equation 6.3]}$$

Combining Equation 6.1 and 6.3, it gives,

$$\frac{ti_x di}{i_M \kappa} = \exp\left(\frac{E - E_M}{\beta}\right) dE \qquad \textit{[Equation 6.4]}$$

Therefore, if we integrate Equation 6.4, at the position x, it gives (at the crevice tip, current $i_T = 0$),

$$\frac{ti_x^{\,2}}{2i_M \kappa} = \beta\left[\exp\left(\frac{Ex - E_M}{\beta}\right) - \exp\left(\frac{E_T - E_M}{\beta}\right)\right] \qquad \textit{[Equation 6.5]}$$

Substituting i_x from Equation 6.5 into Equation 6.1 gives,

$$\frac{dE}{\sqrt{\exp\left(\frac{E_x - E_M}{\beta}\right) - \exp\left(\frac{E_T - E_M}{\beta}\right)}} = \sqrt{\frac{2i_M \beta}{\kappa t}} dx \qquad \textit{[Equation 6.6]}$$

For x = 0, $E_x = E_M$ and x = l, $E_x = E_T$, integrate Equation 6.6, giving,

$$x = \frac{[\tan^{-1}(\sqrt{\exp(\frac{Ex - E_T}{\beta}) - 1}) - \tan^{-1}(\sqrt{\frac{1}{\exp(\frac{E_T - E_M}{\beta})} - 1})] \bullet \sqrt{\exp(\frac{E_M - E_T}{\beta})}}{\sqrt{\frac{i_M}{2\kappa t \beta}}}$$

[Equation 6.7]

6.2.2 Numerical simulation

To calculate numerical value from the analytical solution, we need values from various parameters: some are experimental results, some we need to estimate, since in practice there is no real information pertaining to the interfacial layer at the disbond.

The boundary potential at the mouth of the crevice, E_M = -685 mV which is the experimental result from Section 4.2.6 recorded by the Pico-Log system. The cathodic reaction of oxygen obeys Tafel law with the Tafel equation of E = -453 lgi – 3153, thus, β = -197 mV and $i_M = 3.6 \times 10^{-2}$ mA·m^{-2} (calculated with E_M = -685 mV). Ideally, there are two options for the assumption for the parameters. **Option 1** is the interfacial layer is NaCl solution (assumed to be the same as the bulk solution, here is 3.5% NaCl solution), thus the conductivity κ = 5.1 Ω^{-1}·m^{-1} [135, 136] and the thickness of this layer, t, is 100 nm. **Option 2** is the interfacial layer is the polymer film. Leng *et al.* [55] reported that the diffusion coefficients of species in the regions undergoing cathodic delamination were two orders of magnitude smaller than in aqueous medium. Therefore, the conductivity estimated here is κ = 0.05 Ω^{-1}·m^{-1}. The thickness of the interfacial layer, t = 100 nm. With these parameters, the plots of E_x *vs.* x, i_c *vs.* x and i_x *vs.* x, with different E_T values therefore different crevice lengths of

both options (Fig.6.3 – Fig.6.5 for Option 1 and Fig.6.6 – Fig.6.8), can be obtained according to Equation 6.7, 6.2 and 6.5, respectively. However, we must bare in mind when viewing the following simulated results that the surface area value we took is the whole surface when calculating the current density which may lead to overestimated values. Therefore, the results shown below with the assumed values just show the trend of the potential profiles and the current density within the disbond under simplified conditions. In practice, it may be a lot more complicate.

Option 1

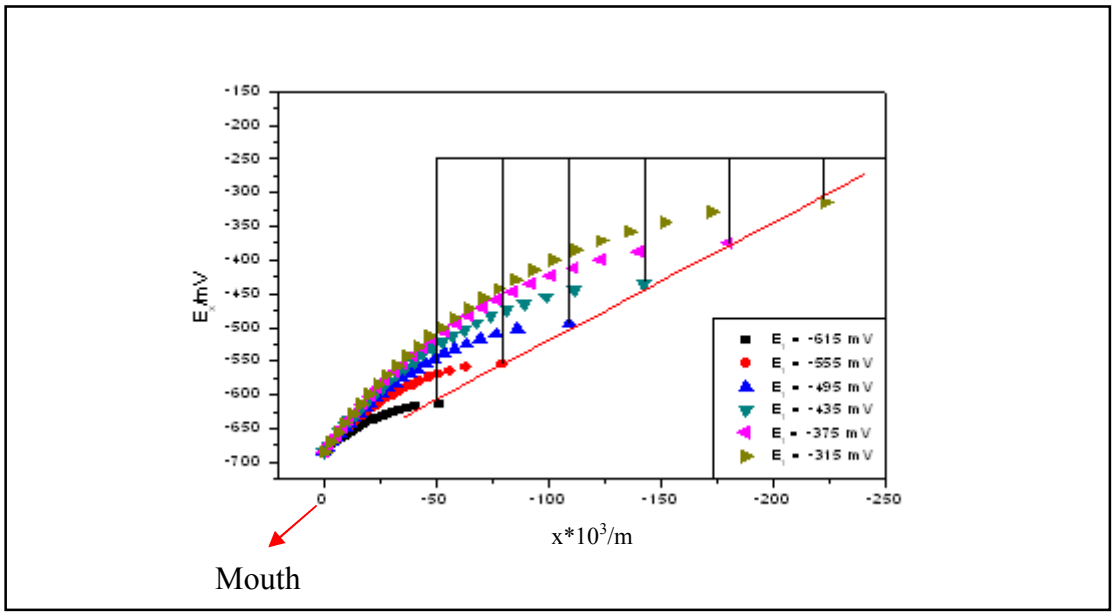


Fig.6.3 Electric potential profiles within the disbond (E_{intact} = -250 mV).

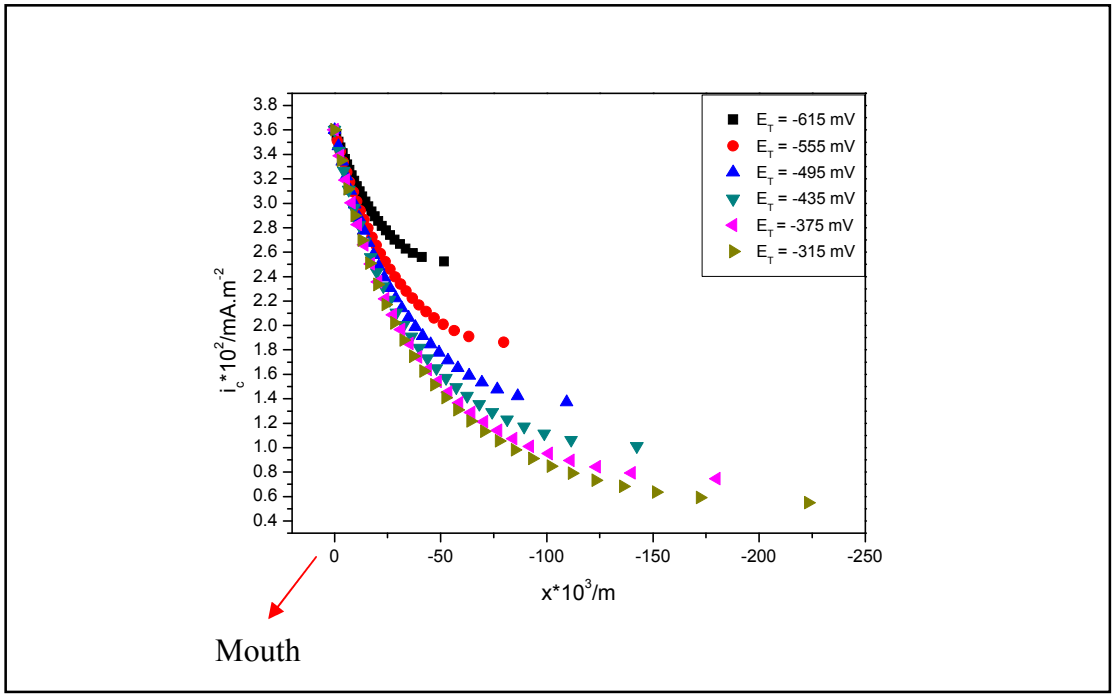


Fig.6.4 Cathodic current density at the electrode surface

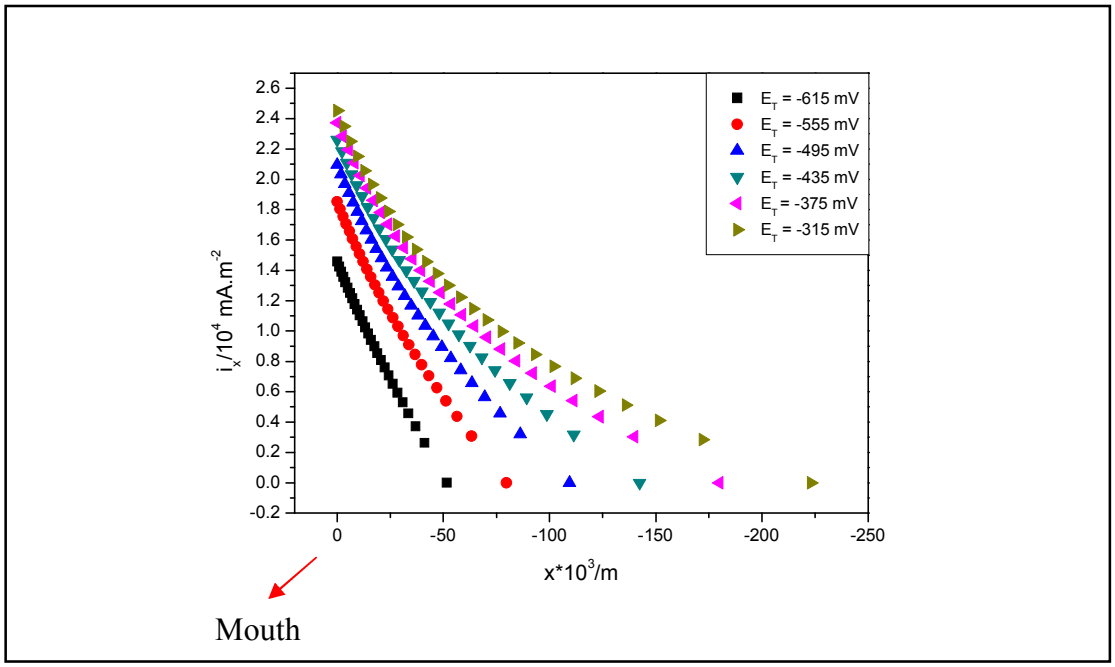


Fig.6.5 Cathodic current within the disbond

Option 2

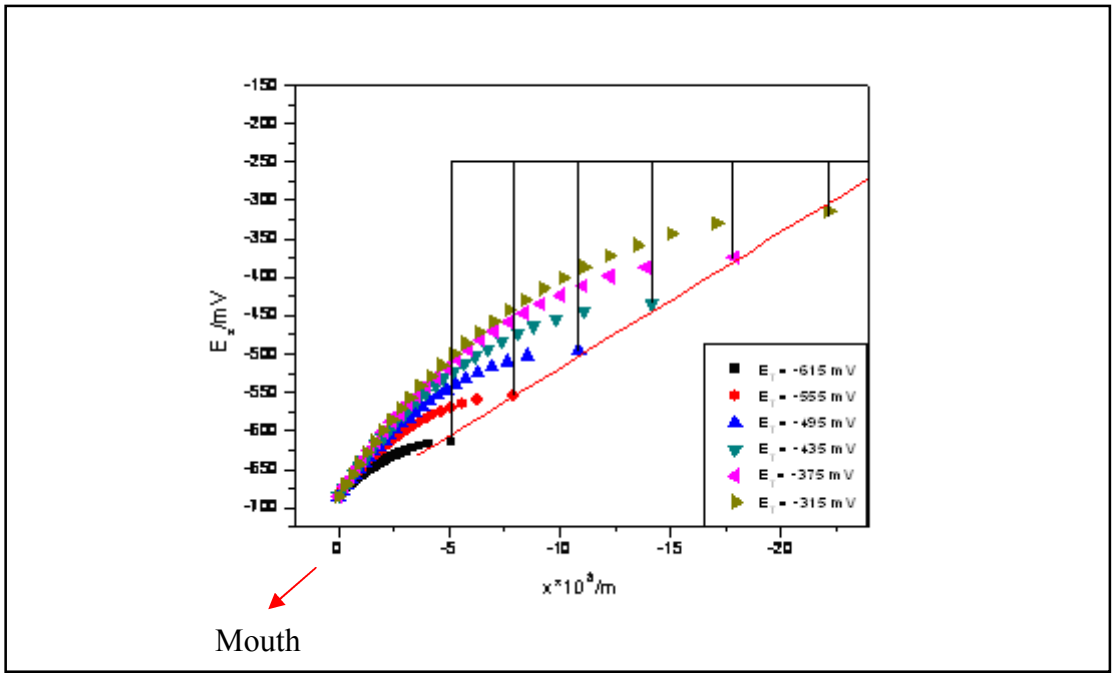


Fig.6.6 Electric potential profiles within the disbond (E_{intact} = -250 mV).

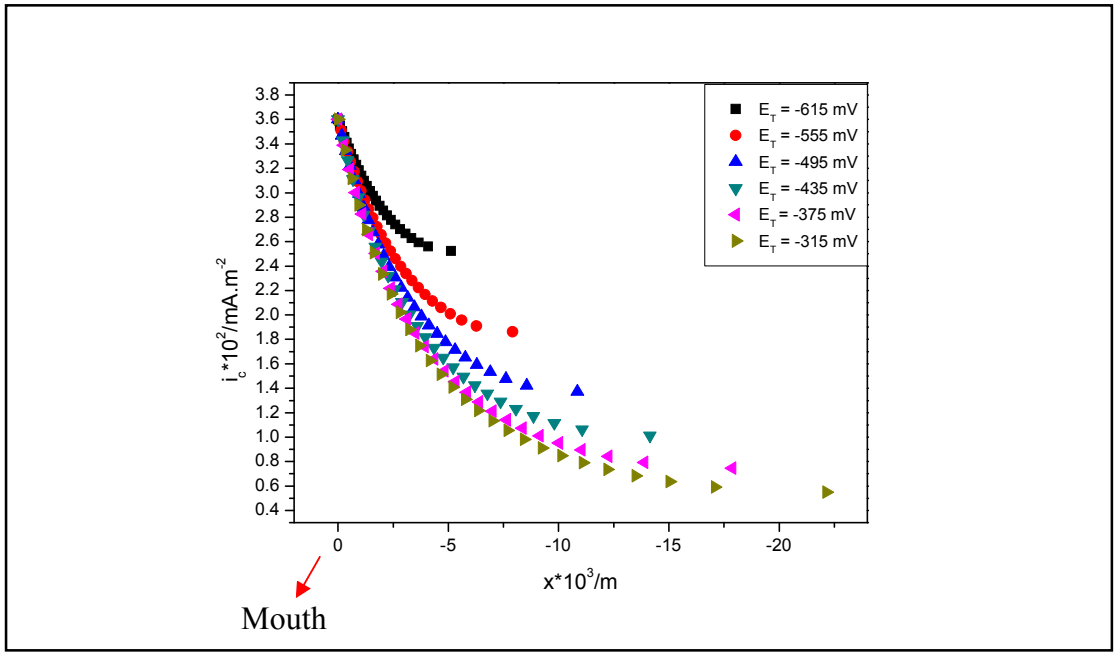


Fig.6.7 Cathodic current density at the electrode surface

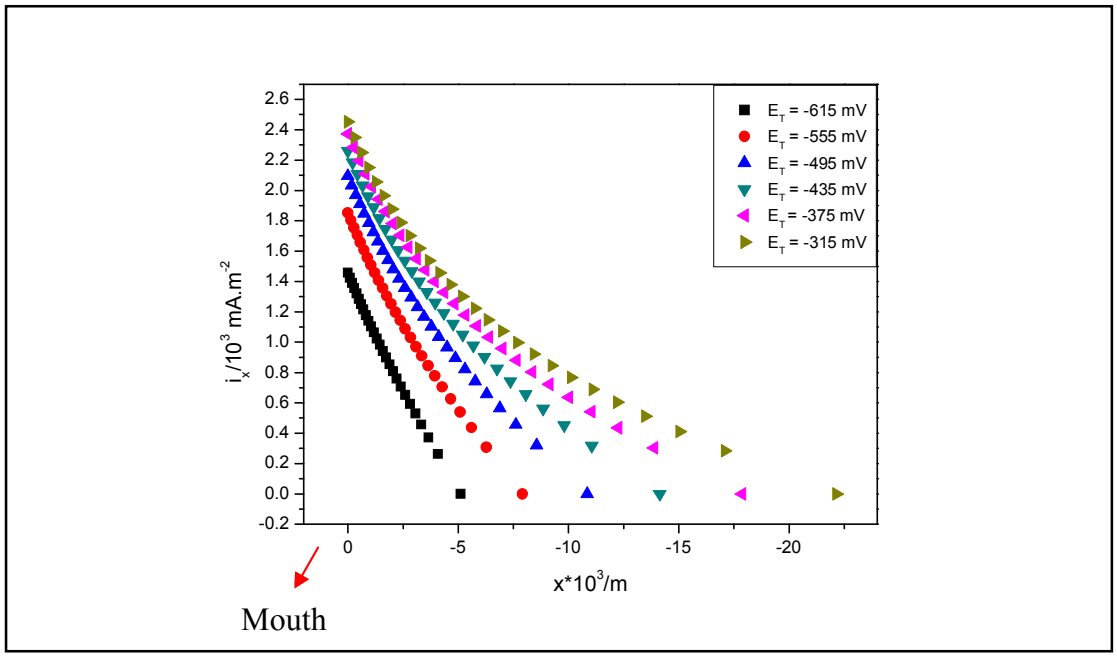


Fig.6.8 Cathodic current density within the disbond

It is clearly shown in Fig.6.3 (based on the assumption of Option 1) that with a tip potential of -315 mV would require a crevice length of 0.2 m for a disbond. With the crevice length within a reasonable range, the potential at the tip of the crevice is still very close to the potential of the mouth. Consequently, the potential is low everywhere within the crevice thus the potential difference between the tip of the disbond and the intact coating is large and the current density is very big which may not be seen in practice. While based on the assumption of Option 2, as Fig.6.6 shows, with a reasonable crevice length, the potential difference between the mouth and tip is reasonable and more close to the one seen in the real case. Also, the trends for the variation of potential and current with position are consistent with the literature data [55-59, 85], suggesting the assumption for the parameters of Option 2 are reasonable, although in practice, the interfacial layer is a lot more complicate than the assumed condition (*i.e.* the interfacial layer is very likely to be a weak layer of degraded

coating).

It is clear that the disbonding distance increases as the potential increases and the potential gradient along the crevice has a massive effect on local current density for a cathode under activation control, most OH^- ions are generated near mouth, but some are generated deeper into crevice though in steady state there are some diffuse out, which results in the highest pH at tip. Also, when the potential of the disbonded region equals that of the intact coating ($E_x = E_{intact}$), disbonding stops which is the real case as seen by Sharman [68] and Crossen [53] (it should be noted that the solution used in his work is very dilute, 0.05M NaCl solution).

6.3 Conclusions

A simple analytical model in which the cathodic reaction obeys the Tafel equation and the disbonded layer is assumed to have uniform conductivity and thickness produces realistic potential profiles and shows that oxygen reduction is mostly located near the disbond mouth. Effect of different parameters (κ, t, β, i_M or E_M) on potential drop, disbonding distance, and current density within the disbond and of the electrode surface can be estimated through this model. It can also account clearly for practical situations where disbonding ceases after some time.

Chapter 7 Summary of Conclusions and Future Work

7.1 Summary of Conclusions

Work presented in this thesis gives new insights into cathodic disbonding of epoxy coatings from mild steel using a combination of techniques (SKP, SAM, EIS and optical microscopy). The conclusions derived from the experiments carried out are summarised below.

- The use of SAM has allowed the examination of processes occurring at the coating/metal interface. SAM study on cathodic disbonding of an unpigmented epoxy coated mild steel with an artificial defect showed that the disbond spreads away from the defect but without complete loss of adhesion, as verified by peel-testing experiments. The reduction in adhesion is attributed to the reduction of oxygen at the coating/metal interface which leads to either alkaline hydrolysis of the bonds (between the coating and the substrate surface) responsible for the adhesion or the generation of free radicals which result in the chemical attack on bonds or degradation of the coating. Blisters were seen forming within the disbonded region with the number and size increasing with the exposure time. SKP potential maps showed that local anodes formed which leads to local accumulation of ions that then generate blisters by osmosis.
- Semi-immersion tests have shown that transport is mainly along the coating/metal

interface leading to a symmetrical disbonding of the opposite sides of the defect, though one was immersed in the solution and the other only exposed to water-saturated air. It did not show any reason why the disbonding of the scribed coated sample immersed in the solution and the coated sample only exposed the defect in the solution and the rest exposed to humid air give different behaviours.

- Increase in coating thickness causes only a slight reduction in disbonding rate, confirming that transport through the paint has only a minor role and the coating/metal interface is the main transport route.
- The disbonding rate depends on the cation type, but the disbonding rates are in the sequence of KCl > CsCl > NaCl > LiCl. KCl > NaCl > LiCl and CsCl > NaCl > LiCl are as expected, but anomalous sequence of KCl > CsCl can not be explained yet.
- The disbonding is much faster in the more concentrated solution which is due to a higher Na^+ flux in compared to OH^- flux out, therefore a higher concentration of alkali formed between the coating and the substrate metal and larger cathodic currents was caused leading to severe disbonding.
- The disbonding rates at 22℃ and 30℃ are much slower than those at 40℃ and 50℃, which leads us to believe that there is a critical point between 30℃ and 40℃ where a transition takes place in the weak layer found by the attack on the bonds between the coating and the metal.
- Cathodic disbonding rate increased with the more negative potential applied which is attributed to the more rapid cathodic reduction or faster ion migration

resulting from the bigger potential difference between the defect and the intact coating or the ability to sustain a bigger potential difference between the disbond tip and the undisbonded region;

- The free corrosion potential during cathodic disbonding dropped about 100 mV in the first 2000s and a relatively larger potential variation during the first day due to the initiation of disbonding but kept constant afterwards which shows that there will be little effect of free corrosion potential on disbonding rate over time, ruling out the possibility that the retardation over time is due to the free corrosion potential change.
- The disbonding of unpigmented coatings follows parabolic kinetics with ion transport along the coating/metal interface as the rate-controlling process; the pigmented coatings follow linear disbonding kinetics but the rate-controlling process of which has not been clear yet.
- Less blisters occurred for the pigmented coatings which is contributed to the ability of the zinc phosphate pigment to suppress the formation of anodes, but it is not clear why talc produces a similar effect.
- The cathodic reaction beneath the intact coating is not controlled by the high coating resistance, nor the oxygen transport through the coating, but obeys Tafel law, with the Tafel slope, bc = 453 mV.
- A mathematical model describing the “crevice corrosion – like” potential profile and current within the disbond of coated metals has been presented. It shows that oxygen reduction is mostly near the disbond mouth and can account for the

practical situation where disbonding ceases after some time. Also, the effects of changing the parameters help make predictions about the conditions beneath the coating.

This work successfully characterised the cathodic disbonding of epoxy coated mild steel both physically (by SAM and optical microscopy) and electrically (by SKP and EIS) along with the investigation of several factors affecting the cathodic disbonding process, which helps the understanding of the cathodic disbonding processes of the epoxy coated mild steel immersed in salt solution. However, it is not very likely that any single or universal disbonding mechanism exists. It is more probable that a number of possible mechanisms that occur in combination. Therefore, it is actually very challenging to get a full understanding of the cathodic disbonding mechanism. Existing mechanisms of the disbonding process cannot account for all the behaviours seen here.

7.2 Future Work

Regarding the questions remained and to better understand the cathodic disbonding process, the areas for additional studies are listed as following.

1) Due to the different behaviours as shown in the SKP potential maps of this work with Stratmann's results [45, 55, 56, 129], experiments with exactly the same setup as Stratmann are necessary. If we get the same results as Stratmann's with our coating system, then the experimental setup plays an important role; if we still get different results, we may need to test with different coating systems.

2) Interfacial chemical analysis could be carried out by using X-ray photoelectron spectroscopy (XPS), Auger electron spectroscopy (AES) or Secondary ion mass spectrometry (SIMS) to study the ion distribution after disbonding to allow better understanding of the cathodic reactions occurring at the coating/metal interface during cathodic disbonding process and confirm the anode/cathode arrangements in the SKP results obtained in this work.

3) pH measurements by inserting probes would be helpful to get the information of the interfacial conditions (reactions, potential or current distribution) along the crevice.

4) Further experiments on studying the effect of cations (0.5M LiCl NaCl KCl and CsCl solutions) with the same coating system used in this work should be carried out to provide more persuasive evidence for the discussion in Section 4.2.7.

5) It has been noted that different results have been obtained by workers in this field using different types of coating (Sørensen *et al*. [87] studied various types of coatings when investigating the influence of free radicals on rate of disbonding and found different behaviours of these coatings.), therefore it is hoped that a combination of SAM and SKP as in this thesis will be applied to a wide range of paint systems.

APPENDIX

SKP Data Processing

Potential Mapping

A test sample for SKP measurement is labelled as in Table.1. Numbers represent the local positions. The blue lines give the tip tracking route.

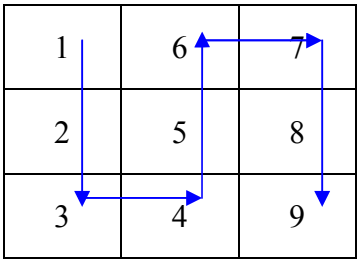


Table.1 Labelled positions on a sample for SKP measurement

The tip scans across the sample surface and WF data obtained by the SKP is as shown in Table.2 (numbers shown are not the real WF values, but represent the values corresponding to the positions labelled in Table.1). It is apparent from Table.2 that the data acquired by SKP is transposed comparing with the position points which is caused by the SKP data acquisition system.

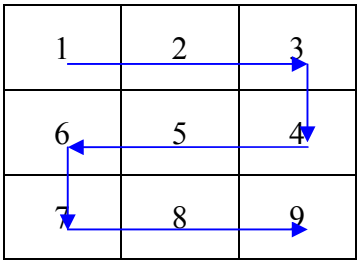


Table.2 Alignment of WF Data obtained directly from SKP

Using the calibration graph, the specimen potential values are able to be converted

from the WF data measured by the SKP by using the software OriginPro 7.5. And the potential distribution is presented in the form of contour map.

After “transpose” and “convert to matrix”, the matrix of potential or current is as Table.3.

1	6	7
2	5	8
3	4	9

Table.3 Potential data over the sample surface

The SKP data has been plotted using OriginPro 7.5 to get the potential/current contour map. The output of the Table.3 by OriginPro 7.5 actually corresponds to the Table.4 with a contour map shown as Fig.1.

3	4	9
2	5	8
1	6	7

Table.4 Output from OriginPro 7.5

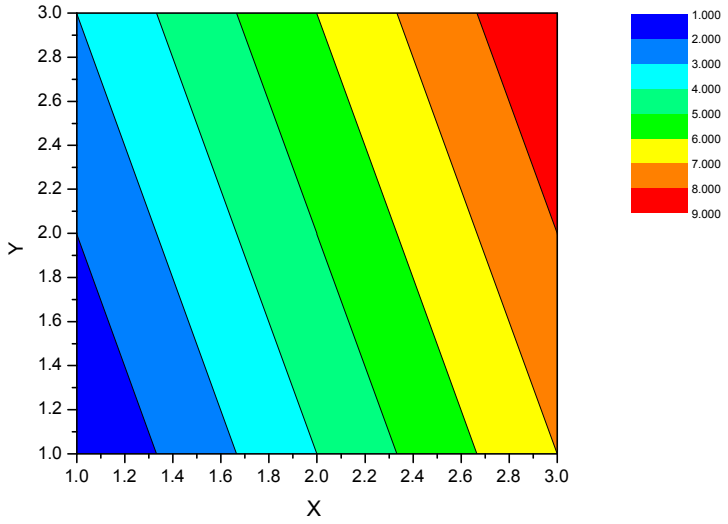


Fig.1 SKP contour map corresponding to Table.4

While, the SKP data wanted is as in Table.3, therefore, by changing the axis in Fig.1, Fig.2 is obtained corresponding to the original orientation.

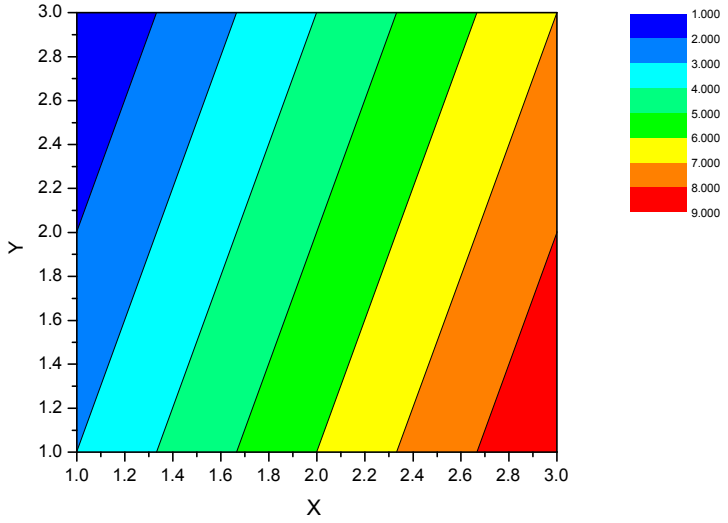


Fig.2 SKP contour map

The SKP potential map results in this thesis are all processed based on this method.

References

1. Landolt, D., *CORROSION AND SURFACE CHEMISTRY OF METALS*. 2007.
2. G.P.A.Turner, *Introduction to Paint Chemistry and Principles of Paint Technology*. 1988, New York, USA: Chapman & Hall.
3. B.Bieganska, M.Zubielewicz, and E.Smieszek, Progress in Organic Coatings, 1988. **16**: p. 219.
4. A.Kalendová, Anti-corros. Meth. Mater 1998. **45**: p. 344.
5. M.Mahdavian A. and M.M.Attar, Electrochimica Acta 2005. **50**: p. 4645.
6. K.R.Trethewey and J.Chamberlain, *Corrosion for Science and Engineering*. 2nd ed. 1995.
7. J.E.O.Mayne, Anti-Corrosion Methods and Materials, 1973. **20**: p. 3.
8. J.E.O.Mayne, J.O.C.C.A, 1949. **32**: p. 481.
9. H.Haagen and W.Funke, J.O.C.C.A, 1975. **58**: p. 359.
10. R.A.Dickie and F. Floyd, Polymeric Materials for Corrosion Control, ACS Symposium Series, 1986. **322.**: p. 1.
11. J.E.O.Mayne, Official Digest 1952. **24**: p. 127.
12. J.E.O.Mayne and D.J.Mills, J.Oil Colour Chemists Assocn., 1975. **58**: p. 155.
13. C. R. Bacon, J. J. Smith, and R.M. Rugg, Ind. Eng. Chem. , 1948. **40**: p. 161
14. R.D.Armstrong, B.W.Johnson, and J.D.Wright, Electrochimica Acta, 1991. **36**: p. 1915-1923.
15. H.Leidheiser, J. and M.W.Kendig, Corrosion, 1976. **32**: p. 69.
16. S.Guruviah, J.O.C.C.A., 1970. **58**: p. 669.
17. E.M.Kinsella and J.E.O.Mayne, in *3rd International Congress on Metallic Corrosion*. 1966: Moscow. p. 117-120.
18. C.C.Maitland and J.E.O.Mayne, Official Digest 1962. **34**: p. 972.
19. J.E.O.Mayne and J.D.Scantlebury, Br.Polym.J., 1970. **2**: p. 240-243.
20. J.E.O.Mayne, D.J.M., J.O.C.C.A. , 1975. **58**: p. 155.
21. K.Wapner, M.Stratmann, and G.Grundmeier, Electrochimica Acta, 2006. **51**: p.

3303.

22. L.Beaunier, I.E., J.C.Lestrade and H.Takenouti, Surface Techn., 1976. **4**: p. .
23. J.D.Scantlebury and K.N.Ho, J.Oil Colour Chem.Assoc., 1979. **62**: p. 89.
24. M.Kendig, F.Mansfeld, and S.Tsai, Corrosion Science, 1983. **23**: p. 317-329.
25. F.Mansfeld, Journal of Applied Electrochemistry, 1995. **25**: p. 187-202.
26. E.P.Whyte and J.M.Sykes, Corrosion Science, 2007. **49**: p. 3361-3380.
27. J.Barraclough and J.B.Harrison, J.Oil Colour Chem. Assoc. , 1965. **48**: p. 341.
28. S.Turgoose, M.Hazzaa, and Y.J.Qian, U.K. Corrosion '86, Inst. Corr. Sci. & Tech., 1986: p. 75
29. S.Turgoose, *Binders & Paints*, in *Symposium on Anticorrosive Pigments*. 1987.
30. S.Turgoose, *The Electrochemical Society*, in *Proc. Symp. Advances in Corrosion and Protection of Organic Coatings*, D. Scantlebury and M. Kendig, Editors. 1989: Pennington, NJ. p. 468.
31. A. Amirudin, et al., Progress in Organic Coatings, 1995. **25**: p. 339.
32. B.P.F.Goldie, JOCCA, 1988. **9**: p. 257-270.
33. R.D.Armstrong and S.Zhou, Corrosion Science, 1988. **28**: p. 1177-1181.
34. B.Chico, et al., Progress in Organic Coatings, 2008: p. 283-290.
35. F.Deflorian and L.Fedrizzi, J.Adehsion Sci.Technol., 1999. **13**: p. 629-645.
36. K.Hoffmann and M.Stratmann, Corros.Sci., 1993. **34**: p. 1625.
37. R.A.Dickie, Prog.Org.Coatings, 1994. **25**: p. 3-22.
38. X.J.Jin., K.R.Gowers, and J.D.Scantlebury, J.Oil Colour Chem. Assoc., 1988. **71**: p. 78.
39. L.Fedrizzi, F.Deflorian, and P.L.Bonora, Electrochim.Acta, 1997. **42**: p. 969.
40. T.R.Bullett and J.L.Prosser, Pro. Org. Coat. , 1972. **1**: p. 45-71.
41. W.Funke and H.Haagen, Ind.Eng.Chem.Prod.Res.Dev., 1978. **17**: p. 50.
42. W.Funke, J.Coat.Tech. , 1983. **55**: p. 31.
43. W.Funke, J.O.C.C.A., 1985. **68**: p. 229-232.
44. W.Funke, J.O.C.C.A., 1986. **69**: p. 78.
45. M.Stratmann, R.Feser, and A.Leng, Electrochimica Acta, 1994. **39**: p.

1207-1214.

46. W.Schwenk, 3-R International 1976. **15**: p. 389.
47. P.Walker, Official Digest, 1965. **37**: p. 1561.
48. P.Walker, J.O.C.C.A., 1974. **57**: p. 241
49. P.Walker, J.O.C.C.A. , 1985. **68**: p. 319.
50. M.Kendig, R.Addison, and S.Jeanjacquet, J. Electrochem. Soc., 1990. **137**: p. 2690.
51. R.Addison, M.Kendig, and S.Jeanjaquet, *Ultrosonics Symposium*, in *IEEE*. 1988. p. 739-742.
52. R.Addison, M.Kendig, and S.Jeanjaquet, Acoustic Imaging, 1989. **17**: p. 143.
53. J.D.Crossen, et al., Faraday discuss., 1997. **107**: p. 417.
54. M.Stratmann, H.Streckel, and B.Bunsenges, Phys. Chem., 1988. **92**: p. 1244
55. A.Leng, H.Streckel, and M.Stratmann, Corrosion Science, 1998. **41**: p. 579-597.
56. A.Leng, H.Streckel, and M.Stratmann, Corrosion Science, 1998. **41**: p. 547-578.
57. W.Fürbeth and M.Stratmann, Corrosion Science, 2001. **43**: p. 207-227.
58. W.Fürbeth and M.Stratmann, Corrosion Science, 2001. **43**: p. 229-241.
59. W.Fürbeth and M.Stratmann, Corrosion Science, 2001. **43**: p. 243-254.
60. M.Stratmann, et al., Progress in Organic Coatings, 1996. **27**: p. 261-267.
61. G..Williams and N.McMurray, J. Electrochem. Soc., 2001. **148**: p. B377-B385.
62. B.Reddy, M.J.Doherty, and J.M.Sykes, Electrochimica Acta, 2004. **49**: p. 2965-2972.
63. B.Reddy and J.M.Sykes, Progress in Organic Coatings, 2005. **52**: p. 280-287.
64. M.J.Doherty and J.M.Sykes, Corrosion Science, 2004. **46**: p. 1265-1289.
65. H.Leidheiser,J., W.Wang, and L. Igetoft, Progress in Organic Coatings, 1983. **11**: p. 19-40.
66. H.Leidheiser, J., J.Adehsion Sci.Technol., 1987. **1**: p. 79-98.
67. H.Leidheiser, J. and W.Wang, Journal of Coating Technology, 1981. **53**: p. 77-84.

68. J.D.B.Sharman, J.M.Sykes, and T. Handyside, Corrosion Science, 1993. **35**: p. 1375-1383.
69. J.I.Skar, *PhD Thesis*. 1990, University of Trondheim: Norway. p. 44.
70. O.Knudsen and J.I.Skar, *Paper No. 08005*, in *CORROSION*. 2008.
71. J.F.Watts and J.E.Castle, J.Mater.Sci., 1984. **19**: p. 2259-2272.
72. X.H.Jin, et al., *Adhesion and disbonding of chlorinated rubber on mild steel*, in *Advance in Corrosion Protection by Organic Coatings*, D. Scantlebury and M. Kendig, Editors. 1987, The Electrochemical Society: Pennington, NJ.
73. J.I.Skar and U.Steinsmo, Corrosion Science, 1993. **35**: p. 1385-1389.
74. H.Leidheiser, J., et al., in *Proc. 7th Intern. Conf. on Organic Coatings*. 1981: Athens, Greece.
75. K.McLeod, *PhD Thesis*. 1984, University of Oxford: Oxford. p. 130.
76. P.A. Sørensen, et al., Progress in Organic Coatings, 2010. **68**: p. 283-392.
77. H.Leidheiser, J. and W.Wang, in *Corrosion Control by Organic Coatings (Natl. Assocn. Corrosion Engrs.)*, J. H. Leidheiser, Editor. 1981: Houston, Texas. p. 70.
78. U.Steinsmo and J.I.Skar, CORROSION, 1994. **50**: p. 934-939.
79. H. Leidheiser, J., J.Coat.Tech. , 1981. **53**: p. 29.
80. J.L.Luo, et al., Progress in Organic Coatings, 1997. **31**: p. 289-295.
81. F.Deflorian and S.Rossi, Electrochimica Acta, 2006. **51**: p. 1736-1744.
82. R.A.Dickie and A.G.Smith, Chem. Tech., 1980. **10**: p. 31.
83. J.J.Ritter and J.Kruger, in *Corrosion Control by Organic Coatings (Natl. Assocn. Corrosion Engrs.)*, J. H.Leidheiser, Editor. 1981: Houston, Texas. p. 28.
84. K.L.Koehler, CORROSION, 1984. **40**: p. 5-8.
85. A.Leng, et al., Corrosion Science, 1998. **41**: p. 599-620.
86. G.Grundmeier and M.Stratmann, Werkstoffee und Korrosion, 1989. **49**: p. 150-160.
87. P.A.Sørensen, et al., J.Coat.Technol.Res., 2010. **Published online, 25 May**.
88. M.Hausbrand, M.Stratmann, and M.Rohwerder, Journal of the

Electrochemical Society, 2008. **155**: p. C369-C379.

89. K.R.Gowers and J.D.Scantlebury, Corrosion Science, 1983. **23**: p. 935.
90. N.A.Brunt, J. Oil Colour Chem.Assoc., 1964. **47**: p. 31.
91. D.M.James, J. Oil Colour Chem. Assoc. , 1960. **43**: p. 391
92. J.A.V.Laar, Paint Varn. Prod., 1961. **51**: p. 31.
93. W.Wettach, Official Digest 1961. **33**: p. 1427
94. T.R.Bullett and A.T.S.Rudram, J.Oil Coulour Chem.Assoc., 1961. **44**: p. 787.
95. W.W.Kittelberger and A.C.Elm, Ind.Eng.Chem. , 1947. **39**: p. 876.
96. H.Grubitsch, K.Heckel, and R.Saumer, Farbe Lack 1963. **69**: p. 655.
97. J.L.Prosser and T.R. Bullett, J.Oil Colour Chem.Assoc., 1962. **45**: p. 836
98. W.Funke, Progress in Organic Coatings, 1981. **9**: p. 29-46.
99. W.Funke, Ind. Eng. Chem.Prod. Res. Dev., 1985. **24**: p. 343-347.
100. L.A.van der Meer-Lerk and P.M.Heertjes, J.Oil Colour Chem.Assoc., 1975. **58**: p. 79.
101. H. Leidheiser, J., Corrosion 1982. **38**: p. 375.
102. J.E.O.Mayne, J.O.C.C.A. , 1950. **33**: p. 538.
103. J.E.Castle and J.F.Watts, Ind. Eng. Chem. Prod. Res. Dev. , 1985. **24**: p. 361
104. C.F.Sharman, Nature 1944. **153**: p. 621.
105. A.Bautista, Progress in Organic Coatings 1996. **28**: p. 49.
106. M.Iwata, et al., J. Jpn. Inst. Light Met., 1984. **34**: p. 531.
107. J.N.Defrancq, in *the Estal Symposium, Eurocoat Section*. 1994: Cannes, France
108. W.H.Slabaugh, et al., J.Paint Technol. , 1972. **44**: p. 76.
109. E.L.Koehler, Corrosion, 1977. **33**: p. 209.
110. H.Leth-Olsen and K.Nisancioglu, Corrosion Science, 1998. **40**: p. 1179.
111. G.Williams and H.N. McMurray, Electrochemistry Communications 2003. **5**: p. 871.
112. R.A.Lemons and C.F.Quate, Appl.Phys.Lett., 1974. **24**: p. 163-165.
113. A.Briggs and O.Kolosov, *Acoustic Microscopy*. Second Edition ed. 2010, UK: Oxford University Press.

114. http://www.bamr.co.za/velocity%20of%20materials.shtml.
115. *SKP Manual*: KP Technology Ltd.
116. I.D.Baikie, et al., Review of Scientific Instruments, 1991. **62**: p. 1326-1332.
117. M.J.Doherty, *PhD Thesis*. 2004, University of Oxford: Oxford, UK.
118. Private communication with Prof. J.M.Sykes., 2010.
119. E.P.Whyte, *PhD Thesis*. 2005, University of Oxford: Oxford, UK. p. 64.
120. M.Stern and A.L.Geary, J.Electrochem.Soc., 1957. **104**: p. 56.
121. D.M.Brasher and A.H.Kingsbury, J.Appl.Chem., 1954. **4**: p. 62.
122. J.M.Sykes, Corrosion Science, 2004. **46**: p. 515-517.
123. O.Knudsen and J.I.Skar, in *CORROSION*. 2008.
124. J.D.Crossen, et al., *Advances in Corrosion Protection by Organic Coatings*, ed. J.D.Scantlebury and M.Kendig. 1995: The Electrochemical Society 274-283.
125. R.T.Ruggeri and T.R.Beck, *Adhesion Aspects of Polymeric Coatings*, ed. K.L.Mittal. 1983, N.Y.: Plenum Press. 329.
126. L.Graham and J.A.Emerson, *Adhesion Aspects of Polymeric Coatings*, ed. K.L.Mittal. 1983, N.Y.: Plenum press.
127. J.D.Crossen, et al., *Organic Coatings for Corrosion Control*, ed. G.P.Bierwagen. 1998, Washington, DC: American Chemical Society. 106-122.
128. J.Wielant, et al., Corrosion Science, 2009. **51**: p. 1666.
129. A.Leng, et al., Corrosion Science, 1998. **41**: p. 599-620.
130. O.Knudsen, *PhD Thesis*. 1998, The Norwegian University of Science and Technology. p. 94.
131. J.M.Sykes and K.McLeod, eds. *Coatings and Surface Treatment for Corrosion and Wear Resistance*. ed. K.N.Strafford, P.K.Datta, and C.G.Googan. 1984, Ellis Horwood: Chichester. 295-314.
132. J.D.Sharman, *DPhil Thesis*, in *Department of Materials*. 1991, University of Oxford: Oxford. p. 74.
133. M.J.Doherty and J.M.Sykes, Corrosion Science, 2008. **50**: p. 2755-2772.
134. W.D.Callister, J., *Fundamentals of Materials Science and Engineering*. 2nd Edition ed. 2005, New York, USA: John Wiley & Sons, Inc.

135. P.W.Atkins, *Physical Chemistry*. Sixth edition. 1998, Oxford: Oxford University Press. 738.

136. *CRC Handbook of Chemistry and Physics, 9th Edition*, D.R.Lide and W.M.M. Haynes, Editors. 2009-2010, CRC Press. p. 5-71.